2016

Investigation of liquid rocket swirl coaxial injection dynamics under self-excited high frequency oscillations

Chad Jonathan Eberhart

INVESTIGATION OF LIQUID ROCKET SWIRL COAXIAL INJECTION DYNAMICS UNDER SELF-EXCITED HIGH FREQUENCY OSCILLATIONS

by

CHAD JONATHAN EBERHART

A DISSERTATION

Submitted in partial fulfillment of the requirements
for the degree of Doctor of Philosophy
in
The Department of Mechanical and Aerospace Engineering
to
The School of Graduate Studies
of
The University of Alabama in Huntsville

HUNTSVILLE, ALABAMA

2016

In presenting this dissertation in partial fulfillment of the requirements for a doctoral degree from The University of Alabama in Huntsville, I agree that the Library of this University shall make it freely available for inspection. I further agree that permission for extensive copying for scholarly purposes may be granted by my advisor or, in his/her absence, by the Chair of the Department or the Dean of the School of Graduate Studies. It is also understood that due recognition shall be given to me and to The University of Alabama in Huntsville in any scholarly use which may be made of any material in this dissertation.

Chad Jonathan Eberhart

08 April 2016

(date)

DISSERTATION APPROVAL FORM

Submitted by Chad Jonathan Eberhart in partial fulfillment of the requirements for the degree of Doctor of Philosophy in Mechanical Engineering and accepted on behalf of the Faculty of the School of Graduate Studies by the dissertation committee.

We, the undersigned members of the Graduate Faculty of The University of Alabama in Huntsville, certify that we have advised and/or supervised the candidate of the work described in this dissertation. We further certify that we have reviewed the dissertation manuscript and approve it in partial fulfillment of the requirements for the degree of Doctor of Philosophy in Mechanical Engineering.

Robert A Frederick Jr 4/11/16
Dr. Robert A. Frederick, Jr. (Date) Committee Chair

Kader Frendi - 4/11/16
Dr. A. Kader Frendi (Date)

4/13/16
Dr. D. Keith Hollingsworth (Date)

4-11-2016
Dr. David M. Lineberry (Date)

LEYVA.IVETT.A.1289757674 Digitally signed by LEYVA.IVETT.A.1289757674 DN: c=US, o=U.S. Government, ou=DoD, ou=PKI, ou=USAF, cn=LEYVA.IVETT.A.1289757674 Date: 2016.04.11 14:26:50 -04'00' 4/11/2016
Dr. Ivett A. Leyva (Date)

4/13/16
Dr. D. Keith Hollingsworth (Date) Department Chair

04/14/16
Dr. Shankar Mahalingam (Date) College Dean

4/27/16
Dr. David Berkowitz (Date) Graduate Dean

ABSTRACT

School of Graduate Studies
The University of Alabama in Huntsville

Degree Doctor of Philosophy College/Dept. Engineering/Mechanical and Aerospace Engineering

Name of Candidate Chad Jonathan Eberhart

Title Investigation of Liquid Rocket Swirl Coaxial Injection Dynamics Under Self-excited High Frequency Oscillations

Liquid-centered swirl coaxial injector elements used within liquid rocket combustion devices can exhibit self-excited and self-sustained oscillations known commonly as self-pulsations. The objective of this dissertation is to experimentally determine under non-reactive conditions how self-pulsation is excited and what fluid oscillators control its frequency. The phenomenon is explored for a study injector element within a range of fluid momentum flux conditions spanning 4 to 93 kPa for water flow and 12 to 585 kPa for gas flow. The recess length of the inner swirl post is also varied from 0 to 2 mm from the injector face.

Self-pulsation is diagnosed with fluctuating pressure measurements gathered both upstream of the injector and downstream in the far-field. High speed schlieren imagery of near-field spray behavior is also captured. Spectral analyses of pressure measurements and objective data-based modal decompositions of the imagery are combined for a characterization of oscillations during self-pulsation. For the conditions investigated, self-pulsation is found to occur over a wide range of frequencies of approximately 900 to 4000 Hz for both the non- recessed and recessed injector element. Self-pulsation is more pronounced with recess.

Near onset, imagery captures periodic, non-pulsatile stripping of liquid from surface waves that are consistent with characteristics of Kelvin- Helmholtz-type instability. The frequency of these spray patterns is found to correspond within approximately 15% of resonant spray patterns that occur at self-pulsation onset, and indicate that liquid stripping behavior is key to exciting the self-pulsation phenomenon.

An analysis of injector eigenmodes identifies fluid oscillator frequencies which could define that of self-pulsation once excited. Longitudinal eigenmodes of the injector are found to correspond in frequency to those of self-pulsation at some conditions. However, these resonant frequencies do not explain the full range of measured self-pulsations.

An analytical response analysis is carried out for the internal hydrodynamics of the swirl injector study element and flow conditions investigated. For the majority of conditions, the calculated frequencies of surface wave response within the injector's vortex chamber are found to correlate well with measured frequencies of self- pulsation to suggest that internal hydrodynamics participate as an additional fluid oscillator.

Abstract Approval: Committee Chair

Robert A Frederick Jr.

Dr. Robert A. Frederick, Jr.

Department Chair

Dr. D. Keith Hollingsworth

Graduate Dean

Dr. David Berkowitz

ACKNOWLEDGMENTS

The opportunity and guidance provided by my advisor, Dr. Bob Frederick, was nothing short of extraordinary in my time as his student. A special thanks is given to him for fostering a research environment in which it was a delight to work and develop within. Dr. David Lineberry's day-to-day counsel during testing is not lost to acknowledgement. Thanks must be extended to Dr. Ivett Leyva, who was influential to my interests as a doctoral student and whose encouragement was invaluable. I'd also like to thank Drs. Hollingsworth and Frendi for providing review and insights that shaped this work for the better. I would be remiss not to recognize the early mentorship of Jim Hulka, who helped to mold a foundation of ideas on which my studies came to be built.

Thank you to my mother and father, Lisa and Eugene Eberhart. As a youth, each impressed upon me a sense of inquisitiveness and hard work that has in no uncertain terms motivated the undertaking and completion of this pursuit. Now, as an adult, I can hope only to be but a shade of the parents that they have been and continue to be.

It is difficult to imagine this work possible without my wife, Antonia, as accessory. Even in the face of everyday sacrifice, her support of me in this endeavor has been carried out with patience, with grace, and with a steadfast love. My appreciation for Toni's assistance along the way runs deep, but it is towered by a larger appreciation for just how breathtaking of a person she is in all regards. Thank you.

TABLE OF CONTENTS

LIST OF FIGURES

LIST OF TABLES

LIST OF SYMBOLS

SYMBOL	DEFINITION
A	area
$\mathbb{A}$	injector geometric constant
a	temporal amplitude coefficient
$\mathfrak{a}$	injector geometric constant
bl	breakup length
Ca	Cavitation number
Cd	discharge coefficient
c	acoustic velocity
$\mathfrak{c}$	disturbance wave speed
d	geometric diameter
e	exponential function
Eu	Euler number
f	frequency
Fr	Froude number
H	linear transfer function
h	film thickness

$\mathbb{I}$	imaginary component
$\mathbb{K}$	bulk modulus
$\mathfrak{K}$	longitudinal index
$\mathfrak{k}$	dissipation factor
k	wavenumber
l	geometric length
M	Mach number
m	mass
$\dot{m}$	mass flow rate
mm	image row index
N	number of samples
N	eigenmode number
n	modal index
nn	image column index
P	momentum
p	pressure
Q	momentum flux
$\mathbb{Q}$	coherence criterion
R	geometric radius

$\mathfrak{R}$	Ritz vector
$\mathbb{R}$	real component
r	flow radius
$\mathfrak{r}$	Ritz value
Re	Reynolds number
$\Re\Re$	recess ratio
S	cross-power spectral density
$\tilde{S}$	companion matrix
St	Strouhal number
T	temperature
$\mathbb{T}$	transpose
t	time
TMR	Total Momentum Ratio
U	total expanded uncertainty
u	velocity
V	autocorrelation matrix
v	pixel intensity
$\tilde{v}$	pixel intensity fluctuation
VR	propellant velocity ratio

w	geometric width
We	Weber number
X, Y	Fourier transforms
x	axial position
Z	impedance
z	array of pixel intensity values, i.e. an image

Greek

α	vortex chamber contraction angle
β	reflection coefficient
Δp	pressure differential
δ	characteristic root
ζ	hydroresistance
η	liquid film surface amplitude
θ	free cone spray angle
κ	wavelength
Λ	dimensionless depth of liquid into gas
λ	eigenvalue
μ	dynamic viscosity
ν	artificial viscosity coefficient

ξ	temporal growth rate
Π	response function
π	3.14159
ρ	density
σ	surface tension
υ	eigenvector
Φ	propellant momentum flux ratio
ϕ	proper orthogonal mode
φ	phase angle
ψ	liquid-to-gas fullness ratio
ω	angular frequency

Other

$\forall$	gas void fraction

Subscripts

0	liquid swirl post injection plane
1	gas annulus injection plane
a	aerodynamic
ann	annulus
att	attenuated

atm	atmosphere
$coll$	collected
cut	cut-off
f	fluid
g	gas
h	hydraulic
he	head end
i,j	temporal indices
in	inner, inlet location
$\mathfrak{K}$	longitudinal index
l	liquid
mix	mixture
$\mathfrak{m}$	diametral index
n	nozzle
$\mathfrak{n}$	circular index
out	outer
r	image sequence index
s	sample
T	total

t	tangential inlet
vc	vortex chamber
X, Y	Fourier transforms
x	axial direction
θ	circumferential direction
$*$	ratio

CHAPTER 1

INTRODUCTION

The main topic covered in this dissertation is a particular phenomenon that encompasses the interaction(s) of several physical processes each, in their own right, complex behaviors with attributes worthy of individual research efforts. As such, it is neither practical nor appropriate to provide in this document detailed background of all of these matters—else this work would quickly become unreadable. These various topics are instead introduced here in a general sense to develop a necessary background through which the hypotheses, objectives, approach, and results of this investigation can be understood. Moreover, discussions in this introduction are put into context with pragmatic motivations and implications related to the principal field of engineering application in which the topic of this dissertation is typically encountered—that is, the design and analysis of liquid rocket engine combustion devices.

So, beginning from a very high level view, conventional liquid propellant rocket engines (LPREs) derive propulsive power from energy released by the chemical conversion of energy stored within their propellant(s). This chemical conversion is facilitated by the process of combustion, and, as such, LPREs require propellant to

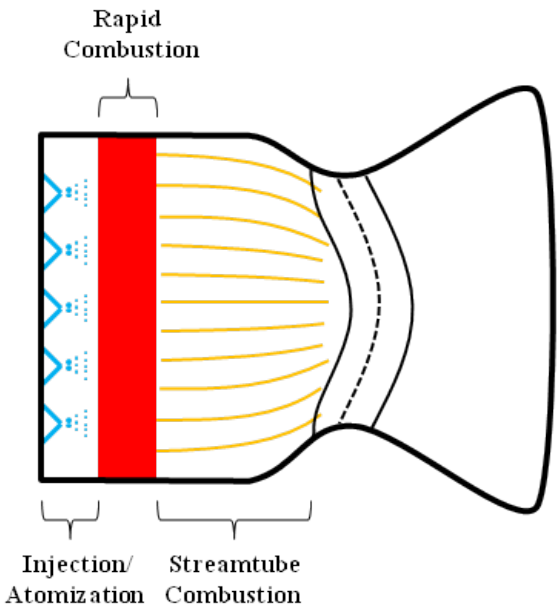

Figure 1.1: Cartoon of steady-state regions of an LPRE thrust chamber depicting Injection/Atomization, Rapid Combustion, and Streamtube Combustion Zones; adapted from Sutton [1].

be delivered and introduced to a device in preparation for chemical reaction. The manner in which propellant is introduced may influence not only the efficiency of the combustion process—and, hence, performance of an engine—but also steadiness of the combustion process, and pursuant stability of an engine. To both ends, the role of propellant injectors is of central importance.

1.1 Injector Implications to LPRE Combustion Performance

The subsonic flow region of an LPRE thrust chamber can be divided into three segments [1]: Injection/Atomization, Rapid Combustion, and Streamtube Combustion Zones. Figure 1.1 depicts these idealized thrust chamber regions.

It is generally believed that the turbulent non-premixed nature of bipropellant LPRE combustion processes is heavily influenced by events within the Injection/Atomization Zone, and, thus by the injector itself. Propellant sub-processes such as injection, atomization, vaporization, and mixing must occur within a finite distance from the combustor head end before rapid combustion occurs.

In a steady-state context, LPRE combustion performance can be linked to the notion of "complete combustion"—the more chemical energy is manifested in the thermodynamics of the combustor, the more complete the combustion process. Efficient propellant atomization (small droplet length scales with high kinetic energies), in part, invite shorter evaporative time/length scales. Shorter mixing time/length scales are thus encouraged, such that a chemically reactive mixture is prepared within the Injection/Atomization Zone in a reduced time and space. The longer the residence time of the chemically reactive mixture within the Rapid Combustion and Streamtube Combustion zones, the more complete the combustion process and the higher the combustion performance of the device.

As may be inferred from this qualitative description for the role of injector hardware towards the notions of residence time, complete combustion, and LPRE combustion performance, the fluid mechanics of propellant injection are recognized to be significant. Pursuant, it appears obvious that the key to injector design is the promotion of 1.) fine atomization/breakup, and 2.) rapid mixing of propellant. In the course of traditional injector development programs, designs are often selected for these fluid mechanic qualities and subjected to both chemically non-reacting and reacting tests to determine suitable performance characteristics.

While there exist a wide variety of injector designs and strategies—ranging from simple orifices to far more complex and exotic geometries—injection schemes which incorporate some type of propellant swirl have consistently exhibited greater levels of combustion performance [2–7] in contrast to alternative schemes under comparable propellant conditions. This is generally believed to be the case because the addition of swirling motions often benefit propellant atomization—creating smaller droplets with higher total velocities—which in turn promotes more rigorous mixing [8]. These attributes typically make swirl injectors desirable over injector types that solely rely upon shearing or impingement processes to generate propellant breakup.

1.1.1 Idealized Pressure-swirl Fluid Mechanics

While propellant swirl can be achieved in a variety of manners, the component implemented most commonly in LPRE swirl injector designs is the pressure-swirl atomizer [9] (also termed any number of names in the literature including simplex atomizer and classic swirl injector). Figure 1.2 depicts idealized fluid flow within a pressure-swirl atomizer—that is, an injection element which generates a flow based primarily on Bernoulli's principle across the element's inlet orifice. The following will provide a qualitative description of the flow.

The ideal fluid mechanics of the swirl injector are governed by conservations of mass, energy, and angular momentum. Liquid is typically introduced through passages tangentially oriented with respect the element's bulk flow injection axis as a means to promote fluid swirl. The resulting circumferential motion creates a thin film of liquid on the inner wall of the element in accordance with the Principle of

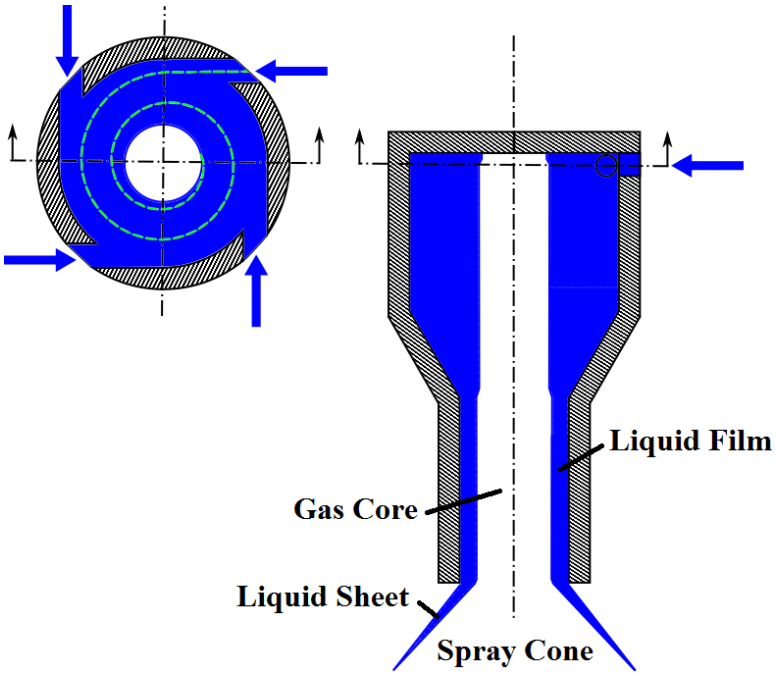

Figure 1.2: Idealized flow characteristics of the pressure-swirl atomizer.

Maximum Flow [10, 11], such that the free surface of the film is bound by a central vortex core of gas entrained from the free-pressure boundary of the element. These internal hydraulics are well described theoretically by, amongst others, Bazarov [12], Khavkin [13], Orzechowski [14], and Chinn [11, 15].

Exiting the element, the liquid's circumferential momentum causes the film to expand in the radial direction—generating a conical, swirling sheet which tapers with downstream distance from the injection plane. The mechanistic characteristics of pressure-swirl generated sprays are typically described by three parameters: the film thickness at the injection plane (h_0), the liquid cone's free-cone spray angle (θ), and the cone's breakup length from the injection plane (bl). Figure 1.3 illustrates these injection characteristics.

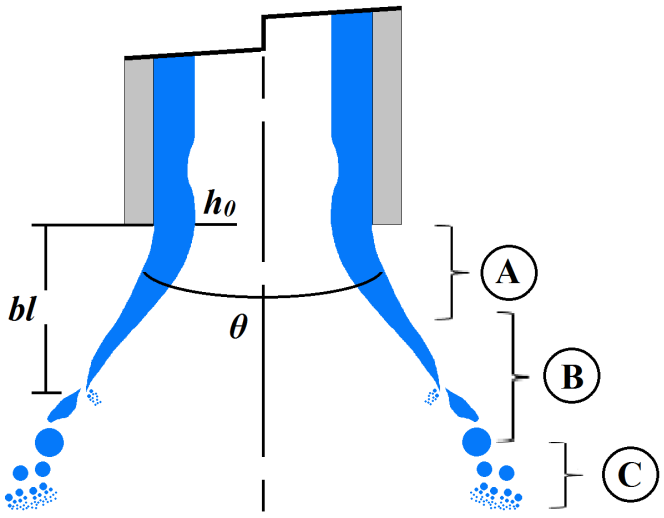

Figure 1.3: Characteristic features of the spray generated by a pressure-swirl atomizer, with regions denoting A.) liquid injection, B.) primary atomization, and C.) secondary atomization.

In a time-averaged sense, the spray cone generated by the pressure-swirl injector is described to be $self - atomizing$. The circumferential momentum works to spread and taper the liquid film, wherein aerodynamic forces eventually disintegrate the contiguous sheet, and ejection of fluid ligaments and droplets occurs. This self-atomizing ability is visualized in an instantaneous sense within Figure 1.4.

Depending on operating conditions and geometric parameters, additional fluid mechanic characteristics can sometimes be observed that are considered non-ideal for the pressure-swirl internal flow field and spray. One example of this is related to "memory" that the liquid flow can retain from its passage through the tangential inlet(s) of the injector. Here, the individual jet(s) of liquid fail to effectively diffuse and form a uniform swirling film, resulting in helical-type structures generated as fluid particles follow a consistent flow path through and out of the injector.

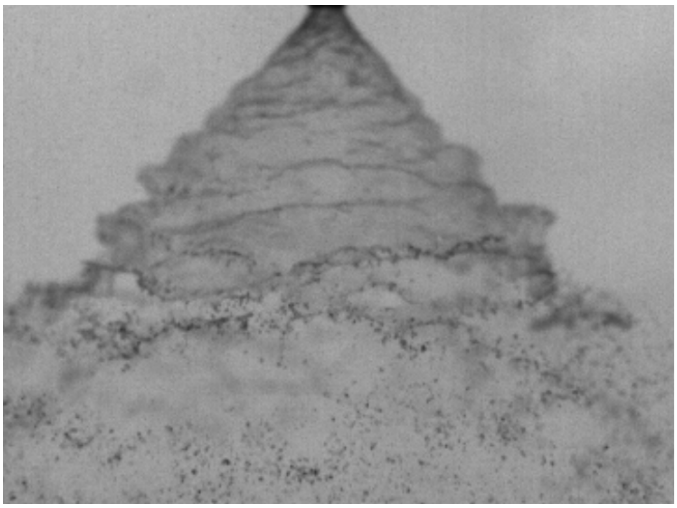

Figure 1.4: An instantaneous snapshot of pressure-swirl injection capturing the self-atomization of the liquid spray cone into amorphous ligaments and droplets.

Figure 1.5 depicts a notional representation of this behavior and its manifestation on the steady state liquid spray cone. Here, helical fluid pathlines spiral around the spray cone. A cross section of the spray might belay a steady state pattern of darker bands showing the helical path from one side of the cone to the other. This view of the flow might indicate a sinuous type shape similar to a waveform pattern along the spray cone edges; however, this type of spray shape is purely due to time-averaged hydraulic behavior, and is not unsteady in nature or temporally periodic as a sinuous waveform would be. Streaklines related to this behavior are clearly visible in the long-exposure image of the pressure swirl spray cone also provided in Figure 1.5.

1.1.2 Idealized Swirl Coaxial Fluid Mechanics

A pressure-swirl propellant flow must be accompanied by a flow of additional propellant when used within storable or oxygen/hydrocarbon bipropellant engines.

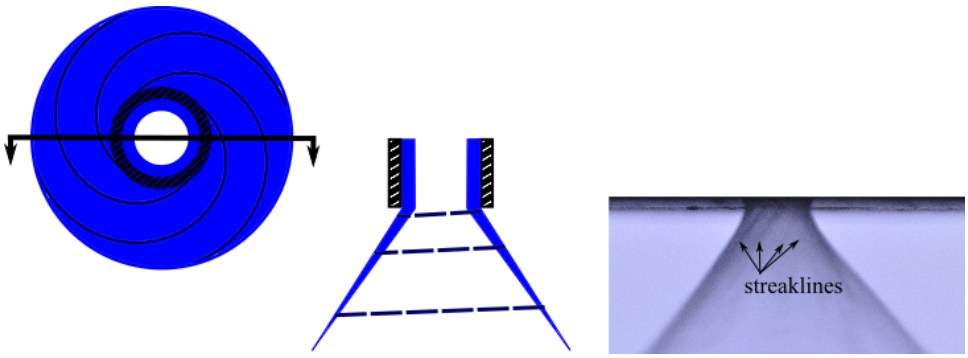

Figure 1.5: Fluid pathlines generated by memory of the tangential inlets with long-exposure image showing steady swirl streaklines in the liquid sheet.

Co-flow is a common technique, whereby a jet of fluid is injected parallel to the axial direction of the flow generated by the pressure-swirl atomizer. Such an arrangement constitutes what is colloquially referred to as a swirl coaxial injector element.

The fluid mechanics of swirl coaxial injection are thought to be particularly attractive in regards to staged-combustion cycle engines. As such, a film of swirling liquid propellant is generated and gaseous propellant is co-axially delivered. In this regard, there exist two prevalent configurations: the gas-centered swirl coaxial element, and the liquid-centered swirl coaxial element.

Gas-centered swirl coaxial elements are employed in the main chambers of several operational staged-combustion cycle engines, including the Russian RD-170 and its derivative, the RD-180. Liquid-centered elements have been the subject of numerous research and development efforts [2, 5, 7] since the 1960s—mainly for use with hydrogen/oxygen staged combustors. While the idealized hydraulics of the pressure-swirl atomizer are common to both swirl coaxial configurations, their re-

spective propellant atomization and mixing physics have been demonstrated to be markedly dissimilar.

Of particular interest in this dissertation are fluid behaviors of the liquid-centered swirl coaxial element. Internal to the pressure-swirl atomizer, the fundamental characteristics remain as previously described; however, at the injection plane, the co-annular jet can impart dramatic influence on the breakup and atomization characteristics of the conical liquid sheet. Most evident is the constriction of spray cone radial spreading—manifested as reduced θ. Impingement of the co-annular jet also promotes enhanced atomization similar to gas-assist [16] atomizers. Expansion of the jet helps to accelerate the liquid film, and momentum transfer from the jet to the film (resulting in increased shear) causes enhanced breakup closer to the injection plane. Further jet expansion entrains droplets into the mean flow of the spray, and creates a hollow spray cone of fine droplets.

1.2 Injector Implications to LPRE Combustion Stability

Combustion stability has been a notable consideration to the design and development of nearly every LPRE development program [17]. Thermo-acoustic fluctuations indicative of unstable combustion can, if unbounded in growth or sustained at elevated levels, lead to the compromise of engine integrity and operation, including: off-nominal thermal loading, increased cyclic mechanical fatigue of combustion device structures, flame blowout, and amplified structural vibration. Not only do combustion instabilities effect the reliability of general engine operability, but also

engine performance—potentially manifesting as fluctuations in combustion efficiency and thrust.

The most simplistic idealization of combustion instability is related to fundamental observations of heat release and acoustic interactions. Such thermo-acoustic behaviors were first qualitatively cited by Lord Rayleigh [18]:

> "*If heat be periodically communicated to, and abstracted from, a mass of air vibrating (for example) in a cylinder bounded by a piston, the effect produced will depend upon the phase of the vibration at which the transfer of heat takes place. If heat be given to the air at the moment of greatest condensation, or be taken from it at the moment of greatest rarefaction, the vibration is encouraged. On the other hand, if heat be given at the moment of greatest rarefaction, or abstracted at the moment of greatest condensation, the vibration is discouraged.*"

Deduced from this statement is the Rayleigh Criterion, such that thermo-acoustic amplification occurs when flame heat release coincides with the rise of a pressure oscillation, i.e. less than 90^o phasing exists between the maxima of oscillatory heat release and oscillatory acoustic pressure. In the case of reciprocal behavior, thermo-acoustic damping is promoted. It is also inferred from Rayleigh's observation that for thermo-acoustic amplification to occur, acoustic and heat release oscillations must occur at the same frequency (or time scale). Thus, it may be further surmised that thermo-acoustic amplification can occur when the rate-limiting time scale of a combustion process is approximately equal to the time scale of an acoustic fluctuation.

In regard to the bipropellant class of LPREs, spontaneous (linear) combustion instability is, as one of many conjectural bases, thought to arise due to the coupling of combustion and thrust chamber acoustics to the unsteady fluid dynamic processes that underpin turbulent non-premixed combustion of the propellants; namely injection, atomization, vaporization, and mixing. Pursuant to this conjecture, the time scale of these processes are hypothesized to serve as the rate-limiting time scale of the entire combustion process. To this end, there exists relatively little understanding of how these processes, their complex interactions, and their influence on unsteady chemical kinetics, coincide with chamber acoustics to possibly drive or sustain the heat release and pressure oscillations characteristic of unstable combustion.

LPRE combustion instabilities excited by propellant atomization, vaporization, and/or mixing are referred to as intrinsic forms of instability [17]. Several mechanisms of intrinsic instability have been observed or proposed [19–22]. At subcritical propellant conditions, vaporization processes are thought to be rate-limiting (with atomization serving as a coupling mechanism), while at trans- and supercritical conditions, the rate of mixing processes (hydrodynamics, turbulence, diffusion, etc.) must be considered.

The precursory unsteady fluid dynamics of injection are surmised to play an important role toward influencing these intrinsic forms of instability. Thermo-acoustic driving based on this premise is referred to as injection-coupled combustion instability [23], and realization of the physics which contribute to this particular form of instability are a step toward augmented understanding, toward enhanced predictive

capability, and toward confident *a priori* stability ratings of LPRE combustion devices.

Similar to the enhanced combustion performance attributes previously discussed, swirl elements have also been practically demonstrated to offer enhanced stability margins [2–4, 7, 24–26] in contrast to alternative injection schemes under comparable conditions. However, the physics which govern these stability characteristics are not well understood. In many aspects, the nature of swirl injection encompasses special considerations that are thought to have potential implications to injection-coupled combustion instability.

1.2.1 Idealized Pressure-swirl Injection and Spray Dynamics

In regards to combustion dynamics and stability, it now becomes appropriate to discuss some of the major dynamic characteristics attributed to the swirl injectors. On small time scales, several dynamic events are thought to impart influence on the injection flow and spray behaviors of the pressure-swirl injector. Not only are surface/vorticity wave motions internal to the swirl injector at work, but so are activities generated by spray interactions that occur outside of the injector element.

1.2.1.1 Linear Dynamics Framework for the Swirl Injector

Beginning within the swirl element, since a gaseous vortex core exists, the free surface of the film is subject to perturbations exerted by the gas core—or visa-versa. Fluctuations in pressure drop across the tangential inlets due to upstream pressure/mass flow perturbations within the element have been shown to generate

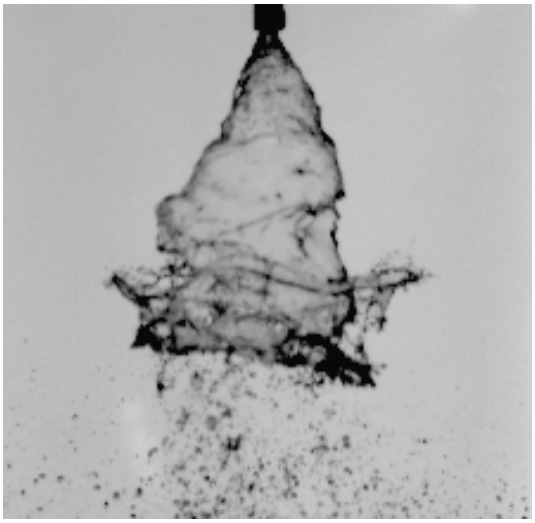

Figure 1.6: Spray cone deformation generated by the propagation of forced upstream pressure/mass flow perturbations [28] imposed by a hydro-mechanical pulsator.

shallow waves on the free surface of the liquid film [27] which may interact with the internal geometry of the injector. Figure 1.6 captures dramatic deformation of the liquid spray cone generated by forced pulsing of liquid pressure/mass flow upstream of a swirl injector. It is further hypothesized that strong fluctuations of the vortex core can deform the free surface as to also create disturbances on the film. These disturbances propagate downstream to the exit of the element, and thus influence properties of the emitted liquid spray.

Bazarov [12,27] provides the most widely cited theory on the dynamic flow processes that govern linear injector response to external perturbations of pressure/velocity boundary conditions. Consider the general framework of the classical hydrodynamics theory, wherein the internal geometry of the injector is segmented and treated as inter-related components. Figure 1.7 illustrates the various conceptual sections of the injector considered in the dynamic system model, with appropriate nomenclature.

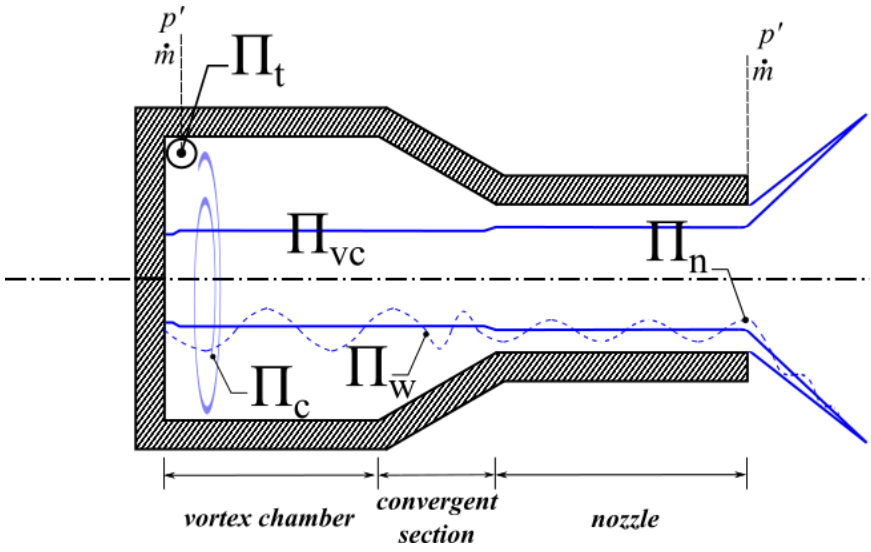

Figure 1.7: Illustration of conceptual components considered in the classical linear model of swirl injector hydrodynamics.

The basic concept of the linear transfer function is used to describe the dynamic behavior of the injector across a range of temporal frequencies. The transfer function notion is described by $\Pi(f) = X(f)/Y(f)$, where $X(f)$ is an input function of frequency and $Y(f)$ is an output function. The overall transfer function of the swirl injector can be expressed as an ensemble of transfer functions for each individual section of the injector.

Bazarov's swirl injector dynamics calculations are based on the linear perturbation of the steady state liquid hydraulics decoupled from the dynamics of the swirling gaseous core vortex. A response model is constructed as an ensemble of transfer functions for individual sections of the injector. The model is formulated to express the relationship between mass flow at the injector nozzle exit and total injector pressure drop cast as an injector admittance function commonly used in LPRE stability analyses [17].

Firstly, by assuming constant liquid density, the dynamic behavior of the tangential inlets can be modelled by the transfer function,

$$\Pi_t = \frac{\dot{m}'_t/\bar{\dot{m}}_t}{\Delta p'_t/\bar{\Delta p}_t}, \tag{1.1}$$

where perturbational liquid mass flow rate (denoted by: $'$) is normalized by steady liquid mass flow, and likewise for unsteady liquid pressure drop across the tangential inlet.

Next, the injector vortex chamber is considered. Within the vortex chamber, two mechanisms of centrifugal pressure disturbance are accounted for—both liquid surface wave action and fluctuations in circumferential velocity (i.e. vorticity/entropy waves)—such that the general vortex chamber transfer function is defined as $\Pi_{vc} = \Pi_w + \Pi_c$. Each component is defined in Equation 1.2 and Equation 1.3,respectively. The consolidated vortex chamber transfer function is expressed by Equation 1.4 by assuming mass flow fluctuation in the tangential inlets is distributed equally amongst surface wave and vorticity wave mechanisms.

$$\Pi_w = \frac{\Delta p'_w/\bar{\Delta p}_t}{2\dot{m}'_t/\bar{\dot{m}}_t} \tag{1.2}$$

$$\Pi_c = \frac{\Delta p'_c/\bar{\Delta p}_t}{2\dot{m}'_t/\bar{\dot{m}}_t} \tag{1.3}$$

$$\Pi_{vc} = \frac{\Delta p'_w/\bar{\Delta p}_t}{2\dot{m}'_t/\bar{\dot{m}}_t} + \frac{\Delta p'_c/\bar{\Delta p}_t}{2\dot{m}'_t/\bar{\dot{m}}_t} \tag{1.4}$$

The total pressure drop fluctuation for the injector element is expressed as a composite of the pressure drop fluctuation across the tangential inlets, as well as the pressure drop fluctuations associated with surface waves and circumferential velocity fluctuations in the vortex chamber. The total pressure drop fluctuation is described as $\Delta p'_T = \Delta p'_t + \Delta p'_w + \Delta p'_c$. Thus, by manipulation of Equation 1.1 and Equation 1.4, the transfer function for the combined tangential inlet-vortex chamber subsystem can be expressed in terms of the total pressure drop fluctuation as:

$$\Pi_{t \rightarrow vc} = \frac{\dot{m}'_t / \bar{\dot{m}}_t}{\Delta p'_T / \bar{\Delta p}_T} = \frac{\bar{\Delta p}_T}{\bar{\Delta p}_t} \frac{\Pi_t}{2\Pi_t \Pi_{vc} + 1}. \tag{1.5}$$

By invoking continuity, the mass flow fluctuation in the vortex chamber is related to that in the tangential inlets. Similarly, the mass flow fluctuation in the injector nozzle is expressed in terms of that within the vortex chamber.

$$\dot{m}'_{vc} / \bar{\dot{m}}_{vc} = \Pi_{vc} (\dot{m}'_t / \bar{\dot{m}}_t) \tag{1.6}$$

$$\dot{m}'_n / \bar{\dot{m}}_n = \Pi_n (\dot{m}'_{vc} / \bar{\dot{m}}_{vc}) \tag{1.7}$$

Again, by continuity, the steady mass flow through each section of the injector remains constant, such that $\bar{\dot{m}}_t = \bar{\dot{m}}_{vc} = \bar{\dot{m}}_n$; thus, upon substitution of these relations, an expression for the overall transfer function of the swirl injector can be obtained. Equation 1.8 describes the linear transfer function for the swirl injector.

$$\Pi_{inj} = \frac{\dot{m}'_n / \bar{\dot{m}}_n}{\Delta p'_T / \bar{\Delta p}_T} = \frac{\bar{\Delta p}_T}{\bar{\Delta p}_t} \frac{\Pi_t \Pi_{vc} \Pi_n}{2\Pi_t \Pi_{vc} + 1}. \tag{1.8}$$

1.2.1.2 Spray Breakup Dynamics

In addition to surface/vorticity waves originating from within the swirl injector, once the liquid has exited the element, it is subject to aerodynamic forces applied by the surrounding ambient environment. Through shear layer interactions, Kelvin-Helmholtz wave growth [29, 30] has been shown [31, 32] to dominant the dynamics of liquid sheet stability, wherein the conical liquid sheet possess inherent modes of oscillation described by the symmetric and antisymmetric (sometimes referred to as varicous and sinuous) spatial phasing between the interior and exterior surfaces of the sheet. A turbulent shear layer between the quiescent gas and the liquid surface is formed both on the inner and outer surface of the sheet, wherein random waves of minute amplitude are generated and organize into coherent perturbations. Perturbations possessing the most dominant growth rates continue to increase in amplitude as they propagate downstream along the conical liquid sheet surface. The most dominant patterns are typically those associated with symmetric modes [32, 33]. These surface waves further propagate until a critical amplitude is achieved [33–36]—resulting in the disintegration of the contiguous liquid sheet. Other forms of instability are also thought important to these spray dynamics; these flow mechanisms include helical instabilities introduced by the swirling nature of the liquid film, as well as capillary instabilities [37]. This more elegant description improves upon the time-averaged, mechanistic perspective of the pressure-swirl injector's self-atomizing ability.

Furthermore, shear layer effects become more important when the liquid sheet is exposed to a gaseous flow. The breakup processes here are commonly referred in

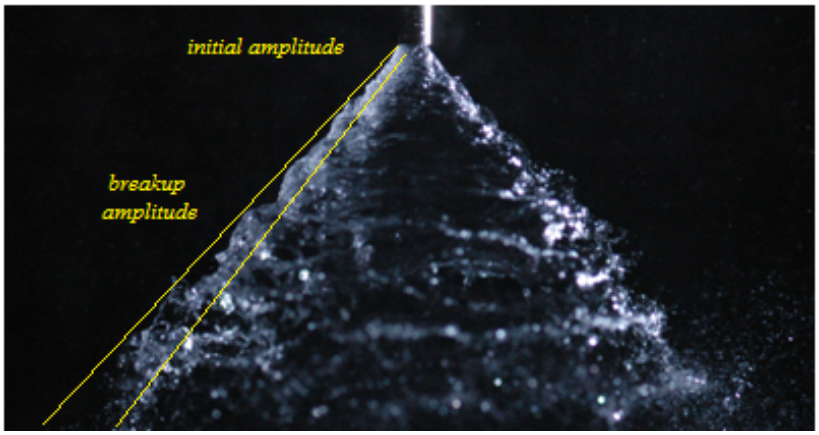

Figure 1.8: Illustration of liquid sheet generated by the pressure-swirl injector and its breakup due to critical amplitude growth of unstable Kelvin-Helmholtz-type waves.

the literature as "air-assisted" atomization [16] processes because of the working fluids used in the particular studies, but are generally dubbed "gas-assist" atomization processes. In this case, the breakup characteristics of the conical liquid sheet exposed to a co-annular jet are similar to the same circumstance for a cylindrical liquid sheet [32, 38]. The relative velocity that exists between the two fluids affects distinct shear layer interactions which lead to K-H-type wave growth that is exacerbated from that which occurs for pressure-swirl injection with no gas co-flow. In this sense, the descriptions of pressure-swirl oscillations leading to self-atomization with no gas co-flow are a limiting case of similar oscillations that lead to "gas-assist" atomization of the liquid sheet.

Figure 1.9 is an adaptation of Lee and Chen's [38] schematic, illustrating the basic forms of liquid sheet oscillation thought lead to breakup in the liquid-centered swirl coaxial injector element [39]. In this "gas-assist" case, oscillatory motions on the liquid sheet are dependent not only on the liquid flow, but also on the gas flow.

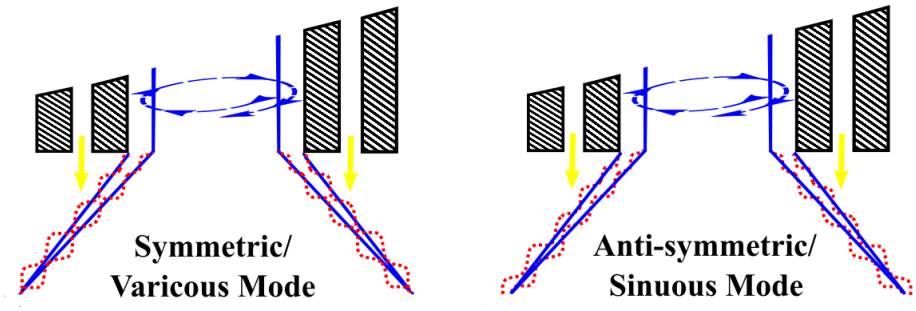

Figure 1.9: Schematic adapted from Ref. [38] depicting basic modes of conical liquid sheet oscillation when exposed to a co-annular jet.

Each flow exerts influence on the formation of inherent spatio-temporal patterns of K-H-type wave growth that eventually promote primary atomization. Here, both the symmetric and antisymmetric modes (varicous/sinuous) of sheet oscillation are depicted. As with pressure-swirl injection, the antisymmetric mode is also known to be the most dominant [38] of the two modes when the liquid sheet is exposed to gas co-flow.

1.2.2 Potential Mechanisms of Injection-coupled Combustion Instabilities

To date, little is understood about the fundamental mechanisms responsible for liquid rocket combustion instability coupled to swirl injection processes; furthermore, few proposed mechanisms have been definitively identified and/or demonstrated. In regard to liquid swirl injectors, several dynamic aspects of the injection process must be considered, in part, because obvious avenues of communication between the chamber and the injector are thought to exist. These aspects pertain to fluid flow both internal and external to the injector element, and their sensitivities to such feedback

remains subject to ongoing research. The following will discuss a variety of important flow characteristics and notional coupling to chamber acoustics—all of which are thought to potentially exacerbate, in varying degrees, periodic fluctuations of propellant flow rate(s) and pursuant fluctuations in injector sub-processes.

Bazarov [12] provides the most widely cited theory on the dynamic flow processes that govern linear injector response to external perturbations of pressure/velocity boundary conditions. The theory addresses surface and vorticity wave propagation through different sections of the swirl injector as a means to define total injector response. While Bazarov's theory does not couple liquid hydrodynamics to oscillatory behaviors in the gaseous vortex core, the characteristic dynamics of the liquid within the injector are known to be sensitive to high amplitude acoustic perturbations [40]. Nevertheless, born from Bazarov's overall theory is the concept of fluid resonance [41], such that constructive and destructive interference of surface waves within the injector undergo superposition to form standing wave patterns on the liquid film. Should the frequency of this standing wave coincide with a resonant frequency of the combustion chamber, potential for coupling is thought to exist.

$$\omega_f = \frac{\mathfrak{K}\pi}{2L_{vc}}\sqrt{C_\theta^2\frac{R_{vc}^2 - r_{vc}^2}{2r_{vc}^4}} \quad for\ \mathfrak{K} = 1, 2, 3... \tag{1.9}$$

A second mechanism of conjectural coupling inherent to swirl injection is based on the resonant characteristics of the gaseous vortex core. The "organ pipe" resonance of the gas core has been proposed as a mechanism of injection-coupled combustion instability [7], wherein the gaseous core is thought to possess a potential to oscillate

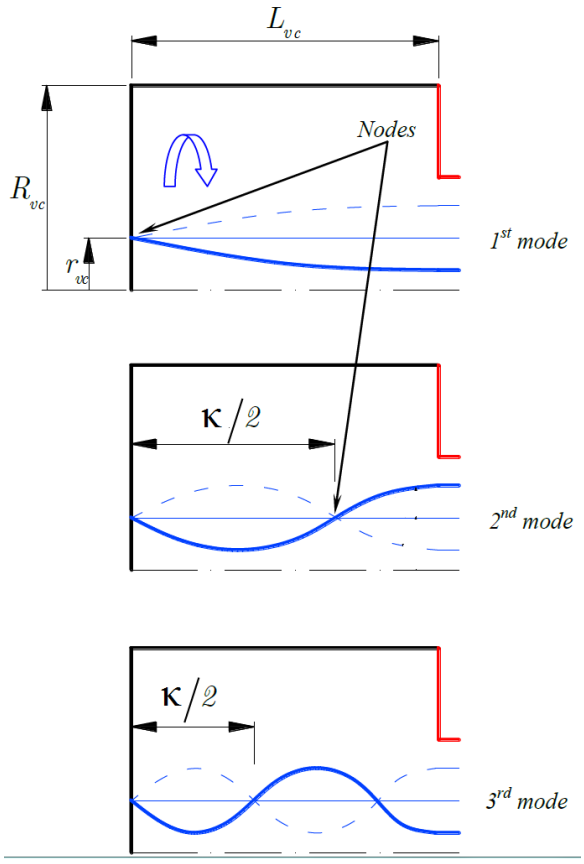

Figure 1.10: Schematic and nomenclature describing fluid resonance within swirl injectors; adapted from Ismailov and Heister [41].

with a resonant frequency sympathetic to pressure wave motions within the combustion chamber. A poor understanding of the vortex core's chemical composition and state properties make this coupling mechanism difficult to explicitly extract from hot-fire test data. Should this coupling occur, the potential exists to excite periodic cavitations and pursuant liquid mass flow fluctuation across the pressure-swirl atomizer's inlet orifices (particularly during throttling procedures). Such coupling might also disturb the flow field of the injector—generating fluctuations in propellant flow rate that might be reinforced by the natural hydrodynamics of the injector.

Thus far, the two discussed mechanisms of swirl injector coupling have dealt only with the injection of liquid through the swirl element and the flow internal to the injector; however, the combined interactions of a co-annular jet with the swirling liquid issued from the injector is also prudent to consider. Since theses interactions occur external to the injector, any such mechanism of unstable combustion produced might technically be referred to as an intrinsic form of combustion instability—implying that no feedback mechanisms exist between spray dynamic phenomena and injector flow dynamics. Exercising this notion for swirl injectors is slightly miscued. While, at several injector diameters downstream, the intrinsic concept is plausible, in the very near-field of the swirl injector, a contiguous conical liquid sheet can remain intact, particularly when injector element recessing from the combustor head end is not practiced. By means of continuity, the presence of an intact liquid sheet provides a feedback medium not only between dynamic motions in the chamber and their communication back upstream to within the injector, but also feedback of inter-stream dynamic motions between propellant circuits. In this context, propellant interactions in the very near-field of swirl coaxial sprays can be reasonably extended as potential sources of injection coupling.

Thus, a third mechanism of coupling exists which is related to the unbound liquid sheet. In the very near-field of injection, the natural wave dynamics generated by aerodynamic/hydrodynamic instability can be driven and/or exacerbated by the relative shear imposed by the ambient backpressure of the chamber gases, co-annular propellant flow, and/or turbulence effects generated by combustion. Should this natural frequency of fluid motion be congruent with—or organize itself to—a

fundamental eigenfrequency of the chamber, injection coupling might be fostered. This notional mechanism is similar in concept to the acoustic excitation of the jet preferred mode of flow instability encountered with shear coaxial injector sprays [42]. In this same vein, swirl coaxial ligament shedding/atomization is also known to respond to modulation by high amplitude transverse sound waves [43]. While it has not been definitively linked to a notional liquid film preferred mode via hydrodynamic instability, it is highly plausible that ligament shedding and subsequent atomization response is driven by liquid film-to-sound wave interactions that occur in the very near-field of injection.

1.3 Swirl Coaxial Self-excited Oscillations

Of special interest is the interaction of the unbound liquid sheet with a co-annular gaseous jet. These behaviors have been observed to have significant, if not governing, influence on the dynamics of swirl coaxial injection and spray breakup. The spreading of the liquid sheet into the stream of co-flow is thought to cause dynamic fluctuations in impedance at the exit of the gas annulus. Fluctuations in impedance have been described to incite time-delayed feedback between the liquid and the gas that results in self-sustained, strong oscillations in propellant pressures and flow rates. This phenomenon is referred to as self-pulsation, and is noted to dramatically change spray atomization and mixing from that typically associated with nominal operation. Furthermore, these self-pulsation spray behaviors are typically associated with sound emissions, and are usually documented to be accompanied by a high frequency screech tone. Figure 1.11 draws contrast between pressure-

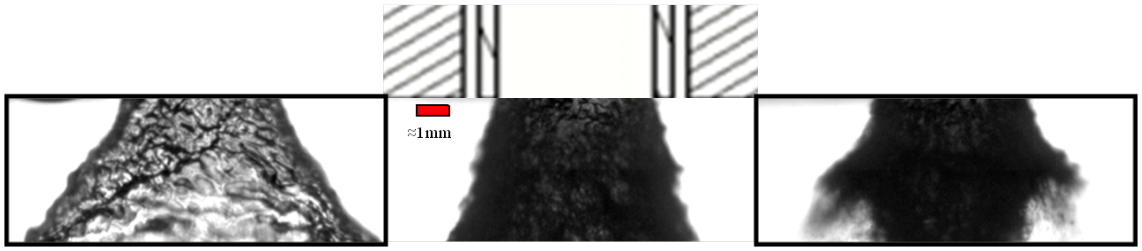

Figure 1.11: Comparisons of spray structure in the near-field for (left-to-right) pressure-swirl, globally stable swirl coaxial, and swirl coaxial injection under self-sustained oscillation.

swirl injection, nominal swirl coaxial injection, and swirl coaxial injection under self-sustained oscillation. Here flow conditions are fixed at the same condition, but gas flow is elevated from left-to-right at various levels.

1.3.1 Literature Review of Self-pulsation

Swirl coaxial self-pulsations were likely first encountered and reported by Russian engine developers in the 1970s [44–46]. However, detailed documentation of these developments, theories, and fundamental findings are difficult to obtain. Nevertheless, several works have been published in the open literature since the mid-1990's that offer valuable qualitative and quantitative descriptions of the phenomenon.

Bazarov and Yang [47] provide a literature hallmark on swirl coaxial self-pulsation studies, wherein the authors detail cold flow experimental results for liquid-centered injectors. Dynamic manifold pressure measurements were analyzed to examine the effects of inner swirl post recess, chamber backpressure, and varied propellant flow conditions. The authors described several key observations, noting self-pulsation dependence on the injection pressure drops of each propellant—such that an increase

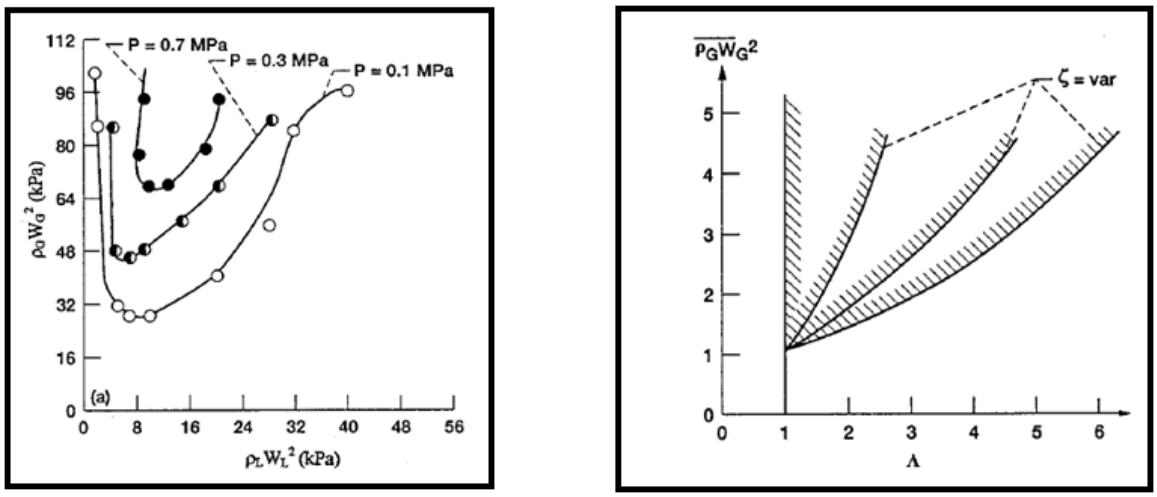

Figure 1.12: The self-pulsation stability boundaries measured (left) and computed (right) by Bazarov and Yang [47].

in $\Delta\bar{p}_g$ resulted in an increase in both pulsation frequency and amplitude. They suggested swirl post recess, $l_{0\rightarrow 1}$, to be the most significant parameter associated with self-pulsations.

Bazarov and Yang's conjecture was supported by a flexible reed valve model, which, in its functional form, seems to have been first put forth in open literature by Andreyev et al. [48]. A non-dimensional evaluation was implied to match well with measured stability boundaries of self-pulsation. The model, formulated in terms of impedance at the gas annulus, is described by Equation 1.10 and applies to the schematic in Figure 1.13.

$$\frac{Z_0}{Z_1} = \frac{\bar{u}_{g0}}{\bar{u}_{g1}}\{1 - \frac{2\Lambda}{\zeta - \Lambda}e^{i\omega t}\} \tag{1.10}$$

In this expression, ζ is defined as the hydroresistance present at the exit of the injector, such that $\zeta = \partial A_1/\partial\Delta p$, where $\Delta p \equiv p_0 - p_1$ for the gas phase. The

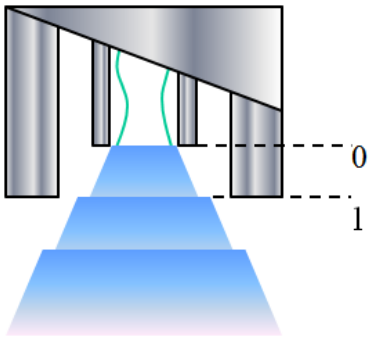

Figure 1.13: Injector Schematic with Denoted Stations Relevant to Equation 1.10

non-dimensional depth of which the liquid sheet penetrates the co-annular jet, Λ, is described as dependent upon propellant momentum flux ratio, insofar as $\Lambda \equiv f(1/\Phi)$.

While good general agreement between the model and the experimental data is implied by Bazarov and Yang, several parameters within Equation 1.10 are ambiguously defined in the literature [49], and difficult to explicitly identify and measure by empirical methods. Furthermore, by inspection, Equation 1.10 cannot be applied in certain circumstances. Namely, the relation cannot be clearly defined in the special case of a flush mounted inner element, wherein the swirl post recess length tends to zero such that the impedance and bulk gas velocity ratios each approach unity.

Another notable peer-reviewed examination of liquid-centered self-pulsation [39] further studied the effects of $l_{0\rightarrow 1}$, propellant flow variation, and downstream chamber pressure. This study focused on the mechanism of self-pulsation. The stability boundary of self-pulsations was again explored, and an effort to discern a fundamental mechanism of self-pulsation excitation was made. Guided by linear stability analogies to the conical liquid sheet, the authors postulated that the frequency of self-pulsation is governed by the natural wave dynamics of the sheet—such that disturbances with

maximum growth rate, i.e. "dominant"/"unstable" waves, are responsible for defining the self-pulsation frequency. To explore this notion, a point measurement laser diagnostic was implemented to measure light scattering produced by the self-pulsating spray, wherein spectral characteristics were extracted from the signals.

For fixed liquid flow rate, Im et al. [39] deduced dominant frequencies of self-pulsation as a function of gas injection Reynolds number. Similarly, dominant frequencies of wave motion on the conical liquid sheet were measured from test cases of pressure-swirl injection (liquid flow only, far downstream in the spray field). Based on extrapolation [38] of their Reynolds number-dependent frequency results, the authors showed $f_{sp}|_{Re_g=0}$ to match well with the frequency of dominant wave motion from the pressure-swirl spray. These findings led to a proposed mechanism of self-pulsation, wherein self-pulsations are excited/sustained by periodic stripping from and pushing of liquid from these waves, which causes the sheet to further oscillate at the frequency of the so-called "dominant waves".

Studies of self-pulsation have also been described in a small number of earlier proceedings [48,50,51]—one [52] of which offers valuable insight from an experimental investigation that varied swirl post recess, swirl post length, gas annulus length, and injector flow rates. The authors paid particular attention to the acoustic characteristics of self-pulsation in the study. Measurements indicated several tones present during testing. The authors describe these tones to exist in 2-4 kHz and 4-8 kHz bandwidths, consistent with those computed by simple 1-D analytical models of gas core and fuel annulus natural eigenfrequencies. Recess of the inner swirl post was shown to be the most significant parameter in defining the frequency of the sound

emissions, wherein the fundamental frequency of the gas annulus was the most influential. It was posited that tones in the lower bandwidth were generated by a coupling of the gas annulus fundamental with the first harmonic of the swirl post gas core, and tones in the higher bandwidth were created by coupling of the first harmonic of the gas annulus with the fundamental of the swirl post gas core. The authors imply that, in the case of no inner post recess, screech occurs only when the fundamental frequency of the gas annulus coincides with the fundamental of the swirl post gas core.

1.3.2 Fluid Oscillator Theory

Here it is sought to cast the phenomenon of liquid-centered swirl coaxial self-pulsations into the light of a more unified philosophy on flow-induced vibration phenomena. For in-depth discussion on this, the reader is directed to the principal text on the topic by Naudascher and Rockewell [53], while, here, only a brief orientation is given. Flow-induced vibration phenomena can consist of three fundamental elements: 1.) body oscillators, 2.) fluid oscillators, and 3.) sources of excitation [53]. Neglecting the structural vibrations associated with potential body oscillators within a system leads to consideration only of the fluid environment. As such, a *system* comprised strictly of one or more fluid oscillators and accompanied by one or more sources of excitation will henceforth be referred to as a *fluid oscillator system*.

The classic definition of a fluid oscillator element is simply a fluid mass susceptible to oscillations governed by compressibility of the fluid or by gravity [53]. The manner in which a fluid mass oscillates can be either distributed about multiple de-

grees of freedom—such as in the form of acoustic or gravity waves—or lumped—such as in the form of volume changes. When excited, fluid oscillators are often observed to behave in a state of pulsation that can include surge or oscillatory waves.

Fluid oscillators are subject to three general types of excitation sources: extraneously-induced excitations, instability-induced excitations, and movement-induced excitations (which are body oscillator related and not considered here). Extraneous induction is a result of flow fluctuations generated independent of the passive fluid mass in consideration, such as a tube forced by a loudspeaker. The forces of excitation here are typically random, such as that of broadband acoustic noise. Instability induced excitations are a result of forces generated by flow processes inherent to the passive fluid mass in consideration—an example being an impinging shear layer across the opening of a Helmholtz resonator. Here these fluid processes result in their own local fluid oscillation even in the absence of a passive fluid oscillator, and are commonly referred to as a self-excited *flow oscillator* [53].

Instability-induced excitations are further characterized by the type and degree of control exerted on the flow instability. Should the exciting force be strictly dependent on control of flow conditions, the excitations are said to be fluid dynamic in nature, whereas should the force be dependent on dynamics between control of flow and resonant characteristics of a fluid oscillator, the control of instability-induced excitation is known as a *fluid-resonant* one. Fluid-resonant control is characterized by an amplification of the exciting force over a certain range of flow conditions and the so-called "lock-in" of oscillation frequency within a bandwidth around resonance of the fluid oscillator element.

Complex fluid oscillator systems are frequently encountered, wherein multiple passive fluid oscillator elements with multiple types of excitation sources can act simultaneously with self-excited flow oscillators. It does not seem unreasonable to presume that the liquid-centered swirl coaxial injector behaves as such. First, consider the potential fluid oscillator elements within the system: the gaseous volume of fluid within the fuel annulus/manifold, the gaseous volume of fluid contained within the LOX swirl post, the liquid volume of fluid contained within the LOX swirl post, and—in some configurations—the gaseous fluid volume contained within the recess region of the injector. Each of these elements are subject to their own excitations and/or a coupled response between a shared excitation mechanism. Figure 1.14 depicts a diagram of fluid oscillator elements accompanied by notional excitations of each. Here the liquid spray cone is the common medium which permits communications of one oscillator element to another. Figure 1.15 illustrates important fluid-resonant and fluid-dynamic oscillators comprised within the swirl coaxial injector element.

One distinct observation is that the liquid spray cone is the most sensitive component of the fluid oscillator system here. Excitations of any individual fluid oscillator element have the potential to generate liquid sheet fluctuations that may in turn transfer perturbational energy to other fluid oscillator elements. Furthermore, should the liquid spray cone behave as a self-excited flow oscillator itself, the self-pulsating system can be activated given just one fluid oscillator element responds in a manner which provides reinforcing feedback to the liquid spray cone.

With a foundational understanding of fluid oscillator characteristics, descriptions of swirl coaxial self-pulsations gathered from literature to date can be now be

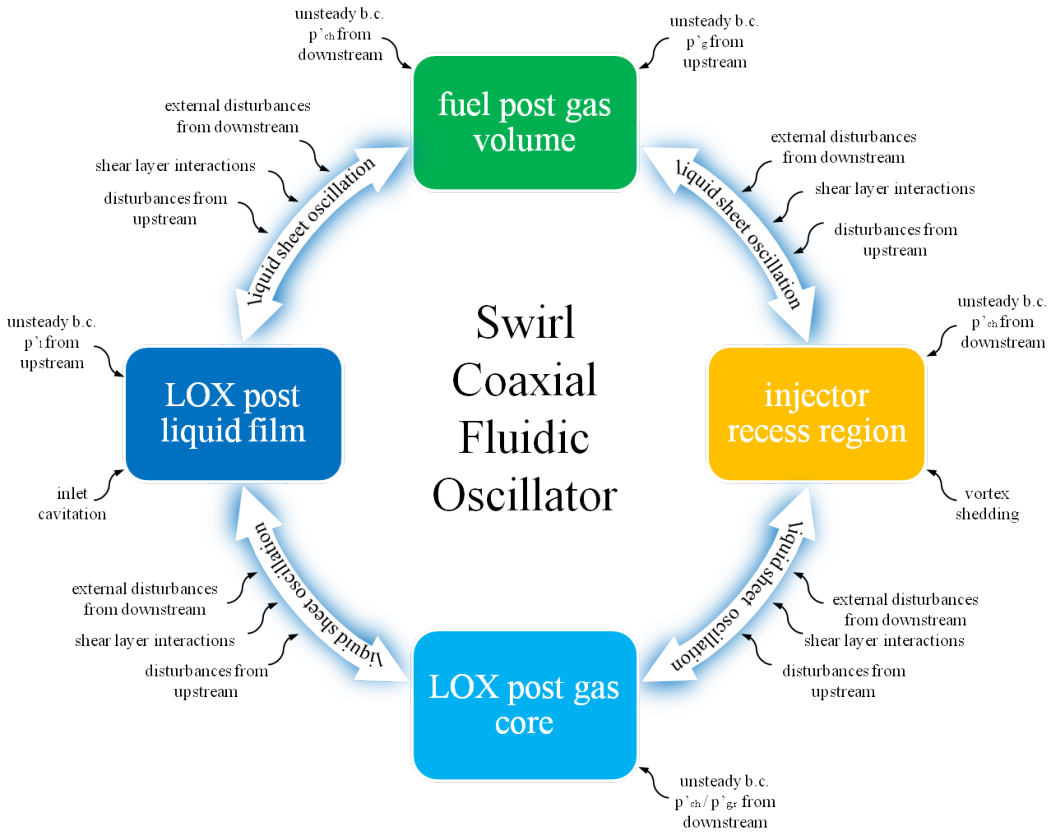

Figure 1.14: Notional diagram of fluid oscillator elements comprising the swirl coaxial fluid oscillator system, where fluctuations of one element may be bound to another through liquid sheet oscillations on the spray cone.

assessed through a new lens. Pursuant: 1.) both the gas core of the swirl element and gas volume within the fuel annulus have the potential to serve as fluid oscillators under distributed resonance following the observations of Huang et al. [52], 2.) the recess region of the injector may participate as a fluid oscillator which couples the swirl post and gas annulus as inferred from the remarks of Bazarov and Yang [47] and Im et al. [39], 3.) the liquid spray cone has the capacity to act as a self-excited flow oscillator which may provide systemic excitation to resonance based on the findings of Im et al. [39], 3.) the amplification of self-pulsation response to varying control of

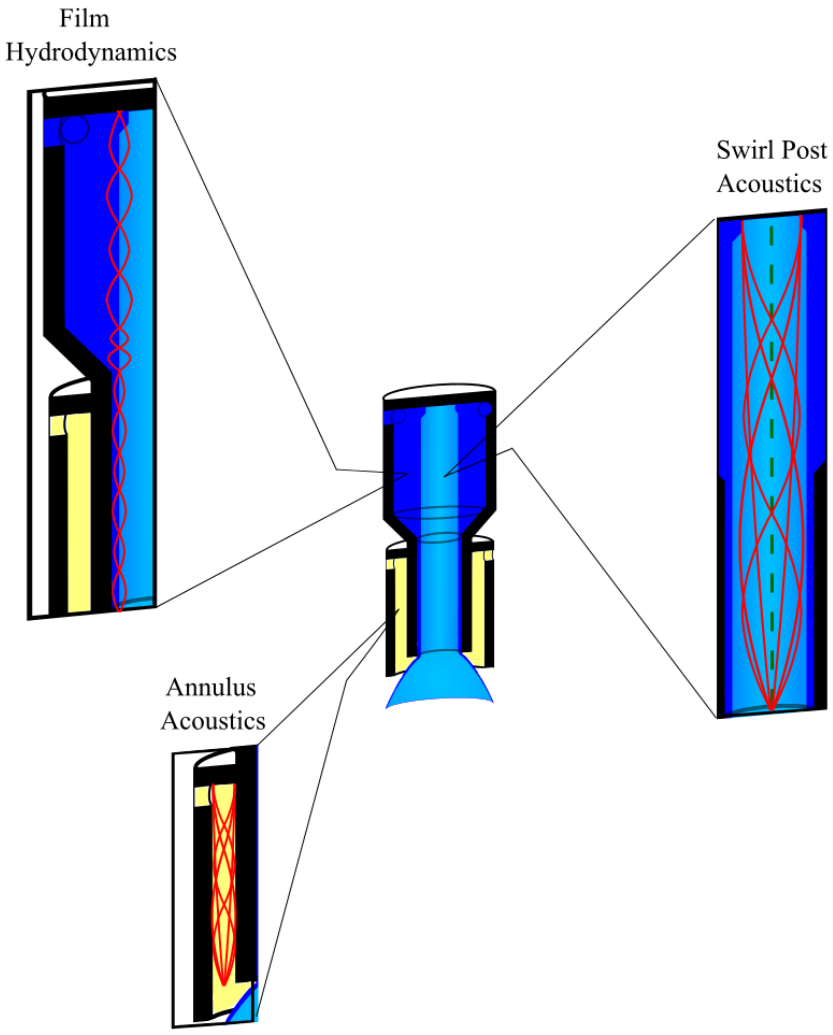

Figure 1.15: Conceptual illustration of important fluid-resonant and fluid-dynamic oscillator elements contained within swirl coaxial fluid oscillator system.

instability-induced excitation as observed by Bazarov and Yang [47], Im et al. [39] and Huang et al. [52] indicates fluid dynamic type control of the fluid oscillator system, and 5.) is complemented by observed bandwidths of frequency lock-in behavior in certain flow regimes as noted by Huang et al. [52] and Im et al. [39] further indicating fluid-resonant type control of self-pulsations.

Succinctly, liquid-centered swirl coaxial injectors can potentially be described as a fluid oscillator system comprised of multiple fluid oscillator elements sensitive to multiple instability-induced and/or extraneously-induced excitations. The fluid oscillator system can be excited to self-pulsation by a flow oscillator which may be controlled in a fluid-dynamic or fluid-resonant fashion.

1.3.3 Summary of Initial Assessment

A preliminary study was conducted by this author to characterize strong, spontaneous self-pulsations encountered with a flush mounted swirl coaxial injector element. The study explored the influence of flow variation on fluid and spray oscillations, and primarily focused on the dynamic behavior of the liquid flow. The influence of the natural dynamics associated with pressure-swirl injection on the characteristics of swirl coaxial self-pulsation was also investigated in an effort to deduce a flow mechanism responsible for excitation. Oscillations were diagnosed with pressure fluctuation measurements upstream of the test article, microphone measurements in the far field of the injector, as well as high speed cinematography of the ensuing spray. Figure 1.16 captures one characteristic cycle of self-pulsation spray dynamics.

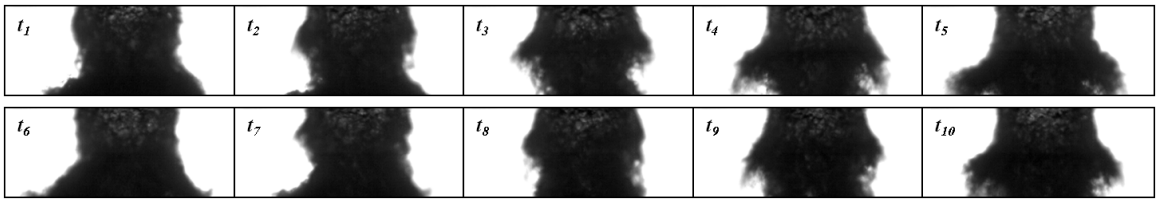

Figure 1.16: Instantaneous snapshots capturing one characteristic cycle of swirl coaxial self-pulsations spray dynamics.

The investigation was successful in applying time-resolved pattern recognition of the high speed imagery as a means to quantify aspects of the global spray dynamics. Figure 1.17 plots the spectra of measured pressure fluctuation and microphone signatures. A variety of spectral features can be seen in each measurement; however, not the shared peak registered near 3 kHz in both liquid pressure fluctuation and far-field microphone data.

Next,Figure 1.18 shows time histories and spectra associated with the dominant spray patterns. This characterization was obtained through modal decomposition analysis, and characterize the temporal characteristics belonging to the principal spray dynamics that occur during self-pulsations. Here, the spray oscillations are are quantified at a frequency near 3 kHz, which coincides the the most dominant peak in the sound pressure level spectrum, as well as pressure fluctuations in the liquid as seen from Figure 1.17.

Interesting initial results were garnered from the study, including apparent harmonic behaviors of wave propagation in the spray field, and close proximity of measured self-pulsation frequencies to those estimated for the fundamental and higher-order frequencies of the swirl post. Additionally, the boundary of the self-pulsation

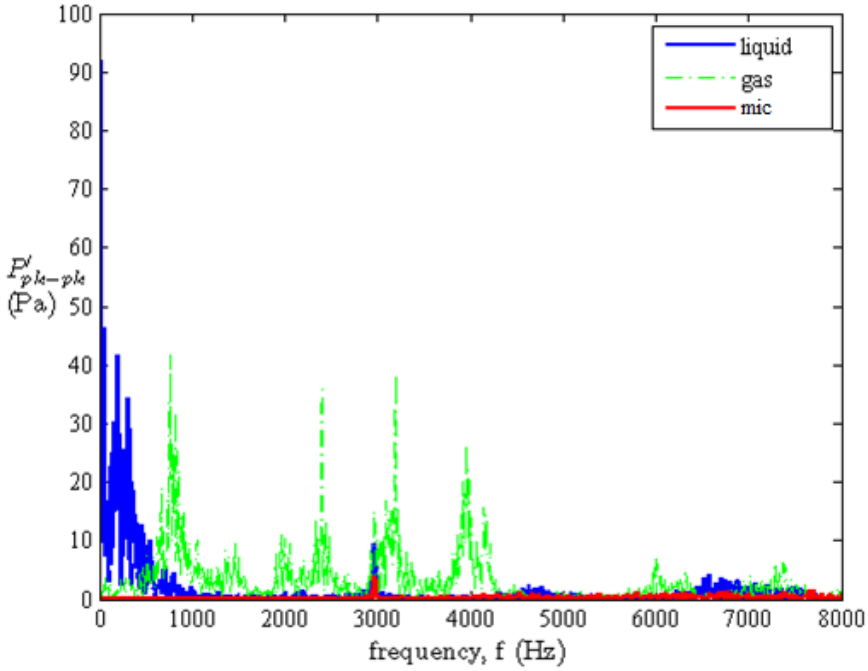

Figure 1.17: Spectra of upstream fluid pressure fluctuations and downstream far-field tones measured during initial assessment of self-pulsation.

onset was explored by probing gas flow conditions, seen in Figure 1.19. In a scaled, qualitative sense, this result seemed to correspond well to the self-pulsation boundary established both analytically and empirically by Bazarov and Yang [47] for recessed injectors. Note that gas momentum flux conditions were originally overestimated in preliminary works [54], but have been corrected in the presentation here.

Observations of strong periodic fluctuations in spray motions, high intensity and high frequency tones in the far-field, and similar pressure fluctuations detected in the upstream manifolding made apparent that swirl coaxial self-pulsations may be of considerable note to design aspects for combustion stability. Moreover, the various physical phenomena at play during these self-excited behaviors are of implicit inter-

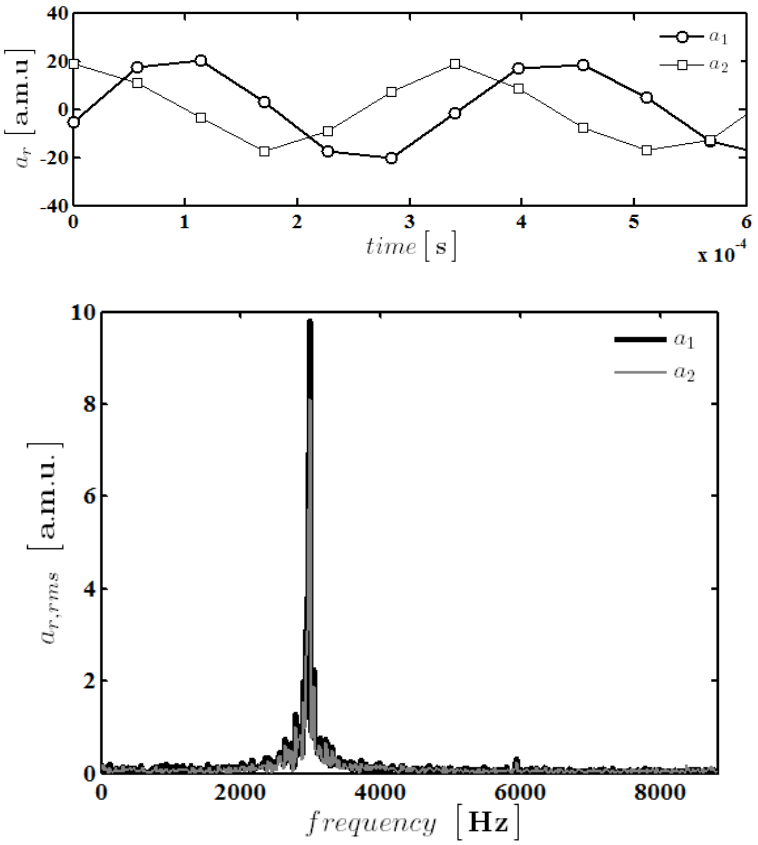

Figure 1.18: Zoomed time histories and frequency content of spray oscillations measured during initial assessment of self-pulsation.

est in regards to potential mechanisms of injection-coupled combustion instabilities discussed earlier. An investigation to further detail these phenomena and to develop an enhanced understanding of self-pulsations was thus proposed.

1.4 Research Outline

1.4.1 Dilemma

The research dilemma is two-fold. From a high level, two basic questions exist. The first question is:

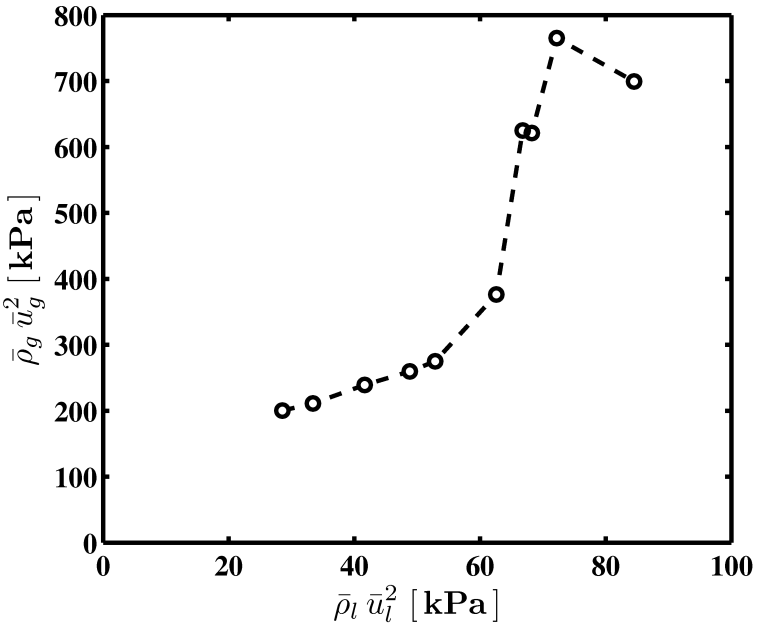

Figure 1.19: Self-pulsation onset boundary measured during initial assessment with non-recessed element.

"*What processes are responsible for exciting self-pulsation?*",

The second question is:

"*Why does self-pulsation occur at a particular frequency?*",

Of course, as more thought is put into these questions, more targeted ones arise. As previously touched upon, recess of the inner swirl post has been noted by several researchers to be the most influential parameter in defining swirl coaxial self-pulsation behaviors. In fact, Bazarov and Yang [47] state:

"*...Further decrease of (recess) leads to a sharp decrease of the self-pulsation zone, which practically disappears at (recess) = 0.,*"

Despite such observations, details on the effect of inner post recess are limited, barring that described for the frequency of self-pulsation. *How else might this effect be detailed in*

relation to other dynamic characteristics of the phenomenon? Further, self-pulsations have been observed with non-recessed elements, but are only described—qualitatively [51], and quantitatively [52]—in a limited sense. In context, results from the initial assessment of self-pulsation bring to light several interesting observations which pose a variety of research questions, wherein answers to these queries possess practical value.

Consider the design engineer whom desires to promote enhanced propellant mixing for a given swirl coaxial injector. Coaxial injector design guidelines [55] would recommend implementation of an inner post recess for such purposes; however, research to date suggest this recess might likely promote self-pulsations. Thus, the engineer faces a dilemma of choosing enhanced performance at the potential risk of diminished stability. Furthermore, the aforementioned results indicate that the self-pulsation phenomenon may still be excited in certain flow regimes even if the designer should choose to avoid recessing.

A curiosity raised by the initial study pertains to the injector element configuration,

> "*Why does the stability boundary of the flush mounted configuration appear to mimic that proposed for recessed configurations?*"

Even if a minuscule recess was present during the initial testing, such a result is largely counter-intuitive to that described by Bazarov and Yang [47], and is simply not addressed by existing gas jet impedance modelling. Since a recess region creating a well-defined flow interaction zone does not exist in the case of no inner post recess, a coherent local velocity oscillation may be difficult to develop at the exit of the gas

annulus. Thus, a jet impedance-based oscillator model must not fully describe the dynamics of self-pulsation.

This observation brings one to wonder about other more detailed flow behaviors that could be at play. The work of Im et al. [39] provides direction in addressing this question, wherein the stripping of fluid from K-H-type waves is thought to be important in exciting/sustaining self-pulsations. While this theory was postulated and indirectly evidenced based on extrapolated estimates, the role of Kelvin-Helmholtz instability was not implicated with strong direct evidence.

The second high level research question driving this dissertation is:

"*Why does the injector oscillate at the observed frequencies?*".

Here, note that the self-pulsation phenomenon is thought to be one of rich physical interactions, including—amongst others—those between the hydrodynamics of the liquid sheet, the jet dynamics of gaseous co-annular flow, shear layer interactions, and the resonant modes of pressure waves within the injector. Further, Huang et al. [52] remark that:

> "*So we can draw(n) a conclusion that the mechanism for the self-oscillation is resonance between gas flow in annular passageway and the gas hollow in liquid injectors.*",

Since there is some level of inconsistency regarding the role of resonant pressure modes of the injector in the self-pulsation phenomena, and since these behaviors are an important aspect of LPRE combustion stability, one might be compelled to ask a series of questions in the vein of:

"*In what capacity do the resonant modes of the injector serve toward the combined physics of self-pulsation?*",

and

Are sound waves responsible for the reinforcement of spray oscillation, or are they simply a consequence?"

The focus of the work on self-pulsations by Im et al. [39] was on the mechanism by which self-pulsations take place, with the major findings related to the role of waves implied to be generated by Kelvin-Helmholtz instability. While these findings have implications for the excitation/sustainment as discussed in their proposed mechanism of self-pulsation, finer points regarding the controlling oscillator of self-pulsations can also be gleaned. The methods used to demonstrate the role of "dominant" K-H wave growth suggests that distinct spray oscillations under *all* conditions follow along the same linear trend, such that the principal fluid oscillator during self-pulsation is the same as that when no self-pulsation exists. What is implied is that the natural modes of sheet oscillation generated by Kelvin-Helmholtz wave growth actively oscillate during full-blown self-pulsation and serve to define its primary frequency.

Additionally, a curious detail regarding the controlling fluid oscillator of self-pulsation is drawn out in the actual mechanism of spray breakup illustrated by Im et al. [39] Here, the so-called "dominant" waves related to external oscillations of the liquid sheet appear to be labeled *within* the nozzle of the swirl post. This is somewhat inconsistent with narrative since K-H-type instabilities are typically thought to be

created by hydraulic/aerodynamic interactions with the ambient environment or co-flowing fluid that occur outside of the element. The origins of these dominant waves are not explicitly discussed by Im et al. [39], but nevertheless raise an interesting specter not clearly investigated by prior researchers:

> *Could the origin of oscillations responsible for defining the frequency of self-pulsation be internal to the swirl injector?*

The research covered in this dissertation is largely motivated by these questions. Addressing them will help more fully describe self-excited oscillations and their propensity to be self-sustained in swirl coaxial injectors, and help expand the limited database of detailed research on the matter. This more clear description of the swirl coaxial fluid oscillator will provide practical data and descriptions which could be used during injector design and development stages of engine development. In general, the results will help spread awareness of flow physics practical to the *dynamic* design of LPRE injector hardware for both high performance and tailored stability characteristics.

1.4.2 Hypothesis and Objectives

Plainly, the two basic questions that this dissertation seeks to answer are:

- *What causes self-pulsations to excite?*, and
- *What causes self-pulsation to oscillate at a particular frequency?*

Since existing literature is largely descriptive of self-pulsations for recessed injector elements, a major goal of this current study is to also assess the basic questions of this research for instances where self-pulsations occur without inner post recess.

This work aims to investigate more closely the proposed mechanism of self-pulsation put forth by Im et al. [39]. As implied in that work, it is thought that Kelvin-Helmholtz-type instabilities are key to the mechanism of self-pulsation, where further stripping/pushing of these waves from the contiguous spray cone is responsible for exciting and sustaining self-pulsations. Here it is postulated that pertubations caused by these types of flow behavior may potentially excite characteristic modes of gas core resonance and/or surface wave dynamics within the swirl post that oscillate in a fluid-resonant manner during self-pulsation.

The overall hypothesis of this dissertation is that the liquid-centered swirl coaxial element is a fluid oscillator system which contains several fluid-resonant and/or fluid-dynamic oscillators whose sensitivity to excitation(s) leads to a state of self-pulsation. The objective of this work is to explore the existence and role of wave growth by Kelvin-Helmholtz-type instability in the mechanism of self-pulsation excitation for both recessed and flush-mounted injector configurations through experimental measurements and advanced analysis techniques. It is also desired to uncover other fundamental fluid oscillator(s) that could participate during self-pulsations and could be responsible in defining the frequencies that characterize the phenomenon.

1.4.3 Approach

The self-pulsation phenomenon encompasses rich physical interactions that occur on a variety of temporal and spatial scales. Contemporary Computational Fluid Dynamics (CFD) simulations are capable of capturing these physics in a time-resolved, highly detailed manner; however, conducting high-fidelity CFD case studies in a parametric fashion remains computationally expensive. For evaluations of the sort, experimental investigations in the vein of those described in the literature still are the most practical at this time.

A series of non-reactive experiments using surrogate propellants will be conducted to asses self-excited flow oscillations of an LPRE swirl coaxial injector element. These tests will be conducted over flow conditions designed to cover and expand upon those previously investigated by other researchers. Time-resolved instrumentation and diagnostics will be implemented to characterize different aspects of the phenomenon. Moreover, advanced analysis techniques will be utilized to bolster the insight that can be extracted through empiricism. Analytical models will be extended to consider the geometric features of test hardware and flow conditions that are experimentally investigated. Model results will be compared with measurements to aid in the interpretation of results.

1.4.4 Strategy

A review of liquid-centered swirl coaxial self-excited oscillations has been completed, and several theories pertaining to instability excitation mechanisms and fluid-

resonant behaviors have been discussed. Further review of notable swirl coaxial flow dynamics has been completed in developing an in-depth familiarization with relevant flow processes that may contribute to self-pulsations. This review has also discussed potential implications of swirl coaxial self-excited oscillations on LPRE combustion performance and combustion stability.

A series of tests will be devised to: 1.) parametrically characterize the influence of varied flow conditions on the dynamic characteristics of self-pulsations, 2.) parametrically characterize the influence of inner post recess variations on the dynamic characterists of self-pulsation, 3.) capture flow behaviors responsible for the onset of the self-pulsations, and 4.) determine the possible influence of fundamental fluid oscillator characteristics on the phenomenon. These tests will gather measurements of dynamic liquid and gas feedline pressure fluctuations, injector far-field sound pressure level signatures, as well as high-speed imagery of the near-field spray dynamics.

Advanced analysis techniques will be applied to extract relevant gas-liquid spray dynamics during self-pulsation, and infer relationships between upstream gas, liquid, and sound emissions downstream of the injector. Existing models for swirl injector flow and eigenmode characteristics will be evaluated and compared to measured results to aid in the interpretation of laboratory observations.

CHAPTER 2

EXPERIMENTAL APPROACH

2.1 Test Philosophy

2.1.1 Conception of Experiment

To remain consistent with existing literature and findings from the initial assessment of self-pulsations, tests were conceived on the premise of using H_2O and air as propellant simulants. These simulants were to be sprayed into an ambient environment of air at STP conditions. Under these conditions, a test bed would be created to accommodate easy setup of experimental instrumentation and diagnostics, as well as easy modification of test article configuration. The unsteady simulant pressures upstream of the test article would be monitored, as well as downstream acoustic signatures collected in the injector far-field. Spray field behaviors would be captured using high-speed cinematography—with a focus on visualizing both liquid and gas flow structures.

To determine parametric flow characteristics, experiments would consist of several tests conducted across a range of predetermined steady-state liquid mass flow setpoints. At each liquid flow setpoint data would be collected for: 1.) pressure-swirl

injection tests characterized without co-annular gas flow, 2.) swirl coaxial injection tests with predetermined steady-state gas mass flow setpoints, 3.) swirl coaxial injection tests to arbitrarily probe transition from stable to unstable behavior. Additionally, these parametric flow tests would be conducted over a set of varied geometric configurations of the test article. Again, in remaining consistent with existing literature, the inner post recess would be varied in distinct increments.

2.1.2 Cold Flow Rationale

In an experimental context, many of the characteristics promoted by an LPRE combustion environment are considered quite hazardous for typical lab-scale facilities and instrumentation, and often require robust sensors and diagnostics. Furthermore, a rigorous investigation of LPRE injector flow behaviors requires that the influence of chemical reaction and pursuant gas dynamic, turbulence, and heat transfer effects be isolated from the underlying fluid dynamic processes of interest. This decoupling of combustion and injector sub-processes is commonly referred to as cold flow, and testing under cold flow conditions is considered more conducive to the study of injection, atomization, evaporation, and mixing processes than an approach under reactive conditions.

While, in a certain sense, full-scale cold flow injector data using reactive propellants are often collected prior to full-scale engine firings, this type of cold flow testing is typically not practical towards detailed unit physics investigations of injector flows. To such an end end, laboratory-scale cold flow experiments are better suited. Depending on the phenomena of interest, most laboratory-scale experiments

aim to simulate realistic LPRE propellant and injection conditions using non-reactive surrogate propellants—owing to advantages such as handling safety and reduced cost. In this regard, linking surrogate propellant flow to real propellant flow is pursued through similitude of basic fluid properties and flow parameters.

Consider Table 2.1.2, which compares thermophysical properties of LOX at typical LPRE injection conditions with those of common simulants, namely liquid nitrogen and water. As an incompressible fluid, H_2O at standard temperature and pressure (STP) conditions closely mimics the density of LOX at a reasonably assumed injection temperature of 90 K. Note the stark contrast in transport properties between the two fluids. This dissimilarity is often times dismissed on the reasoning of inviscid flow by way of large injection Reynolds number, Re [56,57]. On these merits, H_2O is widely regarded as an acceptable simulant for cold flow studies of LOX injector flows [58–60].

Table 2.1: Fluid Thermophysical Properties

Fluid	T (K)	ρ ($\frac{kg}{m^3}$)	σ ($\frac{N}{m}$)	μ (Pa-s)
LOX	90	1146	$13.2x10^{-3}$	$2.00x10^{-4}$
LN_2	90	751	$6.09x10^{-3}$	$1.06x10^{-4}$
H_2O	273.16	1001	$75.6x10^{-3}$	$17.9x10^{-4}$

To further tie lab-scale experiments using propellant simulants to real propellant flows, the use of non-dimensional scaling parameters can be powerful. Fundamental fluid similarity parameters such as the Reynolds, Froude (Fr), Stokes (St), and Weber (We) numbers—amongst others—aid in the matter. Additional simi-

larity parameters more specific to LPRE injector flows—such as propellant velocity ratio, VR, and momentum flux ratio, Φ—are critical in translating laboratory-scale data [8, 61, 62] to full-scale conditions.

2.2 Injector Element Design & Configuration

The swirl-coaxial test article was originally designed for a single-element LOX-GCH_4 research engine. The swirl post, in particular, was designed to deliver a nominal 82 g/s of LOX flow—generating a liquid injection film thickness of 473 μm and a mean free-cone spray angle of 90^o. A legacy of historical data exists pertaining to the element's non-reactive injection and atomization [54, 63] and combustion performance [64] characteristics with liquid/gas propellants, as well as low-pressure combustion stability characteristics [65] with gas/gas propellants.

Classic methodology outlined by Bazarov [12,66] was implemented in the ideal hydraulic design of the pressure-swirl atomizer. The design methodology is considered ideal in the sense that it is derived from inviscid theory described by Bernoulli's equation and that the conservations of mass and angular momentum are used. The main steady hydraulic features, i.e. film thickness and spray cone angle, adhere to the Principle of Maximum Flow [10, 11] (see Appendix C). While other swirl injector design techniques [14, 67] empirically capture viscous effects, Bazarov's methodology offers enhanced detailed design capabilities over alternative techniques. An illustration of the steady state flow internal to the swirl injector is seen in Figure 2.1. Appendix A outlines the general ideal design procedure for swirl injector elements

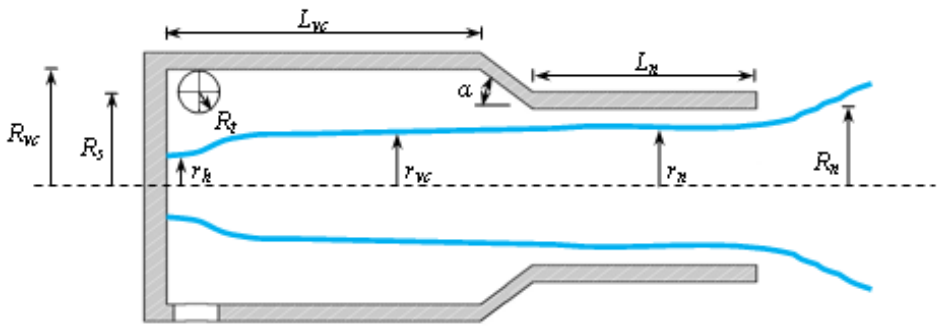

Figure 2.1: Geometric and flow features pertinent to Bazarov's design methodology.

based on steady hydraulic considerations, while calculations for the particular study element are found in Ref. [65].

The fuel annulus design is based on elementary incompressible flow theory in which the driving engineering consideration is to provide appropriate flow rates to meet the desired mixture ratio for O_2/CH_4 combustion. A cross-sectional profile of the swirl coaxial element housed within its cold flow manifold, with near-field detail, can be seen in Figure 2.2. A detailed view of the swirl element is also provided. Table 2.2 lists pertinent injector dimensions; dimensions are provided as normalized by the nozzle radius.

A slight inconsistency between the as-designed geometry of the LOX post and the as-built LOX post should be noted. Consider the nozzle tube component of the swirl injector and its base; these two parts are welded together to form a single component to be mated to vortex chamber component of the injector. To avoid geometric discontinuities on the wetted surface of the injector attributed to original welding specifications, a special weld tack was instead placed on the outside diameter

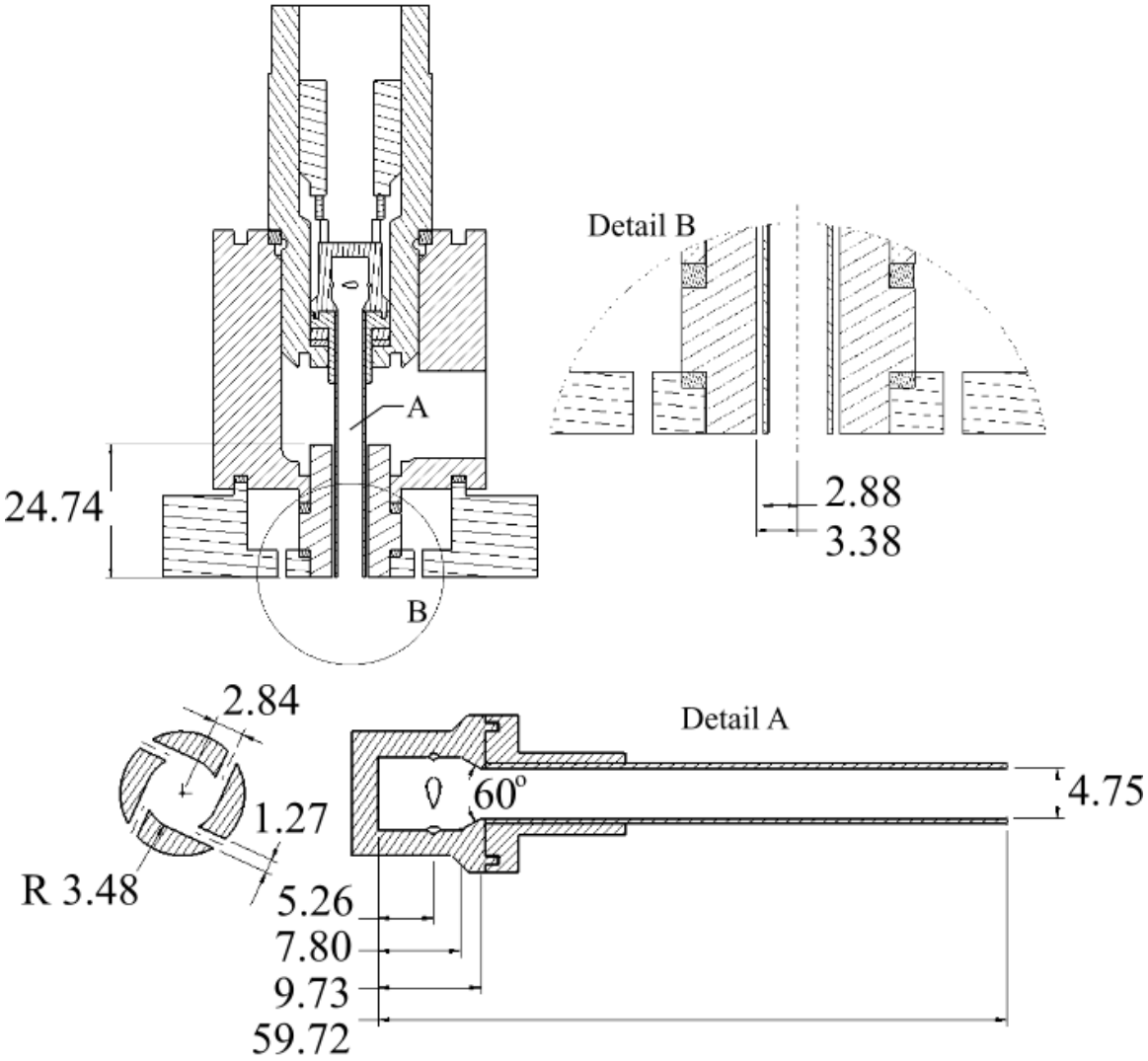

Figure 2.2: Swirl coaxial element housed within its manifold and detailed view of LOX post swirl element; dimension in mm.

of the base-to-tube interface. Despite, a small gap is believed to have remained at the location where the nozzle component interfaces with the vortex chamber component. Figure 2.3 depicts the location of this gap, which is estimated ≈ 0.01 mm in length. Under compression required for the injector assembly, this gap is likely even smaller. Since the suspected gap is located both downstream of the critical contraction of the

Table 2.2: Swirl Element Dimensions

Feature	Value (mm / —)
R_t	0.633 / 0.267
L_t	2.532 / 1.066
R_{vc}	3.480 / 1.465
L_{vc}	7.800 / 3.284
R_s	2.840 / 1.196
L_c	1.930 / 0.813
R_n	2.375 / 1.000
L_n	49.99 / 21.05

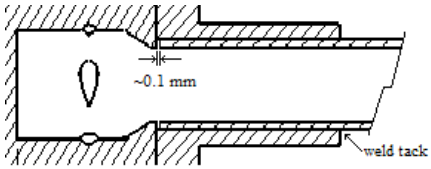

Figure 2.3: Schematic detailing the slight gap at the interface between the LOX post nozzle component and the vortex chamber component.

vortex chamber and is smaller than anticipated length scales of the liquid flow, its presence is important to note, but reasoned—most importantly—insignificant to the fluid dynamics upstream within the vortex chamber and minimally significant to the fluid mechanics of the liquid film in the nozzle and ensuing spray cone.

The modular design of the element and housing grants the ability to modify several geometric parameters of the injector with relative ease. Recess of the inner swirl post is one parameter for which this is the case. Figure 2.2 depicts the test article mounted in a flush configuration; however, swirl post recess can be achieved by inserting precision-machined spacer rings around the base of the post's nozzle segment. This spacing can then be fine-tuned by slight rotation of the swirl post

housing within the fuel manifold cube. Implementing recess in this manner allows for a desired recess configuration without physically altering the characteristic length of the outer annulus.

An additional design feature of the test article housing is its curtain flow faceplate. This component allows optional gaseous flow to be supplied to orifices that run through the faceplate. This flow can be used to remove—or actively deter the formation of—droplet formations on the faceplate. Positive flow through the faceplate orifices was not provided as an active deterrent during testing, but was used only before/after a test run.

2.3 Test Condition Design

Prior to the experimental campaign, a test condition design exercise was conducted with several aims in mind. The first objective was to develop liquid flow set points based on observations of self-pulsation conditions from the initial assessment with the flush mounted configuration. The second objective was to provide research continuity by expanding these flow conditions to more fully cover experimental parameter space investigated in the literature. In expanding the test conditions, a third objective was developed to maintain flow similitude across varied flow conditions and injector configurations by means of non-dimensional scaling.

2.3.1 Flow Scaling

Bazarov and Yang [47] provide guidance on flow parameters of interest, wherein the onset of self-pulsations is described to be sensitive to steady propellant momentum

flux, $\bar{Q}$, defined by Equation 2.1. Furthermore, momentum flux is important to LPRE scaling methodologies [61, 62, 68], such that propellant momentum flux is manifested in the non-dimensional scaling parameter momentum flux ratio, Φ. The definition of momentum flux ratio commonly used for gas-liquid coaxial injectors is expressed by Equation 2.2.

$$\bar{Q} = 2\bar{q} = \bar{\rho}\bar{u}^2 \tag{2.1}$$

$$\Phi = \frac{\bar{Q}_g}{\bar{Q}_l} = \frac{\bar{\rho}_g \bar{u}_g^2}{\bar{\rho}_l \bar{u}_l^2} \tag{2.2}$$

While Im et al. [39] suggest an alternate scaling parameter may exist to better describe self-pulsations, scaling of test conditions based on $\bar{Q}$ was selected with the intent to remain consistent with Bazarov and Yang, as well as those from the preliminary investigation of the phenomenon. Thus, test conditions were specifically designed to span the liquid momentum flux space originally described in the work of Bazarov and Yang. For each $\bar{Q}_l$ set point, a series of $\bar{Q}_g$ conditions was devised in such a way as to also maintain constant Φ conditions across the parameter space. These conditions were applied similarly for all injector configurations for consistency.

2.3.2 Development of Flow Conditions

Test flow conditions were primarily developed around those belonging to the liquid swirl injector. As such, the first step in test condition design around liquid momentum flux is establishing the basic fluid mechanical parameters of the swirl injector which might allow for estimation of $\bar{Q}_l$. Since velocities and densities are not explicitly measured in the experiment, injection condition estimates must be inferred

from fluid mass flow. As such, a span of flow beginning near 25% of the ideal injector design point is explored as a potential range at which self-pulsation testing might be conducted.

To establish fluid mechanical characteristics of the swirl injector over this range of conditions, a series of bench-top calibration experiments were conducted with the aim to develop empirical relations which might help determine key parameters required to estimate injection momentum flux. In addition, rigorous uncertainty analyses were implemented to further estimate the quality of these key parameters. The following will detail those relations.

An elementary calibration test was devised to develop an expression relating liquid manifold pressure to liquid mass flow rate. In these tests, time was recorded while liquid was collected in a reservoir. The mass of the liquid was then measured, permitting an evaluation of mass flow rate by the formula, $\dot{m}_l = m_l/t_{col}$. Figure 2.4 plots measured flow rate as a function of manifold pressure in several flow regimes. These data were combined and linearized, as seen in Figure 2.5, to generate the empirical curve-fit described by Equation 2.3, where $\dot{m}$ is in units kg/s and Δp_l is in Pa.

$$\bar{\dot{m}}_l = 9.379x10^{-5}\sqrt{\Delta p_l} + 3.524x10^{-3} \tag{2.3}$$

In this linearized form, the $\bar{\dot{m}}_l(\Delta p_l)$ expression is well-conditioned for standard uncertainty regression analysis [69]. The uncertainty regression analysis incorporates the total expanded uncertainty of the pressure measurements—also estimated by

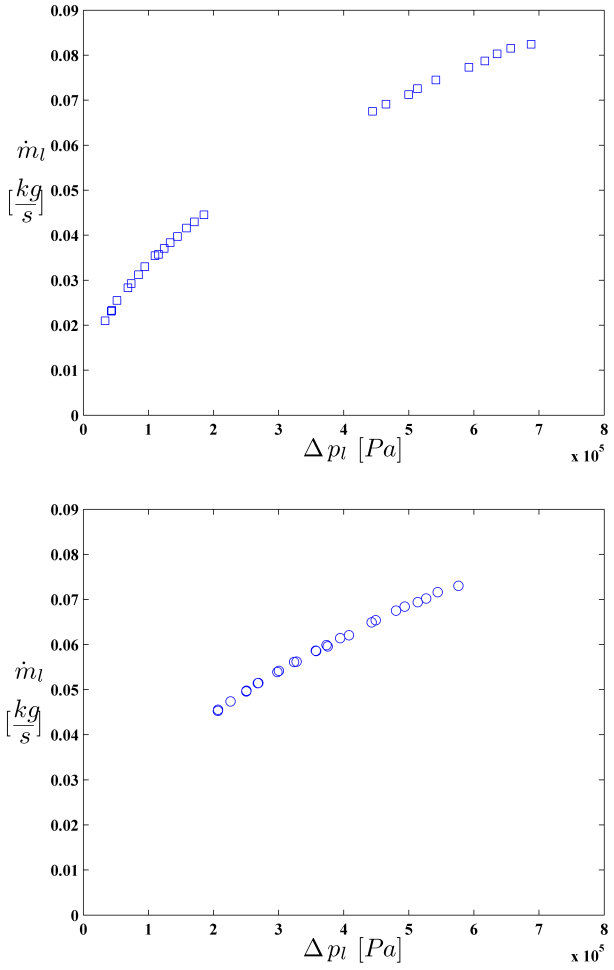

Figure 2.4: Measurements of liquid mass flow rate as a function of injection pressure drop.

uncertainty regression—as well as the total expanded uncertainty of the mass flow measurement (estimated by Taylor series expansion of the mass flow formula). The analysis assumes a mass systematic uncertainty of 2.3 mg and a time systematic uncertainty of 5 ms, while also assuming no correlated uncertainties between the two variables. Figure 2.6 plots the total expanded uncertainty of mass flow regression estimated on a 95% confidence interval.

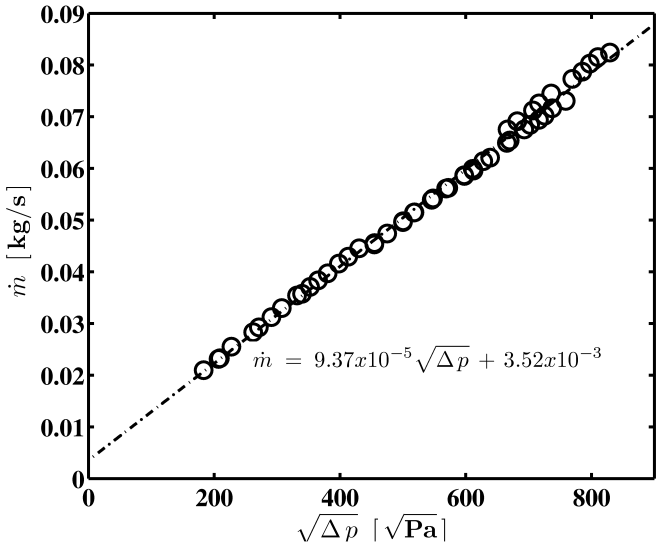

Figure 2.5: Linearized relationship between liquid mass flow rate measurements and injector pressure drop for swirl post with water flow.

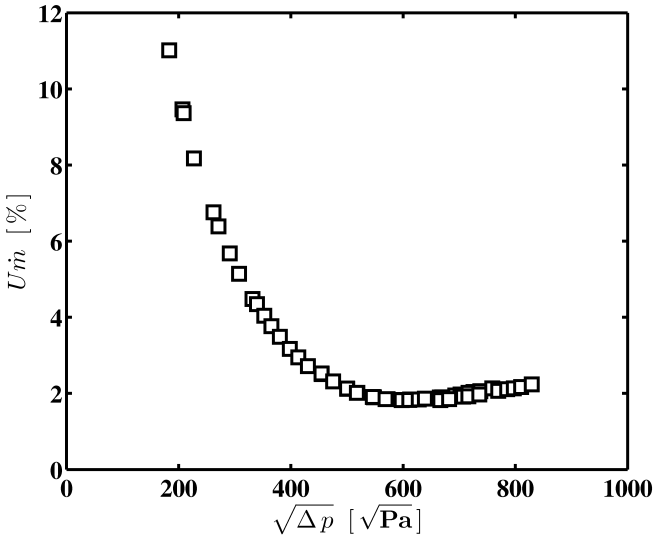

Figure 2.6: Total expanded uncertainty of empirical regression for Equation 2.3.

With an accurate characterization of the swirl injector's flow rate-pressure drop characteristics and a strong characterization of its uncertainty, experimental design could proceed in defining a series of target flow condition set points that would remain statistically exclusive of one another across the flow rate range of interest. Following, basic non-dimensional parameters were estimated to further aid in design of the experiment. If flow is *a priori* assumed inviscid/incompressible and equally distributed between each inlet orifice of the injector, then continuity leads to an estimation of velocity magnitude in each orifice. As such, the Reynolds number of the injector's inlet orifices follows $Re_t = \rho \bar{u} D_t / \mu$ with standard values of ρ and μ for water at STP. The Euler number follows $Eu_t = \Delta p / \bar{q} = \Delta p / 0.5 \rho \bar{u}^2$, and is formulated as the Cavitation number, Ca_t, when $\Delta p = p_{abs} - p_{vapor}$. Table 2.3 tabulates target total liquid flow set points accompanied by approximations of these non-dimensional parameters.

Table 2.3: Target Liquid Flow Conditions

$\bar{\dot{m}}_l$	(g/s)	20	26	31	42	47	52	62	73
Re_t	(—)	5000	6500	7800	11000	12000	13000	16000	18000
Ca_t	(—)	17	12	10	8	7	7	7	6

Two inferences can be made by inspection. First, the Reynolds numbers indicate that flow through the orifices is turbulent at all target conditions—suggesting that inviscid flow assumptions are potentially valid. Secondly, the modified Euler number indicates that cavitation across the orifices should not be expected at any flow condition.

Next, the gaseous flow mass flow rate is estimated simply by the standard isentropic relation for choked flow at the metering orifice upstream in the gas flow circuit; however, compressibility of the flow necessitates a measure of state properties across the injector—particularly temperature—in estimating the injection density and plug-flow velocity magnitude of the gaseous jet. Pursuant, an additional set of calibration tests was conducted to deduce an empirical relation that might be used to compute jet exit temperature as a function of mass flow rate. In these tests, a 0.127 mm diameter K-type thermocouple was used to probe the exit region of the annulus. The thermocouple was attached to a translating micrometer stage, and linearly traversed across the width of the jet. The measurements assumed axisymmetry of the jet's temperature distribution. The arithmetic mean of the three lowest temperatures of each profile was taken as the uniform jet temperature at the exit of the injector.

Figure 2.7 plots jet exit temperature as a function of gaseous mass flow rate, and displays a fourth-order polynomial expression fitted to the data, which is given by Equation 2.4. In an effort to identify uncertainty generated by curve-fit coefficient covariance effects, the empirical relation was evaluated based on 10,000 randomly distributed perturbations of mass flow rate, and a least-squares solution was obtained for each perturbation. Coefficient uncertainties were identified by the convergence of the least-squares mean standard error for each term over the 10,000 iterations. These uncertainties—in addition to those associated with the temperature and mass flow measurements themselves—were then incorporated into a traditional 10,000-point Monte Carlo simulation [69] implemented to estimate total regression uncertainty of

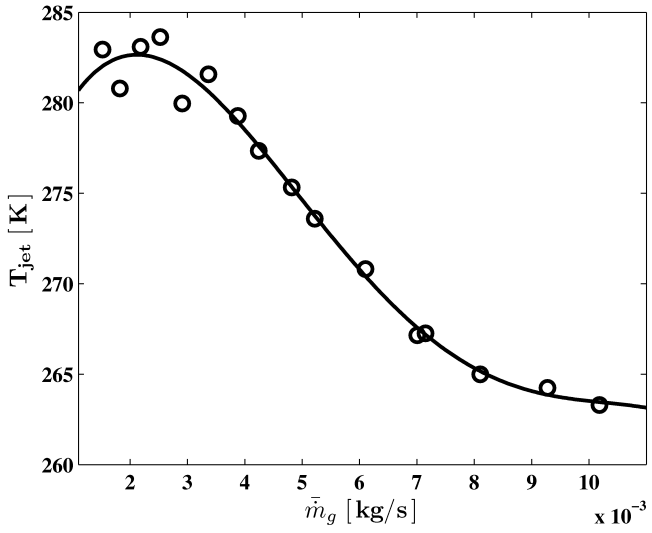

Figure 2.7: Measured jet exit temperature as a function of gas flow rate.

the empirical formula. The total combined uncertainty of the formula is plotted in Figure 2.8.

$$T_{jet} = -1.118x10^{10}\bar{m}_g^4 + 3.594x10^8\bar{m}_g^3 - 3.582x10^6\bar{m}_g^2 + 1.080x10^4\bar{m}_g + 272 \quad (2.4)$$

2.3.3 Geometric Variation

It is generally agreed upon in all studies that the recess of the inner swirl post is the most significant geometric parameter with respect to self-pulsation; however, the literature contains a certain level of inconsistency regarding the normalization of this recess length scale with regards to the self-pulsation phenomenon. For example, Zhou [50] et al. normalize recess length by the diameter of the fuel annulus and do not elaborate on their selection of this dimension. Alternatively, Im [39] et al. normalize

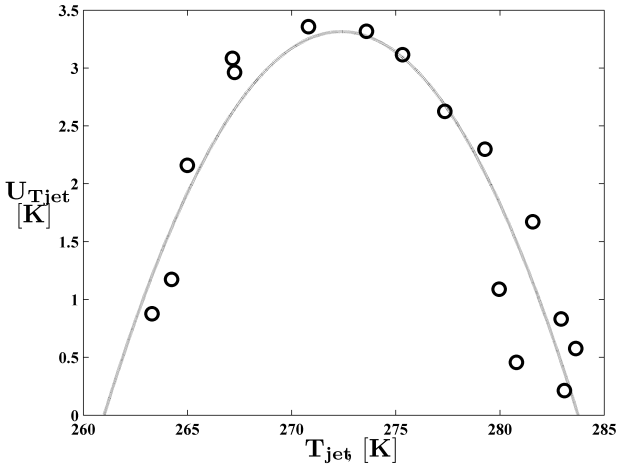

Figure 2.8: Total uncertainty of empirical formula for jet temperature (Equation 2.4).

recess by the diameter of the inner swirl post, and imply this to be related to the normalized recess of shear-coaxial jets—but offer no rationalization.

Consider Figure 1.13 in perspective with the author's original description of the self-pulsation,

> "*The spreading of the liquid sheet into the stream of co-flow can cause dynamic fluctuations in acoustic impedance at the exit of the gas annulus,*"

inferred from Bazarov and Yang [47]. In this context, it would seem there are additional lengths related to the spreading of the liquid sheet and the geometry of the gas annulus that ought to be considered. Since the spreading of the sheet is flow dependent (either influenced by the pressure-swirl injection characteristics, the gaseous jet characteristics, or both), its length scales are typically difficult to explicitly identify/determine. Nevertheless, the diagonal distance between the inner wall of the LOX post and the outer wall of the gas annulus appears an important length scale

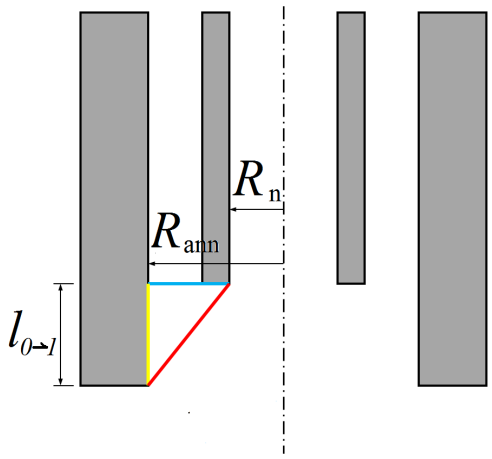

Figure 2.9: Geometric interpretation of the characteristic recess dimension for liquid-centered swirl coaxial injectors.

to consider in relation to the recess. This distance represents a critical condition at which the fuel annulus is completely blocked by the liquid sheet.

Figure 2.9 offers geometric interpretation of this characteristic recess dimension, wherein Pythogoras is called upon to define the term by injector geometry. The hypotenuse is normalized by the radius of the injector element (equivalent to the radius of the fuel post), such that now the non-dimensional recess ratio, $\Re\Re$, is defined as:

$$\Re\Re = \frac{\sqrt{l_{0\to1}^2 + (R_{ann} - R_n)^2}}{R_{ann}} \tag{2.5}$$

Applying this new definition of recess ratio, the tests performed by Zhou et al. [50] translate to span $\Re\Re = 0.51\text{-}2.74$, while Im et al. vary $\Re\Re$ from 0.64-1.25. Table 2.4 lists recess parameters designed to overlap with both studies [39,50] while also expanding upon the range of slightly recessed conditions described in the literature to date.

Table 2.4: Test Recess Ratios

Configuration	$l_{0 \rightharpoonup 1}$	$\Re\Re$
(—)	(mm)	(—)
1	0	0.30
2	1	0.42
3	2	0.66

2.4 Experiment Description

2.4.1 Facility Details

Cold flow tests were conducted in a facility at the University of Alabama in Huntsville's Propulsion Research Center. The High Pressure Spray Facility (HiPSF) is located in the Propulsion Center High Bay 1 at the JRC Complex. The HiPSF is a cold flow test bed specifically commissioned to accommodate non-reactive LPRE injector studies with full-scale hardware under full-scale flow conditions. Figure 2.10 depicts the facility.

The HiPSF is a pneumatic blow-down system, which, in its nominal configuration, delivers high pressure controlled simulant flow through two main circuits—one for double-filtered de-ionized water (H_2O), and one for filtered/dried air. The facility is driven by a 14.2 kL air supply tank pressurized up to 17.3 MPa, and can maintain fluid delivery rates of up to 1.4 kg/s and 2.4 kg/s for liquid and air, respectively. Liquid flow can be metered by a variable-area cavitating venturi. The cavitating venturi is a pintle-style device, that, when fully open, does not critically restrict flow in the circuit. Gas flow is typically metered by interchangeable sonic orifices. Additionally,

Figure 2.10: Various portions of the UAH Propulsion Research Center's High Pressure Spray Facility.

the system can also be configured to be driven by and/or supply alternative pressurant such as pure nitrogen or other exotic gases. A piping diagram of the facility can be seen in Appendix B.

Simulant can be diverted to two separate flow paths—the atmospheric spray loop, and the high pressure spray loop. The atmospheric spray loop allows simulant to discharge to an ambient pressure environment. This fosters a test bed ideal for instrumentation and diagnostics set-up, and permits ease in test article installation and configuration. For tests discussed in this dissertation, sprays were issued into an open-air environment with a catch basin located directly below the injector.

The HiPSF is equipped with a stand-alone data acquisition (DAQ) system for measuring, monitoring, and capturing a variety of pressures, temperatures, and flow rates throughout the facility. It consists of a 32 channel National Instruments (NI)

DAQ card controlled by personal computer that runs NI LabView® software. The LabView® DAQ program actively samples, averages, and displays steady state data in real time. Congruent with active monitoring capabilities, an auxiliary mode in the programming samples raw measurements at 1 kHz and writes to file when manually prompted. This data is retrieved from a buffer and written to file in one second blocks that appended until the program is manually cued to cease recording mode.

2.4.2 Diagnostics

2.4.2.1 Instrumentation & Data Acquisition

The liquid manifold of the test article was instrumented with a dynamic pressure transducer located within the reservoir upstream of the pressure-swirl atomizer. The gaseous circuit of the test article was also outfitted with an unsteady pressure measurement located in the feedline just slightly upstream of the gas manifold reservoir. PCB model 106-B piezoelectric dynamic pressure transducers were used for both liquid and gas simulants; Figure 2.11 details the location of the sensors. Static pressures and temperatures were also measured to establish fluid state conditions at or in close vicinity of the dynamic instrumentation. Additionally, measurements of sound emissions were gathered by a Sony model ECM-44B condenser microphone positioned in the far-field of the injector element at about 460 mm from the injector axis.

Spray behaviors were diagnosed with temporally- and spatially-resolved digital high speed cinematography. Instantaneous images were captured simultaneously by

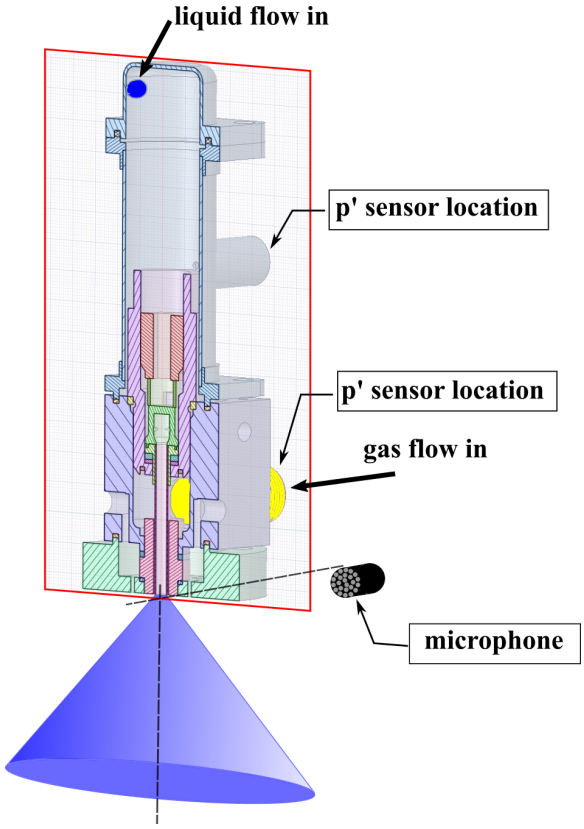

Figure 2.11: Schematic detailing the positions of dynamic sensors relative to the test article.

two high speed CMOS cameras—a Vision Research Phantom® Miro v4 and a Vision Research Phantom® v711. The Miro v4 was equipped with a Nikon 105 mm Micro-Nikkor® lens, while the v711 was outfitted with a Nikon 85 mm Micro-Nikkor® lens. Images from each camera were exposed for 2 μs and captured at a rate of 18.4 kHz at 12-bit depth. Miro v4 and v711 frames were sized at 256x104 pix and 512x384 pix, respectively. Image spatial resolution was calibrated daily. For schlieren imagery, these resolutions ranged between 23.4 and 29.7 $\mu m/pix$ over the course of the test campaign.

Signals generated by dynamic sensors were acquired through a portable system consisting of an NI model USB-6363 DAQ and a data collection laptop computer equipped with LabView® software. Dynamic data were sampled at at rate of 50 kHz and 16-bit depth. High speed imagery was also recorded with the portable system, wherein Phantom Camera Control (PCC®) software was run on the laptop. Commensurate acquisition of dynamic data and high speed images was achieved by implementing a simultaneous external triggering mechanism based on a 5 V TTL pulse with detection set by a 2.5 V down-cross threshold.

2.4.2.2 Setup

Emphasis was placed on capturing the motions of both the liquid spray cone as well as the co-annular jet in the near-field of the injector. Pursuant, Toepler's z-type schlieren [70] configuration was implemented to visualize index of refraction gradients created by the presence of the spray. The schlieren technique was also selected for its ability to capture distinct contrast between the interface of the liquid and gas phases of the spray. Schlieren images were captured by the Phantom v711 camera. The z-type illumination scheme is depicted in Figure 2.12.

Broadband light was generated by a Newport-Oriel model 66912 xenon arc lamp. The lamp created a high flux 7.62 cm diameter beam of collimated light, and was operated at a peak power of 150 $Watts$. Two 10.16 cm parabolic mirrors were implemented in the z-type setup. In addition to their use towards the schlieren technique, these mirrors provided a magnified field-of-view in the near-field of the

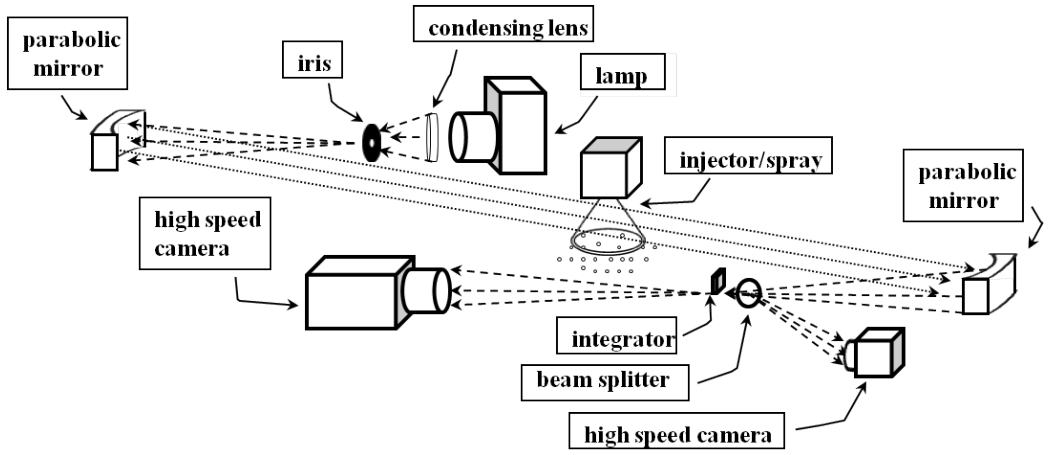

Figure 2.12: Diagram of Toepler's z-type schlieren configuration as applied to imaging setup for spray experiments at ambient backpressure.

injector. A "knife-edge" integrator (a razor blade) was horizontally positioned as to enhance contrast of refraction gradients oriented in the vertical direction.

While the schlieren technique is effective at visualizing two-phase flows and drawing stark distinction between fluid boundaries, several undesirable sensitivities of the technique were anticipated. Convolution/aberration effects resulting in reduced clarity and depth-of-field can be difficult to minimize with schlieren. Back-lit shadowgraphy imaging is less sensitive to these effects, but, conversely, is less effective at visualizing details of two-phase flow. Hence, an auxiliary high speed camera was used to simultaneously gather direct shadowgraphy of the sprays. Implementation of this duel imaging system was achieved by inserting a beam-splitter within the light path upstream of the schlieren integrator, as seen in Figure 2.12. The utilized beamsplitter was a 3 *in* diameter Newport lens. Shadowgraph imagery was gathered by the Phantom Miro v4 camera.

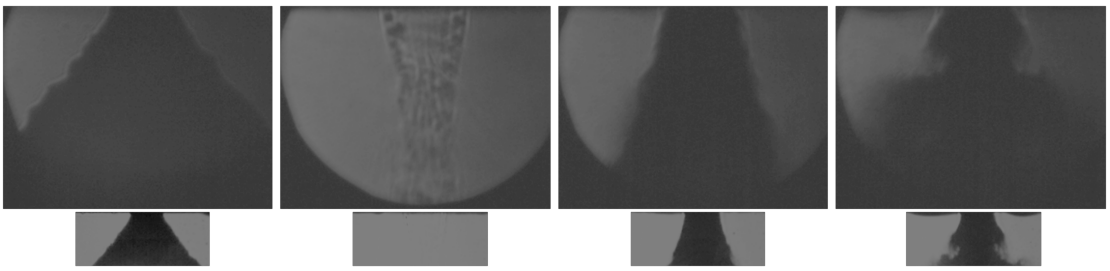

Figure 2.13: Comparisons of instantaneous schlieren and shadowgraphy for (left-to-right): pressure-swirl liquid injection, annular gas injection, non-pulsatile swirl-coaxial injection, and swirl-coaxial injection under self-pulsation (image brightness adjusted for presentation only).

Figure 2.13 showcases the ability of schlieren imagery to capture different aspects of the spray field, where these types of imagery are compared with simultaneous back-lit shadowgraphy imagery. The ratio of scales between the two image types have been preserved for comparison. Also note that the brightness of these images have been artificially increased for presentation purposes, but has been done so uniformly to preserve relative contrast between the two different image techniques.

2.5 Test Execution

All tests consisted of two general components: establishment of steady flow conditions, and data acquisition. In this vein, fluid pressures were set such that when desired steady flow conditions were achieved, data were collected. Since low speed and high speed data acquisition systems were independent of one another, a general test procedure was developed and adhered to for all tests. The low speed data collection system was configured to record data upon manual command and stop data recording with a subsequent manual command, while the dynamic DAQ

was configured to record data upon command and cease when a prescribed amount of data was gathered. Thus, once a desired flow condition reached a steady level, low speed data acquisition was cued followed by independent triggering of dynamic data acquisition. Once sufficient dynamic data were acquired, the low-speed DAQ was commanded to cease. This procedure ensured that, while low-speed and dynamic data were not synchronized, the dynamic data were collected over the time span of the low-speed data to be used to infer the steady state flow conditions.

The shear number of conditions proposed for the tests conceived earlier presented a time expenditure challenge to the experimental campaign. As a solution, cases were not performed distinctly for each individual test, but rather interwoven for a practical, more efficient tack. The following will describe in a general sense how the tests were executed.

- **Pressure-swirl Testing** Testing of the pressure-swirl atomizer was typically performed before all other tests. In doing so, pressure conditions were prescribed to achieve a target liquid mass flow rate condition. Once this condition was achieved and held at a steady level, low speed and high speed data acquisition commenced. After completion of data collection, DAQ tools were switched off while liquid flow was held at steady flowing conditions in preparation for immediate tests to probe for the onset of self-pulsation.

- **Self-pulsation Onset Probing** With liquid flowing at a fixed steady flow rate, probing of self-pulsation onset was initiated by activating low level gaseous flow. Here, the gaseous flow rate was manually throttled until self-sustained spray

oscillations were achieved. A procedure was devised to avoid the effects of potential hysteresis in the system. Once self-sustained oscillations were present, gaseous flow rate was slightly increased. Following, gas flow rate was then decreased until self-sustained oscillations vanished, and data were collected. Next gas flow was immediately increased again to the bound of self-pulsation once more. At these flow conditions, data acquisition was cued, and upon completion, was deactivated. Next, with gas still flowing, the liquid circuit was deactivated and data was collected with only gas flow. Gas flow was then deactivated, and liquid flow was reactivated to steady conditions in preparation for parametric flow variation tests.

- **Parametric Flow Variations** Having completed boundary probing tests, liquid flow rate was held constant and gas flow rate was manually increased to an initial target setpoint condition. Once achieved, data acquisition commenced. Following, liquid flow was deactivated with gas still flowing, and data was collected for gas flow only. A new gas flow rate was then set, and liquid flow was re-established at steady flow conditions, wherein data were collected. The test processes was subsequently repeated until data for all setpoints at the fixed liquid flow rate condition were gathered.

In the event that the liquid run tank became depleted within the sequence of parametric flow tests, both liquid and gas flows were deactivated while the liquid run tank was replenished with water. Liquid flow rate would then be re-established at the steady target test condition, steady gas flow rates would be achieved, and testing

would continue as previously described. Once a set of parametric flow variation data was completed, test execution would recycle to pressure-swirl test procedure and those thereafter.

CHAPTER 3

DATA PROCESSING METHODOLOGY

3.1 Steady Data Reduction

Time-averaged, or mean flow, pressure and temperature data were statistically reduced to meaningful descriptors for each test condition. In doing so, several expressions (including those developed for liquid mass flow rate and jet exit temperature) were implemented to translate these basic state conditions. Key expressions and their associated assumptions are now discussed.

Assuming incompressible, inviscid flow and applying continuity, liquid injection velocity magnitude can be inferred from knowledge of liquid mass flow rate through Equation 3.1. In this case, the appropriate characteristic length required to deduce this velocity is the liquid film thickness at the injection plane, h_0 given by Equation 3.2. While classic ideal [11, 12] and empirical [14, 67] theories suggest that h_0 is primarily dependent upon the geometric characteristics of the atomizer—i.e. h_0 is ultimately independent of mass flow rate—experimental observations [71–73] seem to suggest otherwise. The ideal hydraulic calculations used to design the injector for a particular fluid at a particular flow condition do not capture well the dissipative effects that can arise when flow rate is made to deviate from the injector's design

point or when an alternative fluid to that for which the element was designed is introduced. Surveyed well by Moon et al. [73], it is common practice to estimate swirl injector hydraulic characteristics by semi-empirical correlation in order to more accurately account for such lossy hydraulics and manifest flow/spray features. Therefore, an empirical film thickness expression developed by Suyari and Lefebvre [74] and applicable to liquid flow conditions in this study is used here. Appendix C qualifies in further detail the use of this expression.

$$\bar{u}_l = \frac{\bar{\dot{m}}_l}{\bar{\rho}_l h_0 (d_n - h_0)} \tag{3.1}$$

$$h_0 = 3.66\{\frac{d_l \bar{\dot{m}}_l \mu_l}{\bar{\rho}_l \bar{\Delta} p_l}\}^{0.25} \tag{3.2}$$

In Equation 3.2, the film thickness, and thus injection velocity magnitude, is seen to be a function of mass flow rate, atomizer geometry, and fluid transport properties. The kinematic viscosity of common liquids is known to be more sensitive to variations in temperature than in pressure. Neglecting heat transfer effects, the bulk temperature of the liquid in the manifold is assumed equal to that at the injection plane. Thus, fluid viscosity can be estimated by the well-known Sutherland's law given liquid temperature.

Isentropic expressions are utilized to estimate gaseous mass flow rate through the facility's sonic metering orifice upstream of the injector element, which is easily computed with knowledge of orifice temperature and pressure. Through continuity (and assuming incompressibility for low subsonic flow where $M < 0.3$), the gas injec-

tion velocity magnitude can be retrieved by $\bar{u}_g = \bar{\dot{m}}_g / \bar{\rho}_{jet} A_{ann}$—with the geometry of the gas annulus as an important parameter. An expression estimating the hydraulic diameter of annular spaces [75] is implemented to provide consistent estimates of bulk velocity magnitude in the gas annulus.

$$d_{ann,h} = \{(d_{ann,out} + d_{ann,in})^2 (d_{ann,out} - d_{ann,in})^3\}^{0.2} \tag{3.3}$$

When required to address compressibility effects at higher speeds, gas injection Mach number is determined by Equation 3.4. Gas injection velocity magnitude is then computed by the relation $\bar{u}_g = M\sqrt{\gamma R T_{jet}}$.

$$M = \sqrt{\frac{2}{\gamma - 1}\{(\frac{\bar{\rho}_{jet}}{\bar{\rho}_g})^{1-\gamma} - 1\}} \tag{3.4}$$

3.2 Dynamic Data Analysis Techniques

Quantitative analysis of spray dynamics is accomplished through image processing techniques applied to the digital high speed imagery. Temporally- and spatially-resolved pattern recognition was implemented to extract coherent light intensity fluctuations that occur primarily on the edges of contiguous portions of the flow field and/or through non-contiguous regions of the flow field. From these measurements, distinct dynamic behaviors of the flow can be inferred, and—coupled with traditional spectral analysis—frequencies, phase angles, and wavelengths of the behaviors can be quantified. These data, in conjunction with information extracted from spectral

analyses of the pressure signatures, help to decipher key physics at play during self-pulsations.

3.2.1 Data-based Modal Decompositions

Before the pursuant discussion, it is prudent to first draw distinction between what might be confused with coincident or conflicting usage of the term *mode*. *Mode* is common terminology in a variety of engineering fields such as: acoustics, combustion, and vibration, and is typically used to describe organized motions that are distributed in space, time, or both. This fundamental notion of organized behaviors distributed in space/time is carried over in the usage of *mode* in the following text, but should not be confused with the familiar—e.g. a 1^{st} tangential mode of thermo-acoustic oscillation, a 2^{nd} diametral mode of shell vibration, etc. Hence forth, it may be beneficial to the reader to envision a mode simply as a pattern of correlated, organized behavior.

Data-based modal decomposition analyses have seen increased use amongst the engineering community as useful tools in reducing high-dimensional data sets to lower-order descriptions, wherein important physics can be isolated and identified. These techniques can be applied to reveal dominant dynamic behaviors of a system, such that the extracted information may be used to develop reduced-order dynamical models. Such is the typical approach towards quantitative data (velocity, pressure, heat release, etc.) generated by CFD or captured by experiment. In addition, the application of modal analyses to empirical data such as light intensity is considered a form of quantitative pattern recognition methods discussed in principal image processing texts [76].

A high speed video can be regarded as a sequence of individual "instantaneous" frames collected in time. Each frame is an image containing a structured array of spatially discrete values known as pixels. Pixels can contain information that represent luminance, hue, and saturation of light which can be scaled in a variety of manners to represent any number of physical features of an imaged object. While these pixel data may be somewhat obscure in relation to fluid flow parameters such as pressure, temperature, etc., the dynamic *change* in pixel data hold potentially useful information describing the physical dynamics of an imaged object. Analysis of how pixel data change from frame-to-frame and from pixel-to-pixel can be utilized to identify organized activities in both space and time. Objective treatment of pixel data in this fashion is the essence of video pattern recognition.

The Proper Orthogonal Decomposition [77] (POD) has recently developed popularity as not only a powerful tool in computational fluid dynamics and turbulence modeling [78] but also experimental fluid dynamics and combustion [79,80]. The ability of the POD to segregate and extract the influence of coherent flow structures—differing in both length and time scales—on the global dynamic motion of a fluid over a given period, has proven to be a powerful tool toward the analysis of experimental data sets. Time-resolved POD has been applied to the evaluation of various spray phenomena, and, in this vein, an influential work is introduced by Arienti and Soteriou [81]. The authors describe the application of the POD to time-resolved images of a liquid jet in high speed cross flow. Arienti and Soteriou's analysis resolved travelling waves which, quantified by frequencies and wavelengths yielded by POD analysis, corresponded to the Kelvin-Helmholtz instability mechanism. Narayanan [82] et al.

implemented the POD in the study of gas-centered swirl-coaxial sprays. Their study applied POD analysis as a means to quantify oscillation frequencies in spray width and angle, and also used the results as a preprocessing tool to improve spray boundary detection. Teshome [42] et al. exploited the POD of high speed imagery to identify effects of an externally forced acoustic field on the dynamic behavior of supercritical cryogenic shear-coaxial injection. The authors demonstrated the ability of the POD to resolve dynamic response of the jets to high frequency acoustic disturbances.

While the extension of POD analysis to the study of turbulence and coherent structures was first brought forth through the ideas of Lumley [83], the mathematical framework [84–86] from which the POD and other data-based modal decompositions stem is fundamental. The POD roots itself in the idealization that a given space-time sequence can be represented as a series of linearly combined temporal and spatial components, provided that the ergodic hypothesis is satisfied over the sequence. In this generalization, the spatial components represent the basis vectors (sometime referred to, generally, as topos) of the sequence and the temporal components represent amplitude scalars (sometimes referred to as chronos) of the topos in time. The topos—or basis functions—can be idealized as any type of mathematical function provided they are bounded and continuous over the domain. However, in defining the basis functions, say as a Fourier series, the determination of a single chronos will be dependent on multiple topos.

$$z(x,t) = \int_{r=0}^{r\to\infty} a_r(t)\phi_r(x) \tag{3.5}$$

The POD aims to alleviate such an outcome. In choosing to stipulate *orthonormal* basis functions, decomposition of the series will yield distinct chronos solutions which are dependent upon singular topos solutions as seen in Equation 3.7. Furthermore, the selection of orthogonal basis functions minimizes the least-squares error for any ordered basis function reconstruction of the sequence. In this sense, the POD is optimal for modeling or reconstructing a sequence to satisfy Equation 3.5. [87].

$$\int_x \phi_{r1}\phi_{r2}dx = \delta_{r1r2} \tag{3.6}$$

such that

$$a_r = \int_x z\phi_r dx \tag{3.7}$$

For this study, basic application of POD analysis follows that outlined by Arienti and Soteriou [81]. In context to high speed imagery, a video may be regarded as an approximately continuous sequence of "instantaneous" frames, $z(\mathrm{v}_i)$. As experimental data, the frame sequence is considered bounded and discrete such that integration may be approximated by summation. The POD principle is thus slightly reformulated in Equation 3.8, wherein the chronos are regarded as temporal amplitude coefficients, $a_{r,i}$, and the topos are regarded as Proper Orthogonal Modes (POMs), ϕ_r.

$$z_{r,i} \approx \sum_{r=1}^{N} a_{r,i}\phi_r \tag{3.8}$$

These instantaneous frames can be mean-centered about the time-average of the entire sequence as to generate pixel data that represent light intensity fluctuations.

The time-average is referred to as the "base mode", and is considered the mean flow component of the series. In the mean-centered approach to the POD, this base mode is a reference of activity about which all POMs fluctuate.

$$\tilde{\mathrm{v}}_i = \mathrm{v}_i - \phi_0 \tag{3.9}$$

where

$$\phi_0 = \frac{1}{N}\sum_{i=1}^{N} \mathrm{v}_i \tag{3.10}$$

To decompose Equation 3.8, the linear eigenvalue problem, expressed by Equation 3.11, for a characteristic matrix is solved. Values within the characteristic matrix represent the relationships between any two frames in the sequence. The basic measure of these relationships are calculated through the inner product of data points, i.e. two-point correlation, which constitute autocovariance (also referred to as autocorrelation) of the data. In the case of the direct POD method, this characteristic matrix is high-dimensional and may consist of a large number of values.

$$V^{i,j}\upsilon_{r,i} = \lambda_r \upsilon_{r,i} \tag{3.11}$$

Since the computational domain area of each constituent frame (mm x nn) is often much larger than the total number of frames in the sequence (N), the Method of Snapshots/Strobes [88] may be conveniently implemented to reduce the computational intensity typically associated with that of the direct POD method. The Method of Snapshots casts a single characteristic matrix for the series, and is expressed by

Equation 3.12 wherein a reduced-order NxN array is formulated.

$$V^{i,j} = \frac{1}{N} < \tilde{\mathrm{v}}_i, \tilde{\mathrm{v}}_j >= \frac{1}{N} \sum_{1}^{nn} \sum_{1}^{mm} \tilde{\mathrm{v}}_i \tilde{\mathrm{v}}_j \tag{3.12}$$

Solution to the eigenvalue problem yields eigenvectors, $\upsilon_{r,i}$, and eigenvalues, λ_r, that represent directional correlation and scalar magnitude, respectively, and are naturally arranged in ascending order in magnitude. The eigenvalues are real and non-negative, and are often described as a measure of "modal energy" that may be used to describe a mode's significance. Furthermore, since the eigenvalue solutions minimize error in a least-squares sense, eigenvalue convergence may be used to infer the quality of sequence reconstruction by modal combination in satisfaction of Equation 3.8.

POMs are calculated by linear combination of the eigenvector solutions with the individual frames. By mapping each POMs onto the sequence of frames by inner product operation, temporal amplitude coefficient vectors are generated—completing the decomposition. Equation 3.13 and Equation 3.14 describe the computation of the POMs and temporal amplitude coefficients.

$$\phi_r = \frac{1}{\sqrt{N\lambda_r}} \sum_{i=1}^{N} \upsilon_{r,i} \tilde{\mathrm{v}}_i \tag{3.13}$$

$$a_{r,i} =< \tilde{\mathrm{v}}_i, \phi_r > \tag{3.14}$$

The Dynamic Mode Decomposition [89] (DMD) is a modal analysis technique closely related to Proper Orthogonal Decomposition, wherein eigenvalue solutions to the information contained in temporally sequential data similarly provide the basis for

identification of organized behaviors. Unlike the nature of spatial POD which enforces orthogonality in space at the expense of modes with multiple spectral components, DMD aims, when carried out on a time series, to extract modes with pure spectral content (hence temporal orthogonality is enforced) but that are not necessarily orthogonal in space. As such, dynamical information such as frequency, growth rate, and wavelength can be gleaned. Such characteristics have made DMD a popular tool in developing low-order global dynamic models from higher order data sets generated by CFD simulation and experiment alike. To this end, Schmid [89, 90] provides an important example of DMD formulation, execution, and metrics for interpretation of results for experimental data.

DMD calculations follow those established by Schmid [89], with slight modification as proposed by Chen [91] et al. The DMD is formulated as a column vector operation. To begin, two reduced basis sequences are generated, such that $z^{N-1} = \{\mathrm{v}_1, \mathrm{v}_2 ... \mathrm{v}_{N-1}\}$ and $z^N = \{\mathrm{v}_2, \mathrm{v}_3 ... \mathrm{v}_N\}$. The ensemble average is not removed from these sequences. Next, the temporal POD modes are computed for the z^{N-1} by Singular Value Decomposition (SVD) described in Equation 3.15. The SVD is a reduction known to be identical to the Method of Snapshots POD calculation [87].

$$z^{N-1} = \underline{\Lambda A}^{\mathbb{T}} \underline{\Sigma} = \sum_{r=1}^{N-1} \sqrt{(N-1)\lambda_r} a_r^{\mathbb{T}} \phi_r \tag{3.15}$$

The temporal POD results are used to compute the companion matrix, $\tilde{S}$, as expressed in Equation 3.16. At this juncture, the DMD departs from the POD.

$$\tilde{S} = \underline{\Lambda}^{H} z^{N} \underline{A\Sigma}^{-1} \tag{3.16}$$

In effect, the DMD is completed by solving the linear eigenvalue problem for the companion matrix, where $\mathfrak{r}\mathfrak{R}=\tilde{S}\mathfrak{R}$. The eigenvector, $\mathfrak{R}$, and eigenvalue, $\mathfrak{r}$, solutions are referred to as the *Ritz* vectors and values, and are complex. The Ritz vectors are mapped onto the POD modes of the z^{N-1} snapshot basis to yield dynamic modes (DMs) by Equation 3.17.

$$DM_r = \mathfrak{R}_r \underline{\Sigma}_r \tag{3.17}$$

In order to compute the dynamic mode spectrum, sinusoidal periodicity is assumed. In doing so, the Ritz values are fit onto a logarithmic function and normalized by the snapshot bases' temporal spacing as described by Equation 3.18. This operation results in natural logarithm-mapped Ritz values that are complex and in units rad/sec. The real component of the Ritz values signify modal growth rate ξ, while the imaginary portion corresponds to the temporal frequency of a given mode.

$$\omega_r = \frac{ln(\mathfrak{r}_r)}{\Delta t} \tag{3.18}$$

The growth rate of a given mode is useful in stability characterization, wherein positive growth rates indicate increased instability, while negative growth rates indi-

cate damped behavior. DMD of fluid dynamic data sets result in Ritz spectra that are symmetric about a saddle point. The saddle point indicates a neutrally stable mode that is typically the steady mean flow, or D/C, component of the flow field.

While this neutrally stable mode may be similar to the ensemble-average of the flow field, in many instances, they are not equivalent. In the spirit of *a priori* mean-centering of the flow field commonly practiced with POD, Chen et al. [91] propose an iterative augmentation to standard DMD such that the snapshot bases be centered about the neutrally stable mode of the sequence. This method was implemented here in this current study, such that an initial DMD was performed to identify the neutrally stable mode, the mode was removed from the original snapshot bases, and then a secondary DMD was computed.

3.2.2 Spectral Analyses

A variety of basic analyses were implemented as tools in deducing relative flow behaviors and in characterizing important dynamics from the measured/extracted temporal data. Of these, the most fundamental are the auto-spectral functions. Such functions assume that a given time-domain signal is comprised of one or more discrete signals that are linearly superimposed to form a composite. These discrete signals are assumed sinusoidal and expressed as a truncated Fourier series. The auto-spectral functions can thus be used to quantify the amplitude and phase of the discrete components in the frequency domain. This is achieved by the well known Fast Fourier Transform (FFT) [92], wherein the real component, $\mathbb{R}\{X(k)\}$, is half-peak amplitude in engineering units EU while the imaginary component, $\mathbb{I}\{X(k)\}$, is phase angle in

rad.

$$X(k) = \frac{1}{N}\sum_{i=0}^{N-1} x(n)e^{-i(2*\pi/N)kn} \quad for\ k = 0, 1, ...N-1 \tag{3.19}$$

The FFT function is often presented in the form of *power spectral density* (PSD), with power amplitude given in EU^2/Hz. Moreover, accurate extraction of waveform amplitude is achieved by calculation of the *auto spectrum*, wherein the root mean square (rms) amplitude is given in engineering units.

$$PSD(k) = \frac{2N|X(k)|^2}{f_s} \tag{3.20}$$

$$S_X(k) = \sqrt{2}\sqrt{|X(k)|^2} \tag{3.21}$$

These powerful analytics can be expanded to relate the spectral characteristics of multiple composite signals, which, in turn authorize the deduction of correlated behaviors. These functions are what are referred to as linear cross-spectral functions. Equation 3.22 expresses the $cross-power\ spectrum$, which can be used to compute the combined power spectra between two similar signals, and, as with the FFT, is often expressed in the form of cross-power spectral density (CPSD). Building on the cross-power spectrum is non-dimensional *linear coherence*—used to determine the magnitude of dependence between two spectra. Another commonly used non-dimensional relation is the *transfer function*, expressed by Equation 3.24. The magnitude of the transfer function is referred to as *gain*, while the imaginary portion of the transfer function gives the relative phase between the signals. The transfer

function is powerful in indicating the degree at which two spectra are directly related.

$$S_{XY}(k) = 2X_i(k)Y_i(k) \tag{3.22}$$

$$COH_{XY}(k) = |\frac{S_{XY}(k)S_{XY}(k)}{S_{XX}(k)S_{YY}(k)}| \tag{3.23}$$

$$H_{XY}(k) = \frac{S_{XY}(k)}{S_{XX}(k)} \tag{3.24}$$

3.3 Data Processing Details

Dynamic pressure and image fluctuation data were processed with a variety tools included in MATLAB® and PC-Signal® software. A priori knowledge of the flow was used to develop rationale for aspects of the data processing methodology. Take, for example, the self-sustained nature of the self-pulsation phenomenon. This notion of self-sustained behavior implies that the system oscillates in a limit cycle fashion. From a system dynamics standpoint—during limit cycle, fluctuations of various flow characteristics are indefinitely stationary and maintain a stable orbit in phase space unless parameters change which alter the systems trajectory. Based on the self-sustained, stationary limit cycle characteristics of the self-pulsation phenomenon, the analysis of one second of dynamic data (fluctuating pressures) during sustained self-pulsation was deemed appropriate.

Facility and mean flow data were statistically reduced using a combination of MATLAB® and Microsoft Excel® tools. In analyzing these data, one second of data was reduced to mean and standard deviation measurements for each test

condition once steady-state was achieved. The total expanded uncertainties of these measurements were thus able to be identified and propagated through calculations based on the fundamental techniques outlined by Coleman and Steele [69].

The processing methodology was focused around analysis of POD temporal signals and their equivalent characteristic DMD time scales. Since N number image samples is directly related to frequency resolution of the temporal amplitude coefficient spectra, a total number of images to analyze was chosen based on the reasoning that, for a low frequency disturbance at approximately 500 Hz, it would be desired to capture a minimum of 10 cycles in order to assure statistical significance on the order of 95%. Thus, N number images spanning 0.02 seconds of real time sampled at the camera frame rate was analyzed, resulting in spectral bin widths of approximately 25 Hz. Since the frequency content of self-pulsations for this test article were known to be in the range of 1-4 kHz, a 500 Hz floor was deemed sufficient to resolve the spectra or characteristic time scale of self-pulsations well by modal decomposition analyses. For investigation into lower frequency disturbances in the pressure-swirl injection cases, N number of images over 0.10 seconds were analyzed.

One important characteristic of modal-based decomposition analyses—particularly POD—is that they are grid dependent, in the sense that ordered significance of the spatial modes is relative to their individual contribution of light intensity fluctuation in the entire domain. For example, should a group of 5 pixels—within an image of 1000 pixels—coherently fluctuate, their spatial mode relative to the entire 1000 pixels may not be significant if there are larger groups of pixels (e.g. 50, 250, 400, etc.) that also coherently fluctuate. However, if that same group of 5 pixels is restricted rela-

tive to an image of 100 pixels, then the group's fluctuation will be more significant relative to this restricted domain. Practically, this thought exercise brings to light that POD is sensitive to image cropping, and that, should a particular region in the flow be of interest, the image can be cropped such that dominant local flow behaviors in that region will be more readily resolved and ordered by the analysis. In the case of modal decompositions, the global injection/spray dynamics of self-pulsations were of primary interest. Frames were thus cropped only to remove inactive portions of an image (recall the dark borders around the frame edges seen in Figure 2.13) rather than to focus on local dynamics of the spray.

3.4 Swirl Coaxial Analysis Example Case

The following section will demonstrate the typical processing and analysis of data for an example case of swirl coaxial injection under self-excited and sustained oscillations. Considering the shear quantity of data collected during the test campaign, the processing tactics and operations to follow were automated in syntax deployed in the MATLAB® environment and/or in routines configured within PC-Signal®. This automation granted the ability to reduce vast amounts of data in a relatively short period, and helped facilitate more streamlined interpretation of the results.

The examined test case occurred at $[\bar{\rho}_l \bar{u}_l^2, \bar{\rho}_g \bar{u}_g^2] \approx [40{,}283]$ kPa in the flush-mounted configuration. This particular condition was well above the stability boundary for the $\Re\Re = 0.30$ configuration. Figure 3.1 plots the auto-spectra of pressure fluctuations registered in the liquid manifold and the gas feedline of the injector, while the auto-spectrum of far-field SPL during self-pulsation is also presented. The spec-

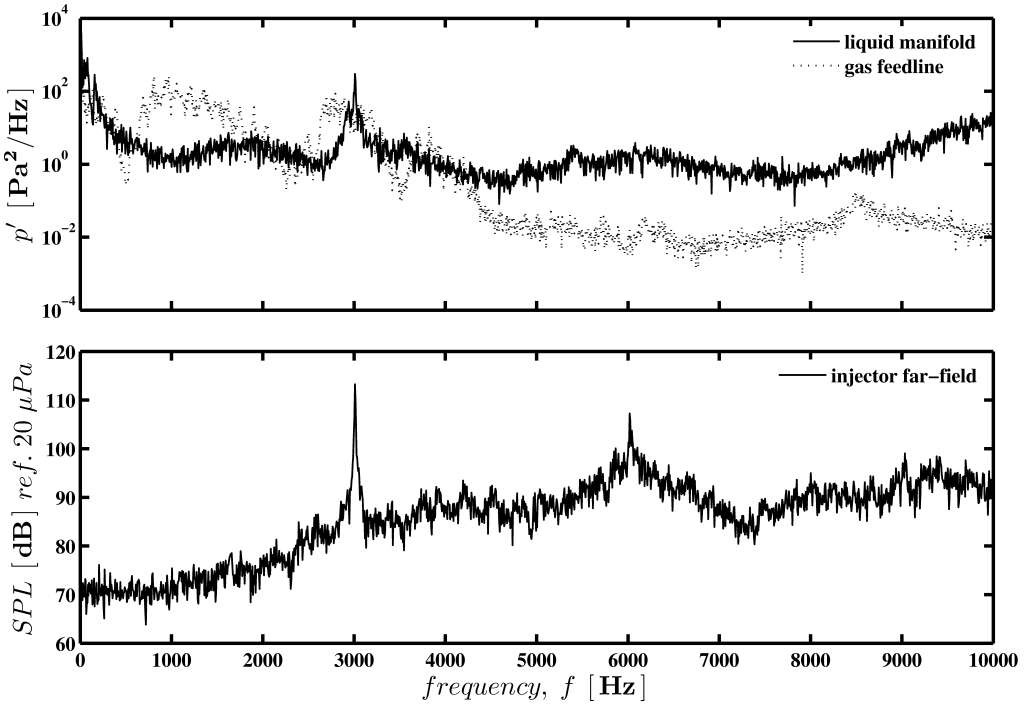

Figure 3.1: Auto-spectrum of top: dynamic pressures upstream of the injector element, and bottom: SPL in the far-field measured during self-pulsation with the $\Re\Re = 0.30$ recess configuration at $[\bar{\rho}_l\bar{u}_l^2,\bar{\rho}_g\bar{u}_g^2] \approx [40,283]$ kPa.

tral characteristics indicate a high intensity tone at approximately 3 kHz. Pressure fluctuations at similar frequencies are also registered upstream in both the liquid and gas circuits of the injector. Coherence functions plotted in Figure 3.2 reveal liquid pressure fluctuations are strongly correlated to the fundamental tone in the far-field while the gas fluctuation is only weakly correlated. Fluctuations between the liquid and gas are also weakly correlated near 3 kHz.

To begin processing and analysis of the imagery, basic image preparations were performed. The Vision Research $.RAW$ format video file was cropped to dimensions 432x248 pixels, then converted and exported as individual frames output in 12-bit

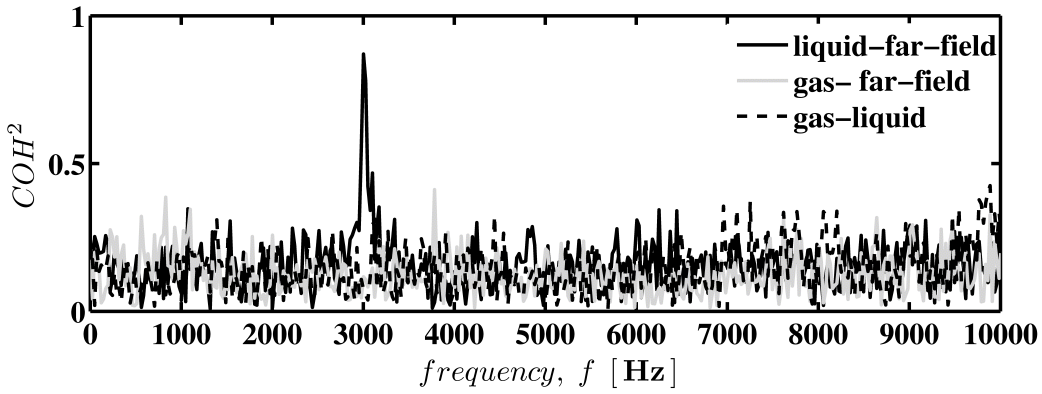

Figure 3.2: Liquid-to-far field SPL, gas-to-far field SPL, and liquid-to-gas coherence functions showing significant coherence between the 3 kHz tone and pressure fluctuations in the manifold upstream of the LOX swirl element.

grayscale *.tif* format using PCC software tools. Figure 3.3 depicts one characteristic cycle of spray field oscillations captured by the high speed schlieren imaging technique. Recalling the small dynamic range of the raw schlieren imagery seen in Figure 2.13, here contrast has been enhanced only in the presentation of these images. The principal liquid spray dynamics are distinct in this image, wherein strongly periodic contraction and rarefaction of the spray cone provokes the propagation of large scale disturbances in the axial direction of flow. Approximate phase stations of the spray oscillation are provided for reference.

3.4.1 Analysis by Proper Orthogonal Decomposition

As discussed in the prior section, approximately 0.02 seconds of real time data were analyzed for most cases such that a sequence of $N = 369$ images were decomposed by the POD. Figure 3.4 illustrates the ensemble average of spray motions over the sequence. Flow features in the grayscale image are difficult to deduce by eye

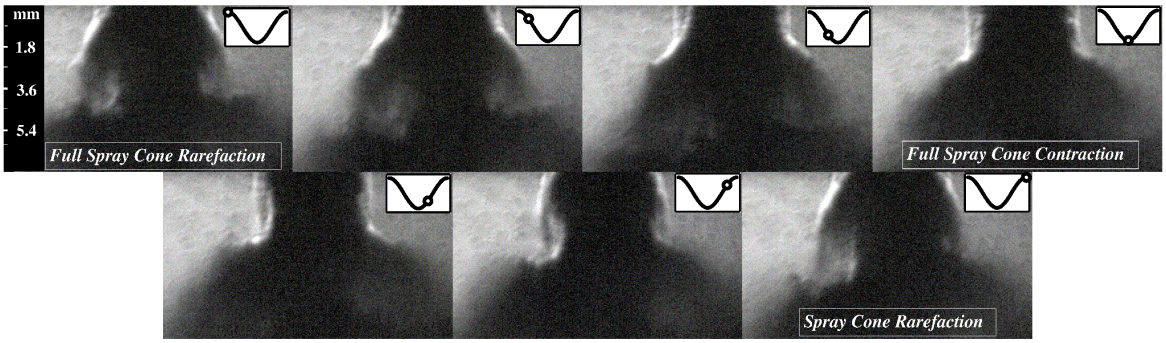

Figure 3.3: Sequence of images depicting the contraction and rarefaction of the liquid spray cone and convection of disturbances downstream over one characteristic cycle of self-pulsation. The inter-frame time step is approximately 54.24 μs.

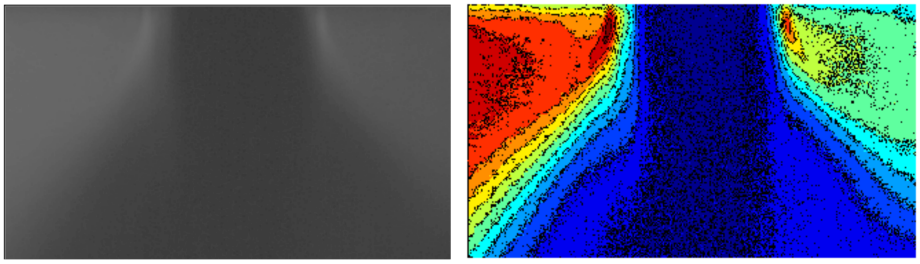

Figure 3.4: The POD base mode, ϕ_0 presented as a brightened grayscale image (left) and as an artificially-colored plot for enhanced visualization (right); contour regions do not indicate fluctuation.

since the dynamic range of the raw imagery is somewhat limited; however, this time-averaged image is also presented as an artificially-colored contour plot for enhanced visualization. Note that these contours here do not indicate regions of correlated fluctuation. This is the base POD mode, ϕ_0, by which all subsequent decomposed modes fluctuate about. Note the distinct margins of spray cone fluctuation visualized by ϕ_0.

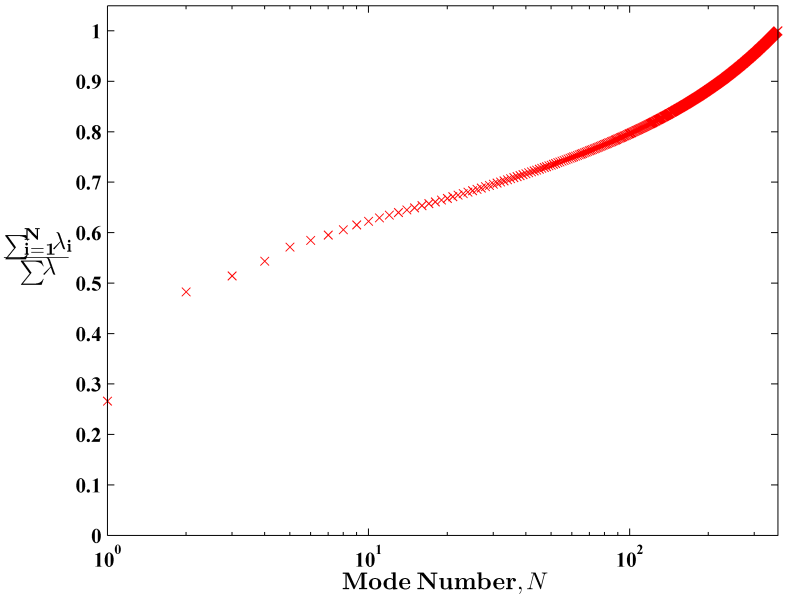

Figure 3.5: POD eigenvalues plotted to convey the cumulative distribution of modal energy over the sequence.

Eigenvalues resulting from the POD are plotted in Figure 3.5. They are plotted as to convey the cumulative distribution of modal energy over the sequence. For intuitive convenience, nomenclature referring to the ordered eigensolutions is reversed from the natural, such that the Nth mode is now that which possess the least modal energy.

The first two points in the distribution reveal that ≈50% of the total modal energy in the entire sequence is comprised within the dynamics described by only ϕ_1 and ϕ_2, suggesting that these dynamics are dominant. It can be inferred from the eigenvalue distribution that the overall dynamics of the sequence reach 90% convergence at a modal index of ≈200, where the remainder of higher order modes are considered to be either, 1.) small length scale/high frequency fluctuations that con-

tribute little to the global dynamics of the sequence, or 2.) noise attributed with the data and/or decomposition. In either case, these higher order modes are neglected from consideration. Furthermore, in order to streamline the data analysis process, only the first ten modes containing ≈60% of the total modal energy were considered. Spatial mode shapes for these first few modes are featured in Figure 3.6. The modes are left unscaled by their respective eigenvalues.

A variety of spray behaviors are resolved by the POD, wherein the length scale of modal patterns are seen to decrease as modal energy decreases. Consider the two spatial modes with the largest modal energies; contour plots of these characteristic spray modes are detailed in Figure 3.7. The mode shapes are noted to portray a pattern associated with the cyclical contraction/rarefaction behaviors of the spray cone as observed in Figure 3.3. This cyclical behavior generates regions in the imagery which oscillate from dark to light in a periodic fashion as liquid moves through the frame during self-pulsation. This behavior is manifest in the POD modes shapes as distinct lobe patterns that describe the residency and vacancy of liquid within certain correlated regions. For example, dark colored regions represent those in which liquid resides, while lighter colored regions represent those where liquid is vacant. Of course, these regions are correlated with one another. Since pixel intensity is an arbitrary parameter to the actual physics of the spray dynamics, the color scale or "magnitudes" of the lobe patterns are themselves not considered quantitative or important in any way to this study other than as a metric to visualize patterns of correlated behavior in the spray field.

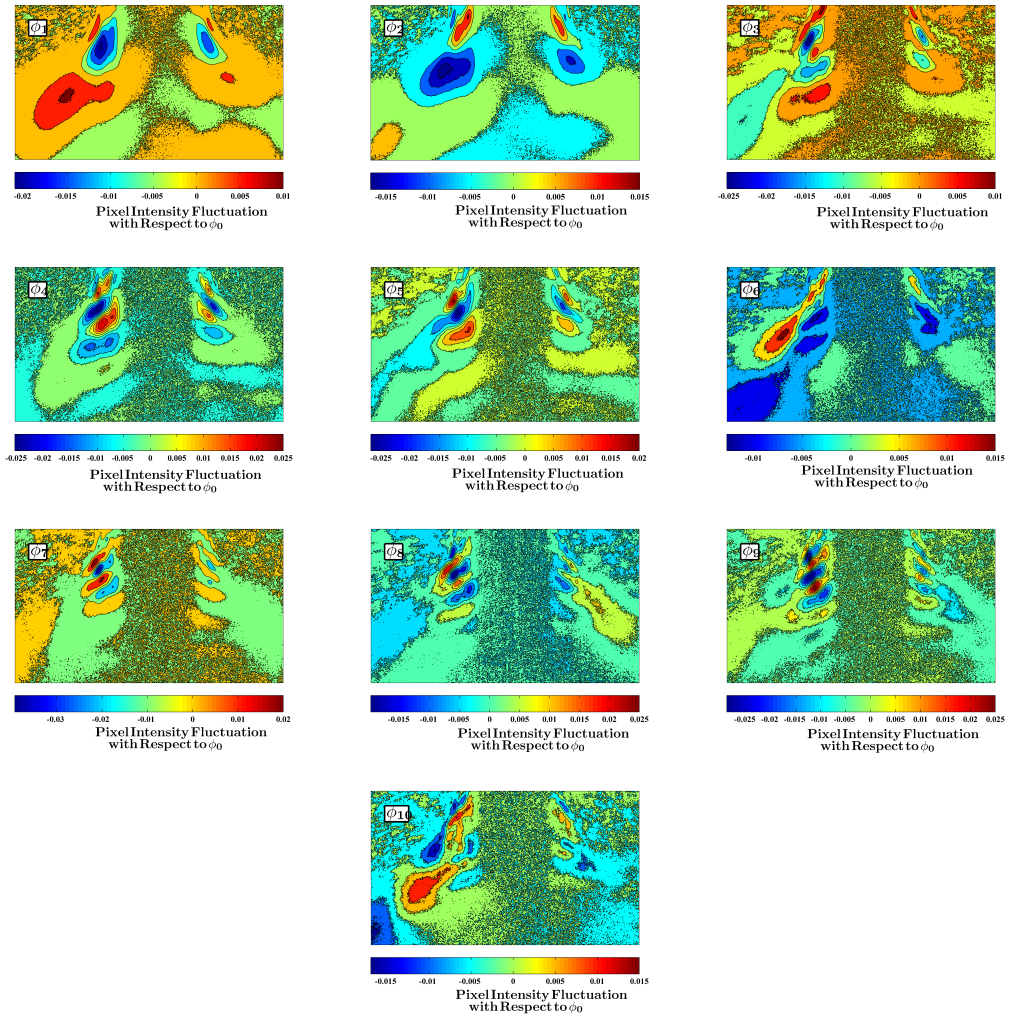

Figure 3.6: Contour plots of POMs 1-10 from upper-left and moving across and down to bottom; blue-to-red color scales represent positive-to-negative pixel intensity fluctuation about the time-average mean flow mode, ϕ_0.

In regard to the sinusoidal periodicity of the self-pulsation phenomenon, it is assumed that the characteristic POD modes shapes are also sinusoidal in nature. Figure 3.8 confirms this assumption, wherein their associated temporal waveforms appear highly oscillatory. The signatures are left unscaled by their respective eigenvalues. Temporal amplitude coefficients are considered the natural signatures of each

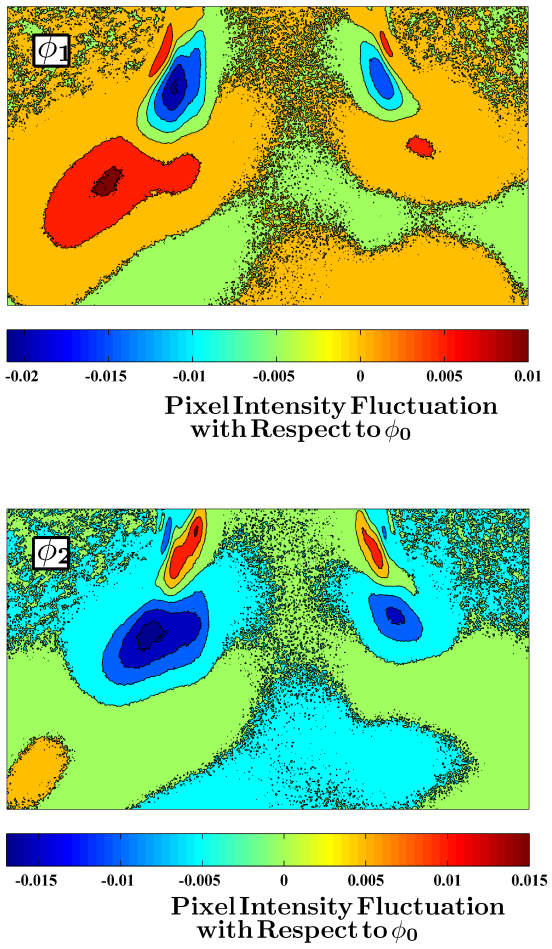

Figure 3.7: Contour plots of the two characteristic spatial modes of self-pulsation, ϕ_1 (top) and ϕ_2 (bottom).

mode in time. Since they are in fact continuous periodic functions, further Fourier decomposition of the signals is self-evidently valid. The individual average power spectra of each signature accompany their time histories in Figure 3.8. Figure 3.9 plots the additional power spectra for POMs 3-10.

Consider the similar lobe patterns displayed in each characteristic mode shape in Figure 3.7, but note their antithetical appearance. Next, consider the similarity

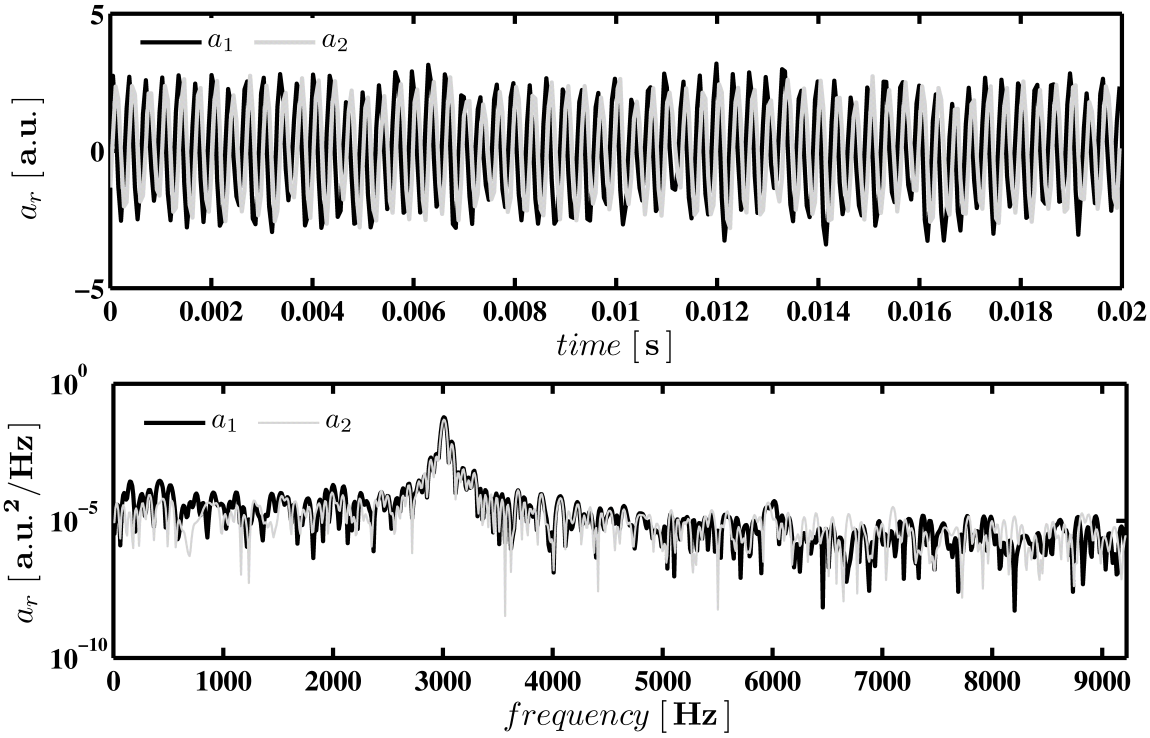

Figure 3.8: Temporal signatures associated with ϕ_1 and ϕ_2 showing five cycles of oscillation and accompanied by the average power spectral densities of each mode over the 0.02 second decomposition time. Each mode is characterized by a dominant frequency of 3 kHz (with $\pm$ 9 Hz frequency resolution).

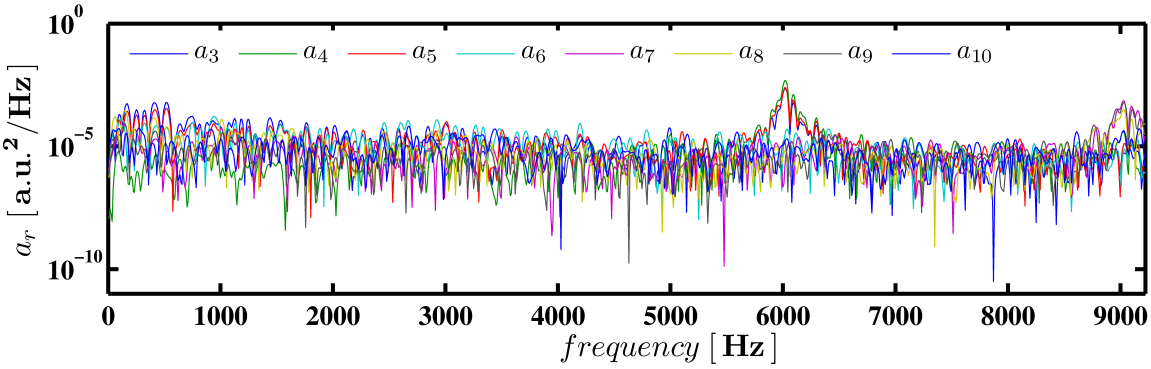

Figure 3.9: Additional average power spectral densities for ϕ_3-ϕ_{10} indicating harmonic modes registered near 6 and 9 kHz.

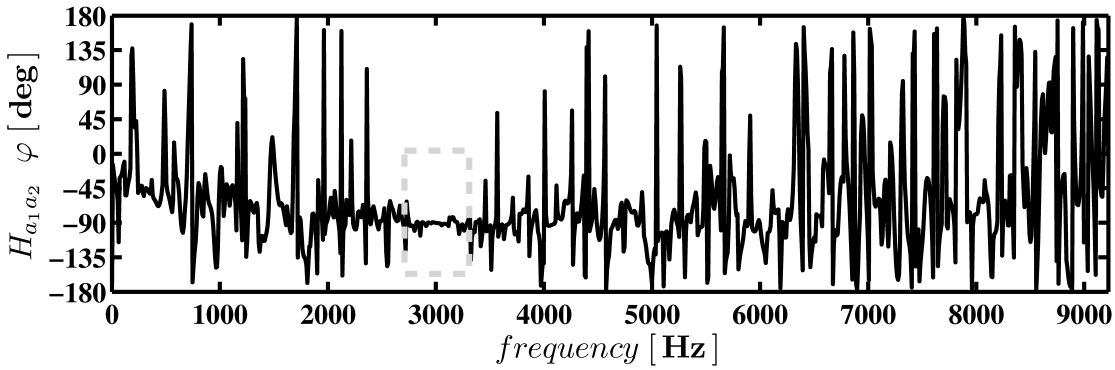

Figure 3.10: $H_{a_1 a_2}$ phase spectrum revealing constant relative phasing at ≈ -90^o at the conjoint frequency of 3 kHz.

between each mode's temporal waveform, but also note the phasing of the signals. Moreover, Figure 3.8 reveals each mode to share a common dominant frequency resolved at 3 kHz.

Figure 3.10 plots the cross-spectral characteristics of the two modes, wherein transfer function relative phase of the temporal signatures are presented. The plot indicates a ±90^o phase delay and high levels of coherence at the conjoint frequency of 3 kHz.

The spatial similarity and cross-spectral characteristics of the modes indicate a conjugate relationship to exist. The linear superposition principle can be exercised to better approximate travelling wave motions by combination of spatially stationary waveforms. The general trigonometric identity used for superposition is expressed as:

$$cos\,\omega t\,cos\,kx + sin\,\omega t\,sin, = cos\,\omega t - kx. \tag{3.25}$$

Thus, POD modal superposition may be approximated by Equation 3.26, given that the following criteria are satisfied [81]: 1.) spatially similar, antithetical mode shapes, and 2.) $\approx \pm 90^o$ relative phasing at a conjoint frequency.

$$a_i\phi_i + a_j\phi_j \approx cos\,\omega t\phi_i + sin\,\omega t\phi_j \tag{3.26}$$

Modal superposition is thus exercised to generate the conjugate mode shape seen in Figure 3.11. This mode shape approximates the principal travelling oscillatory dynamics witnessed in the raw imagery. The spectral characteristics of the conjugate mode are computed by the cross-power spectral density of a_1 and a_2 and featured in Figure 3.11.

Note the same lobe pattern individually displayed by ϕ_1 and ϕ_2 is retained in the new conjugate mode shape. Moreover, the dominant 3 kHz frequency in the cross-power spectrum remains consistent with that indicated in the individual power spectra. This mode gives the most accurate static representation of the travelling wave behavior. Furthermore, since the POD mode represents a spatially-distinct pattern (via the spatial orthogonality of the results), it is possible to assess an apparent wavelength of the spray oscillation—or in this case, 1/2-wavelength—given knowledge of the image's scale factor. However, this type of information is not collected in this study due to a number of potential pitfalls. These pitfalls include uncertainty is how to correct for motion in directions other than the streamwise, and uncertainty in defining precisely where the sheet is and is not contiguous.

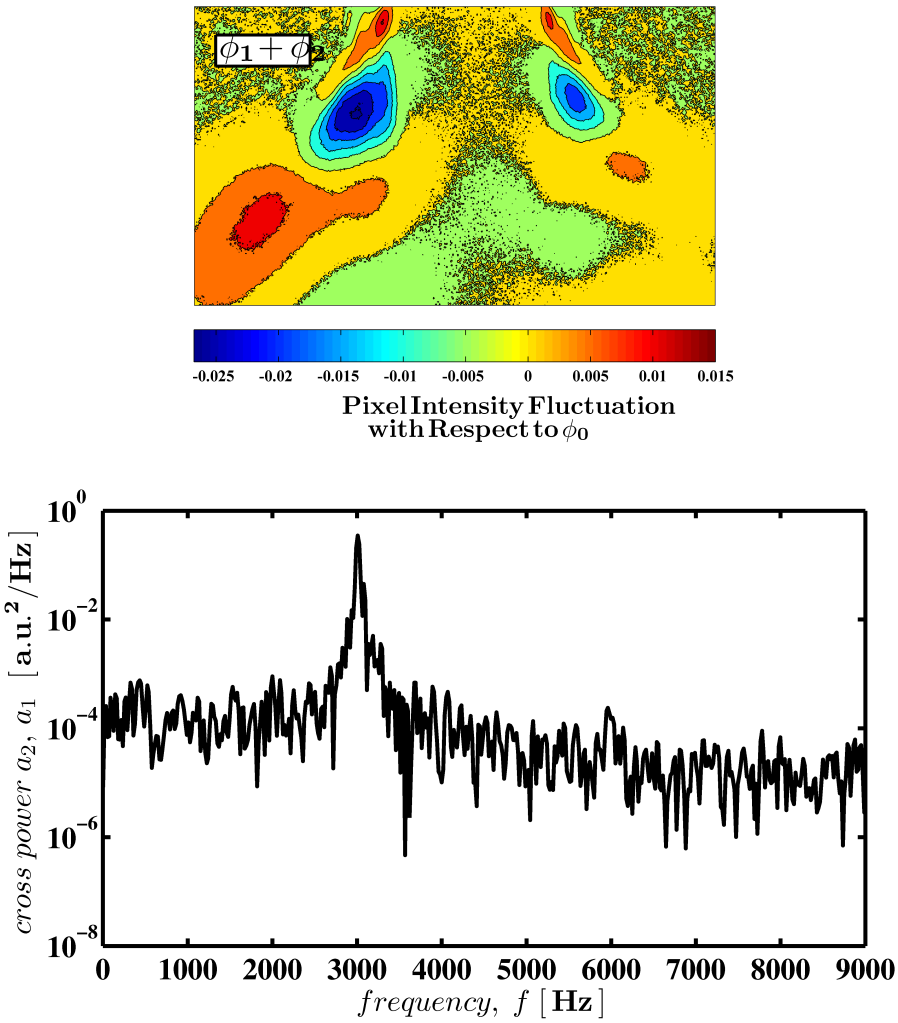

Figure 3.11: Approximated travelling mode shape and the cross-power spectral density of its composite temporal amplitude coefficient identified through the POD.

On a final note, this mode of spray oscillation can be reconstructed as an animation to more fully show the principal travelling behavior of self-pulsation as it evolves in time. Modal reconstruction is achieved by use of the modal superposition approximation. Note that the formulation of Equation 3.26 should be slightly mod-

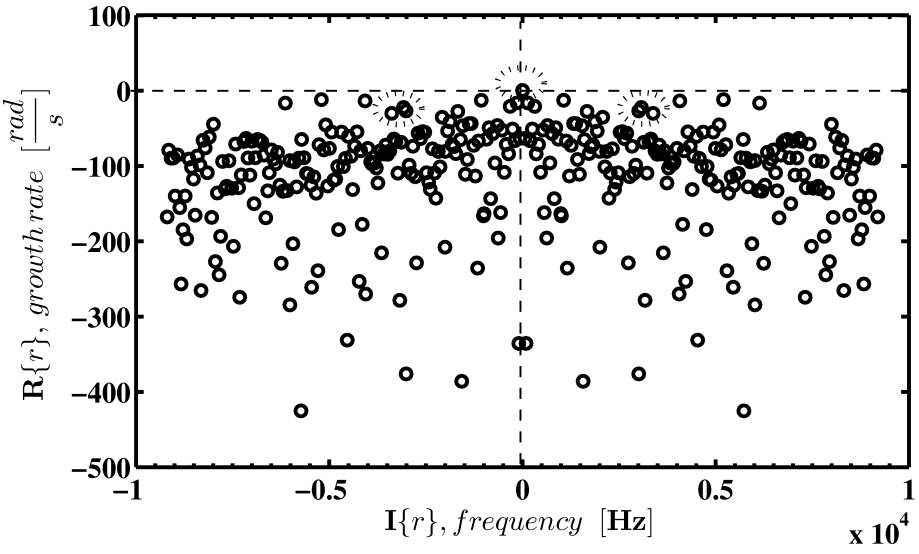

Figure 3.12: The DMD spectrum of the self-pulsation data—plotting imaginary against real components of the complex Ritz values.

ified to include scaling by each mode's respective eigenvalues (which in this case are essentially equivalent) as a means to account for their respective dominance.

3.4.2 Analysis by Dynamic Mode Decomposition

Consider the same sequence of high speed image data analyzed by the Proper Orthogonal Decomposition. Rather, if now temporal Dynamic Mode Analysis is applied to these data, results may be extended to assess the stability characteristics of the self-pulsation phenomenon. Figure 3.12 plots the spectra of data decomposed by DMD, where the the imaginary components (frequency) are plotted against the real components (growth rate) of the complex Ritz values computed by Equation 3.18. Here frequency is presented in Hz through $\mathbb{I}\{\mathfrak{r}\}/2\pi$.

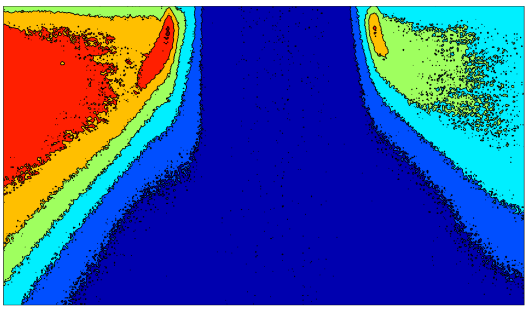

Figure 3.13: Contours of the neutrally-stable mode at $\mathbb{I}\{\mathfrak{r}\} \approx 0$, color scaling is arbitrary. Comparison is drawn to the POD base mode depicted in Figure 3.4.

Characteristic symmetry about $\mathbb{I}\{\mathfrak{r}\} = 0$ is noted in the DMD spectrum. The saddle point, or equilibrium mode, located at $\mathbb{I}\{\mathfrak{r}\} \approx 0$ represents the D/C component of the flow field, i.e. the mean flow. A near-zero growth rate corresponds to the equilibrium mode—describing its neutrally-stable nature. An arbitrarily-colored contour plot of the equilibrium mode is seen in Figure 3.13, wherein comparison to the POD base mode of the sequence in Figure 3.4 can be drawn; the two, however, are not precisely equivalent.

To quantify this spatial similarity, a metric established by Schmid [89] is extended, whereby the norm of a given temporal DMD mode projected onto a given spatial POD mode is utilized as a measure of relative 'coherence', $\mathbb{Q}$, between the structures or patterns described in each mode. When computed between the POD base mode and the DMD equilibrium mode, $\mathbb{Q} \approx 0.9$. This parameter can also be utilized to help identify which DMD mode most closely corresponds to the charac-

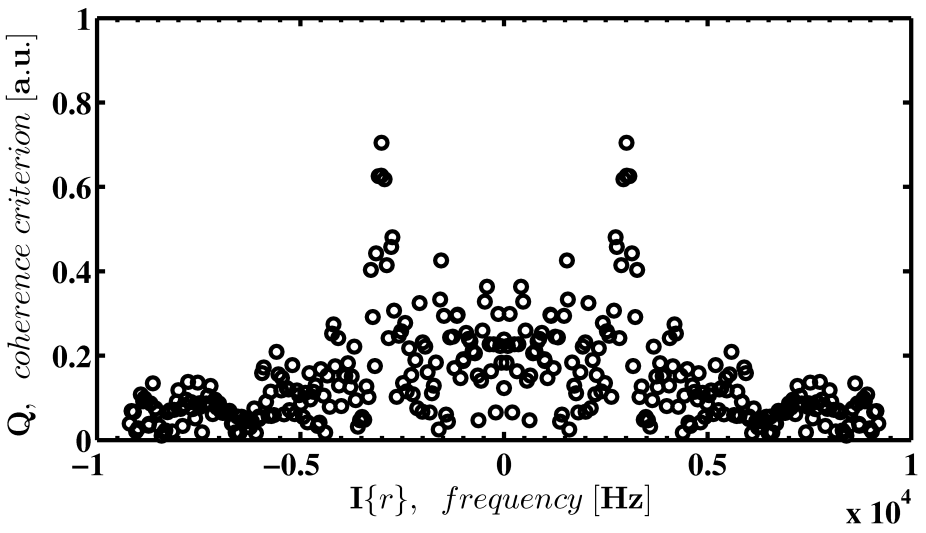

Figure 3.14: Schmid's [89] coherence criterion extended to compare temporal DMD mode shapes with the dominant mode of self-pulsation extracted by spatial POD.

teristic mode of spray oscillation extracted by the POD. As such, regard this spatial coherence criterion evaluated across the DMD spectrum with respect to the 3 kHz conjugate POD mode in Figure 3.14; highest coherence exists near 3 kHz, with a value of $\approx$0.7 in this case.

Figure 3.15 shows the imaginary (left) and real (right) components of the mode shape near 3 kHz that shares peak coherence with the principal mode of spray oscillation retrieved by the POD. Notice that the lobe patterns between the two components appear to be shifted in space by a factor of about $\pi/2$. This suggests that the patterns are sine/cosine analogues that can be combined much in the same way as the POD modal superposition to resolve a static representation of the travelling wave behavior during self-pulsation. Figure 3.16 shows contours for the principal mode of spray oscillation formed by combination of real and imaginary parts. When

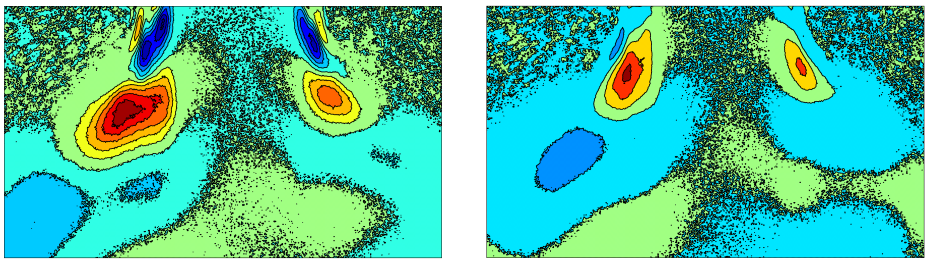

Figure 3.15: Imaginary (left) and real (right) components of DMD mode of spray oscillation near 3 kHz and sharing peak coherence criterion with the principal mode extracted by the POD.

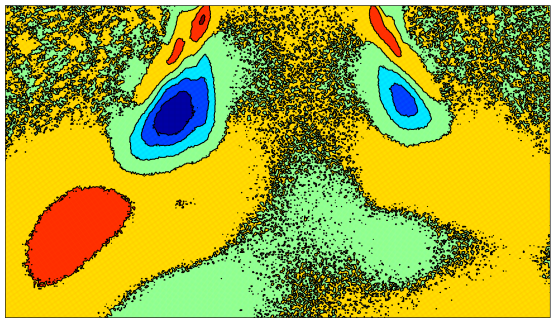

Figure 3.16: DMD mode formed by superposition representing principal travelling wave mode of self-pulsation at 3 kHz.

adjusted for superposition, the coherence criterion metric of this mode improves to greater than ≈0.9. Colors have been scaled by a factor of -1 for visual comparison with Figure 3.11.

The temporal DMD mode of spray oscillation as resolved near 3 kHz compares within one Hz to that quantified for the conjugate POD mode describing the travelling behavior of spray oscillations. Noting the level of agreement both qualitatively and quantitatively shared between the DMD and POD analyses, it stands to reason

that characteristics of the temporally orthogonal DMD modes can be extended to complement the characteristics of the spatially orthogonal POD modes in this case.

Pursuant, the high growth rate of the self-pulsation mode (relative to other modes in the spectrum) characterizes its dynamic significance over the analyzed window of time. While high in magnitude, the mode's growth rate remains negative—indicating lightly damped behavior. This characterization is consistent with the observed limit cycle behavior of self-pulsation. Having identified oscillation frequency and apparent wavelength through POD, the deduced growth rate of the spray oscillations identified through DMD provides a more complete characterization of the spray dynamics. Furthermore, these spray behaviors closely correspond to the dominant frequencies of fluctuating pressures and sound pressure level measurements. These combined information form a strong basis on which to more fully characterize the phenomenon of self-pulsation.

3.4.3 Methodology Review

To review how this characterization has been carried out, consider Figure 3.17 which graphically shows the general analysis methodology which has been applied to the test data here. For pressure time series data, basic spectral analysis is performed to understand pressure amplitude in the Fourier domain, such that a dominant frequency of oscillations that occur during self-pulsation can be identified for each individual measurement. The calculation of coherence functions between various pressure measurement pairs allows for a quantification of how correlated each signal is to one another in the frequency domain.

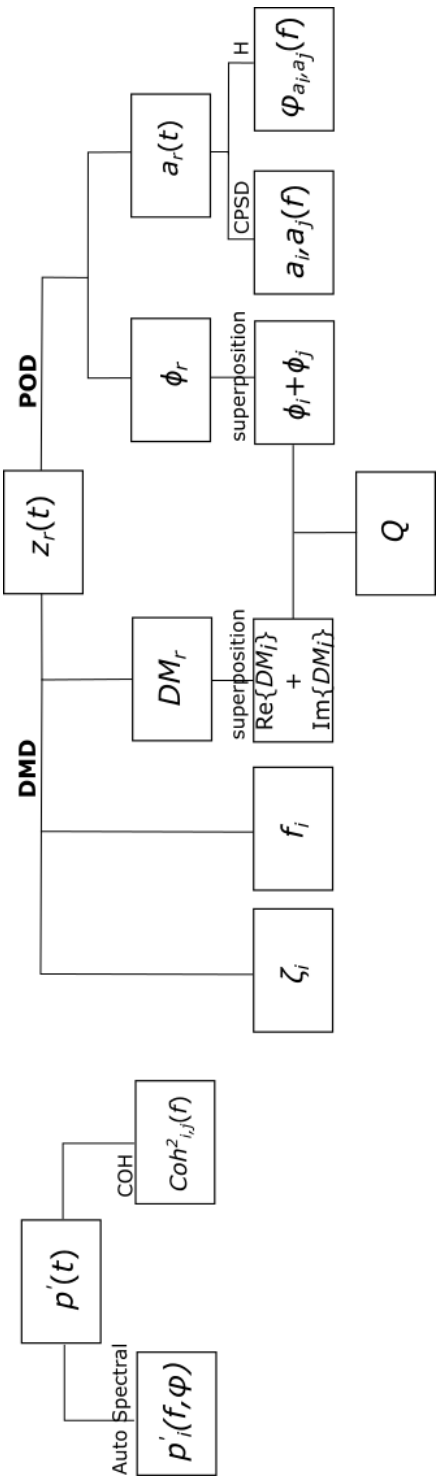

Figure 3.17: Graphical representation of the general data analysis methodology used to characterize self-pulsation dynamics.

For data contained within a sequence of imagery, the Proper Orthogonal Decomposition is applied to extract spatially-distinct patterns of spray oscillation and their corresponding temporal signatures. Guided by estimates of relative phase by transfer function calculations, if a given mode pair meets superposition requirements, then their shapes are summed to form an accurate static representation of travelling wave behavior. Cross-spectral analysis of temporal signatures belonging to each constituent mode is then performed to quantify the dominant frequency of the spray oscillation.

Additionally, the Dynamic Mode Decomposition is applied to extract temporally-distinct patterns of spray oscillation. If the real and imaginary components of a given mode shape display characteristics indicative of a travelling wave, they are summed to form an accurate static representation. With both a DMD and POD characterization of principal spray oscillations, the coherence criterion then serves as a measure to link the temporally-distinct characteristics of the spray oscillations resolved through DMD to the spatially-distinct characteristics of the same spray oscillations resolved through POD.

CHAPTER 4

TEST RESULTS

An expansive test campaign was carried out. During these experiments, a large collection of data was obtained. These data were not only quantitative physical parameters measured by sensors and devices, but also consisted of valuable qualitative information gathered by the *human sensor*. In this chapter, anecdotal observations will be documented, followed by presentation of consolidated quantitative results from the experiments.

4.1 Qualitative Accounts

A variety of interesting behaviors were noted throughout the test campaign both by sensory perception and active monitoring of dynamic data. The following section will describe in a qualitative manner such observations in order to provide context for the quantitative measurements presented later in this chapter. These accounts are, to some extent, captured in Figure 4.1 which depicts a conceptual domain of self-pulsation with key observations encountered during experimentation. It should be noted that the notional upper 'globally-stable' region is mostly speculative since there was little to no test experience gathered there during this investigation.

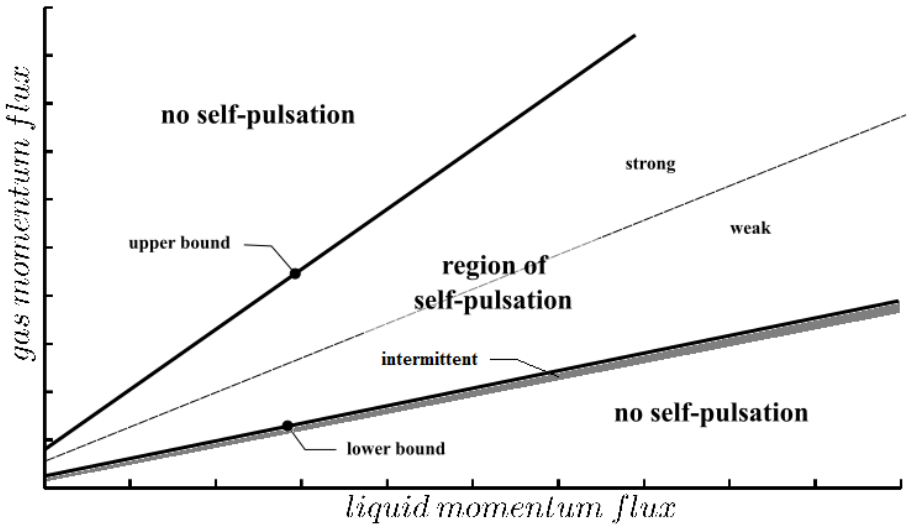

Figure 4.1: Illustration of a conceptual self-pulsation domain mapped to test parameter space. Specific regions of the domain are supported by qualitative observation during experiment.

4.1.1 Boundaries of Self-pulsation

Concurring with prior descriptions [39,47], the generation of the self-pulsation phenomenon was noted to be most sensitive to co-annular jet throttling. For a given steady liquid flow rate, self-sustained oscillations could be excited by systematically varying gas flow to a certain threshold. This critical condition was deemed to represent the lower bound of the self-pulsation phenomenon, above which all higher energy gaseous flows might modulate and/or exacerbate the flow dynamics.

As gas flow was increased from the lower bound condition, in some instances the characteristics of self-pulsation were observed to dampen and become imperceivable, e.g. spray oscillations and/or acoustic emissions, at a second seemingly critical flow condition. These observations were consistent with results inferred from the lit-

erature [48, 50]—suggesting, at the very least, a bounded region(s) of self-pulsation. In cases where self-pulsations did not vanish with increasing gas flow, identification of an upper bounding condition was prohibited by the capabilities of the experiment's flow facility.

4.1.2 Onset of Self-pulsation

It was observed in some steady liquid flow test cases that, just slightly before the onset of self-sustained oscillations, spray and acoustic emissions were intermittent. During so, the self-pulsation phenomenon was witnessed to excite, blossom, and decay in seemingly random intervals. A minor, immeasurable increase in gas flow rate would cause self-pulsation to develop; a slight decrease would cause it to vanish.

This region of intermittent behaviors was observed to impact the mechanistic manner in which the threshold of self-pulsation was determined. Its influence was manifested as a hysteresis effect on the precise location of the self-pulsation boundary. Thus, in probing flow conditions for the boundary, it was necessary to first reach self-sustained oscillations, increase gas flow slightly, decrease below the stability boundary to a globally stable spray, then finally increase again to reach self-sustained oscillation. The hysteresis effect was not explored for the upper bound of instability or transition from weak to strong self-pulsations.

4.1.3 Magnitude of Self-pulsation

Pursuant to the observation of self-pulsation boundaries (and positing even further, self pulsation regimes), for a steady liquid flow rate, significant changes in

self-pulsation magnitude were noted in many tests as gas flow was increased. These observations suggested that the self-pulsation phenomenon be segregated into at least two categories. These categories might tacitly be referred to for the purposes of this discussion as weak pulsations and strong pulsations.

In general, weak pulsations were noted to exist in the lower flow regimes wherein acoustic emissions were nearly imperceivable to the human ear but small self-sustained spray oscillations could be witnessed. As such, the spectral characteristics of the phenomenon were not readily deduced from acoustic or manifold pressure signatures due to low signal to noise ratios. However, since spray response was noticeably present, videography remained effective in capturing the weakly pulsating injection characteristics. Strong pulsations tended to exist in the higher flow regimes. In this group, spray oscillations were dramatic and acoustic emissions were distinct; the manifestations of self-pulsation were readily captured by all diagnostics.

In numerous instances, transition from weak pulsation to strong pulsation was observed. These transitions were noted to coincide with a discrete jump from weak pulsation characteristics to those of strong self-pulsations. The loudness of the self-pulsation tone was perceived to be amplified when so-called transition occurred, but its pitch was perceived unmodulated.

4.2 Quantitative Assessment

Figure 4.2 plots the parametric space achieved in all swirl coaxial conditions in the test matrix. For reference, an interpolated trend of each measured stability boundary (lower bound) is presented; these will be elaborated upon later. Uncertain-

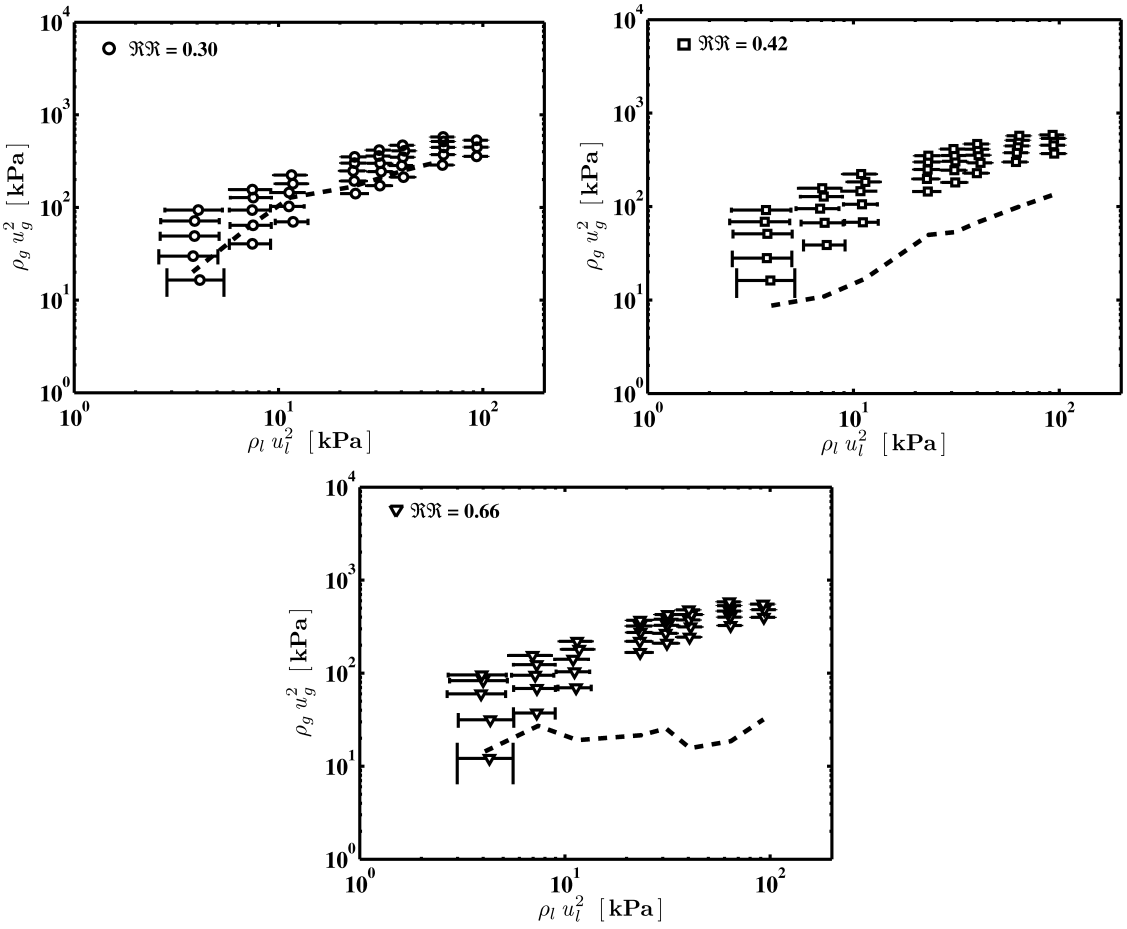

Figure 4.2: Fluid momentum flux conditions achieved for each injector configuration, from Left-to-Right: ℜℜ=0.30 (no recess), ℜℜ=0.42, ℜℜ=0.66. Interpolated lower stability boundary trends are also plotted for reference.

ties for liquid momentum flux are estimated on a 95% confidence interval. Tables documenting the achieved flow rate and state conditions from which momentum flux is estimated are listed in Appendix D for all cases and injector configurations. Note that specific conditions listed within parentheses are conditions which were inferred for that test based on data from other tests. These inferences were necessary because of faulty readings (due to a single unplugged sensor) that were not discovered until after completion of the test campaign. This was limited to a single day of testing.

In this section quantitative results documenting various oscillations that occur within and near the achieved test parameter spaces will be presented. As demonstrated in Chapter 3, results from quantitative image analysis will be compiled to characterize the principal spray dynamics that were measured. In addition, various fluid-borne oscillations including internal pressure fluctuations and external acoustic signatures that occur during self-pulsation will also be characterized.

4.2.1 Spray Oscillations During Self-pulsation

Modal decomposition analysis results from the swirl coaxial parametric test data are compiled in Appendix E. Contour plots of characteristic mode shapes and their associated spectra identified through the POD are consolidated for each recess configuration. Note that contour color scales range the maximum and minimum values particular to each mode, and do not imply relationships between different test cases based on similarly colored regions.

In exploring flow and geometry parameter spaces, two general types of spray patterns were observed depending on flow conditions: patterns descriptive of non-pulsatile oscillations, and those descriptive of pulsatile oscillations. Non-pulsatile spray patterns were typically those that showed smaller-scale disturbances seen along the contiguous outer surface of the spray cone. These patterns generally had some periodicity associated with them, but were not indicative of distinct limit cycle pulsing of the spray cone. On the other hand, pulsatile spray patterns were mostly consistent with those shown for the example case in Chapter 3. These mode shapes describe the large-scale contraction/rarefaction of the spray cone and/or travelling wave behavior.

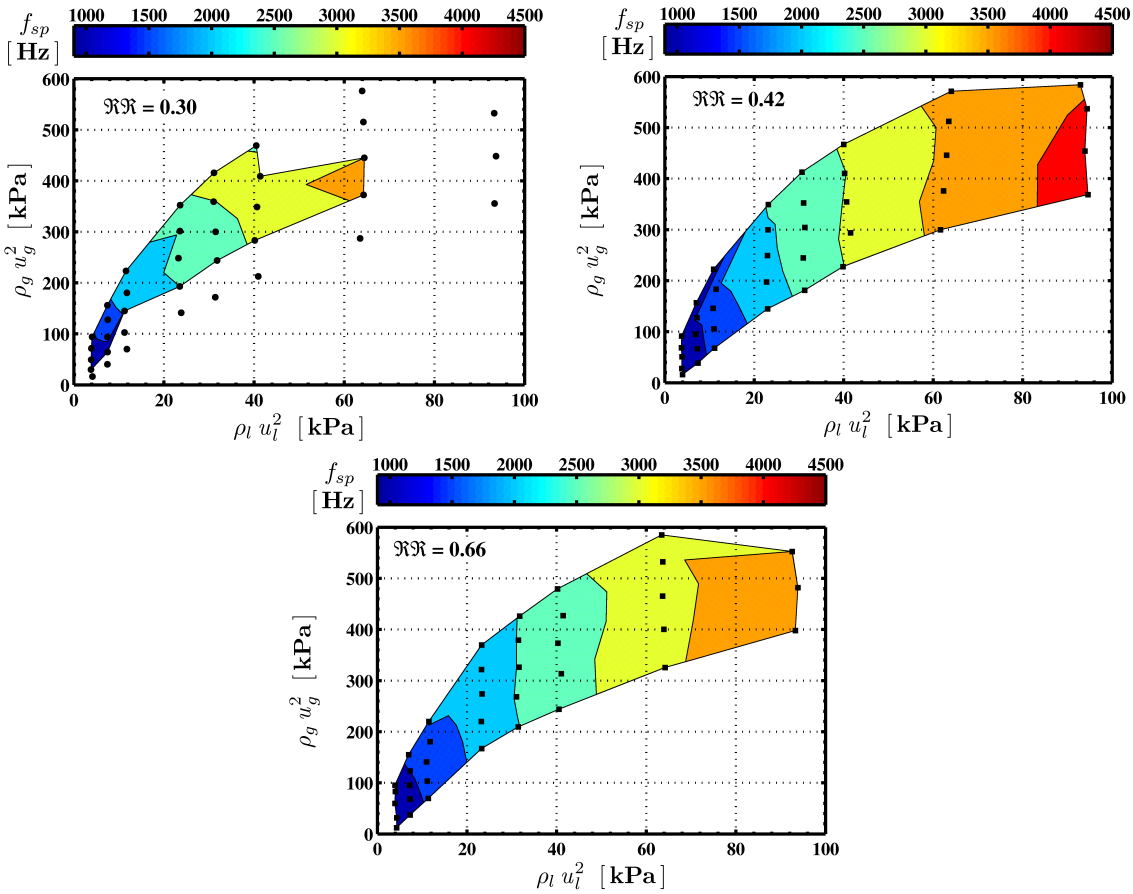

Figure 4.3: Self-pulsation frequency projections showing frequency modulations with respect to the flow conditions for each recess configuration: $\Re\Re = 0.30$ (upper left), $\Re\Re = 0.42$ (upper right), $\Re\Re = 0.66$ (bottom).

Since the primary focus of this study is on the self-pulsation phenomenon, here, coarse linear interpolations of characteristic pulsatile spray frequency are mapped to momentum flux space for each $\Re\Re$ configuration in Figure 4.3 to help consolidate results from the modal decompositions and visualize activity observed in the test parameter space. Data points within the colored region are those at which self-pulsation was encountered. Self-pulsation was not detected at data points outside the colored regions where non-pulsatile oscillations were observed.

This figure captures modulation of the self-pulsation spray frequency with increases in gaseous momentum flux; however, these modulations for a given liquid flow condition occur within a relatively narrow bandwidth. The effect of liquid flow rate on the frequency of spray oscillations during self-pulsation is most significant. These frequencies modulate over a bandwidth of $\approx$ 1000-4500 Hz as a function of the liquid flow condition. It can be reasonable stated from observations drawn here that the dynamics of self-pulsation are more dependent on the liquid flow of the swirl injector rather than the gaseous flow of the exterior annulus. This is a finding which is consistent with observations made both by Bazarov and Yang [47] and Im et al. [39].

By comparison of the different maps, consider now the effect of inner post recess. Self-pulsation is limited to a smaller momentum flux parameter space without recess. This is a clear indication of self-pulsation's sensitivity to recess, and is consistent with observations noted by all researcher of the phenomenon. For the non-recessed injector, self-pulsations tend to occur at slightly lower frequencies than those that occur at similar flow conditions when recess is present. This suggests, in addition to frequency modulation caused by variation in flow conditions, self-pulsation experiences some modulation due to recess. The mechanism by which this modulation takes place is unknown, but interesting inferences can still be made. At lower liquid flow conditions the modulation due to recess appears linear in the sense that $f_{sp,\Re\Re=0.3} < f_{sp,\Re\Re=0.42} < f_{sp,\Re\Re=0.66}$ when compared for similar gas flow conditions. However, at some high liquid flow conditions, $f_{sp,\Re\Re=0.42}$ is greater than both $f_{sp,\Re\Re=0.30}$ and $f_{sp,\Re\Re=0.66}$ when compared at similar gas flow conditions to suggest a potential nonlinear effect takes place. Without additional data points at different

recess conditions, it seems difficult to confidently deduce if this is a real nonlinearity and/or what the cause might be.

4.2.2 Fluid Oscillations During Self-pulsation

The following results consolidate and summarize unsteady pressure measurements and spray dynamic measurements. Self-pulsations are known to generate discrete fluctuations in pressures. What if the periodic motions active during self-pulsation were to be considered a forcing function on the fluid flow conditions upstream of the injector element? It would then be practical to characterize the intensity of injector response to such forcing. Consider the manifestations of self-sustained spray oscillations within the fluctuating pressure levels upstream of the injector element. Here, the influence of gas flow variation on the intensity of self-pulsation is assessed.

Figure 4.4 plots liquid and gas pressure fluctuations plotted as a function of estimated injection Reynolds number of the gas; each plot is for a different recess configuration. Here, averaged RMS pressure amplitude has been extracted over one second of time at the frequency of the self-pulsation spray dynamics associated with a particular condition. To provide a sense of pressure fluctuation intensity relative to the flow, amplitudes are normalized by respective dynamic flow pressures, $\bar{q} = 1/2\bar{\rho}\bar{u}^2$.

In some cases, increases in gas flow introduce a general decrease in the magnitude of pressure fluctuation generated during self-pulsation at a given liquid flow condition; however, in many others, gas flow does not influence these responses in a significant way. Increases in gaseous flow generally decrease gas fluctuating pressure

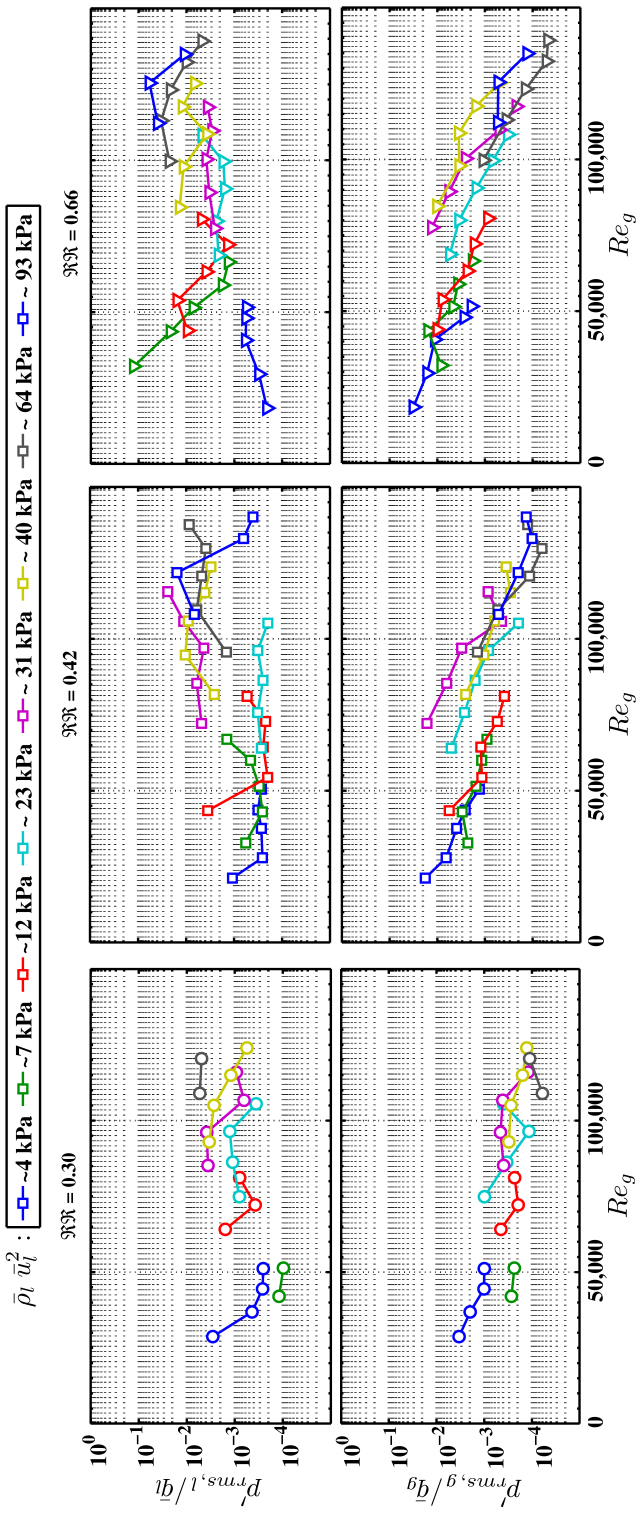

Figure 4.4: Normalized unsteady pressure responses to self-pulsation registered in upstream liquid manifold and gas feedline as a function of gas injection Reynolds number; recess ratio increases from left-to-right.

response in a fashion roughly akin to a power law manner. This result is likely due to the high velocities of the flow field wherein a sonic or near-sonic condition develops at the inlet of fuel annulus post and highly impedes upstream propagation of downstream pressure disturbances. The most striking affect on liquid pressure fluctuation magnitudes are not introduced by variation in gas flow, but rather variations in the liquid flow conditions themselves. This effect serves to aggravate pressure amplitudes upstream of the swirl injector.

Recessing appears to also aggravate liquid pressure response levels. In some cases of recess, liquid pressure response during self-pulsations are registered on the order of 1-10% of the flow's dynamic pressure. These levels are still far below the static pressure in the liquid manifold or the pressure drop across the swirl injector, such that cavitation induced by self-pulsation in all likelihood did not occur.

The effect of gas flow conditions and recess on the sound generated during self-pulsations can be examined in Figure 4.5. Here the amplitude of each dominant tone associated with self-pulsation is plotted for each flow condition as a function of gas Reynolds number as similarly presented for the injector pressure responses. These far-field measurements are plotted as sound pressure level (SPL) in reference to 20 μPa in air, which have been corrected for 0^o incidence for readings registered at frequencies greater than 2 kHz.

Similar to trends seen with liquid fluctuating pressure levels, for the most part, increases in gas flow alter sound pressure levels by only a few dB—in contrast, changes in the liquid flow exacerbate sound emissions much more significantly. Furthermore, at all liquid flow conditions, inner post recess fosters strong increases in SPL. In the

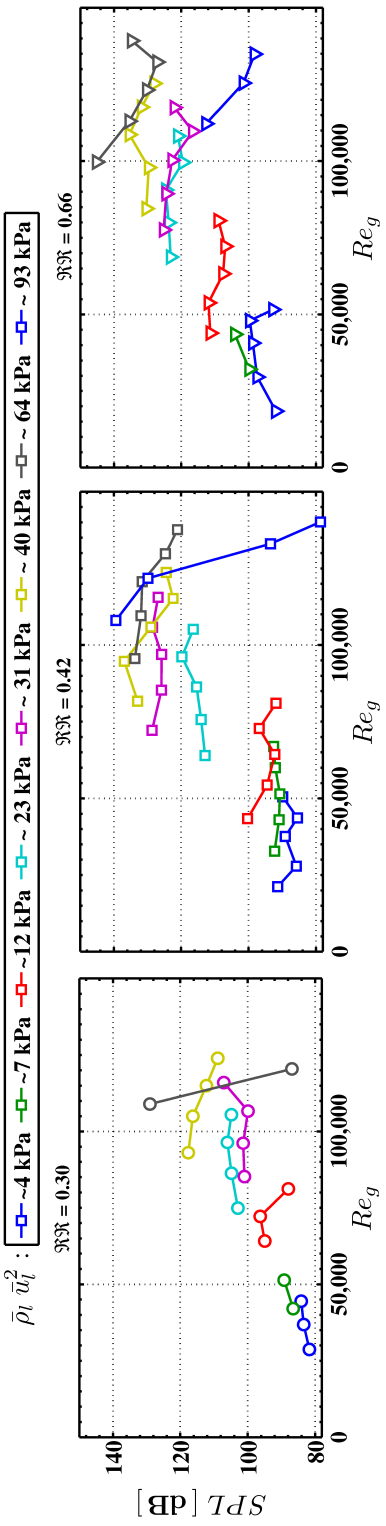

Figure 4.5: Far-field sound pressure levels registered during self-pulsation plotted as a function of gas injection Reynolds number for all injector recess configurations.

presence of recess, the majority of cases exceed acoustic intensities of 120 dB, while a few reach levels near 140 dB.

4.3 Self-pulsation Boundary Measurements

As described earlier, steady-state liquid flow rates were systematically probed with increasing gas flow until self-pulsations were excited. The effects of hysteresis on the stability boundary were also explored, but only in a qualitative manner. Here, gas flow was further increased, decreased to where self-pulsation ceased, and finally again increased to excitation. Figure 4.6 compares the measured stability boundaries of each $\Re\Re$ configuration, with uncertainties estimated on a 95% confidence interval. Flow conditions and state conditions for each case are documented in Appendix D.

Since parameters related to the self-pulsation admittance function are difficult to analytically or empirically determine, a direct evaluation for this injector here is not made. However, given that liquid momentum flux parameter space is shared between tests conditions in this study and those presented in Ref. [47], some qualitative comparisons can be at least be drawn. First, consider the lower boundary of self-pulsation resolved for the flush mounted configuration of the test article and its significantly elevated flow levels compared to configurations with inner post recessing. Figure 4.7 contrasts this stability boundary with that furnished by Bazarov and Yang [47] for a recessed element. Here a noticeable difference in the morphology of the lower stability boundary is shown, particularly at elevated liquid momentum flux conditions.

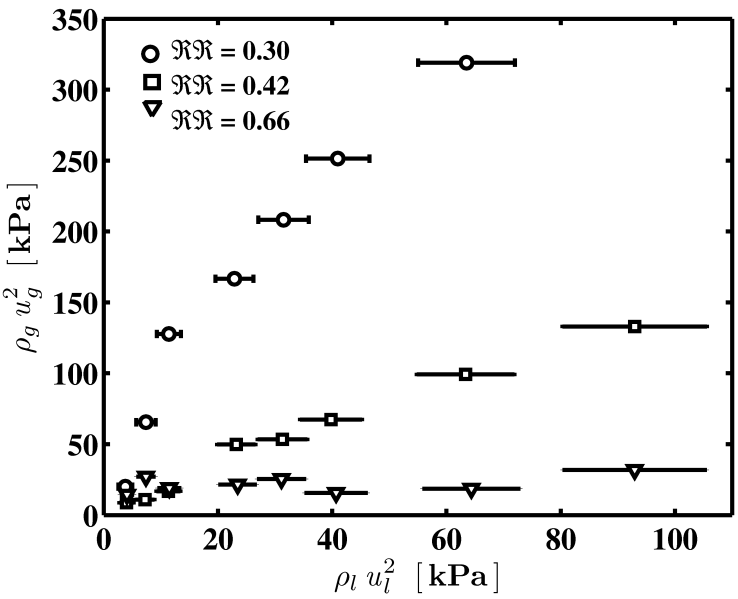

Figure 4.6: Lower boundaries of self-pulsation with respect to propellant injection momentum flux conditions, where square symbols correspond to the $\Re\Re = 0.30$ recess configuration (flush), circular symbols to $\Re\Re = 0.42$, and triangular symbols to the $\Re\Re = 0.66$ recess configuration.

However, reasonable comparison can be drawn—except for the low liquid injection conditions—for the recessed configurations shown in Figure 4.8. Here some morphological similarities in the stability boundaries can be seen, where at some flow conditions—particularly for $\Re\Re = 0.42$—the self-pulsation boundary agrees within experimental uncertainty. Note that the level of recess present in Bazarov and Yang's data is unknown.

By classic descriptions following the gas admittance model, the lower boundary of self-pulsation ought to resemble an exponential-like function in momentum flux space. This is certainly not the case for the boundary established for the non-recessed element tested here, where the fundamental relationship between fluid flow conditions

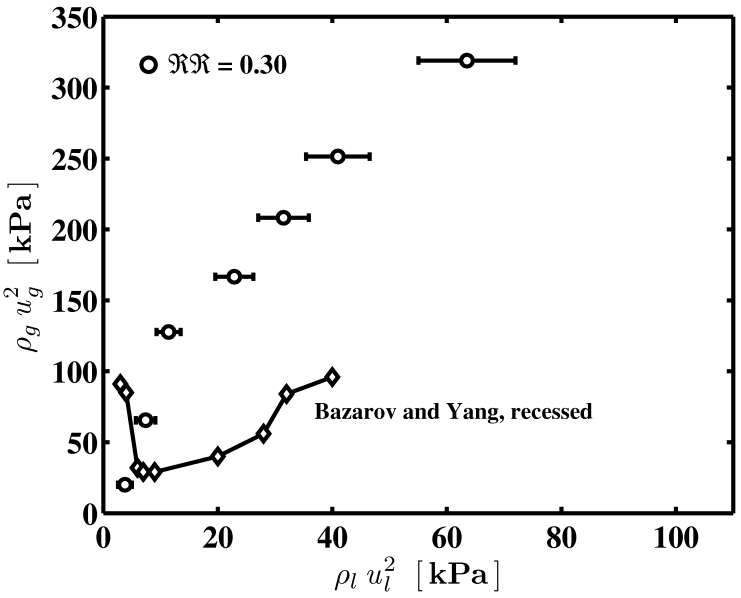

Figure 4.7: Lower boundary of self-pulsation without inner post recess plotted with the stability boundary measured/modelled by Bazarov and Yang [47].

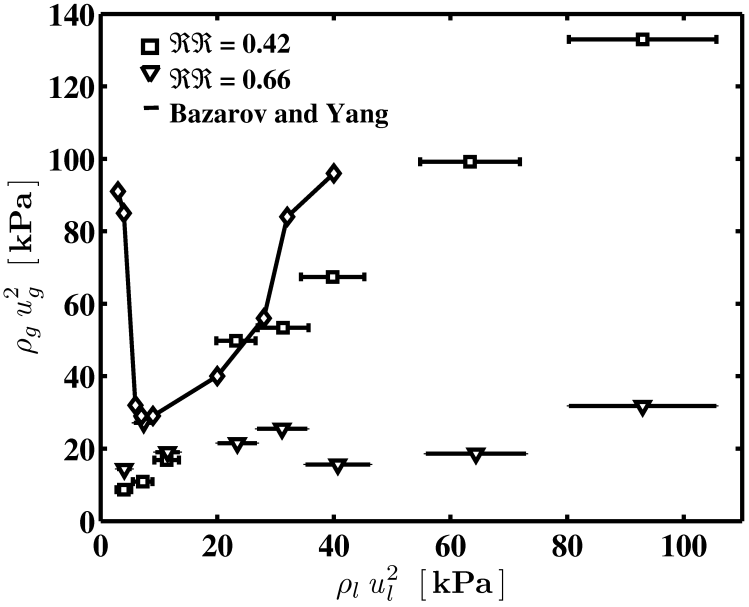

Figure 4.8: Lower boundaries of self-pulsation for the recessed configurations compared with the stability boundary measured/modelled by Bazarov and Yang [47].

describing the boundary appears mostly power-law in momentum flux space shown in Figure 4.7. In fact, this seems to also be the case for the recessed configurations shown in Figure 4.8 as well.

The general qualitative disagreement between the self-pulsation boundaries resolved here and those that might be described by a gas admittance function are not unique. Im et al. [39] also established boundaries that did not compare well with those classically described in momentum flux space. The authors deduced that the onset of self-pulsation is not well-defined by the momentum flux parameter based on results from boundary interrogations using different types of gas flow.

Figure 4.9 depicts the dominant modes shapes of spray oscillation measured at the lower boundaries of self-pulsation. These modes are provided for all injector element recess configurations, and are ordered from left-to-right/top-to-bottom by approximate liquid injection Reynolds number. Organized in a similar fashion, the spectrum belonging to each of the POMs is shown in Figure E.7. Discrete frequency of self-pulsation is identified from the spectra in Appendix E. These dominant frequencies are also tabulated in tab:fbound, each with a resolution of approximately $\pm 12.5\ Hz$.

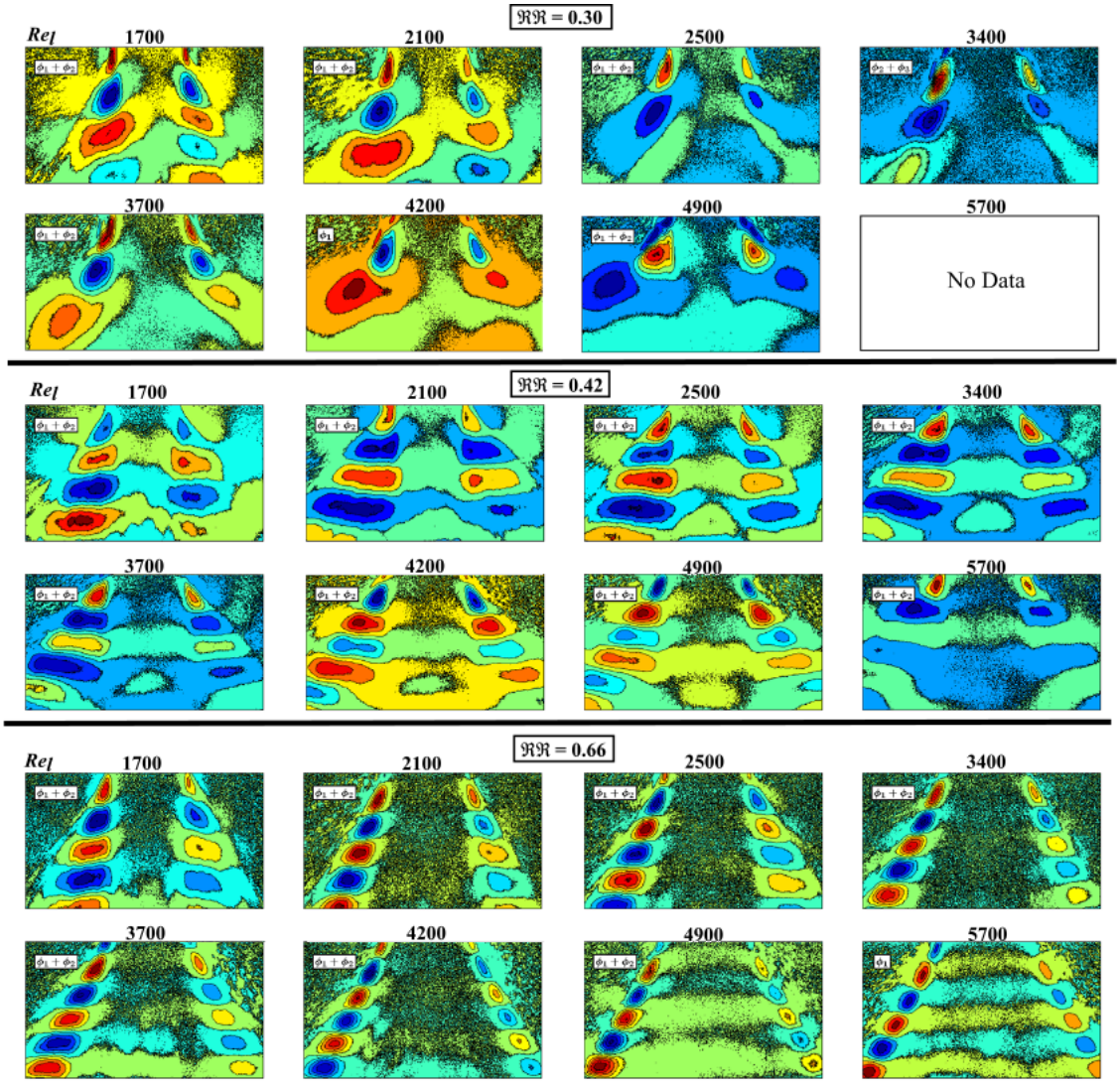

Figure 4.9: Principal mode shapes of spray oscillation generated during self-pulsations encountered at the lower boundaries for all test recess configurations of the injector element.

Table 4.1: Self-pulsation Frequency at Lower Boundaries

$f_{sp}(Hz)$			
$Re_l/\Re\Re$	0.30	0.42	0.66
1700	973	901	901
2100	1225	1189	1225
2500	2017	1621	1477
3400	2666	2269	1981
3700	2918	2594	2269
4200	3026	2882	2522
4900	3602	3494	3026
5700	—	4034	3530

CHAPTER 5

EXCITATION MECHANICS OF SELF-PULSATION

Two possible unsteady external flow phenomena which might generate local self-excited oscillations of the liquid spray cone: A.) shedding of coherent structures from the exit of the gas annulus which convect downstream and deform the surface of the liquid spray cone, and B.) *shear layer* perturbations originating from regions of turbulent interaction that form organized disturbances on the surface of the liquid spray cone. The occurrence of vortex shedding phenomena are not readily observed in the experimental data; however, small scale perturbations of the liquid surface in the very near-field of the injection plane are obvious. In fact, similar small scale surface perturbations of the liquid can be observed even in cases of pressure-swirl injection where the influences of high relative shear layers are not imposed by a co-annular jet (see, for example, Figure 1.11). Disturbances are seen to develop simply from the relative velocity between the liquid and the ambient, quiescent environment. These disturbances are directly observed on the exterior surface of the spray cone, and may also exist on the inner surface of the cone but cannot be observed from these data here.

Following proposals in the literatures, this chapter will address aspects of the mechanism thought responsible for inducing flow oscillations that drive sustained pulsations of the fluidic oscillator system. Attention is focused on flow instability on the liquid sheet since the common binding medium between all potential fluid oscillator elements in the system is the liquid sheet/spray cone.

5.1 Regimes of Liquid Breakup

The self-pulsation phenomenon is generally thought to be excited by complex gas-liquid spray interactions in the near-field of the injector. The high momentum flux ratio that occurs for most of the test conditions (particularly near the lower boundaries of self-pulsation for the non-recessed injector) indicates that the dynamic flow pressure of the gaseous jet is significantly greater than that of liquid film at the injection plane. The jet has much higher velocity than the liquid, making it possible that underlying flow instabilities are generated by the high relative velocities.

An important example of coaxial liquid jet breakup and its different mechanisms is provided by Chigier and Reitz [93]. The authors consider shear coaxial sprays which exhibit breakup in the so-called *fiber type* disintegration mode and subsequent *pulsating/superpulsating* submodes of disintegration—each depicted in Figure 5.1. They describe these breakup behaviors to be dependent on various forms of flow instability including capillary, helical, and Kelvin-Helmholtz-type instabilities. For shear coaxial injectors, the spray experiencing fiber type breakup slightly expands at an angle into the co-annular gaseous jet, and exhibits fine tendrils of liquid which are stripped from the core of the liquid jet by the high speed co-annular flow and further

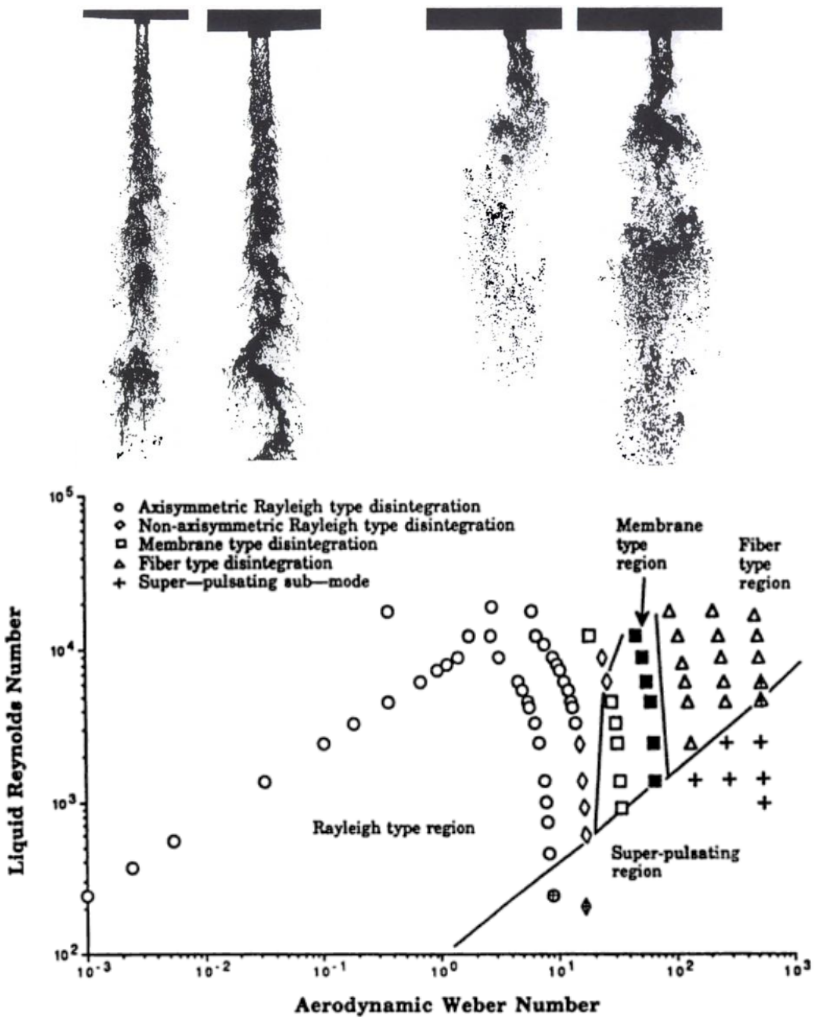

Figure 5.1: Fiber type liquid breakup (left) and "super pulsating" submode (right) seen for high speed shear coaxial injection, with breakup behaviors mapped to flow space by Chigier and Reitz [93].

atomized through Rayleigh-type disintegration. Figure 5.1 also plots the summarized findings of Chigier and Reitz, where regimes of coaxial breakup are mapped to flow parameter space expressed by liquid injection Reynolds number and aerodynamic Weber number, We_g.

Figure 5.2 depicts the 'globally-stable', non-pulsitile spray field that occurs at flow conditions slightly below those at which self-pulsation occurs at the lower self-

pulsation boundary of the non-recessed injector element. Here image contrast has been enhanced from the raw imagery to show detail. In the first frame (t_1), the spray cone is contracted and liquid fine tendrils are seen stripped away by high gas velocity. In the subsequent frame (t_2), these fibers are seen organized as a quasi-waveform on the outer surface of the film. The breakup features propagate downstream along the outer spray cone surface in both the axial and radial directions following the mean flow path of the liquid sheet. The azimuthal component of these features appears negligible at these conditions. *Roll-up* of the wave crests can be witnessed in the third frame of the imagery (t_3)—suggesting these liquid waves are a result of hydrodynamic/aerodynamic interactions of the liquid film and co-annular jet. The small depth-of-field in the imagery prevents clear identification of these behaviors on both sides of the spray cone, but close inspection does show some signs that tendrils and similar waveform development/rollup occurs on the right-hand-side as well. These local, small scale breakup behaviors of the non-pulsatile spray are much different in nature to the larger scale spray oscillations that take place during self-pulsation.

These spray breakup behaviors are similar to those observed and described by Chigier and Reitz' [93] for shear coaxial sprays using water and air. To compare, Figure 5.3 plots $\Re\Re = 0.30$ (non-recessed configuration) data and self-pulsation boundary representations for all recess configurations with respect to breakup regimes described in Ref. [93] for a non-recessed shear-coaxial injector. Here aerodynamic Weber number of the liquid sheet is calculated following $We_g = \rho_g(\bar{u}_g - \bar{u}_l)^2 h_0/2\sigma_l$.

Note that lines depicted in Figure 5.3 do not represent fits through the data, but rather represent conditions at which spray breakup transitions between distinct

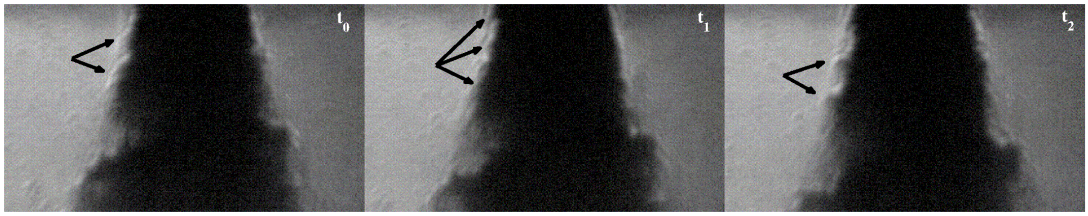

Figure 5.2: Typical spray patterns produced at flow conditions below the lower boundary of self-pulsation, showing fiber type breakup generated by high relative velocity of the two fluids in the near-field of the $\Re\Re = 0.30$ injector; these patterns organize as quasi-waveforms on the exterior surface of the liquid spray cone, where wave crests roll up and are stripped away from the contiguous cone.

non-pulsatile to pulsatile behavior (i.e. the boundary of self-pulsation). It can be qualitatively observed that at conditions above the self-pulsation boundary representation, the swirl coaxial spray patterns look similar to classic observations of fiber-type disintegration for shear coaxial sprays. Below, swirl coaxial breakup patterns are consistent with descriptions of the so-called "super-pulsating" submode of breakup in shear coaxial sprays.

Quantitative comparisons can also be drawn. Chigier and Reitz [93] find super-pulsation to occur at conditions where $Re_l/\sqrt{We_a} < 100$, while for the liquid-centered swirl coaxial spray, self-pulsation for $\Re\Re = 0.30$ occurs when $Re_l/\sqrt{We_a} < 127$. With swirl post recess, the self-pulsation boundary relation is different and much more sensitive to gas flow conditions, where $Re_l/\sqrt{We_a} \approx 252$ for $\Re\Re = 0.42$. For the $\Re\Re = 0.66$ configuration, self-pulsation transition seems to occur when $Re_l/\sqrt{We_a} \approx 378$, but scatter in the data makes it difficult to comment on this with certainty. For the sake of plot clarity, the test conditions in terms of Re_l and We_g for the recessed

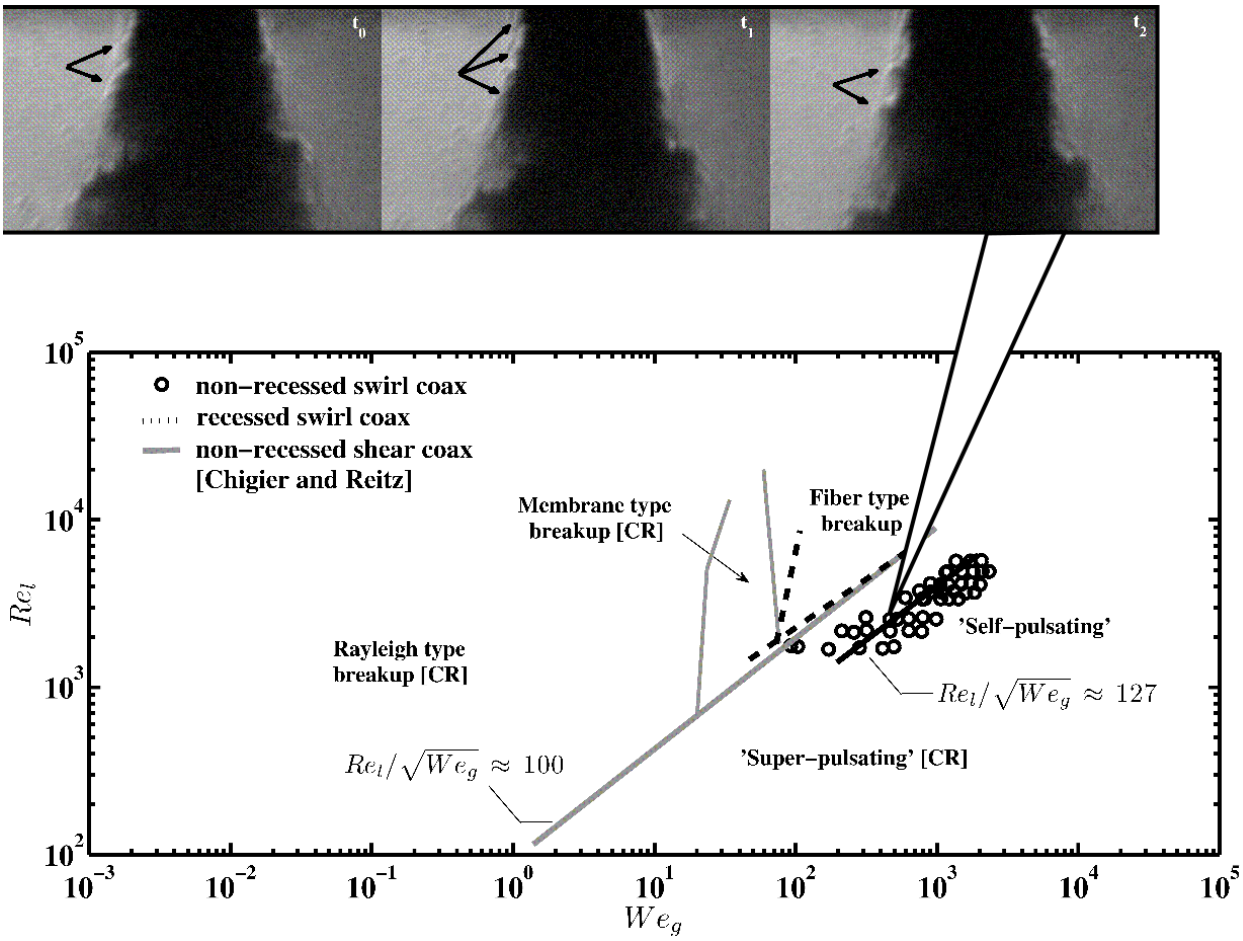

Figure 5.3: Non-recessed swirl coaxial setpoints and self-pulsation boundary representations compared in Re_l vs. We_g space with regimes of coaxial breakup established by Chigier and Reitz [93].

configurations are not plotted in Figure 5.3 since they are essentially identical to those tested for the non-recessed injector. However, representations of the transition conditions from fiber-type to self-pulsation for the recessed injector are provided.

These observations suggest that the spray breakup characteristics between shear coaxial and liquid-centered swirl coaxial injection in the transition from fiber type disintegration to a pulsating type regime of breakup are consistent. Since in this regime of liquid breakup the gas jet velocity dominates that of the liquid sheet, it

can be inferred that the degree of liquid swirling motion and instability mechanisms associated with it play a less significant role in the fiber type breakup than does streamwise motion. Therefore, the underlying mechanisms responsible for the near-field tendril formation and breakup processes for the liquid-centered swirl coaxial injection is reasoned to be similar to those responsible for fiber type breakup in other coaxial injectors—that is, shear layer interactions leading to K-H-type instability.

5.2 Percursor Spray Dynamics

Im et al. [39] posit that liquid breakup processes are critical to the onset and sustainment of self-pulsation spray oscillations. Periodic stripping/pushing of so-called "dominant" or "unstable" waves are described as key to the mechanism of self-pulsation excitation and sustainment. Since from experiments here the spray has been observed to experience fiber type breakup in the transition from non-pulsitile to self-pulsation behavior, it becomes important to quantitatively characterize the liquid stripping phenomenon as a precursor to self-pulsation.

The spray dynamics that are active at flow conditions near the lower boundary of self-pulsation are compared with those at the threshold where self-pulsation occurs. Figure 5.4 plots measured lower boundaries of self-pulsation along with points taken at test conditions slightly below—whereat self-sustained oscillations were not present. Appendix D contains tabulated flow and fluid state conditions measured during these tests with all injector recess configurations.

At these conditions just below the self-pulsation boundaries, the spray field is considered non-pulsatile and 'globally stable', where liquid atomization characteristics

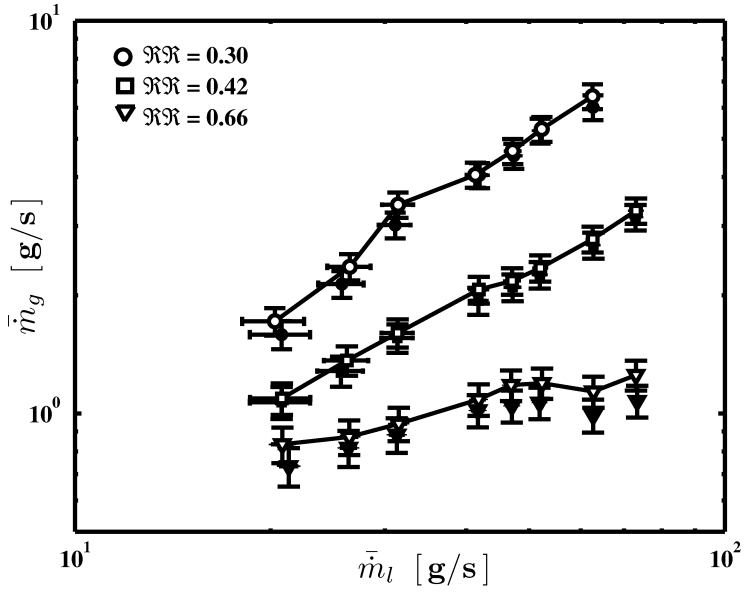

Figure 5.4: Test conditions at and slightly below the lower bound of self-pulsation.

are not accompanied by audible tones and the spray cone does not dramatically contract/expand as it does during self-pulsation. The momentum of the co-annular jet constricts the full spreading of the liquid spray cone in the near-field of the injector. The liquid sheet remains contiguous in this region, while further downstream the sheet undergoes strong atomization due to expansion of the jet.

At non-pulsatile conditions slightly below the self-pulsation boundaries, distinct patterns representing oscillatory spray structures generated within the fiber type breakup regime are readily identifiable through modal analysis of the image data. Figure 5.5 compiles contours of dominant patterns for each recess condition, organized by approximate liquid Reynolds numbers that correspond to momentum flux conditions in Figure 5.4. Each mode reveals spatially-coherent patterns on the outer surface of the liquid sheet. These lobe patterns describe alternating light and dark regions

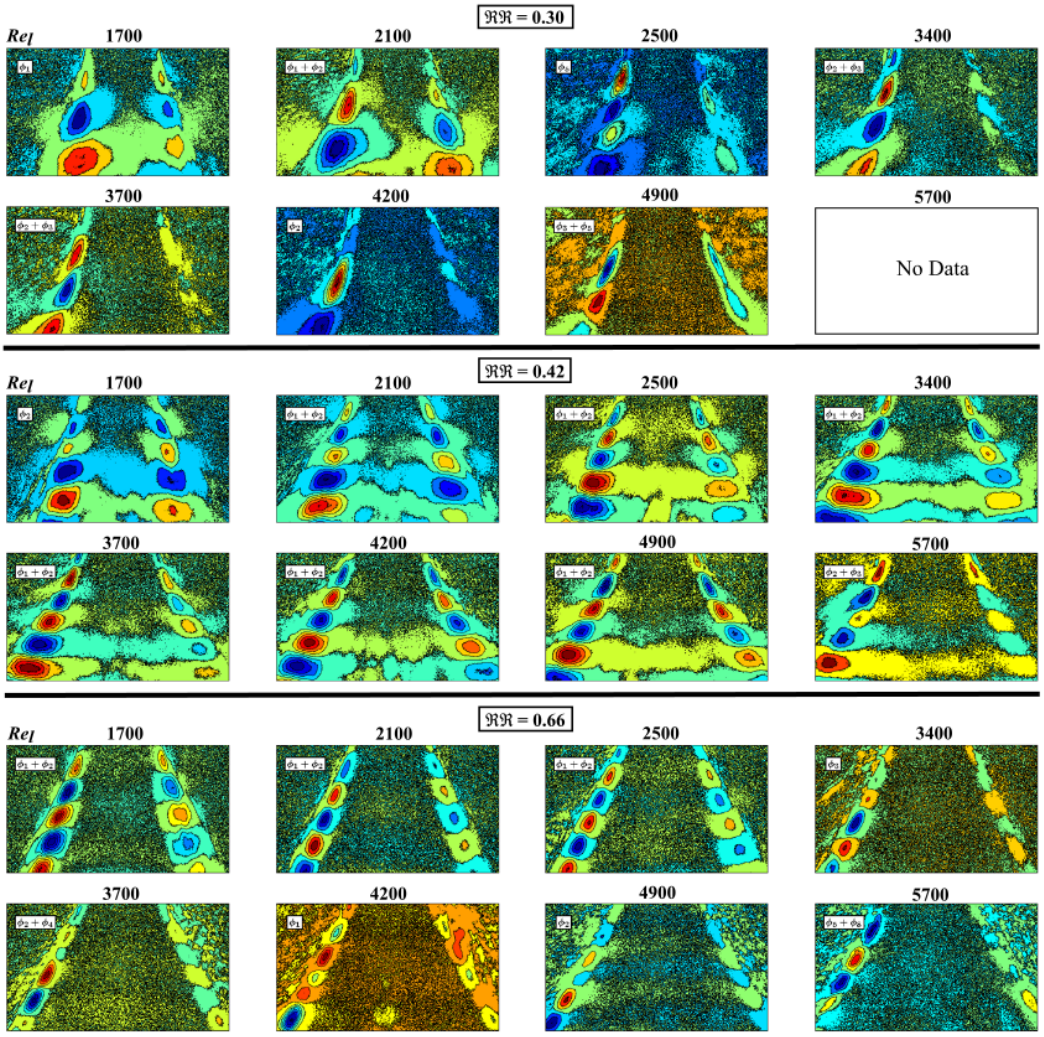

Figure 5.5: Precursor modes of non-pulsatile spray oscillation that develop slightly below the self-pulsation boundaries for all test recess configurations of the injector element.

along the exterior surface of the spray cone that signify spatially periodic waveforms similar in appearance to that shown in Figure 5.3.

Notice that inner post recess fosters the formation of well-organized patterns on the exterior of the liquid spray cone. Such strong organization allows periodic boundary conditions at the exit of the gas annulus to more easily develop when stripping occurs. The qualitative wavelength and frequency of the recessed spray

patterns compare closely for similar Re_l values even though corresponding gas flow conditions are quite different. By contrast, the spray modes for the flush injector are not as well organized, have larger qualitative wavelengths, and show indications of angularity when compared with spray modes of the recessed cases. The wavelength and frequency of the non-recessed patterns have dependencies with liquid flow, but also have a different, much more significant dependence on high levels of gas co-flow than the cases where the inner swirl post is recessed.

Since the dynamics associated with the non-pulsatile spray patterns in Figure 5.5 occur in such close proximity to the established boundaries of self-pulsation, they are considered, naturally, excitation precursors of the phenomenon. As such, Figure 5.6 makes a direct comparison of their time scales with those of self-pulsation, where the frequency ratio between each non-pulsatile spray pattern and the corresponding frequency of spray oscillation that develops during self-pulsation at the lower boundaries are plotted. These values are compared with respect to liquid injection Reynolds number for all inner post recess configurations.

The primary frequency associated with the non-pulsatile spray oscillations shows excellent agreement with that of active self-pulsation at the boundary, where, with the exception of two cases, relative deviations in comparison do not exceed 14%. This result indicates that flow patterns in the fiber type breakup regime that arise from hydraulic/aerodynamic interactions and instability on the outer surface of the conical liquid sheet are present at conditions essentially identical to those at which self-pulsation occurs, and shows that their time scales are approximately equivalent, or at least comparable, to those of eventual self-pulsation. The result is consistent

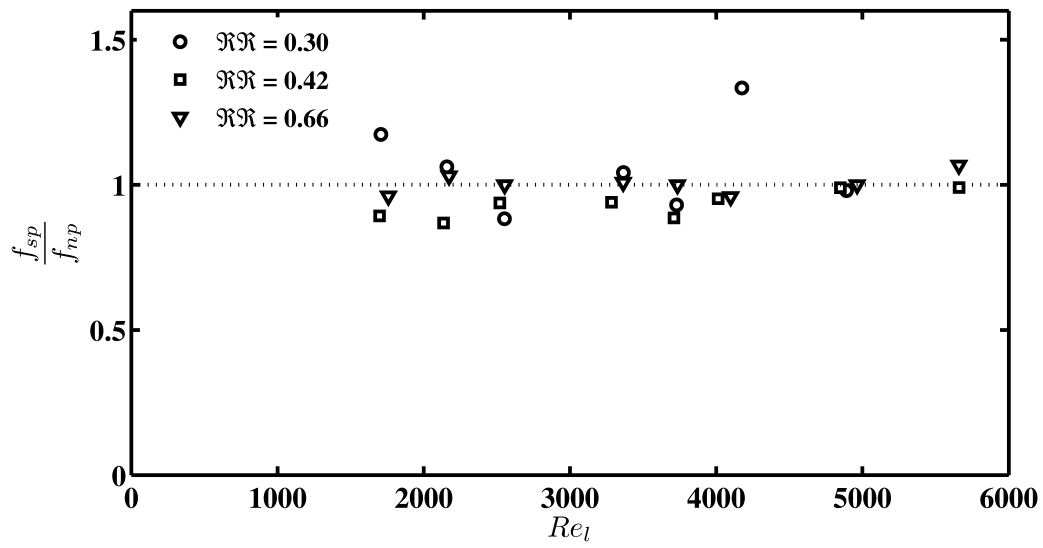

Figure 5.6: Frequencies of self-pulsation at the lower stability boundary normalized with those of non-pulsatile precursor spray oscillations measured at injection conditions slightly reduced from the lower stability boundary.

with discussion by Im et al. [39] that periodic stripping away of liquid from the spray cone is key to the mechanism of self-pulsation.

These precursor patterns are visually consistent with patterns of K-H-type wave growth and also occur within the fiber type breakup regimes where these types of oscillations are known to occur. Additional analysis comparing the frequency behavior of these precursor behaviors and those which occur at self-pulsation can be seen in Appendix F which aid in establishing the similarity of these flow oscillations to those generated by K-H-type instability.

5.3 Transition to Self-pulsation

In the precursor spray behaviors to self-pulsation, the organization of lobe patterns for each mode shape suggests spatially periodic oscillation with distinct temporal

periodicity. The observations of non-pulsatile spray patterns active just beneath the self-pulsation boundaries imply that underlying fluid oscillations that undergo fiber-type breakup by gas/liquid interaction. These underlying flow oscillations could be attributed to a variety of flow behaviors dependent on 1) both the liquid and gas flows, or 2) only one of the flows.

First recall from Chapter 1 that according to theory, unstable K-H-type wave growth is responsible in defining the spatio-temporal characteristics of liquid sheet oscillation that lead naturally to liquid breakup. These oscillations take on the form of either sinuous or varicous (symmetric or antisymmetric) modes that describe the waveform relationship between the exterior and exterior surfaces of the liquid sheet. Sinuous modes of oscillation are known to be the most dominant mode of oscillation for spray cones generated by pressure-swirl injectors [33], and are characterized as oscillations with the highest growth rate. These type of modes and their spatio-temporal characteristics are dependent on both liquid and gas flow conditions. That is, the frequency at which the liquid sheet will oscillate through K-H-type instability is unique for each permutation of liquid and gas flow conditions. With this in mind, inspection of the non-pulsatile spray patterns seem to be dependent both on the liquid and the gas flows, where spray pattern frequency increases and apparent wavelength decreases as flow conditions become more elevated. This basic observation is consistent with theoretical descriptions of K-H wave growth on liquid sheets in gas co-flow [38].

In their work, Im et al. [39] imply Kelvin-Helmholtz wave growth active leading up to self-pulsation as they analyze the flow as a function of gas Reynolds number

following Lee and Chen [38]. The authors go on to suggest that periodic stripping from and pushing of the liquid spray cone is the mechanism by which self-pulsation occurs. The authors provide indirect evidence of K-H-type wave growth, wherein the dominant frequency of wave motion on the liquid sheet at $u_g = 0$ was found similar to values of self-pulsation frequency linearly extrapolated to $Re_g = 0$. The results offered by Im et al. [39] is considered *indirect* evidence of K-H-type instabilities being responsible for the onset of the self-pulsation phenomenon.

For the sake of comparison, similar analysis as taken by Im et al. [39] is briefly explored by using modal decomposition on the pressure-swirl data. This treatment of the data is described in Appendix G. In a few example cases, the approach yields plausible results; however, in most cases the results are somewhat subjective and have a reduced level of confidence due to complications in applying and interpreting the POD or the DMD to the pressure-swirl spray imagery data.

A different analysis approach is taken in order to advance upon the indirect implication of K-H type instabilities that has been established in the literature to date, and help supplement the circumstantial evidence provided by direct visualizations presented in the previous section. For a given liquid flow condition, the threshold of self-pulsation can be approached by variation in gas flow rate. Since the near-field interactions that take place within the recess region are not directly visible, the detailed role that recess plays in promoting these types of spray oscillation is not entirely clear from the data gathered in this study. However, the near-field region is fully exposed for the injector configured with no recess. This vantage grants the ability to study the transition of non-pulsatile patterns in order to supplement the connection

between liquid breakup processes, underlying flow oscillation(s), and the onset of self-pulsation. It now becomes interesting to employ Dynamic Mode Decomposition analysis in order to study these behaviors as self-pulsation is approached.

5.3.1 Instability-Induced Oscillations

First—before evaluating transition behavior—it is valuable to establish the nature of self-pulsation spray dynamics at the onset of the phenomenon. Consider the following modal decomposition analysis carried out at flow conditions on the lower boundary of self-pulsation, where $[\bar{\rho}_l \bar{u}_l^2, \bar{\rho}_g \bar{u}_g^2] \approx [11,128]$ kPa for the injector configured with no recess.

Figure 5.7 plots the principal spray pattern associated with self-pulsation identified through POD. The travelling wave nature of self-pulsation spray oscillations is obtained as a static representation through modal superposition as described in Chapter 3. These principal spray oscillations occur at 2016 Hz as evidenced by the distinct peak in the cross-power spectrum of the temporal amplitude coefficients from the constituent POMs.

Figure 5.8 presents a zoomed-in view on the DMD spectrum of spray oscillations, where the equilibrium mode highlighted in blue described the mean flow field which appears mostly axisymmetric. Here, each point is a distinct dynamic mode, where the x-axis is modal frequency and the y-axis is modal growth rate. Arching branches emphasized in the red indicate a flow field which is advective in nature [89], which is generally consistent with the established travelling wave behavior of spray oscillations under self-pulsation. These arches represent flow patterns that are thought

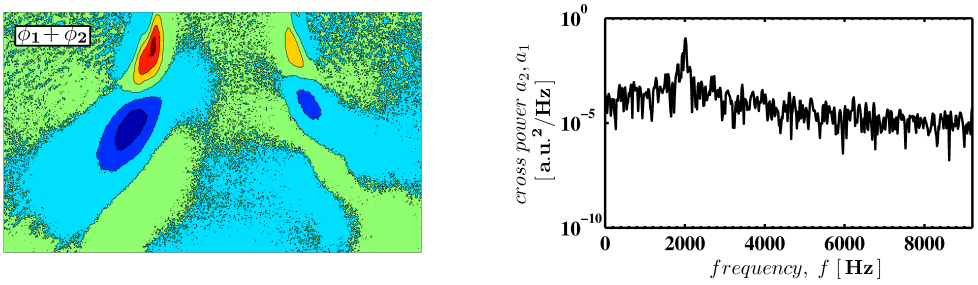

Figure 5.7: The principal mode of spray oscillation (left) that occurs at the lower boundary of self-pulsation at $[\bar{\rho}_l \bar{u}_l^2, \bar{\rho}_g \bar{u}_g^2] \approx$ [11,128] kPa for $\Re\Re = 0.30$; oscillations occur at 2016 Hz (left).

to describe the salient dynamics of self-pulsation. Mode shapes highlighted in red show behaviors that become increasingly complex in a spatial sense as temporal scale increases, while damping of the oscillations also increases. The DMD mode shape at 2016 Hz qualitatively resembles the principal spray dynamic pattern extracted by POD, and shares peak spatial coherence in the spectrum of about $\mathbb{Q} \approx 0.7$ with the POD mode in Figure 5.7.

Figure 5.9 shows the spatially phased real and imaginary components of the 2016 Hz DMD mode. When combined by linear superposition to describe known travelling wave behavior, spatial coherence with the POD mode improves to a level exceeding $\mathbb{Q} \approx 0.95$. This mode is thus confidently identified as describing the principal spray dynamics that occur during self-pulsations.

As such, the temporal growth rate of these spray dynamics is identified to be $\approx +7\ rad/s$. The positive value indicates that this spray pattern at these flow conditions grows in amplitude over the analyzed time interval. That is, these spray dynamics are, by classic definition, *unstable*. This realization seems trivial, but is a

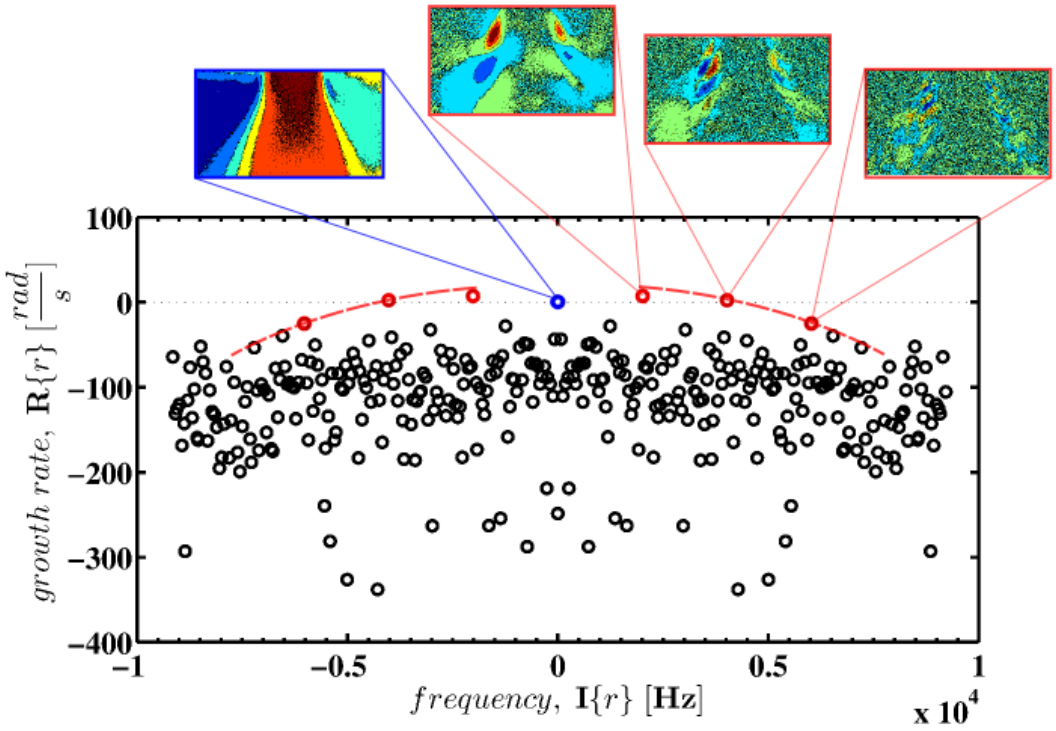

Figure 5.8: The DMD spectrum of spray oscillations that occur at $[\bar{\rho}_l\bar{u}_l^2,\bar{\rho}_g\bar{u}_g^2]\approx$ [11,128] kPa for $\Re\Re = 0.30$, showing (left) the equilibrium mode and moving right the unstable spray oscillation characterized at 2016 Hz belonging to self-pulsation.

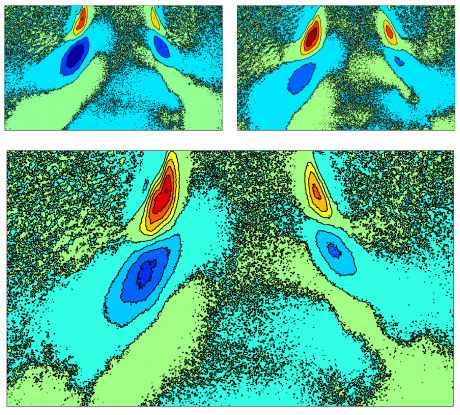

Figure 5.9: Imaginary (top left) and real (top right) components of the complex DMD mode, and their superposition describing the principal spray dynamics at 2016 Hz that occur at $[\bar{\rho}_l\bar{u}_l^2,\bar{\rho}_g\bar{u}_g^2]\approx$ [11,128] kPa for $\Re\Re = 0.30$.

new and important understanding of liquid-centered swirl coaxial self-pulsations. For these conditions it is established that the nature of the spray dynamics at the onset of self-pulsation can be classified as being *instability-induced*—that is, the stripping behaviors established earlier are driving temporal growth of spray oscillations.

5.3.2 Dynamic Effect of the Co-flow

Having characterized spray dynamics at the onset of self-pulsation, this study is now postured to explore the effect of gas flow in the approach and breach of self-pulsation onset. Figure 5.10 plots the characteristic temporal spray dynamics of the non-recessed swirl coaxial spray as a function of gas injection Reynolds number for three fixed liquid flow conditions. Here, the identification of temporal characteristics from the DMD spectra is guided by spatial similarity with the POD results. The temporal characteristics belonging to DMD modes exhibiting peak $\mathbb{Q}$ coherence criterion with counterpart POD spatial modes are plotted.

A distinct transition of principal spray dynamics from those dominated by non-pulsatile oscillation to those of self-pulsation is clearly shown, and the co-annular jet is found to have a clear destabalizing/stabalizing effect. A notable feature of these plots is an increase in oscillation growth rate as gas flow energy transfer is increased to the conical liquid sheet. This indicates that the fiber type breakup patterns are related to K-H-type instabilities whose levels of temporal stability decrease as gas flow is increased. An ensuing transition from damped non-pulsatile patterns to unstable—or in the lowest liquid flow case, very lightly damped—self-pulsation occurs at the stability boundary (self-pulsation conditions are denoted by points to the right of

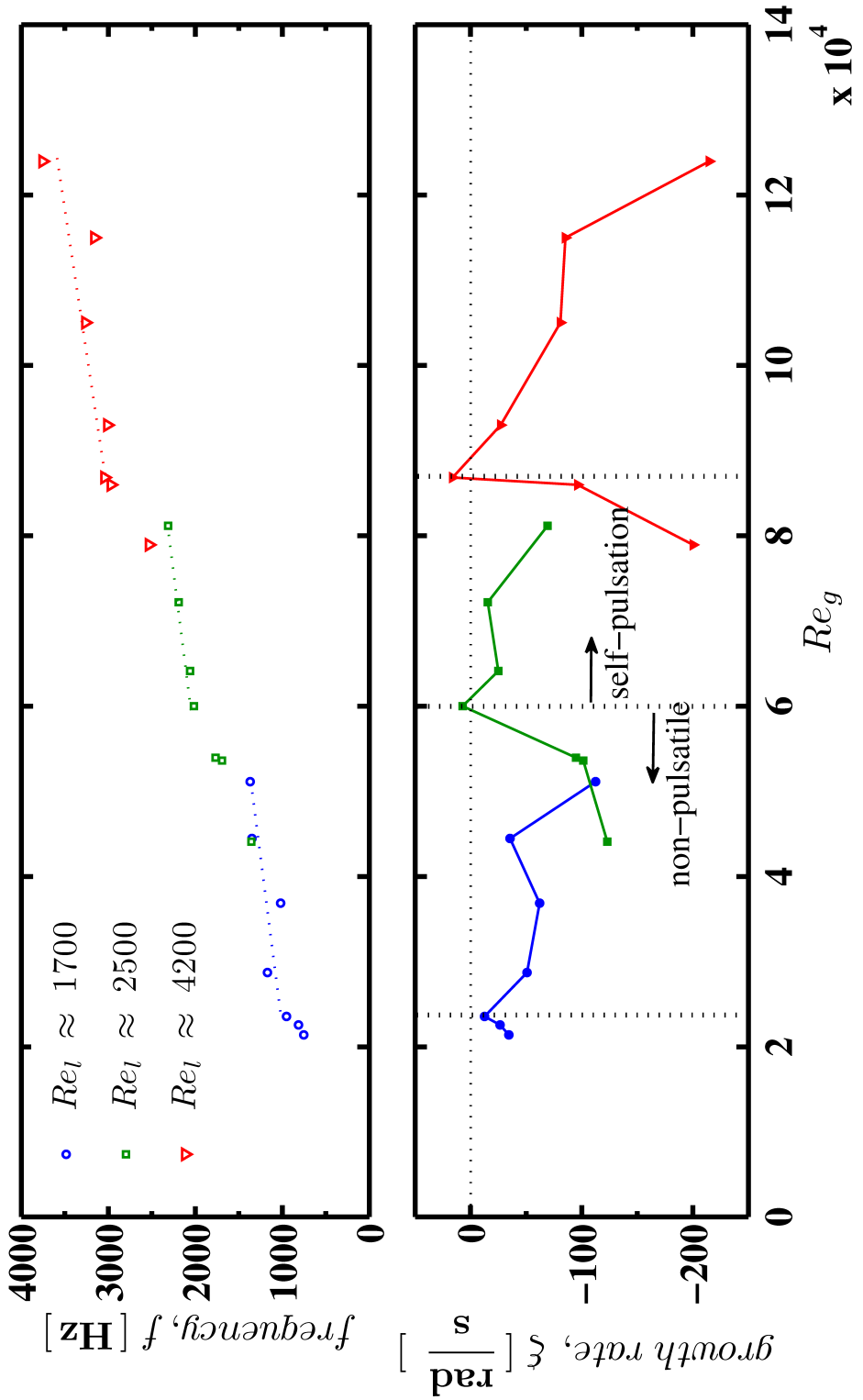

Figure 5.10: The frequency and temporal growth rate of characteristic modes of spray oscillation via DMD as a function of gas injection Reynolds number with ℜℜ = 0.30.

the meridians of each growth rate curve). These spray patterns at the boundary are pulsatile and either dynamically unstable or very lightly damped, and establishes that some type of coupling of flow instability has occurred.

Continuing immediately beyond the boundary, the self-pulsations exhibit lightly damped characteristics consistent with limit cycle oscillatory behavior. Characteristic spray dynamics become increasingly stable as gas flow is increased through the regime of self-pulsation. These data suggests that the inertia of the co-annular jet adds stabilization to the fluid oscillator(s) that participate during self-pulsation.

5.4 Interpretation

Having extracted precursor patterns attributed to fiber type breakup of K-H-type wave patterns slightly below the stability boundary which correspond closely in frequency to self-pulsations at onset, spray breakup processes involving Kelvin-Helmholtz-type instability are confidently established to be responsible for the instability-induced excitation of self-pulsations for the injector configured without inner post recess. These types of patterns capture the periodic stripping of liquid from the spray cone which are organized as a quasi-sinusoidal waveform along the exterior surface of the liquid sheet, and are consistent with and direct evidence of key elements to the proposed driving mechanism of self-pulsation given by Im et al. [39].

Noting the well-organized patterns for $\Re\Re = 0.42$ and 0.66 in Figure 5.5 when compared to the non-recessed cases, these data seem to suggest recess serves to organize stripping of waveforms by providing a geometric constraint on the spray field. It is hypothesized, in consistency with preliminary observations of similarity param-

eters, that the characteristic dimension of this constraint is related to the distance at which surface waves can form along the liquid film flow path from the axial plane of liquid injection to impingement upon the walls of the gas annulus, i.e. the characteristic dimension described in Figure 2.9. This important dimension might also be a function of other length scales related to the finer details of swirl injector hydraulics that remain not well-understood when combined with co-annular jet effects, such as a momentum transfer-dependent liquid spray cone angle (which defines the mean flow path of the liquid) and the consequential thickness that the unbound liquid film may take on. The characteristic length scale required to organize surface waves in the near-field of the non-recess configuration is the non-dimensional parameter 1-R_n/R_{ann}. In this case, the key geometric dimension of the injector with respect to the non-pulsatile disturbances responsible for self-pulsations is defined by $R_{ann} - R_n$.

Figure 5.10 shows that spray oscillation frequencies and growth rates during self-pulsation, in general, appear to follow different functional forms with Re_g than before its onset(particularly growth rate). However, the self-pulsation spray patterns seem entirely different than the non-pulsatile ones. During self-pulsation, the inverse relationship between spray growth rate and Re_g indicates that, if extrapolated, additional increases of gas flow would continue to stabilize the global spray dynamics such that self-pulsation might eventually cease. This trend implies an upper boundary of self-pulsations may exist, which is consistent with qualitative observations from this test campaign and also with accounts from other studies [50].

The excitation mechanics of self-pulsation seem to be clearly exposed by the increasingly unstable spray oscillations that reach a critical threshold of temporal

stability at conditions on the lower boundary of self-pulsation. Additional information pertaining to the self-pulsation phenomenon can be interpreted from these results. Recall that Im et al. [39] suggest through extrapolation [38] that the frequency of self-pulsation follows the same linear relation as the frequency of sheet breakup by K-H-type wave growth when extrapolated to $Re_g = 0$. This implies that during both non-pulsatile conditions and self-pulsation conditions, the fluid oscillator which defines response of the system is the natural inherent modes of liquid sheet oscillation itself. Here, it is not entirely clear that the frequency of these two different behaviors follow the same trend when extrapolated to no gas flow conditions.

These potentially differing trends in spray dynamics behavior indicate that perhaps the inherent modes of liquid sheet oscillation due to K-H-type wave growth are not the only fluid dynamics that participate during self-pulsations. Rather, this observation suggests that fluid stripping behavior in the near-field may actually *engage* an altogether different fluid oscillator(s) in the system. Comparison of self-pulsation Strouhal number estimates in Appendix F indicates a type of 'lock-in' of self-pulsations that might suggest this type of fluid oscillator engagement. The engagement and lock-in behaviors are common characteristics of instability-induced fluid resonant oscillations as detailed by Naudascher and Rockwell [53] and discussed in Chapter 1. The question left by findings in this chapter is:

> "*If sheet oscillation generated by Kelvin-Helmholtz wave growth is not the only underlying oscillator to define the frequency of self-pulsations, what other oscillators might participate?*"

The following chapters of this dissertation will be dedicated to identifying fluid oscillator characteristics inherent to the injector which might be vulnerable to interaction with and/or excitation by the near-field spray dynamics that have been described here thus far.

CHAPTER 6

FLUID OSCILLATOR IDENTIFICATION: EIGENMODE SURVEY

Test results show high intensity, audible tones generated during the majority of test conditions at which self-pulsations are noted. An obvious point of interest is in deducing what level of participation these pressure waves take on in the overall phenomenon. First, recall some queries stated in the introduction to this research:

> "*In what capacity do the fluid eigenmodes of the injector serve toward the combined physics of self-pulsation?*",

and,

> *Are audible tones responsible for reinforcement of the fluid oscillator system, or are they simply a consequence of pulsations?*"

This chapter examines passive mass(es) of fluid contained within the swirl coaxial injector element which might participate as fluid oscillators during self-pulsation. The nature of these fluid eigenmodes will be discussed. The primary focus will be to survey the resonant eigenfrequencies of the injector and compare them with the measured frequencies of self-pulsation.

The observation of high frequency screech tones emitted during self-pulsations has led other researchers to assume that the gaseous fluid mass contained within the injector responds in a distributed fashion during self-pulsation. Huang [52] et al. model two independent analytical natural frequencies of the gas annulus and of the swirl post gas core with 1-D treatments. Equation 6.1 and Equation 6.2 describe quarter-wave resonator expressions for each.

$$f_{ann,\mathfrak{K}} = \frac{(2\mathfrak{K}-1)c_g(1-\bar{M}_g^2)}{4l_g} \quad for\ \mathfrak{K} = 1,2,3,... \tag{6.1}$$

$$f_{gc,\mathfrak{K}} = \frac{(2\mathfrak{K}-1)c_{gc}}{4l_{gc}} \quad for\ \mathfrak{K} = 1,2,3...$$

$$where \tag{6.2}$$

$$\frac{1}{c_{gc}^2} = \frac{1}{c_g^2} - \frac{\bar{\rho}_g \bar{A}_l}{\bar{\rho}_l \bar{A}_{gc}(c_{gc} \pm \bar{u}_l)^2}$$

In this chapter, the natural distributed oscillations of fluid within the swirl coaxial injector element will be assessed in a modular fashion. The origins of acoustic velocity and mean flow effects embedded within the above proposed expressions will be given. Additionally, the effects of geometric configuration through inner post recessing will also be examined. The bandwidths of natural oscillation might aid identify the main fluid oscillator(s) which control the self-pulsation phenomenon.

6.1 Swirl Post Eigenmode Analysis

This section presents analysis of swirl post resonance de-coupled from the fuel annulus. The effects of liquid-to-gas volume ratios, propagation of acoustic pressure

waves within thin liquid films, and exit impedance effects are considered. The swirl post is modelled as a rigid-walled, uniform diameter cylinder. Barrere's equation [94], is extended to estimate the natural frequencies of complex eigenmodes within the injector element. Here, the boundary conditions represent a tube open at one end and closed at the other.

The axial dimension is denoted as l' which captures pipe radiation impedance [95] into an open environment, or end effects, using $l' = l + 0.6R$. In the eigenfrequency expression, $\mathfrak{K}$, $\mathfrak{m}$, and $\mathfrak{n}$ are spatial indices where the axial (denoted by "L"-longitudinal) index ranges $\mathfrak{K} = 0, 1, 3, 5...$ (reflecting 1/4-wave behavior), while diametral ("T"-tangential) and circular ("R"-radial) indices range $\mathfrak{m} = \mathfrak{n} = 0, 1, 2, 3....$ The characteristic roots $\delta_{\mathfrak{mn}}$ are tabulated in Table 6.1. The injector eigenfrequencies are then calculated following:

$$f_{\mathfrak{Kmn}} = \frac{c}{2\pi}\sqrt{\frac{\delta_{\mathfrak{mn}}^2}{R^2} + \frac{\pi^2 \mathfrak{K}^2}{4l'^2}}. \tag{6.3}$$

Table 6.1: Characteristic Roots for a Rigid-walled Cylinder with Closed-Open Boundary Conditions

		$\mathfrak{n}$			
		0	**1**	**2**	**3**
$\mathfrak{m}$	**0**	0.000	3.833	7.015	10.172
	1	1.841	5.331	8.526	11.706
	2	3.050	6.707	9.968	13.170
	3	4.200	8.014	11.344	14.743

Note that Huang et al. also consider effects of the liquid in the expression of acoustic velocity. The volume held within the swirl post is composed of a heterogeneous mixture of both gaseous and liquid fluids, and the rate at which pressure waves

propagate through this medium must be considered in the analytical treatment of the swirl post eigenmodes. While the gaseous fluid volume remains essentially stagnant in the axial direction (neglecting vortical motions), the liquid flows and should also be considered.

Evans [96] discusses acoustic pressure wave propagation through water films. The acoustic pressure wave cut-off frequency is defined as $f_{cut} = (2\Re + 1)c/4h$. For example, the fundamental mode cut-off frequency of a 400 μm thick film would be approximately 972 kHz. For frequencies much less than the cut-off, the axial distance at which a fundamental mode pressure wave will attenuate by a factor of e^{-1} is given by $\mathrm{x}_{atten} \approx 2h/\pi$, indicating that low frequency pressure waves will dramatically decay over a distance of approximately 65% of the film thickness itself. In addition, viscous effects on the wall and high shear forces due to turbulence will further attenuate axially propagating pressure waves in the film.

This shows that acoustic pressure wave propagation in the swirl post is rapidly attenuated. Pressure waves will therefore propagate most significantly within the gaseous core [96]. Evans empirically finds that for void fractions $\forall = A_g/A_T$ spanning approximately 0.5-1.0, measured acoustic velocity in a H_2O-air annular pipe flow approaches that of pure air. However, axial inhomogenieties including large surface waves and variations in inlet conditions of the liquid film were thought to generate some deviations in measured acoustic velocities.

Noting these observations leads to the supposition that the gas core dominates the longitudinal pressure wave dynamics within the swirl post. The acoustic velocity of the two-phase annular flow medium is estimated by Equation 6.4 [97] assuming

constant cross-sectional free gas void fraction from a steady liquid film surface within the swirl post. In this expression, $\bar{\rho}_* = \bar{\rho}_g/\bar{\rho}_l$ and $\mathbb{K}_* = \mathbb{K}_g/\mathbb{K}_l$ where fluid bulk modulus $\mathbb{K}$ is defined as $\mathbb{K} = c^2/\bar{\rho}$.

$$\frac{c_{mix}^2}{c_g^2} = \frac{\forall + (1-\forall)/\rho_*}{\forall + (1-\forall)/\mathbb{K}_*} \tag{6.4}$$

Figure 6.1 plots the acoustic velocity of both H_2O-air and H_20-He mixtures evaluated by Equation 6.4 with a regime of swirl post void fractions representative of liquid flow conditions from testing. Density and sound speed of the constituent fluids are those estimated at ambient conditions (STP) for H_2O-air and at elevated conditions (0.75 MPa, 295 K) for H_2O-He. The pressure wave propagation speeds converge to the sound speed of the gaseous medium at large void fractions, and are consistent with the findings of Evans. Thus, modelling the swirl post fluid as a volume of gas modified with the acoustic velocity of the mixture appears a logical approach. As such, since the acoustic velocity of the mixture does not vary appreciably with void fraction over the tested throttling conditions, it is reasonable to expect the frequency of swirl post eigenmodes (particularly longitudinals) to remain essentially constant in this regard. Furthermore, since the acoustic velocities of the mixture over the given void fractions are essentially equal to that of the gaseous medium, the effects associated with the liquid in Equation 6.4 can be reasonable neglected.

Table 6.2 documents eigenmode frequencies for the idealized swirl post geometry by Equation 6.3 for H_2O-air and assuming acoustic velocity of air at STP. The pure tangentials and pure radials resonate at very high frequency. Quarter-wave

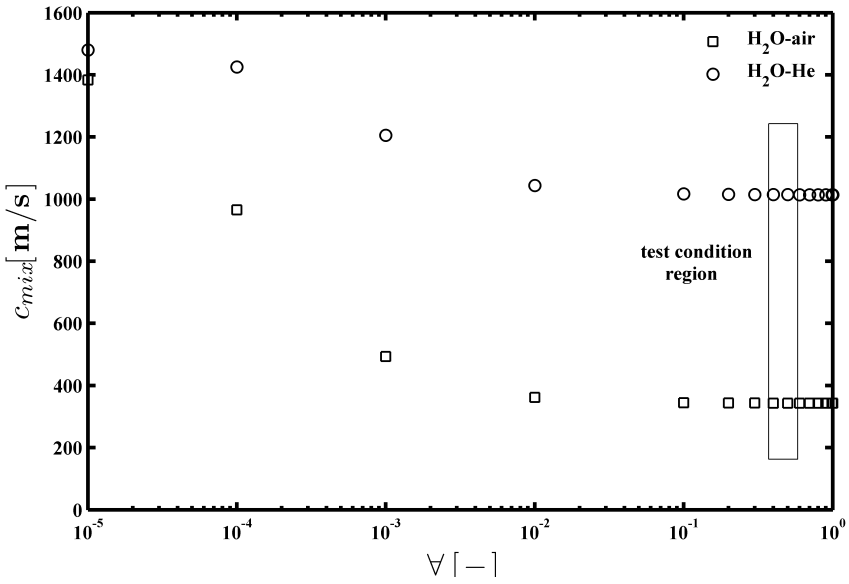

Figure 6.1: Acoustic velocity of liquid-gas mixtures based on the gas void fraction, $\forall = A_g/A_T$.

longitudinal modes are active at much lower frequencies. The eigenmodes most of interest are those within the bandwidth of observed self-pulsation frequencies from ≈ 900-4000 Hz.

Table 6.3 documents analytical solutions to the pure quarter-wave longitudinal modes where $\mathfrak{m} = \mathfrak{n} = 0$. It can be concluded that only the 1/4L and 3/4L ($\mathfrak{K}$=1,3,5...) should lie within the observable bandwidth of oscillation.

Table 6.2: Analytical Eigenfrequencies of Idealized Swirl Post

$f_{\mathfrak{K}\mathfrak{m}\mathfrak{n}}(kHz), \mathfrak{K} = 1$				
$\mathfrak{m}/\ \mathfrak{n}$	0	1	2	3
0	1.40	88.2	161	234
1	42.4	123	196	269
2	70.3	154	229	303
3	96.6	184	261	339

Table 6.3: Analytical Longitudinal Quarter-wave Frequencies of Swirl Post

$\mathfrak{K}$	$f_{\mathfrak{K}}(Hz), \mathfrak{m} = \mathfrak{n} = 0$
1	1402
3	4207
5	7012

6.2 Fuel Post Eigenmode Analysis

In the case of the annular fuel post, the natural frequency of pressure oscillation will be dependent not only on geometric and thermophysical properties but also on characteristics of the mean flow. The nominal internal geometry of the fuel post is configured with no swirl post recess and is connected to a manifold volume much larger than the volume of the post itself in this first analytical treatment. Mean flow and the presence of the fuel manifold are neglected, and the analytical model [98] for an open-open annular cylinder expressed by Equation 6.5 for $\mathfrak{K} = \mathfrak{m} = \mathfrak{n} = 0, 1, 2...$ is used. The formula for estimating characteristic roots based on the annulus radii ratio is also given. The effective length of the annulus is considered that for a flanged end.

$$f_{\mathfrak{K}\mathfrak{m}\mathfrak{n}} = \frac{c}{2\pi}\sqrt{\frac{\delta^2_{\mathfrak{m}\mathfrak{n}}}{R^2_{out}} + \frac{\pi^2\mathfrak{K}^2}{l'^2}} \tag{6.5}$$

where

$$\delta^2_{\mathfrak{m}\mathfrak{n}} \approx (\frac{\mathfrak{n}_{out}}{R_{out} - R_{in}})^2 + (\frac{2\mathfrak{m}R_{out}}{R_{out} + R_{in}})^2 \quad for \;\; \frac{R_{in}}{R_{out}} > 0.5 \tag{6.6}$$

The analytical results in Table 6.4 show that transverse, complex and higher order longitudinal eigenmodes need not be considered because the frequencies are far higher the measured bandwidth of self-pulsation frequencies. Only the low order longitudinals are of interest. In this case, Equation 6.5 reduces to the basic expression $f_{\mathfrak{K}} = c\mathfrak{K}/2l'$ for $\mathfrak{K} = 1, 2, 3....$ Evaluation for air at STP conditions yields an idealized first 1/2-wave eigenfrequency of about 6.7 kHz, which is also far outside the bandwidth of self-pulsations.

Table 6.4: Analytical Eigenfrequencies of Idealized Annulus

$f_{\mathfrak{K}\mathfrak{m}\mathfrak{n}}(kHz), \mathfrak{K} = 1$		
$\mathfrak{m}$ / $\mathfrak{n}$	0	1
0	6.71	343
1	18.7	7280

The convective effects of a mean flow field on the propagation of pressure waves within the fuel post cannot be ignored. Mean flow through a pipe negates radiation impedance, such that end effects encapsulated within the l' term are neglected. Rectified estimates result in a shift of the fundamental 1/2-wave frequency up to about 6.9 kHz. Also, over a limited range of test conditions, the mean flow takes on subsonic velocities which introduce phase distortion of propagating pressure waves within the fuel post. Naudascher and Rockwell [53] account for this effect in an expression for half-waves given by:

$$f_{\mathfrak{K}} = \frac{c\mathfrak{K}}{2l}(1 - M^2) \tag{6.7}$$

At low velocities, the effects of mean flow on the half-wave eigenfrequencies of the fuel post are negligible, but as flow approaches sonic conditions the longitudinal mode frequencies dramatically reduce. Applicable to a limited number of tests at subsonic conditions—when the fundamental half-wave frequency is adjusted for mean flow effects by the $(1-M^2)$ term in Equation 6.7, the fuel post 1/2L mode oscillates in a potential bandwidth of $\approx$ 1608-6140 Hz that essentially covers the entire bandwidth of self-pulsations.

However, the sonic flow condition brings to light considerations for the treatment of fuel post eigenmodes under other test conditions at which the mean flow field is at, or exceeds, M=1. At low injection velocities, this volume will be coupled to the fuel post volume, but as injection velocity is increased to the sonic condition at the fuel annulus entrance, backward propagating acoustic communication between the post and the manifold will be blocked. The high impedance imposed by a sonic choke point at the fuel post entrance serves as an acoustically closed boundary condition. The natural pressure wave oscillations of the this effectively closed/open fuel annulus will take on quarter-wave mode shapes rather than half-waves. These eigenfrequencies can be calculated by the appropriately modified version of Equation 6.5 for $\mathfrak{K} = 0, 1, 3, 5....$ Table 6.5 documents analytical estimates of quarter-wave frequencies for the fuel post choked at its entrance and without radiation impedance effects. The fundamental quarter-wave frequency falls within the bandwidth of observed self-pulsations and should be considered.

By these estimations, the 1/4L frequency of the fuel annulus near 3500 Hz lies within the upper portion of the measured self-pulsation bandwidth. This suggests

Table 6.5: Analytical Longitudinal Quarter-wave Frequencies of Choked Annulus

$\mathfrak{K}$	$f_{\mathfrak{K}}(kHz)$
1	3.47
3	10.4
5	17.3

that the higher order modes of fuel annulus could also participate in the self-pulsation phenomenon.

6.3 Fluid Oscillator Assessment

Having established estimates of natural resonances associated with the injector element, it now becomes interesting to respectively evaluate the measured signatures of self-pulsation in an effort to determine which fluid oscillators are most influential. Figure 6.2-Figure 6.4 plot the self-pulsation parameter space with calculated eigenfrequencies of the injector. It can be seen that several of the self-pulsation data points coincide with potential injector eigenfrequency activity, particularly at the lower and higher regions of the test parameter space. Also note low liquid flow conditions where gaseous flow ranges across subsonic flow conditions at the entrance of the gas annulus. Here, self-pulsations are potentially coupled to: A.) swirl post fluid oscillation of its distributed 1/4L mode, B.) fuel post/manifold fluid oscillation of its 1/2L mode, or C.) both. Consistent with other research efforts, the quarter-wave resonances of the injector seem to be the most significant fluid oscillators in the system at these conditions. The excitations of the liquid spray cone oscillation could couple to and excite the longitudinal eigenmodes of the injector, such that standing pressure waves

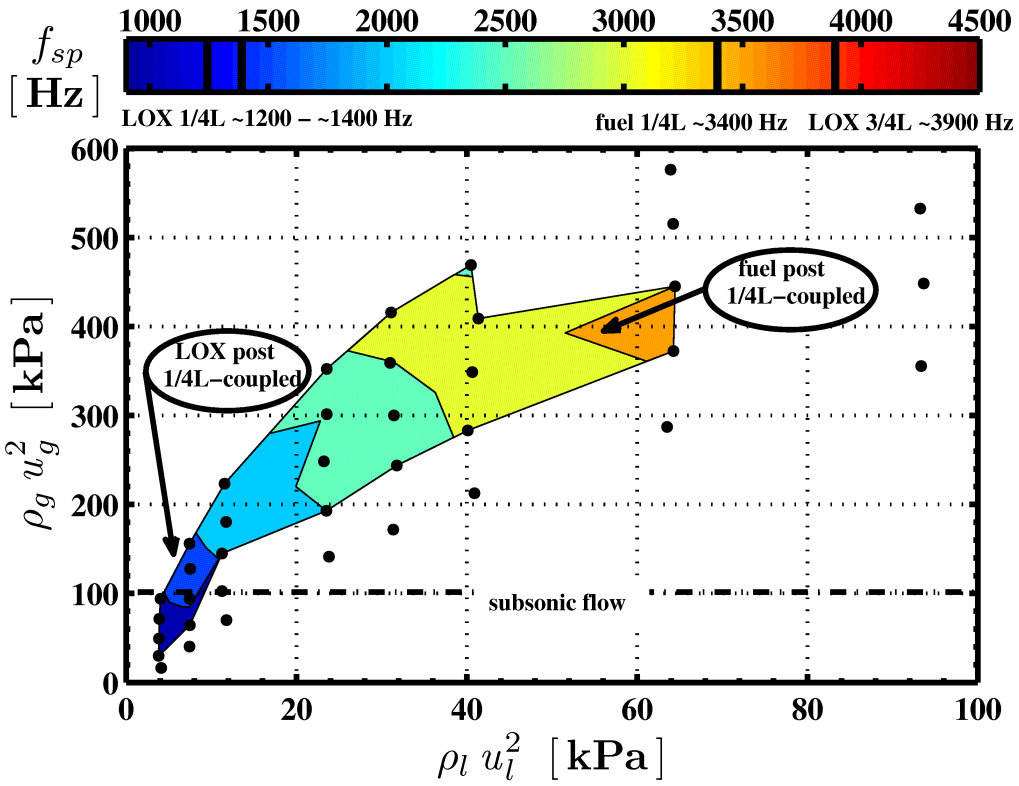

Figure 6.2: Self-pulsation frequencies mapped to parameter space indicating flow conditions potentially coupled to eigenmodes of the flush mounted injector element.

both generate tonal emissions and reinforce liquid film/spray cone oscillations as a feedback in sustaining the self-pulsating fluidic oscillator system.

However, significant regions of parameter space do not clearly coincide with estimated eigenfrequency bandwidths—particularly at the majority of mid-ranged flow conditions. Here, the influences of injector eigenmodes on the overall fluidic oscillator are less straightforward than at the extrema where quarter-wave injector modes exist. In this mid-range region, the absence of any eigenfrequency indicates that injector pressure resonances are not active. The concurrent observation of discrete sound emissions suggests that the swirl post gas core and/or fuel annulus might oscillate at

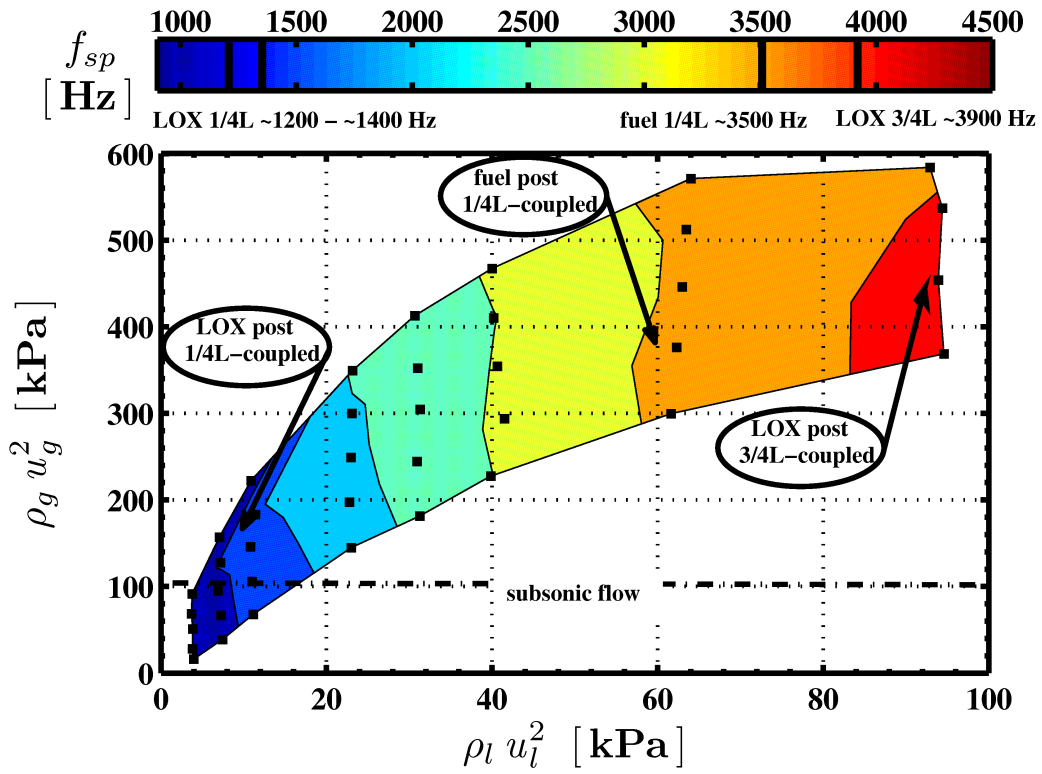

Figure 6.3: Self-pulsation frequencies mapped to parameter space indicating flow conditions potentially coupled to eigenmodes of the $\Re\Re = 0.42$ recessed injector element.

damped off-resonant frequencies that may not necessarily provide feedback to sustain self-pulsations. However, a possibility that should also be considered is that in these mid-range flow conditions, irregularities in the liquid film of the swirl post might alter the acoustic velocity of the post enough to modulate the 1/4L eigenfrequeny of the swirl post into the 1500-3000 Hz bandwidth. However, without direct observation of these internal hydrodynamics, such a notion is difficult to advance beyond speculation.

The question now left by these results is:

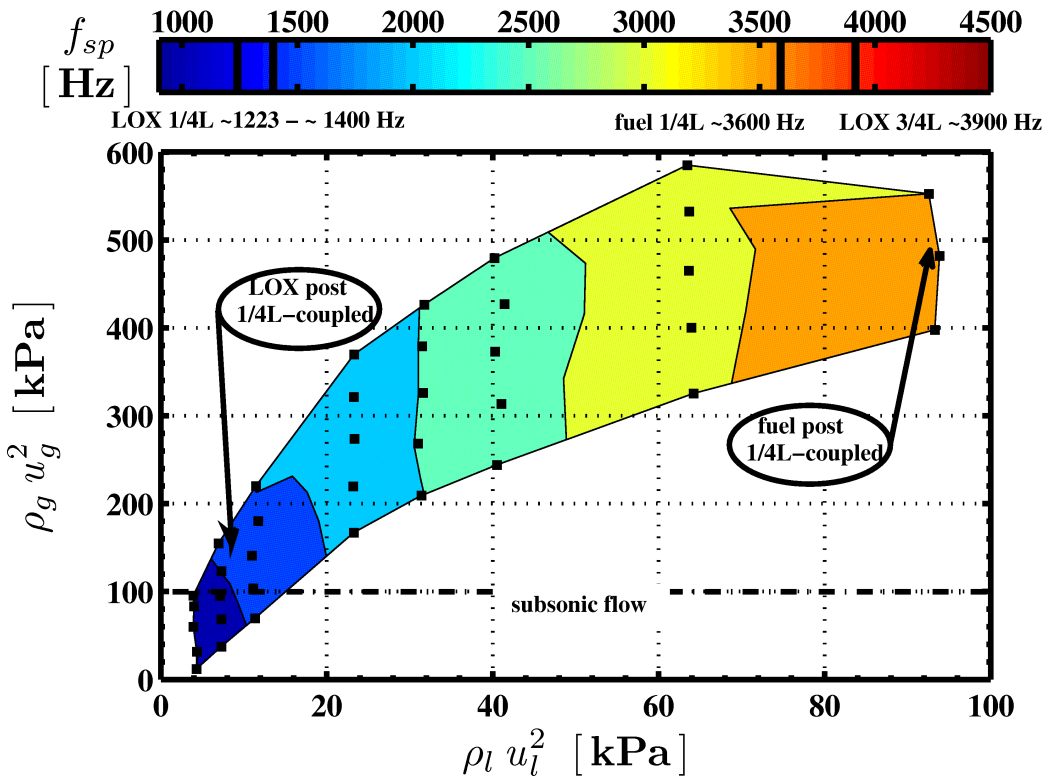

Figure 6.4: Self-pulsation frequencies mapped to parameter space indicating flow conditions potentially coupled to eigenmodes of the $\Re\Re = 0.66$ recessed injector element.

"If injector eigenmodes do not provide reinforcement of liquid film and spray cone oscillations, what physics are responsible for providing feedback in the oscillating system?"

CHAPTER 7

FLUID OSCILLATOR IDENTIFICATION: SWIRL INJECTOR HYDRODYNAMICS

In light of injector eigemode identification results, it is now sought to investigate other fluid physics which might also serve to control self-pulsations of the swirl coaxial fluidic oscillator. A logical extension of this study is to examine the surface wave hydrodynamics internal to the LOX post swirl element. The topic of swirl injector fluid resonance was touched upon in Chapter 1. The idea of characteristic standing surface wave patterns fostered by the geometry of the swirl injector vortex chamber is represented by Equation 1.9, where the vortex chamber is idealized with a 90^o step discontinuity between itself and the injector nozzle. Cursory evaluation of the fluid resonant expression over the range of tested liquid flow conditions yields a wide bandwidth of possible resonance at ≈2000-5000 Hz. However, this formula is idealized with assumptions that are likely not applicable to the test article/conditions described here, and a more measured examination of swirl injector hydrodynamics is necessary. Here a classic analytical response model is modified in several manners and used to evaluate wave motions of the swirling liquid film which might constitute a fluid oscillator element in the system.

Two basic observations from the empirical data offered thus far are: 1.) during self-pulsation the swirl injector experiences dramatic spray oscillations which generate periodic oscillation in liquid flow rate near the exit of the swirl injector, and 2.) during self-pulsation the liquid manifold registers pressure response which is coherent to the self-pulsations (via the tonal emissions generated). These observations are consistent with the two fundamental parameters of Bazarov's response theory—perturbational mass flow and unsteady pressure response.

The results of the last chapter's survey suggest that not all self-pulsation cases can be confidently attributed to coupling with eigenmode resonance, so that the self-pulsations could be explained by characteristic hydrodynamic oscillations inherent to the swirl injector design and flow conditions. However, to tractably extend this model to the high frequency range and for the swirl injector test article at hand requires a review of critical modelling aspects that may require modification.

7.1 Modifications to Bazarov's Linear Dynamic Theory

A small number of researchers have focused efforts to model and validate the classic linear theory of swirl injector hydrodynamics. Several works offer both theoretical and numerical implementation improvements/extensions to Bazarov's analytics [99–101], and others have sought to present empirical data [28, 102–104] which might aid in validation/verification of the calculations. While limited empirical evidence exists to suggest potential viability of the theory in the low frequency range (in this case, $f < 1000\ Hz$), Bazarov's linear dynamic theory continues to remain unevaluated at higher frequencies due to limitations in experimental techniques for

generating strong unsteady pressure/mass flow conditions to which test articles might respond.

It is impractical here to commit a chapter of derivations that constitute Bazarov's full hydrodynamic theory; several rigorous works are dedicated to such efforts. Rather, for a brief overview, the reader is referred back to Chapter 1. For detailed derivation of the equations leading to Bazarov's linear hydrodynamic theory and a full description of underlying assumptions, the reader is directed to Ismailov's dissertation [101].

Figure 7.1 illustrates the 'classic' swirl injector geometry, with steady and unsteady flow features important in the modelling of the injector hydrodynamics. This current work adheres to the general framework developed around these characteristics, and seeks to build upon the established calculations in order to develop a more tractable model for the study injector geometry and conditions discussed in this dissertation. Specific extensions and modifications must be incorporated, and will now be be described.

7.1.1 Disturbance Celerity

The most significant challenge in extending Bazarov's original theory to the high frequency range is the *long wave approximation* for disturbance propagation speed on the free surface of the liquid film. The approximation is formulated for both the vortex chamber and nozzle by Equation 7.1 and Equation 7.2. The approximation neglects any radial component of fluid velocity on the liquid film, resulting in non-dispersive relations. Bazarov assumes the long wave approximation on the premise that wave lengths generated by low frequency combustion instabilities such

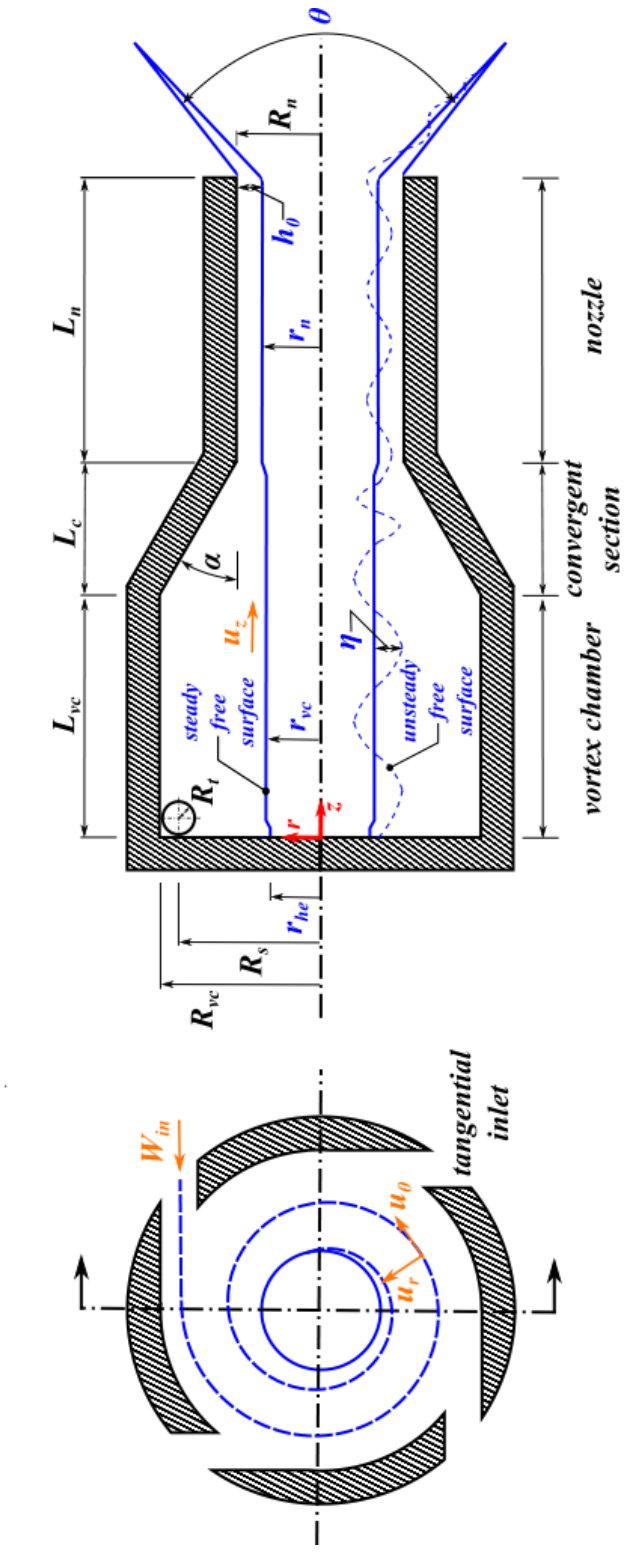

Figure 7.1: The 'classic' swirl injector geometry with steady hydraulic and unsteady hydrodynamic flow features pertinent to the linear hydrodynamics model; adapted from Ref. [101].

as chug would likely be much larger than the geometrical length scales of the injector itself, as is commonly found in the analysis of lumped acoustic elements [95]. However, for high frequency combustion instabilities and the resulting wavelengths of pressure/velocity disturbances can approach the dimensions of an injector such that the long wave approximation is no longer a viable approach.

$$\mathfrak{c}_{vc} = \bar{u}_{x,vc} + \sqrt{\frac{\bar{C}_\theta^2(\bar{R}_{vc}^2 - \bar{r}_{vc}^2)}{2\bar{r}_{vc}^4}} \tag{7.1}$$

$$\mathfrak{c}_{n} = \bar{u}_{x,n} + \sqrt{\frac{\bar{C}_\theta^2(\bar{R}_{n}^2 - \bar{r}_{n}^2)}{2\bar{r}_{n}^4}} \tag{7.2}$$

Ismailov [101] discusses in great detail Bazarov's long wave approximation and highlights its implications to the model. As an alternative, Ismailov proposes the implementation of the classic Kelvin dispersion relation [105] in computing celerities valid not just in the low frequency limit, but across the entire spectrum of disturbance frequency, and demonstrates its effectiveness. The Kelvin dispersion formula is given by Equation 7.3 in generic variables where both the zeroth- and first-order Bessel and modified Bessel functions are exercised.

$$\frac{\omega}{k} = \bar{u}_x \pm \sqrt{\frac{C_\theta^2}{kr^3}\frac{-I_1(kr) + \frac{I_1(kR)J_1(kr)}{J_1(kR)}}{I_0(kr) + \frac{I_1(kR)J_0(kr)}{J_1(kR)}}} \tag{7.3}$$

A graphical solution approach to the dispersion relation is described by Ismailov, where Equation 7.3 is formulated as a set of three functions Equation 7.4 - Equation 7.6. These formulae are cast in forms relevant to the swirling liquid film

flow by incorporating appropriate swirl injector parameters.

$$g_{1,vc} = \omega^* - k\bar{u}_{x,vc} \tag{7.4}$$

$$g_{2,vc} = +\sqrt{\frac{\bar{C}_\theta^2}{k\bar{r}_{vc}^3}\frac{-I_1(k\bar{r}_{vc}) + \frac{I_1(k\bar{R}_{vc})J_1(k\bar{r}_{vc})}{J_1(k\bar{R}_{vc})}}{I_0(k\bar{r}_{vc}) + \frac{I_1(k\bar{R}_{vc})J_0(k\bar{r}_{vc})}{J_1(k\bar{R}_{vc})}}} \tag{7.5}$$

$$g_{3,vc} = -\sqrt{\frac{\bar{C}_\theta^2}{k\bar{r}_{vc}^3}\frac{-I_1(k\bar{r}_{vc}) + \frac{I_1(k\bar{R}_{vc})J_1(k\bar{r}_{vc})}{J_1(k\bar{R}_{vc})}}{I_0(k\bar{r}_{vc}) + \frac{I_1(k\bar{R}_{vc})J_0(k\bar{r}_{vc})}{J_1(k\bar{R}_{vc})}}} \tag{7.6}$$

The graphical solution to the dispersion formulae is demonstrated in obtaining frequency-dependent wavenumbers within the vortex chamber region as seen by example in Figure 7.2. The intersections of the linear function $g_{1,vc}$ with $g_{2,vc}$ reveal similar but not identical wavenumbers that represent waves both in the downstream (+) and upstream (-) directions. Non-dimensional wave speed is then computed by the relation $\mathfrak{c}_{vc} = \omega^*/k$. Note the higher negative slope of $g_{1,vc}$—at some elevated frequency from the example, $g_{1,vc}$ will take on a slope so aggressive that it will no longer intersect with $g_{2,vc}$. At such a frequency, backward travelling disturbances will have decreased to an equivalent speed with the bulk axial flow in the downstream direction. This is the physical condition at which the backward travelling disturbances can no longer propagate upstream.

Wave speed in the nozzle region of the injector can be computed in a similar manner, wherein Equation 7.7 through Equation 7.9 express the Kelvin dispersion expression as a set of formulae applicable to the swirling liquid film flow within the

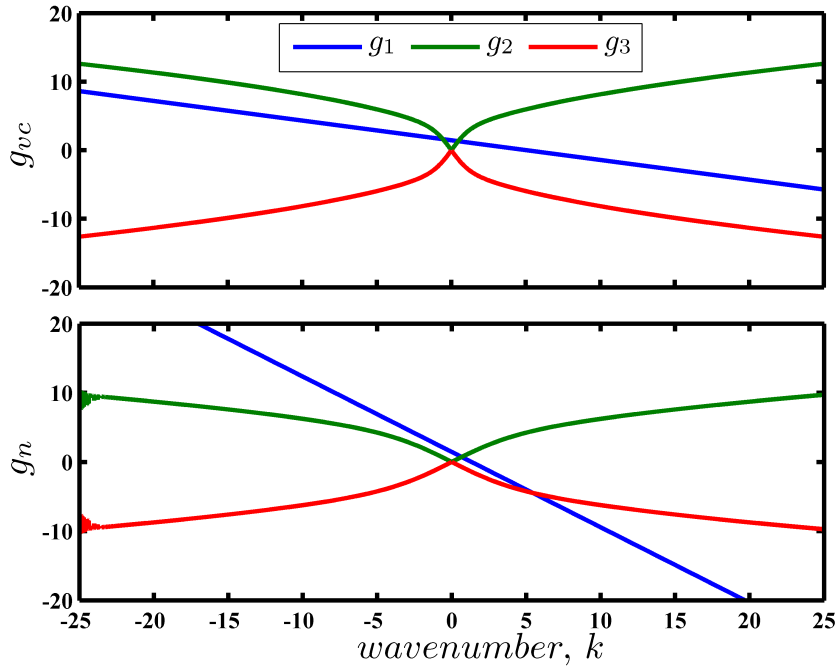

Figure 7.2: Graphical solutions of the Kelvin wave dispersion relation for (top) the vortex chamber and (bottom) the nozzle section of the swirl injector; intersections with $g_{1,vc}$ indicate wavenumber solutions in both the forward and backward directions.

injector nozzle.

$$g_{1,n} = \omega^* - k\bar{u}_{x,n} \tag{7.7}$$

$$g_{2,n} = +\sqrt{\frac{\bar{C}_\theta^2}{k\bar{r}_n^3}\frac{-I_1(k\bar{r}_n) + \frac{I_1(k\bar{R}_n)J_1(k\bar{r}_n)}{J_1(k\bar{R}_n)}}{I_0(k\bar{r}_n) + \frac{I_1(k\bar{R}_n)J_0(k\bar{r}_n)}{J_1(k\bar{R}_n)}}} \tag{7.8}$$

$$g_{3,n} = -\sqrt{\frac{\bar{C}_\theta^2}{k\bar{r}_n^3}\frac{-I_1(k\bar{r}_n) + \frac{I_1(k\bar{R}_n)J_1(k\bar{r}_n)}{J_1(k\bar{R}_n)}}{I_0(k\bar{r}_n) + \frac{I_1(k\bar{R}_n)J_0(k\bar{r}_n)}{J_1(k\bar{R}_n)}}} \tag{7.9}$$

Again, based on the same non-dimensional parameters evaluated for the vortex chamber, frequency-dependent wavenumbers in the nozzle region are assessed by graphical means in Figure 7.2. Here, $g_{1,n}$ intersects once with both $g_{2,n}$ and $g_{3,n}$, such that only positive wave numbers indicating strict propagation in the down-

stream direction are intuitively resolved. However, the wavenumber corresponding to intersection with $g_{3,n}$ is interpreted to indicate disturbances prone to be swept away by current in the downstream direction [101]. This dispersion solution is thus non-physical and considered irrelevant.

7.1.2 Vortex Chamber Surface Wave Interactions

The treatment of surface wave interactions in the vortex chamber is carried out by linear superposition of an "infinite" series of decaying wave reflections. These wave motions transpire between boundaries at the upstream wall of the vortex chamber and at the downstream geometric contraction near the nozzle entrance. The idealized vortex chamber geometry on which the surface wave dynamics are modelled is illustrated in Figure 7.3—a geometry reminiscent of idealized ocean harbor wave models [106] from which Bazarov draws analogy. This geometry is contrasted with the actual geometry of the vortex chamber in the test article of this study. As such, three aspects of the wave reflection superposition calculations that must be closely considered include: the underlying assumptions of wave speed, the underlying assumptions of the geometry, and the underlying assumptions of wave damping.

The consideration is the manifestation of wave speed. Bazarov's original calculations assume the long wave approximation. Furthermore, it is assumed that reflected waves travelling in the upstream direction propagate at the same speed as those in the downstream direction. As seen in the Kelvin dispersion solutions, downstream and upstream waves may not propagate at identical rates and should be addressed. Ismailov provides formulations of the infinite series at both upstream and

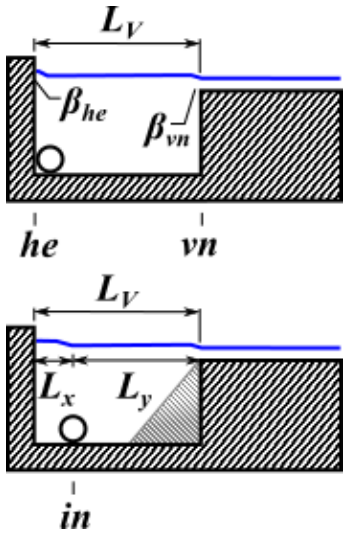

Figure 7.3: Schematic illustrating the idealized vortex chamber applicable to Bazarov's orginal formulation and the actual vortex chamber geometry considered here.

downstream locations that accounts not only for frequency-dependent phase lags, but also the directional-dependency of their values.

The infinite series also assumes two locations of surface wave perturbation in the vortex chamber. This assumption is related to the geometry of the idealized injector, wherein the tangential inlets are located directly adjacent to the upstream wall of the vortex chamber. However, if the tangential inlets are positioned at L_x from the upstream wall, then additional locations of surface wave perturbation must be included. This aspect was analytically addressed by Richardson [100], who sought to capture such effects when *multiple* rows of tangential inlets were placed within the vortex chamber. The geometry of the test article presented in the current study must be addressed in order to develop a tractable model of surface wave reflections.

What follows is a description of surface wave reflection processes which accounts for directional-dependency of surface wave propagation speed and leads to an algorithm used to model the linear superposition of surface waves in the vortex chamber applicable to the test article used in this study. Phase delay, ϕ, is defined here as $\phi_d = \omega^* L/c_d$ in the downstream direction and $\phi_d = \omega^* L/c_u$ in the upstream direction, where c_u is a negative value by Kelvin wave solution making the upstream delay term positive [101]. Also, regardless of direction, the viscous exponential term only decays wave amplitudes [12].

Consider an initial perturbation of the liquid film surface which occurs at position "in" (from Figure 7.3) located at the centerline of the tangential inlets—given by the expression for amplitude, $\eta_{t0} = \hat{\eta} e^{i\omega^* t}$. Upon traversing an axial distance "x" in reaching the posterior wall of the vortex chamber, "he", upstream and traversing an axial distance "y" to the position of nozzle interface downstream, "vn", disturbance amplitude is expressed, respectively, as:

$$\begin{aligned} \eta_{he0} &= \frac{1}{2}\hat{\eta} e^{i(\omega^* t + \phi_{x,u}) - \nu\phi_{x,u}} \\ \eta_{vn0} &= \frac{1}{2}\hat{\eta} e^{i(\omega^* t - \phi_{y,d}) - \nu\phi_{y,d}}. \end{aligned} \tag{7.10}$$

Reflection of the disturbance occurs, resulting in a new amplitude at location "in" expressed as a summation of forward and backward propagating disturbances such that:

$$\eta_{in1} = \frac{1}{2}\hat{\eta}\beta_{he} e^{i(\omega^* t + \phi_{x,u} - \phi_{x,d}) - \nu(\phi_{x,u} + \phi_{x,d})} + \frac{1}{2}\hat{\eta}\beta_{vn} e^{i(\omega^* t - \phi_{y,d} + \phi_{y,u}) - \nu(\phi_{y,d} + \phi_{y,u})}. \tag{7.11}$$

It is assumed no surface wave impedance occurs across location "in". Thus, the initially reflected waves continue to traverse the entire length of the vortex chamber where $L_v = L_x + L_y$, such that their upstream and downstream phase shifts can also be summed. Upon reaching "he" and "vn", amplitude now becomes:

$$\begin{aligned} \eta_{he1} &= \frac{1}{2}\hat{\eta}\beta_{vn}e^{i(\omega^* t - \phi_{y,d} + \phi_{v,u}) - \nu(\phi_{y,d} + \phi_{v,u})} \\ \eta_{vn1} &= \frac{1}{2}\hat{\eta}\beta_{he}e^{i(\omega^* t + \phi_{x,u} - \phi_{v,d}) - \nu(\phi_{x,u} + \phi_{v,d})}. \end{aligned} \tag{7.12}$$

Reflections at and propagations from the boundaries occur once again that result in amplitude at location "in" given by, and simplified to:

$$\begin{aligned} \eta_{in2} = \frac{1}{2}\hat{\eta}\beta_{vn}\beta_{he}e^{i(\omega^* t - \phi_{y,d} + \phi_{v,u} - \phi_{x,d}) - \nu(\phi_{y,d} + \phi_{v,u} + \phi_{x,d})} + ... \\ \frac{1}{2}\hat{\eta}\beta_{he}\beta_{vn}e^{i(\omega^* t + \phi_{x,u} - \phi_{v,d} + \phi_{y,u}) - \nu(\phi_{x,u} + \phi_{v,d} + \phi_{y,u})} \\ = \hat{\eta}\beta_{vn}\beta_{he}e^{i(\omega^* t + \phi_{v,u} - \phi_{v,d}) - \nu(\phi_{v,u} + \phi_{v,d})} + ... \\ ... + \hat{\eta}\beta_{he}\beta_{vn}e^{i(\omega^* t - \phi_{v,d} + \phi_{v,u}) - \nu(\phi_{v,d} + \phi_{v,u})}. \end{aligned} \tag{7.13}$$

Amplitude at the boundaries is now described by:

$$\begin{aligned} \eta_{he2} &= \frac{1}{2}\hat{\eta}\beta_{he}\beta_{vn}e^{i(\omega^* t + \phi_{v,u} - \phi_{v,d} + \phi_{x,u}) - \nu(\phi_{v,u} + \phi_{v,d} + \phi_{x,u})} \\ \eta_{vn2} &= \frac{1}{2}\hat{\eta}\beta_{vn}\beta_{he}e^{i(\omega^* t - \phi_{v,d} + \phi_{v,u} - \phi_{y,d}) - \nu(\phi_{v,d} + \phi_{v,u} + \phi_{y,d})}. \end{aligned} \tag{7.14}$$

A third cycle of propagations occurs, wherein surface wave amplitudes at all three locations are expressed by:

$$\begin{aligned}\eta_{in3} = \frac{1}{2}\hat{\eta}\beta_{he}^2\beta_{vn}e^{i(\omega^* t+\phi_{v,u}-\phi_{v,d}+\phi_{x,u}-\phi_{x,d})-\nu(\phi_{v,u}+\phi_{v,d}+\phi_{x,u}+\phi_{x,d})} + ... \\ ... + \frac{1}{2}\hat{\eta}\beta_{vn}^2\beta_{he}e^{i(\omega^* t-\phi_{v,d}+\phi_{v,u}-\phi_{y,d}+\phi_{y,u})-\nu(\phi_{v,d}+\phi_{v,u}+\phi_{y,d}+\phi_{y,u})} \\ \eta_{he3} = \frac{1}{2}\hat{\eta}\beta_{vn}^2\beta_{he}e^{i(\omega^* t-\phi_{v,d}+2\phi_{v,u}-\phi_{y,d})-\nu(\phi_{v,d}+2\phi_{v,u}+\phi_{y,d})} \\ \eta_{vn3} = \frac{1}{2}\hat{\eta}\beta_{he}^2\beta_{vn}e^{i(\omega^* t+\phi_{v,u}-2\phi_{v,d}+\phi_{x,u})-\nu(\phi_{v,u}+2\phi_{v,d}+\phi_{x,u})}.\end{aligned} \tag{7.15}$$

These patterns repeat themselves *ad infinitum* within the vortex chamber, where continual reflection and surface wave dissipation occurs with every cycle. This linear superposition of surface wave amplitude can be approximated by infinite summations of $\eta = \hat{\eta}\sum_{n=0}^{\infty}\eta_n$ given the following relations.

$$\begin{aligned}\eta_{he,n} = \frac{1}{2}\beta_{he}^{n/2}\beta_{vn}^{n/2}e^{i(\omega^* t+\phi_{x,u}+(n/2)(\phi_{v,u}-\phi_{v,d}))-\nu(\phi_{v,u}+(n/2)(\phi_{v,u}+\phi_{v,d})} \\ \eta_{vn,n} = \frac{1}{2}\beta_{vn}^{n/2}\beta_{he}^{n/2}e^{i(\omega^* t-\phi_{y,d}+(n/2)(\phi_{v,u}-\phi_{v,d}))-\nu(\phi_{y,d}+(n/2)(\phi_{v,u}+\phi_{v,d})} \\ \eta_{in,n} = \beta_{vn}^{n/2}\beta_{he}^{n/2}e^{i(\omega^* t+(n/2)(\phi_{v,u}-\phi_{v,d}))-\nu(n/2)(\phi_{v,u}+\phi_{v,d})} \\ for\ \ n = 0, 2, 4, ...\end{aligned} \tag{7.16}$$

$$\eta_{he,n} = \frac{1}{2}\beta_{vn}^{(n/2+1/2)}\beta_{he}^{(n/2-1/2)}e^{i(\omega^* t-\phi_{y,d}+(n/2+1/2)\phi_{v,u}-(n/2-1/2)\phi_{v,d}))-\nu(\phi_{y,d}+(n/2+1/2)\phi_{v,u}+(n/2-1/2)\phi_{v,d})}$$

$$\eta_{vn,n} = \frac{1}{2}\beta_{he}^{(n/2+1/2)}\beta_{vn}^{(n/2-1/2)}e^{i(\omega^* t+\phi_{x,u}-(n/2+1/2)\phi_{v,d}+(n/2-1/2)\phi_{v,u}))-\nu(\phi_{x,u}+(n/2+1/2)\phi_{v,d}+(n/2-1/2)\phi_{v,u})} \tag{7.17}$$

$$\eta_{in,n} = \frac{1}{2}\beta_{he}^{(n/2+1/2)}\beta_{vn}^{(n/2-1/2)}e^{i(\omega^* t+\phi_{x,u}-\phi_{x,d}+(n/2-1/2)(\phi_{v,u}-\phi_{v,d}))-\nu(\phi_{x,u}+\phi_{x,d}+(n/2-1/2)(\phi_{v,d}+\phi_{v,u}))} + ...$$

$$... + \frac{1}{2}\beta_{vn}^{(n/2+1/2)}\beta_{he}^{(n/2-1/2)}e^{i(\omega^* t+\phi_{y,u}-\phi_{y,d}+(n/2-1/2)(\phi_{v,u}-\phi_{v,d}))-\nu(\phi_{y,u}+\phi_{y,d}+(n/2-1/2)(\phi_{v,d}+\phi_{v,u}))}$$

$$for \;\; n = 1, 3, 5...$$

The idealized geometry of the vortex chamber and its implications for the degree at which surface waves reflect at the boundaries is examined next. Bazarov captures this aspect in the reflection coefficient term, β, defined with respect to injector geometry and hydraulic parameters—given by the expression:

$$\beta = 1 - \frac{2\sqrt{\psi}}{\sqrt{R_{vc}^2 - \mathfrak{a}}} \tag{7.18}$$

By inspection, β is a scalar with extrema at one and zero, each representing conditions of perfect and zero wave reflection, respectively. The term $2\sqrt{\psi}/\sqrt{R_{vc}^2 - \mathfrak{a}}$ is equivalent to the ratio of volumetric flow fluctuation in the nozzle to that in the vortex chamber with respect to the idealized geometry [66]. This same assumption is applied to the analytical model here; however, real effects of contraction angle and resulting flow acceleration, wave refraction, etc., are 1.) not well understood, and 2.) are not considered in Bazarov's estimation of the reflection coefficient by Equation 7.18. In fact, based primarily on the insufficiency of the reflection coefficient term, other research [101] abandons Bazarov's linear calculation framework in favor of alternative methods. It is clear that this assumption ought to be addressed in context to the geometric features associated with the test article of this current study. In the case of little or no vortex chamber-to-nozzle contraction, β_{vn} at the downstream boundary should take on a value approaching zero [100]. Additionally, surface waves impacting the posterior wall of the vortex chamber are likely to experience strong reflections where β_{he} is reasoned to take on values approaching one. The reflection

coefficient continues to be assumed independent of frequency—lacking any tractable fashion in which to address the matter.

Finally, consider aspects of surface wave damping captured in the superposition calculations. Attenuation of wave amplitude is accounted for through prescription of an artificial damping parameter dubbed the *artificial viscosity* coefficient, ν. This damping term is used to account for fluid viscous effects, but might also constitute a composite damping parameter that incorporates other effects such as loss of energy to acoustic processes in the gaseous vortex core. Little guidance is available on appropriate selectionof ν, and the mechanisms of energy loss is not well discussed in the literature. Frequency and amplitude dependencies of damping is also not considered.

7.1.3 Analytic Injector Transfer Function

In Bazarov's treament, the vortex chamber transfer functions are evaluated at the head end and nozzle interface location based on the surface wave amplitudes resolved by the linear superposition model. The analytic expressions for these transfer functions are given by the expressions:

$$\begin{aligned} \Pi_{vn} &= \hat{\eta} \sum_{n=0}^{\infty} \eta_{vn,n} \\ \Pi_{he} &= \hat{\eta} \sum_{n=0}^{\infty} \eta_{he,n} \end{aligned} \tag{7.19}$$

These transfer functions are critical components of the overall analytic transfer function of the swirl injector, typically defined as:

$$\Pi_{inj} = (\frac{R_{vc}}{r_{he}})^2 \frac{\Pi_t \Pi_{vn} \Pi_n}{2\Pi_t(\Pi_{he} + \Pi_\theta) + 1}, \tag{7.20}$$

where Π_t is the transfer function of plane waves through the tangential inlets, Π_n is the transfer function of surface waves within the nozzle, and Π_θ represents the transfer function of vorticity waves within the vortex chamber. These individual transfer functions are implemented and estimated in this work by the same manner as described in detail elsewhere [101].

However, the surface wave response functions derived in the previous section are implemented within the overall injector transfer function in a slightly different manner. Here a modified version that includes surface wave response functions evaluated near the generalized axial location of the tangential inlets, "in", rather than that at the vortex chamber head end is now defined.

$$\Pi_{inj} = (\frac{R_{vc}}{r_{he}})^2 \frac{\Pi_t \Pi_{vn} \Pi_n}{2\Pi_t(\Pi_{in} + \Pi_\theta) + 1}, \tag{7.21}$$

This modified form is necessary to remain consistent with descriptions of mass flow and pressure relations given in Chapter 1 upon which the response function analysis is built. Notice that the fluid radius at the head end term, r_{he}, is retained in this modified transfer function. This is done so with the following reasoning. The fluid radius at the head end is defined by a steady circumferential velocity component which

is maximum and a steady axial component which is zero. At location "in", the fluid radius is similar to that at the head end, where steady circumferential velocity is at its maximum. Here, the flow is purely circumferential and this particular component of velocity dominates the axial component. This is supported by observations by Kim et al. [72], where direct imagery indicates that the fluid radius both at location "in" and at the posterior wall are virtually identical.

7.2 Evaluation and Comparison of Models

A MATLAB analysis script inspired by that created by Ismailov [101] was generated to employ Bazarov's linear dynamic model augmented with modifications to wave celerity and vortex chamber reflection activity described in the previous section. The script, *intersections.m*[Schwarz], was used to estimate intersections of the Kelvin wave formulas therein used to identify appropriate wavenumbers for the Kelvin waves. Here, the linear hydrodynamic model is constructed such that three empirical input parameters are required to define the injector hydraulics—$\bar{\dot{m}}_l$, μ_l, and $\bar{\rho}_l$—following the semi-empirical scaling calculations discussed in Appendix C. The model requires three user-defined input parameters—f, ν and β_{vn}—to be stipulated. Injector dimensions are also required. These calculations are carried out in non-dimensional form.

Here, three linear hydrodynamics models are evaluated for an example case where $\bar{\dot{m}}_l = 0.52\ g/s$, $\nu = 0.05$ and $\beta_{vn} = 0.1$ are assumed (sensitivities to these parameters will be explored shortly). Response models are evaluated from 25-5000 Hz with a 25 Hz resolution. The flow conditions under which the linear response

functions will first be evaluated at are given in Table 7.1 along with non-dimensional geometric parameters of the swirl injector provided in Table 7.2. The objective is to draw first order comparisons between the results of prior models and that which incorporates the modifications discussed in this section.

Table 7.1: Model Flow Conditions for Example Case

$\bar{\dot{m}}_l$	$\bar{\rho}_l$	μ_l
(g/s)	(kg/m^3)	(Pa-s)
52	997.9	0.001

Table 7.2: Injector Geometric Parameters in Non-dimensional Form

Parameter	Value
R_t	0.27
L_t	1.07
N_t	4.00
R_{vc}	1.47
L_{vc}	2.21
R_s	1.20
L_c	0.81
R_n	1.00
L_n	21.05

Figure 7.4 compares wave speed estimates in the vortex chamber of the study injector at the example flow conditions. First, recall that Bazarov's original formulation implements the long wave approximation for wave speeds, while in Ismailov's treatment and also that proposed here, dispersive calculations are carried out. The primary observation in Figure 7.4 is that the long wave approximated speed is comparable only at low frequencies, where significant divergence arises at frequencies greater

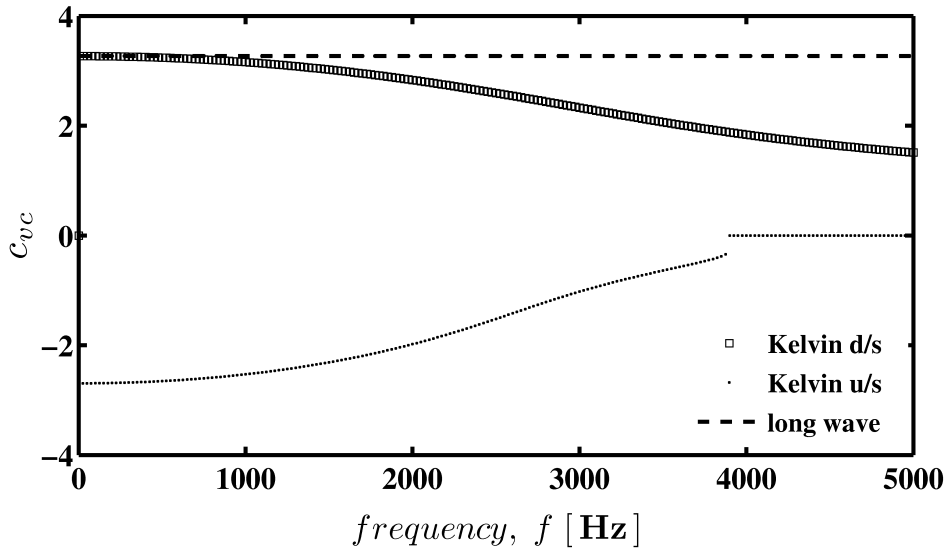

Figure 7.4: Non-dimensional wave speed in the vortex chamber of the study injector at the $\bar{\dot{m}}_l$=52 g/s condition, where the long wave approximation is compared with dispersive calculations.

than ≈500 Hz. This is intuitive and entirely consistent with the derived equivalence given in Ref. [101]. The divergence effectively highlights the known shortcoming of the long wave approximated speed for high frequency disturbances, and demonstrates the marked improvement that the Kelvin dispersion offers the the linear hydrodynamics model. Also noted, as discussed earlier, are conditions at which u/s travelling disturbances can no longer propagate.

It now becomes important to assess and compare how these different wave speeds—and their pursuant phase delays—manifest in the overall injector response function. Figure 7.5 overlays total injector response function magnitude calculated by classical formulation compared with slightly alternate analytical treatments. Recall that the classical model assumes inlets located directly adjacent to the posterior wall

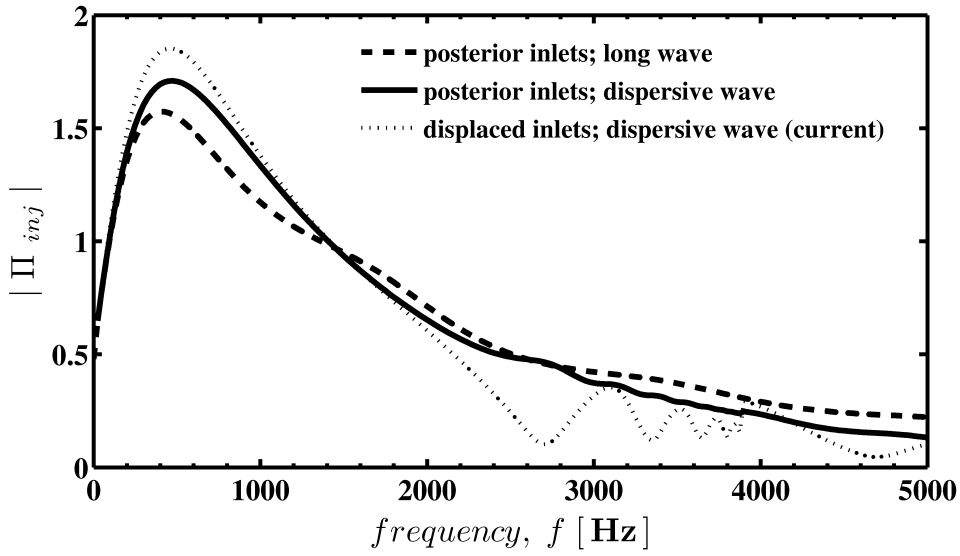

Figure 7.5: Comparison of overall injector magnitude response functions evaluated with various analytical treatments at the example condition.

of the vortex chamber such that in the analytic response function Equation 7.21, $\Pi_t = \Pi_{he}$. Under this same assumption, injector response magnitude is also plotted while incorporating dispersive wave speeds following Ismailov's treatment [101]. Finally, injector response magnitude is evaluated by modifications proposed earlier—that is by incorporating both dispersive wave speeds *and* the surface wave model with inlets displaced from the posterior wall of the vortex chamber.

Each evaluation resolves similarly elevated response magnitude at frequencies below 1000 Hz. At higher frequencies, evaluation by the original surface wave formulation with the long wave approximation shows broad-banded response characteristics, where similar calculations using dispersive wave speeds reveal increased detail in response magnitude. Notice the effect of the dispersive wave speeds. The response function using these calculations assuming inlets at the posterior wall exhibits

several common frequency responses as those seen in the current model. However, these particular calculated responses have more pronounced peaks with the modified vortex chamber model given by this present work.

7.3 Parameter Sensitivities

The two most significant parameters noted to influence the computed hydrodynamic response of swirl injectors are 1.) the vortex chamber-nozzle reflection coefficient β_{vn}, and 2.) the artificial viscosity parameter ν. Here, these parameters are varied to deduce values which are appropriately suited for the test article and conditions in the study. The following will detail response function sensitivity to variations in these parameters at the example flow conditions stated earlier.

Consider the relatively shallow angle at which the vortex chamber transitions to the nozzle. Here, Bazarov's expression for β is avoided in favor of a heuristic sensitivity analysis of the parameter. Following, a steep angle close to 90^o would merit a correspondingly large value of β_{vn}; however as such, it seems most reasonable to begin model evaluation assuming a small value of $\beta_{vn} = 0.1$. Fixing this parameter, the effects of varied artificial viscosity will be assessed.

Figure 7.6 plots injector response evaluated with variation in the artificial viscosity parameter. Note that the wave speed of backward travelling disturbances suddenly changes near 4 kHz. At this frequency, the wave speeds in the upstream direction approximately equals that of the bulk axial, such that backward disturbances can no longer propagate [101] and become negligible to the dynamics of the injector in this particular case. Responses with high magnitudes can be see below 1000 Hz

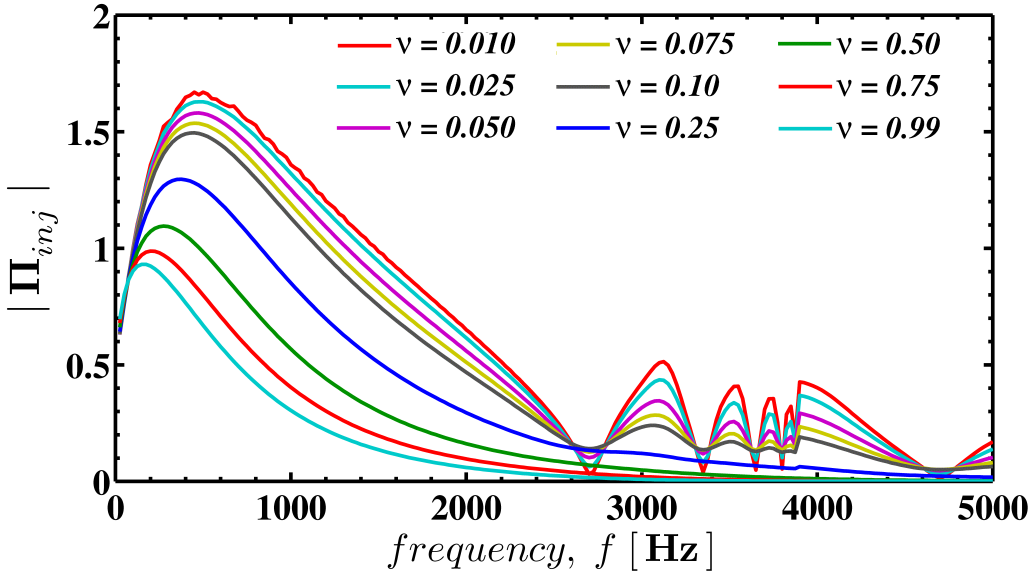

Figure 7.6: The sensitivity of injector response to variations in the artificial viscosity parameter, ν; model evaluated with fixed reflection coefficient $\beta_{vn} = 0.1$ at the $\bar{\dot{m}}_l = 52\ g/s$ condition.

regardless of variation in the artificial viscosity. Low levels of dissipation attenuate magnitude of this response by about 5% and shifts its frequency by approximately 50 Hz; the influence of artificial viscosity on this particular response becomes significant at levels exceeding 0.1. The small local response peaks located in the range of 2.5-4 kHz remain observable and essentially invariant in frequency at low-to-moderate levels of damping. However, as ν is increased to elevated levels, any significant detail in the high frequency range of the response function disappears.

From these results, an artificial viscosity of $\nu = 0.05$ seems to preserve most of the key features of the magnitude response function. This value, for practical purposes

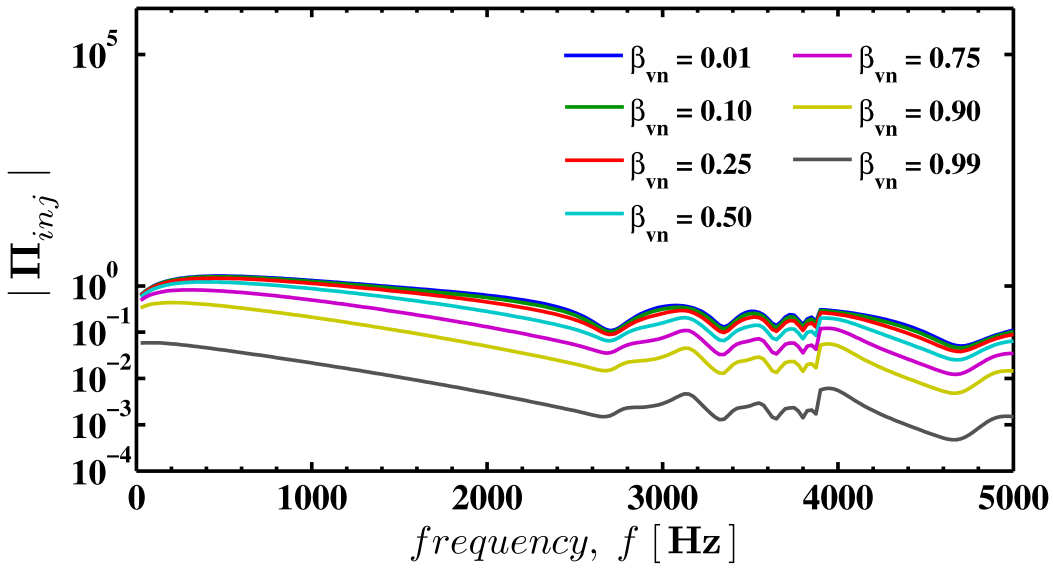

Figure 7.7: The sensitivity of injector response to variations in the reflection coefficient, β_{vn}; model evaluated with fixed artificial viscosity $\nu = 0.05$ at the $\bar{\dot{m}}_l = 52\ g/s$ condition.

of this sensitivity study, appears to be one which is qualitatively reasonable to now hold fixed and evaluate injector response by variation in the reflection coefficient.

Figure 7.7 plots injector response functions with variation in β_{vn}, and is shown in log scale for detail. Here the effect of strong reflection at the vortex chamber-nozzle interface is made apparent by accentuation of response peaks/troughs and resolution of distinct lower frequency response peaks which appear to decrease by as much as 200 Hz as reflection coefficient is increased across the range. As wave reflection levels are decreased (or, conversely, wave transmission levels are increased), the relative magnitudes of the higher frequency peaks become attenuated, but remain mostly

unchanged along the abscissa. This indicates that the frequency of these responses are relatively insensitive to changes in the reflection coefficient, and suggests that the time scales associated with these high frequency dynamics are essentially independent of the β_{vn} parameter.

Practical conclusions can be drawn for modelling of this injector and flow conditions from the results of the sensitivity analyses here. Regarding artificial viscosity, two points can be made. Firstly, since the aim of this study is to potentially deduce injector response to what amounts to a limit cycle forcing function that is minimally damped (self-pulsation), it might be reasoned that a small damping parameter on surface wave amplitude is appropriate. As such, high values of ν are eliminated from consideration. Secondly, Bazarov [12] advocates a specific value of dissipation in modelling water flows at room temperature conditions, where $\nu = 0.08$. From Figure 7.6, $\nu = 0.08$ resides within a range where seemingly significant features of response function magnitude are preserved—suggesting that this values is a an appropriate one moving forward with the hydrodynamic calculations. Of course, this value is only arrived at in an anecdotal sense. Without further more detailed study, effects of notional frequency-dependence and other mechanisms of wave energy dissipation encapsulated within the ν term remain points of research that could potentially improved assumptions about this parameter.

Conclusions on an appropriate reflection coefficient are less clear. Figure 7.7 indicates that a high reflection reveals more detail in the response magnitude of the injector than a low value. However, since reason favors a smaller reflection coefficient rather than a larger value based on geometrical arguments, there exists no qualitative

nor quantitative rationale in choosing a strong β_{vn}. Therefore, the original value of $\beta_{vn} = 0.1$ seems a logical value at which to assume for this injector, given A.) it is geometrically defensible, and B.) it preserves principal features of the response function which remain consistent with variation in reflection coefficient barring none at all.

7.4 Response Function Analysis

Having set appropriate input parameters of ν and β_{vn} the injector response model is now exercised to assess the result. The objective here is to analyze various aspects of the response function in order to gain a physical interpretation of various hydrodynamic behaviors of the study injector at example conditions in order to more confidently extend understanding of the calculations later in the study.

Figure 7.8 shows the magnitude and phase of the overall injector response function evaluated in the frequency domain. The values of $\nu = 0.08$ and $\beta_{vn} = 0.1$ are used in evaluation at the example case. Close examination of the plot reveals a sharp magnitude response which occurs near 3900 Hz. As previously noted from Figure 7.4, this is the frequency at which upstream propagating Kelvin waves lose dynamic significance, but forward propagating waves still propagate.

The phase of the response function in Figure 7.8 indicates a lag relationship between injector output and input that is typical of models developed on a transfer function basis. This behavior is common for injector admittance/impedance function-based frequency response models [17]. The phase-wrapping in the response function

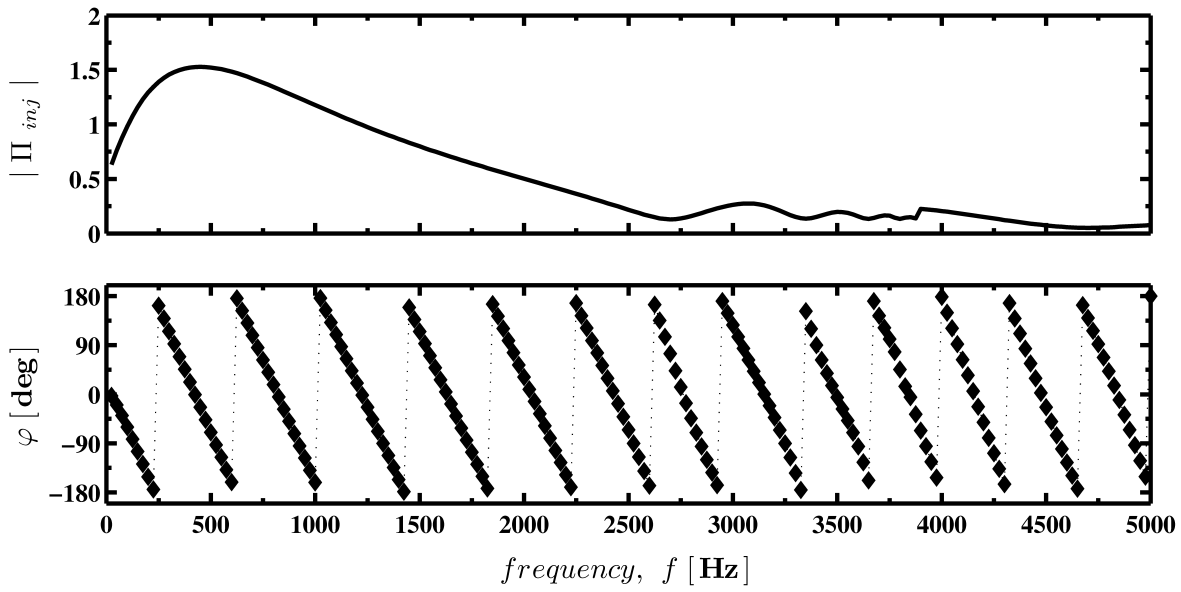

Figure 7.8: Injector Response function magnitude and phase evaluated at the $\bar{\dot{m}}_l = 52\ g/s$ condition with $\nu = 0.08$ and $\beta_{vn} = 0.1$.

is primarily due to the influence of the injector's relatively long nozzle region and will be discussed later.

Next, it becomes interesting to survey which aspects of the injector dynamics meaningfully contribute to characteristics that manifest in overall response of the injector. As such, recall that the previous section highlighted the obvious effect(s) of the modified surface wave treatment carried out in these calculations, where high frequency response characteristics were also resolved.

Figure 7.9 which plots the surface wave response functions evaluated within the vortex chamber at the tangential inlet location,"in", and nozzle interface location, "vn". The surface wave dynamics contribute directly to response features observed in the 2000-5000 Hz range of the calculated total injector response function. A distinct family of local magnitude minima and maxima can be observed in the vortex

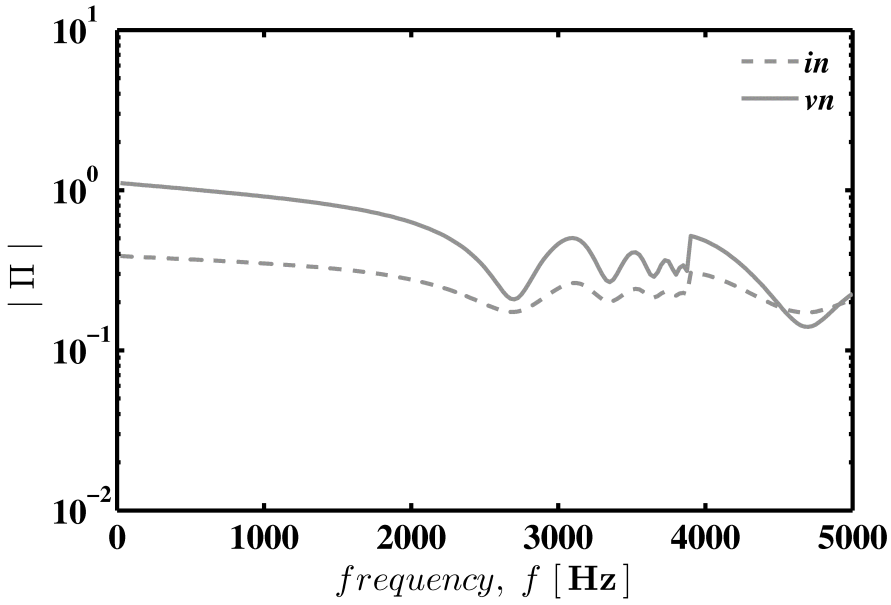

Figure 7.9: Surface wave magnitude response within the vortex chamber, evaluated at the inlet location and nozzle interface.

chamber response functions. Wavelengths associated with these frequencies can be approximated in dimensional form based on the expression $\kappa = 2\pi \mathfrak{c}_{vc} R_n/\omega^*$. As such, $\kappa \approx L_V, 2/3L_V, 1/2L_V...$ and $\kappa \approx 4/3L_V, 4/5L_V, 4/7L_V...$, respectively, where $L_V = L_{vc} + L_c$ is the characteristic length of the vortex chamber. Such scaling implies that these surface wave response peaks correspond to quarter-wave resonance patterns which are well-known to occur in the analogous ocean harbor with a narrow inlet channel [106]. For this injector, a fundamental quarter-wave response is elevated but obscure in the low frequency range, while a fundamental half-wave trough is not discernible because it's node is located close to position "in". Other responses resolved within the vortex chamber imply additional surface wave dynamics attributed to positioning of the tangential inlets. The response near 3525 Hz has a wavelength approximately equivalent to $4/3L_y$, indicating a waveform similar to a quarter-wave

pattern is present between stations "in" and "vn". Since L_x and L_y are nearly equal, it is difficult here to identify higher frequency response characteristics without increasing the frequency resolution of the calculations.

Recall how Figure 7.5 compares the response models evaluated with dispersive waves both with and without inlets displaced from the head end. When the inlets are adjacent to the head end, a local response peak near 2700 Hz can be seen, which is a half-wave pattern of the vortex chamber. However, in Figure 7.9 and subsequently Figure 7.8, a local minimum occurs near 2700 Hz. In modelling multiple rows of tangential inlet channels, Richardson [100] noted response minima to correspond with destructive interference of waves set up in the axial distance separating the inlet rows, L_x. In the same way, L_x is here defined as the distance from the posterior wall of the vortex chamber to the centerline of the tangential inlets as previously detailed. Destructive interference will occur when the wavelength of a given disturbance is exactly equal to $2L_x$—resulting in an opposite phase relationship between the locations. As such, near 2550 Hz, $\kappa \approx 2L_x = 0.0106\ m$, and effectively satisfies the $1/2\kappa$ interference criterion. This observation demonstrates that destructive interference effects created by inlets displaced from the posterior wall of the vortex chamber also serves to suppress 2700 Hz.

Overall, the magnitude of total injector response in Figure 7.8 at the example flow condition is most significant in the low frequency range; however, high frequency response peaks are consistent with spatially distributed oscillations which result from surface wave motions within the vortex chamber. The characteristic frequencies of these waves are generated by both constructive and destructive interference according

to their wave speed and the dimensions associated with the location of the tangential inlets relative to the boundaries of the vortex chamber.

Practical injector design insight related to this is discussed by Richardson [100]. The injector response characteristics may be tailored by both by modification to L_V and by positioning inlet channels with respect to injector boundaries to promote destructive interference at a frequency of interest, such as that of a say to be insensitive to coupling with a resonance of combustor eigenmode or some other external forcing function.

To demonstrate this general idea, consider the effect of a simple design modification to the injector nozzle on the overall response characteristics of the injector. For this injector, the phase characteristics of the overall response are in part attributed to surface wave dynamics that occur within the nozzle region. Polar plots of phase-amplitude presented in Figure 7.10 indicate the effect of nozzle length on overall injector response evaluated at the example flow conditions. In general, any feature of the response function located in the left-half of the polar plot is significant to the stability characteristics of the swirl injector. At the nominal length, nozzle dynamics are responsible for the numerous clockwise rotations with increasing frequency (as first noticed in Figure 7.8), where the high amplitude/low frequency responses have corresponding phase angles between $\pm 90^o$ and $\pm 270^o$. As the length of the nozzle is decreased, the number of clockwise rotations is seen to decrease, and the low frequency/high amplitude responses are noted to shift moreso toward the right-half of the plot. The shortened nozzle response functions reveal more intricate phase-amplitude patterns that emerge at higher frequencies.

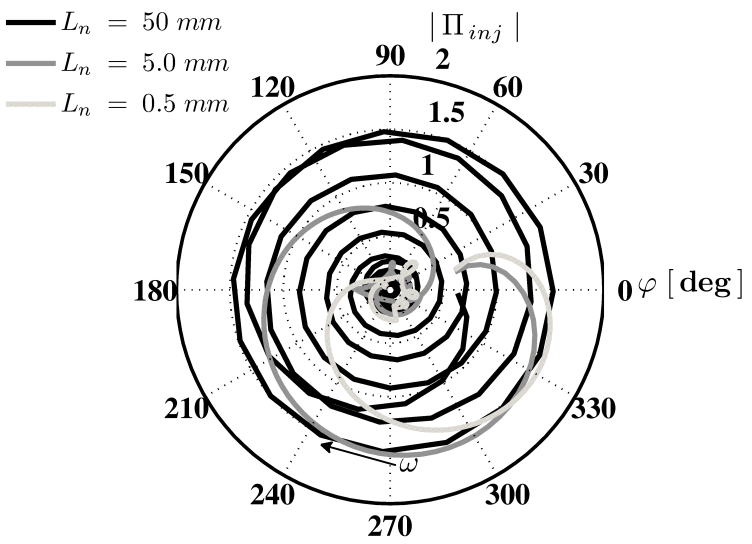

Figure 7.10: Intricate phase-amplitude characteristics of the swirl injector with simple modification to nozzle length.

7.5 Qualitative Comparisons to Test Data

The most appropriate manner in which to make comparisons to the analytical response model developed for the study injector here is to perform pulse testing at discrete frequencies. Based on a compilation of pulse test response data, an empirical response function can be obtained to make a direct quantitative comparison of injector response phase and magnitude. These types of controlled pulse test data do not exist for the study injector element treated in this study. However, measurements from the self-pulsation experiments represent injector pulsing that naturally occur. While the discrete forcing function of pressure and flow rate may not necessarily be known, response data to the pulsing during these tests can be qualitatively compared to the modeling results.

The classic linear hydrodynamics model theoretically does not account for coupled interactions between multiple fluids. Of course, in reality these interactions occur — to a limited degree — on the free surface within the injector, and — more significantly — on the spray cone at the exit of and in the near-field of the injector where continuity exists. Invariably, these types of interactions create natural perturbations to the internal hydrodynamics of the injector element. If disorganized and/or superposed with other disturbances on a variety of different spatial and temporal scales, these perturbations can be conceptualized as a type of broad-banded, random forcing function on internal injector hydrodynamics. On the other hand, if perturbations are organized to a dominant or even just a distinct scale in time, then the forcing function imposed on the injector will be more discrete.

The available test data that is most akin to the analytic hydrodynamic response function is the unsteady pressure registered in the upstream manifold of the swirl injector. Recall from Equation 1.8 that perturbational pressure is but a single component of overall injector admittance, where perturbational mass flow also contributes to the injector response function. Since unsteady mass flow measurements are not available, the measured unsteady pressure is considered to be a system response proxy that can be qualitatively compared to calculations. Note that qualitative comparisons between analytical injector response and measured response parameters other than perturbational flow rate/pressure are not unprecedented. Ismailov and Heister [41] make qualitative comparison between a computed injector response function and measured fluctuation of liquid spray cone angle.

Here, a qualitative comparison of measured system response under naturally imposed perturbations is drawn with the computed injector response magnitude in Figure 7.11. The test condition is theoretically equivalent to the modeled example case, where pressure-swirl injection of water at a steady flow rate of 52 g/s occurs into a quiescent environment of air near STP conditions. An instantaneous image from the test is provided to show how surface wave growth formed by Kelvin-Helmholtz-type instability is generated within the shear layer between the flowing liquid and the ambient environment. These waveforms — along with other types of near-field oscillations on the liquid sheet — create fluctuation in the liquid film thickness at the exit of swirl injector. These fluctuations in turn perturb liquid flow rate/pressure.

The power spectral density of unsteady pressure upstream of the injector is taken as a representation of system response to a low amplitude, broad-banded downstream forcing function that is generated by various spray dynamics that occur in the near-field of the injector. This general idea of natural spray oscillations serving as a low-amplitude, broad-banded forcing function is to a degree supported by results from analysis of pressure-swirl spray imagery given in Appendix G. The DMD spectrum highlights the nature of the spray dynamics, where a variety of highly damped behaviors over a large range of frequencies occur simultaneously.

The averaged power spectrum of unsteady pressure is taken over one second of time data collected at a rate of 50 kHz, and is computed with frequency bins near 25 Hz for appropriate comparison with the analytic hydrodynamic response magnitude function. In the frequency range below 2000 Hz, modeled response of vorticity waves within the injector element is not clearly registered in the measured unsteady pres-

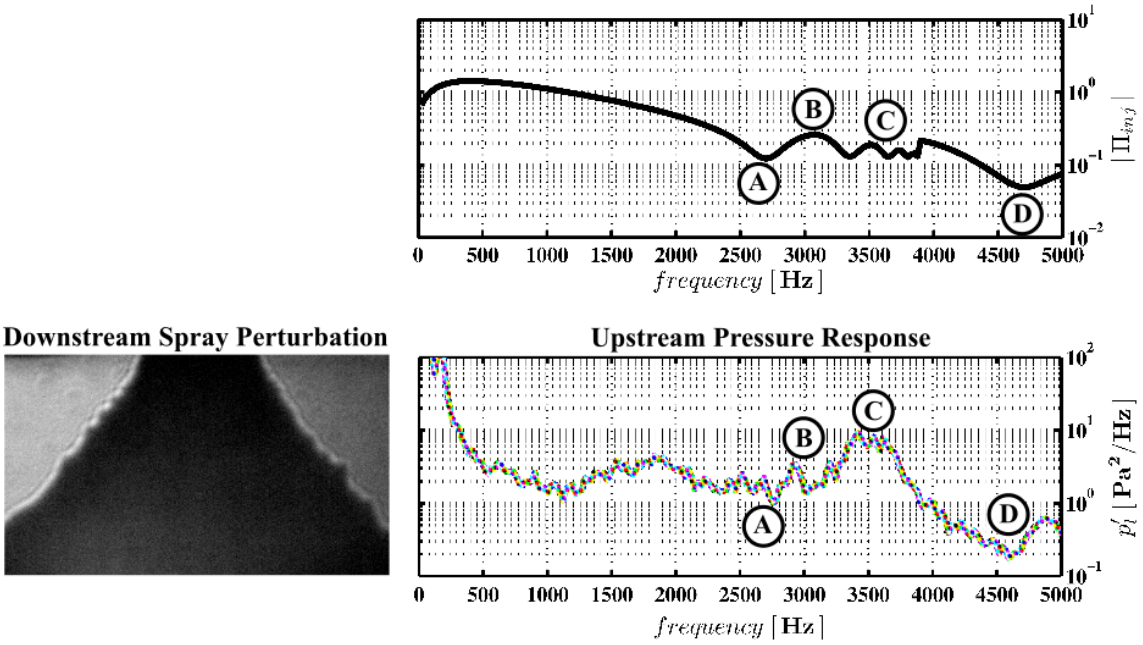

Figure 7.11: Qualitative comparison of computed injector magnitude response at 52 g/s with measured pressure fluctuation power spectral density during pressure-swirl injection where the injector experiences low amplitude broad-banded perturbation by near-field spray dynamics.

sure upstream of the injector, while a wide rolling of the spectrum between 1-2.1 kHz indicates a benign modal response likely related to the first quarter-wave eigenmode of the swirl post. However, at higher frequencies, the measured power spectrum indicates that modeled response characteristics associated with vortex chamber surface wave dynamics are detectable. Note the favorable analytical/empirical comparisons between response feature A: the local minimum near 2700 Hz, response feature B: the peak near 2900 Hz, response feature C: the peak near 3500 Hz, and response feature D: response minimum near 4700 Hz.

From results presented in Chapter 6, it has been determined that the spray tends to oscillate in a more organized manner when co-annular gas flow is provided

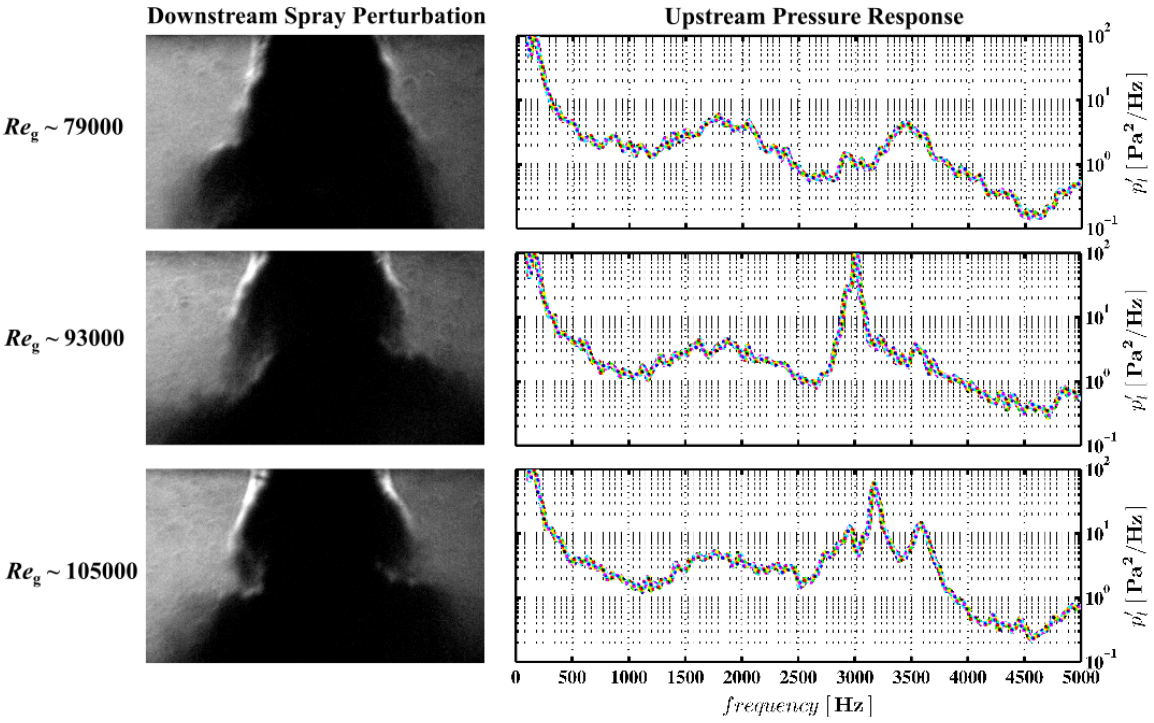

Figure 7.12: Measured pressure response at 52 g/s to perturbation generated by different types of near-field spray dynamics that occur when gas co-flow is adjusted.

along with the liquid flow. This is because near-field oscillations are exacerbated by more intense shear layer activity. It now becomes interesting to observe how the unsteady pressure of the liquid – taken as the injector response — changes when near-field spray oscillations are promoted by different levels of gas co-flow.

Measured power spectra of fluctuating pressure in the liquid manifold are shown Figure 7.12 when the swirl injector is accompanied by various degrees of gas co-flow. Again, the inner swirl post is flowing at a steady rate of 52 g/s, where each image snapshot shows the injector spray with a different steady gas injection Reynolds number. At $Re_g \approx 79000$, the non-pulsatile near-field spray dynamics create a similar pressure response as seen in the case of no gas flow ($Re_g = 0$) shown

previously in Figure 7.11 with the same type of response features. A transition to self-pulsation occurs as gas Reynolds number is increased to $Re_g \approx 93000$, where the contraction/rarefaction of the spray cone at a single dominant scale generates strongly discrete fluctuation of pressure and flow rate at the exit of the injector. The pressure response upstream of the swirl post to this behavior is clearly seen, where a discrete high amplitude peak near 3100 Hz is registered to suggest that the modeled surface wave response feature A is excited or $amplified$ in this test. An additional smaller amplitude peak can also be seen near 3600 Hz. When gas flow is increased to $Re_g \approx 105000$, the first discrete peak remains in the bandwidth of vortex chamber surface waves and shifts slightly higher in frequency than at lower flow conditions. The additional lower amplitude peak near 3600 Hz also becomes more distinct. This response also belongs to the family of vortex chamber surface waves captured by the hydrodynamics model.

The qualitative comparisons shown here of calculated response functions with measurements show several promising results. Firstly, the comparisons indicate that particular characteristics of the injector response — namely vortex chamber surface wave dynamics — are detectable in test data. These surface wave dynamic responses are seen in the pressure-swirl data, but are much more distinct when the injector experiences discrete, pulsatile spray oscillations. This suggests that the hydrodynamics model is accurate is describing the surface wave behaviors within the swirl injector, and can be used reliably as an oscillation identification tool. Secondly, it would seem from observations that the vortex chamber surface wave responses are a key component to the more complex self-pulsation phenomenon. This is established

by the existence of surface waves responses under non-pulsatile conditions and their subsequent amplification during self-pulsation that is clearly seen to occur. This type of observation is principal to the objectives of this chapter and to hypotheses of this study. The focus of this study is now progressed to understand these internal injector hydrodynamics not only at the example case presented here, but across other flow conditions at which the self-pulsation phenomenon has been experimentally observed.

7.6 Parametric Evaluation

The response function of the swirl injector is now computed for varied flow conditions. The objective is to map significant hydrodynamic characteristics of the swirl injector with the refined model established in the previous section. To facilitate this study, corresponding injector hydraulics are estimated based on the semi-empirical evaluation discussed in Chapter 1 and extended/qualified for this injector in Appendix C. Thus, swirl injector response functions are evaluated and compiled by varying steady mass flow rate from 32.0-73.0 g/s with a resolution of 1.0 g/s and 50 Hz; at each condition, liquid density and dynamic viscosity assume constant standard values of 998 kg/m^3 and 0.001 Pa-s, respectively. Model parameters ν and β_{vn} are 0.08 and 0.10, respectively.

Figure 7.13 shows swirl injector frequency response magnitude in three-dimensions — evaluated as a function of varied steady mass flow rate. At all flow conditions, injector response shows highest magnitude in the low frequency range attributed to vorticity wave contributions. Above 2000 Hz, significant response characteristics belonging to vortex chamber surface wave dynamics established in the previous sec-

tion are noted to clearly manifest within the entire parameter space that has been evaluated.

Figure 7.14 maps both the magnitude and phase of injector response, showing how various dynamic characteristics scale across injector operating conditions. Response characteristics consistent with vortex chamber surface wave dynamics as deduced in the earlier example case manifest at all flow conditions. As flow rate is increased, the general bandwidth in which these dynamics occur also increases. Frequencies which satisfy the $\kappa/2$ criterion of destructive interference between the posterior wall of the vortex chamber and the axial position of the tangential inlets are indicated by the first local minimum response band that streaks across the parameter space.

The phase of the injector response function is also mapped in Figure 7.14. Here dark blue striping immediately adjacent to dark red striping indicates phase crossover at $\pm 180^o$. At low flow conditions, the bandwidth between these crossover frequencies is tight, where the nozzle surface wave dynamics rapidly shift injector phase over numerous bandwidths across the evaluated spectrum. As flow rate is increased, these bandwidths increase and fewer crossover frequencies exist within the spectrum.

7.7 Fluid Oscillator Assessment

The parametric evaluation of swirl injector dynamics by the modified linear hydrodynamics calculations developed in this chapter has generated results valuable toward assessing fluid oscillators potentially active during measured self-pulsations. The results bring this study closer to answering principal questions outlined in this

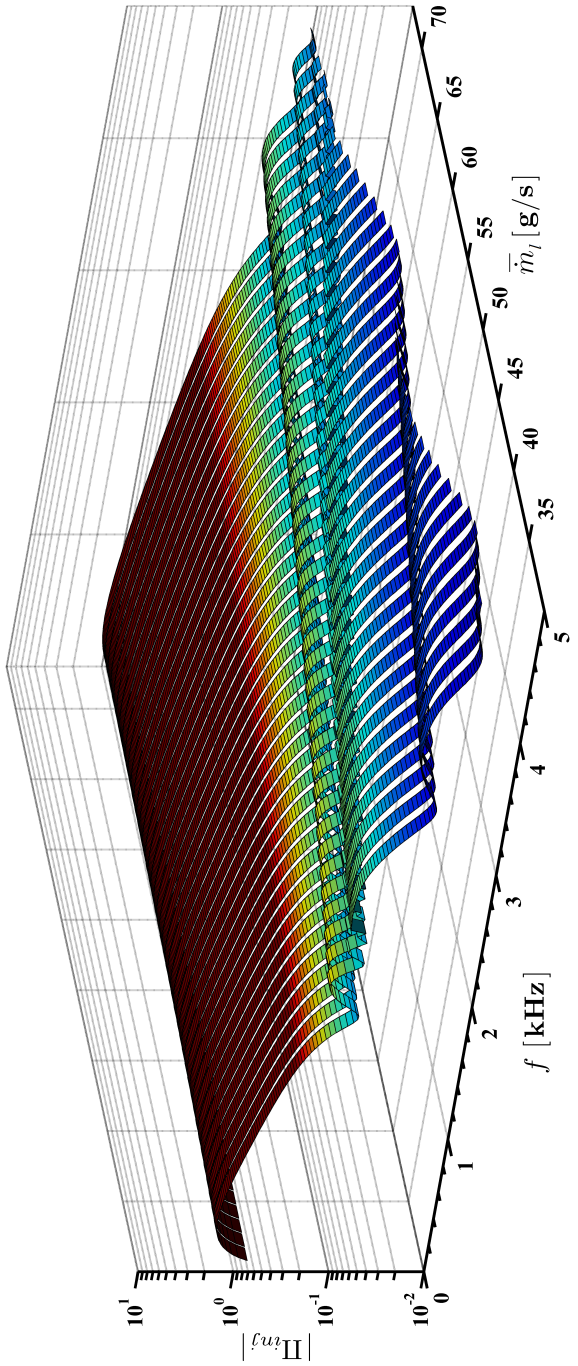

Figure 7.13: Swirl injector linear hydrodynamics model compiled across different steady flow conditions.

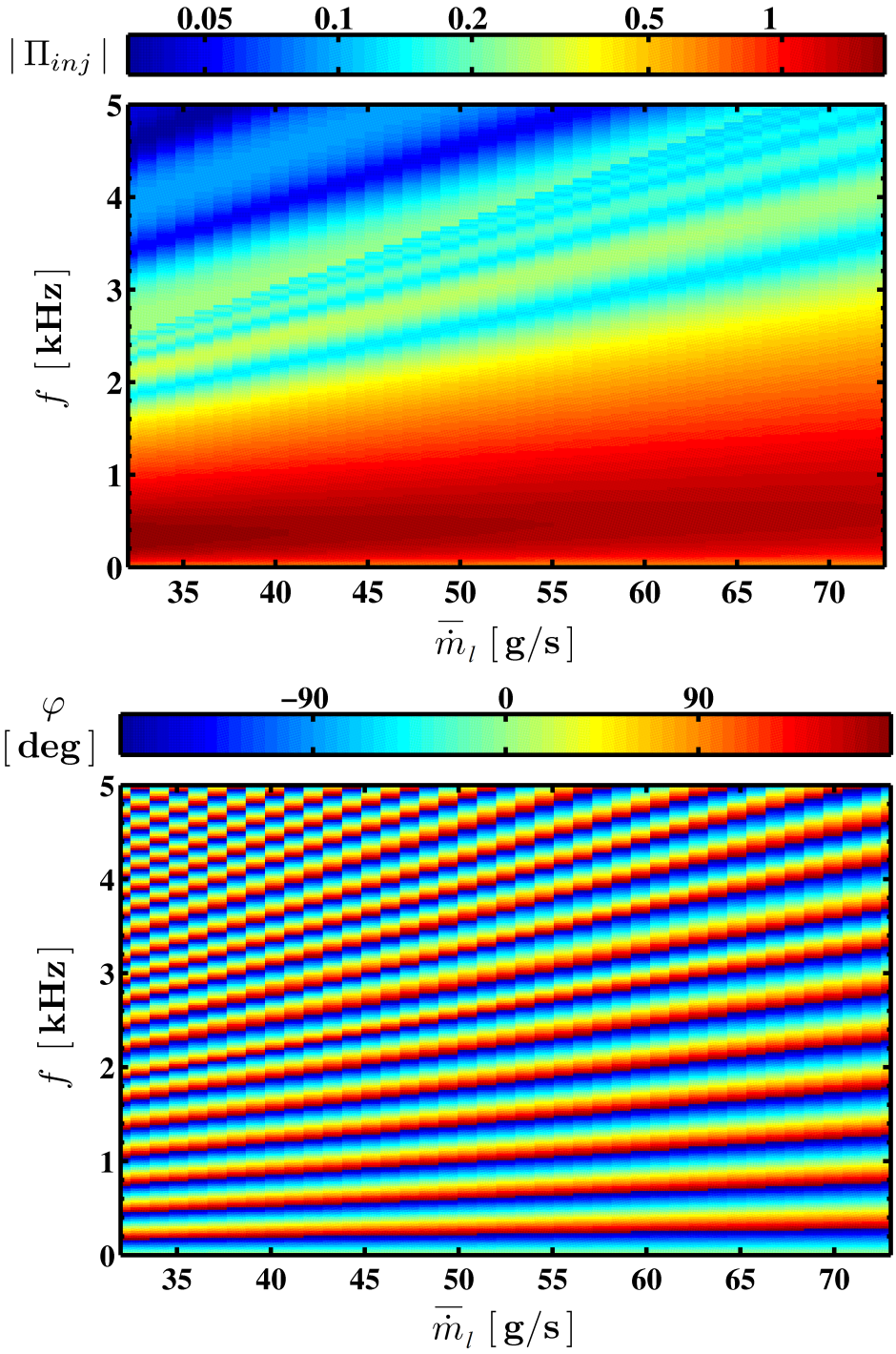

Figure 7.14: Top - swirl injector response magnitude mapped with liquid flow rate, and Bottom - swirl injector response phase mapped with liquid flow rate.

dissertation. By convention, the response calculations indicate that under certain conditions the natural surface waves within the swirl injector may have capacity to respond when disturbed and therein participate as an active fluid oscillator during the self-pulsation phenomenon. A direct comparison is made between the measured frequency of self-pulsation and where those behaviors exist within the parametrically calculated hydrodynamic response function space.

A comparison of non-recessed self-pulsation analysis and test data is now made to assess the role of swirl injector hydrodynamics in self-pulation. First, recall that frequency modulation introduced by the tested recess conditions (typically near 10% when compared for similar conditions) is considered a higher order effect when compared to the more significant observation of how self-pulsation frequency changes when liquid flow conditions are varied. The particular mechanism of frequency modulation introduced by recess, whether by Doppler or some other effect, is not explicitly determined from these data. However, measurements obtained for the non-recessed injector are not subject to modulation processes promoted by recess, and make these data best for analysis and comparison.

Figure 7.15 overlays the measured frequencies of self-pulsation from the $\Re\Re = 0.30$ injector with an interpolated map of the swirl injector hydrodynamic response magnitude. Measurements come from test conditions not confidently linked to eigenmode resonance during self-pulsation. At each liquid flow condition modelled, the measured frequencies of self-pulsation reside within the bandwidth belonging to the family of resonant vortex chamber surface wave dynamics calculated by the hydro-

dynamics model, coinciding very well in most cases. Experimental uncertainties are estimated on 95% confidence interval.

The wide green band streaking from ≈2-3.5 kHz across parameter space in Figure 7.15 is a distinct surface wave response in the vortex chamber, where the wavelength of the disturbance is approximately $4/3L_{vc}$ making it akin to a quarter-wave pattern as established earlier. It is inferred from this comparison that this response is consistently excited during self-pulsations, where different gas flow conditions only slightly shift the discrete frequency within the energy band of the resonant surface wave pattern. In some cases, it even appears that higher order surface wave resonances within the vortex chamber are excited during self-pulsation. Such behavior is consistent with classic descriptions of instability-induced oscillation dictated by fluid-resonant feedback, which tends to exhibit frequency 'lock-in' near a dominant resonant frequency of the system.

Figure 7.16 overlays measured self-pulsation frequencies with mapped phase of the parametric hydrodynamic response function. In most cases, self-pulsation is observed to occur at or near frequencies that not only correspond to surface wave dynamics in the vortex chamber, but near frequencies that are also characterized by $\pm 180^o$ phase crossover (as indicated by thin yellow lines with adjacent bands of blue and red). The frequencies at which the majority of self-pulsation test cases occur are separated in phase by only $\pm 50^o$ (or less if experimental uncertainties are considered) from the response frequencies at phase crossover.

Such responses are located in the left-half of the complex plane and are important to the stability characteristics of the injector [66] when exposed to negative

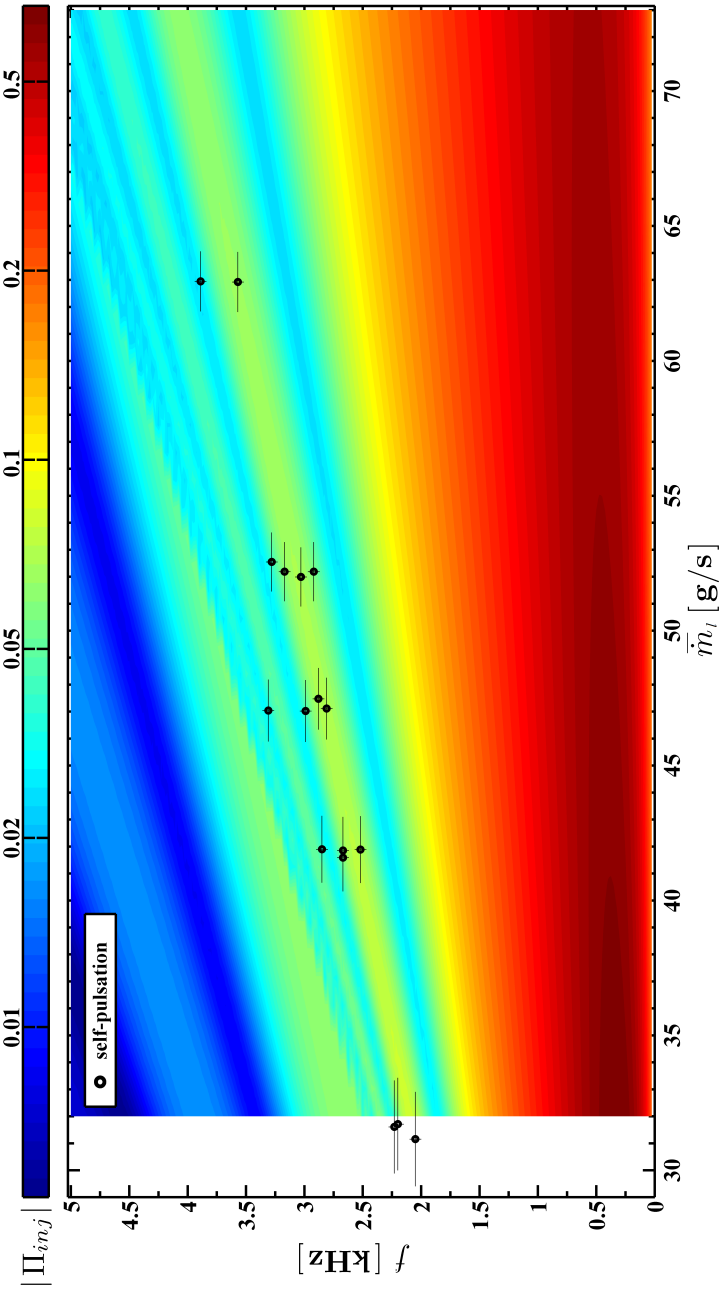

Figure 7.15: Measured frequency of self-pulsation for the non-recessed element overlaid with magnitude of swirl injector response function.

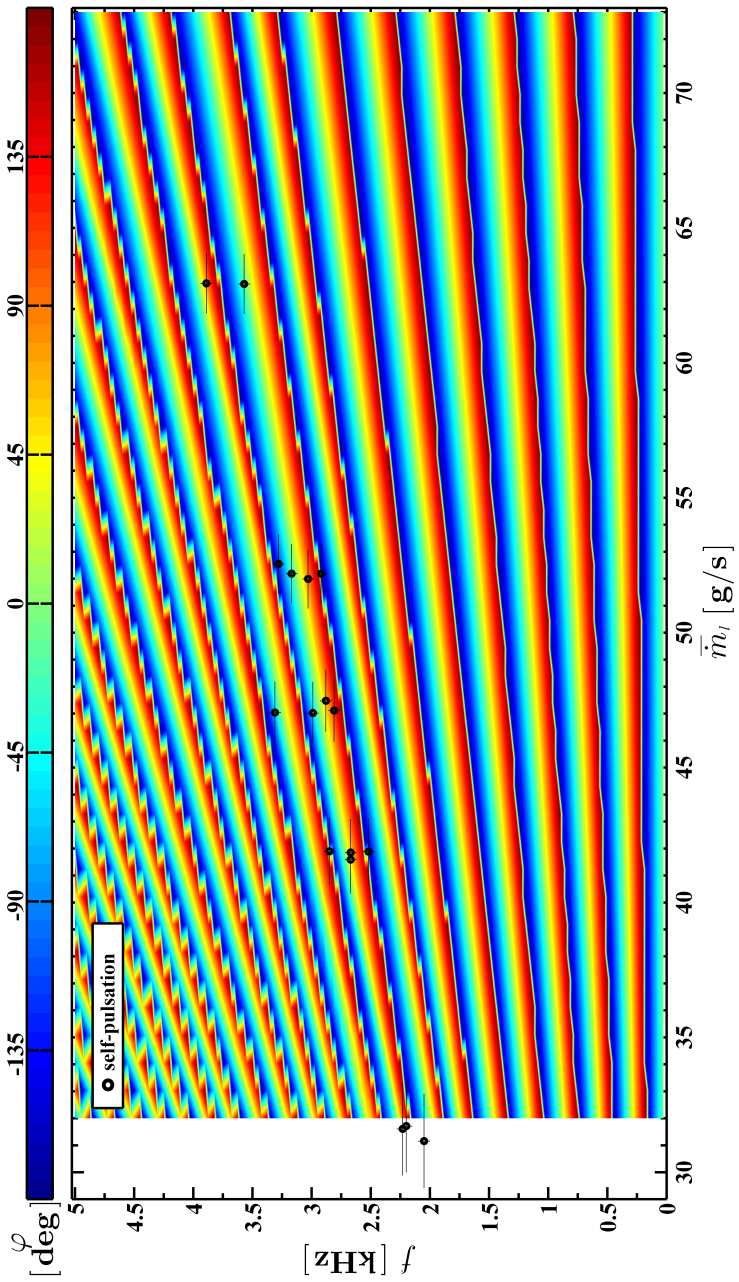

Figure 7.16: Measured frequency of self-pulsation for the non-recessed element overlaid with phase of swirl injector response function.

feedback. By Bode methods [17], response at these frequencies have little phase margin associated with them. Following Nyquist criteria, with enough gain these responses could be susceptible to instability, i.e. unbound growth. At present, it is difficult to comment on the exact phase relationship required to sustain self-pulsation between vortex chamber surface wave resonance and a downstream excitation that might supply such a gain from these calculations without more detailed anchoring of the hydrodynamics model.

7.8 Summary

In this chapter the internal hydrodynamics of the swirl injector were analytically evaluated in order to understand how they participate during resonant self-pulsations. To do so, classical frequency response calculations were augmented to incorporate high frequency wave speeds and were modified to appropriately model surface wave interactions for the injector studied here.

Analysis of the injector response calculations showed a family of high frequency surface waves attributed to the geometry of and flow conditions within the swirl injector's vortex chamber. When the hydrodynamics calculations for the study injector are evaluated across a range of different flow conditions, the frequencies belonging to these surface wave response peaks scale linearly.

The frequencies measured for self-pulsation with the non-recessed injector element were compared directly to the parametric evaluation of the injector response function. The measurements were found to correlate well with the most dominant surface wave within the vortex chamber for all conditions modelled. This result in-

dicates that these surface waves are excited by pressure/flow rate disturbances that occur at the onset and during self-pulation, and indicates that the internal hydrodynamics of the swirl injector are key in determining how the injector responds during self-pulsations witnessed with the injector in this study.

CHAPTER 8

FINAL REMARKS

We shall not cease from exploration
And the end of all our exploring
Will be to arrive where we started
And know the place for the first time.

—Thomas Stearns Eliot, Little Gidding

8.1 Conclusions

Chapter 1 set the stage for this investigation, providing background and motivation for the study of liquid-centered swirl coaxial self-pulsations. Results from an initial assessment of the phenomenon elicited a variety of questions that were systematically detailed in this dissertation through experimental results in concert with analytical assessments. An improved understanding of the liquid-centered swirl coaxial injector and physics which lead to self-pulsations has been achieved in context to fluid oscillator theory. Furthermore, observations potentially practical to the design of swirl injectors for improved LPRE combustion performance and stability have been generated by this work. In review, quantitative statements supported by empirical observations can be made; these principal conclusions are as such:

- **Experiments determined the lower boundaries and range where self-pulsation occurs as a function of water/air momentum flux conditions and swirl post recess**. The self-pulsation phenomenon was measured at frequencies from $\approx$ 900-4000 Hz over the range of flow conditions investigated, and was observed for both non-recessed and recessed configurations of the injector. The frequency of self-pulsation was found to be more dependent on liquid flow rate than any other parameter investigated. Inner post recess Self-pulsation was observed over a wider range of flow conditions when the injector was tested with inner post recess than without recess.

- **Spray oscillations are primarily excited by fluid stripping behavior in the near-field of the injector**. Test conditions lie within in a flow regime where high speed coaxial flows are known to experience fiber type liquid breakup. At conditions just prior to the onset of self-pulsations, waveforms on the exterior surface of the liquid sheet have consistent characteristics with those generated by K-H-type instability. These waveforms were witnessed to undergo stripping by the co-flowing gas. The spray patterns created by the stripping behavior were non-pulsatile, but were found to be periodic. Their frequencies were within 15% of those that occur during resonant oscillation at the lower boundaries of self-pulsation, and were considered precursors to self-pulsation.

- **At the lower boundary of self-pulsation, the spray dynamics transition to instability**. For a fixed liquid flow rate, the gas flow was found to have a destabilizing/stabilizing effect on the spray dynamics in analyzed cases. DMD

analysis showed that below the lower boundary of self-pulsation, the spray was non-pulsatile and had negative damping. As gas flow was increased, damping decreased. At the onset of self-pulsation, damping became positive to indicate self-pulsation is instability-induced. Further increase in gas flow above the lower boundary then led to increased damping to the self-pulsations.

- **Resonance of injector eigenmodes do not explain the full range of measured self-pulsation frequencies**. While at some conditions self-pulsation occurred near longitudinal quarter-wave frequencies of the injector, these specific resonances could not account for the full continuous range of self-pulsation frequencies that were measured.

- **For the conditions modeled, frequencies associated with surface wave response within the swirl injector's vortex chamber correlate well to the measured frequencies of self-pulsation**. The classic linear theory of swirl injector hydrodynamics was extended to the high frequency range with Kelvin dispersion relations and an appropriate surface wave treatment for the study injector. This model resolved new peaks in the injector response function that represent a family of surface wave resonances within the injector.

In summary, observations from this work support the following conclusion on the self-pulsations observed here. For a given liquid/gas flow condition, shear layer instability leads to natural oscillations of the liquid sheet in the near-field of the injector that are non-pulsatile. At a critical condition, liquid stripping from these or other non-pulsatile oscillations generates periodic disturbances in pressure/flow rate

that occur near the exit of the injector element. The internal hydrodynamics of the swirl injector are prone to respond to this external forcing function. Under certain conditions, an elevated surface wave response is excited within the swirl injector that propagates to the liquid sheet in the near-field spray. Stripping of these waves through spray interaction further perpetuates the self-pulsations.

8.2 Recommendations

Bazarov's linear calculations remain the most intuitive and practical theory of swirl injector hydrodynamic behaviors available. Despite, the model and it's several extensions remain largely un-anchored to detailed empirical benchmarking—particularly in the high frequency range. In fact, the effort detailed here constitutes the only convincing empirical and analytical coupling of results to suggest the analytical model can describe aspects of swirl injector hydrodynamics in the high frequency range at all. To address this shortcoming, detailed pulse testing of the swirl injector ought to be carried out to rigorously quantify not only the magnitude response of the injector, but more importantly, the phase response characteristics to pulsed pressure/flow rate conditions across a range of frequencies/amplitudes.

Still, key aspects of how this class of swirl injector dynamics calculation is exacted, particularly those aspects related to the prescription of artificial viscosity and reflection coefficient terms, lack a desired level of detail in precisely what physical processes they encompass. Detailed empiricism or high fidelity computational studies of wave damping mechanisms or flow acceleration and oblique wave reflection/refraction

in the presence of convergent geometry could aid in providing appropriate parameter definition for an engineering-level model.

Future investigations born from questions brought to light from this current work might be better assessed with experimental data that capture the internal fluid dynamics of the swirl injector when under self-pulsation. As such, many of the fluid-resonant characteristics of self-pulsation implicated here could be characterized to a fuller extent with direct visualization.

Finally, aside from their potential to resonate at some conditions, the role of fluid eigenmodes in self-pulsation is not fully understood from data presented here. This is evident by the fact that strong, discrete audible tones are emitted at frequencies far from the nearest eigenfrequency of the injector during a variety of conditions at which self-pulsation is observed. This begs deeper questions related to how injector acoustical phenomena might serve as a feedback mechanism to other internal fluid oscillators such as the liquid film, and whether injector eigenmodes are principal to the phenomenon at all. It is recommended that experimental studies should be conducted to alter pressure wave propagation within the injector and assess effects. This could be potentially achieved in any number of ways, such as by scaling of the gas annulus geometry or swirl injector nozzle length (while impact on the swirl injector hydrodynamics would need be examined). However, likely the most effective manner in which to assess the influence of injector eigenmodes on the self-pulsation phenomenon would be to scale in some way the existing test conditions and test with the same injector hardware studied here. By markedly altering the acoustic velocity

of the injector element, the natural frequencies of the injector would also scale in a significant way.

APPENDICES

APPENDIX A

SWIRL INJECTOR IDEAL HYDRAULIC DESIGN

The study swirl injector was designed based on ideal hydraulic calculations for liquid oxygen flow. As such, the element was sized to generate a nominal liquid film thickness near 473 μm and a total free-cone spray angle of 90^o at 82 g/s flow. Detailed design calculations for this injector can be found described by Ikard [65]. Here the general design procedure is outlined.

The ideal hydraulic design of swirl injectors as documented in Ref. [12] is generally followed here. The methodology employed also incorporates suggestions provided by personal notes and documented instruction [66]. A priori, a series of desired design parameters must be specified, including: steady liquid propellant density, steady mass flow rate, steady injection pressure drop, total spray cone angle, non-dimensional swing arm radius, and number of tangential inlets—$\bar{\rho}_l$, $\bar{\dot{m}}_l$, $\bar{\Delta p}_l$, θ, $\bar{R}_s$, and N_t.

To begin, five non-dimensional parameters based on the principle of maximum flow are computed: the geometric parameter ($\mathfrak{a}$), the nozzle fullness coefficient (ψ), the mass flow coefficient (μ), the characteristic geometric parameter (A), and non-

dimensional liquid film thickness ($\bar{h}$) as such:

$$\mathfrak{a} = \frac{tan^2(\frac{\theta}{2})}{1 + tan^2(\frac{\theta}{2})}, \tag{A.1}$$

$$\sqrt{\mathfrak{a}} = (1 - \psi)\sqrt{\frac{2}{2 - \psi}}, \tag{A.2}$$

$$\mu = \frac{\psi\sqrt{\psi}}{\sqrt{2 - \psi}}, \tag{A.3}$$

$$A = \frac{\sqrt{\mathfrak{a}}}{\mu},\ and \tag{A.4}$$

$$\bar{h} = 1 - \sqrt{1 - \psi}. \tag{A.5}$$

Based on inviscid and incompressible flow, properties of an ideal liquid jet are next computed where jet velocity is defined as:

$$\bar{u}_{jet} = \sqrt{\frac{2\bar{\Delta}p_l}{\bar{\rho}_l}}, \tag{A.6}$$

such that the area of the jet can be deduced as

$$A_{jet} = \frac{\bar{\dot{m}}_l}{\bar{\rho}_l \bar{u}_{jet}}. \tag{A.7}$$

Next, dimensions of the injector's nozzle can be calculated via:

$$A_n = \frac{A_{jet}}{\mu},\ \ where\ \ R_n = \sqrt{\frac{A_n}{\pi}} \tag{A.8}$$

Following, the dimensions of the tangential inlets can thus be computed based on the scaling relation A_t=$\bar{A}_t A_n$ which relates the tangential inlet area to the nozzle area by means of a non-dimensional scalar. The scalar is related to the non-dimensional swing arm radius and the characteristic geometric parameter by $\bar{A}_t = \bar{R}_s/A$. The non-dimensional swing arm radius is suggested to be specified in the range of 1 to 3 [66]. Thus, the radius of the tangential inlets can be expressed as:

$$R_t = 4\sqrt{\frac{\bar{R}_s A_n}{N_t \pi A}}. \tag{A.9}$$

The tangential inlet length is suggested to be at least double that of the tangential inlet diameter [66], such that L_t=$(4...5)R_t$.

Finally, the injector vortex chamber length radius is sized as a function of the non-dimensional swing arm radius and the tangential inlet radius such that:

$$R_{vc} = \bar{R}_s R_n + R_t. \tag{A.10}$$

The vortex chamber length is suggested to be sized as at least 250% of the tangential inlet diameter [66], where L_{vc}=$(5...6)R_t$. Additional parameters of interest include nozzle liquid radius, computed by r_n=R_n-$\bar{h}R_n$, and the head end liquid radius following r_{he}=$\mathfrak{a}R_n$.

APPENDIX B

FACILITY PIPING DIAGRAM

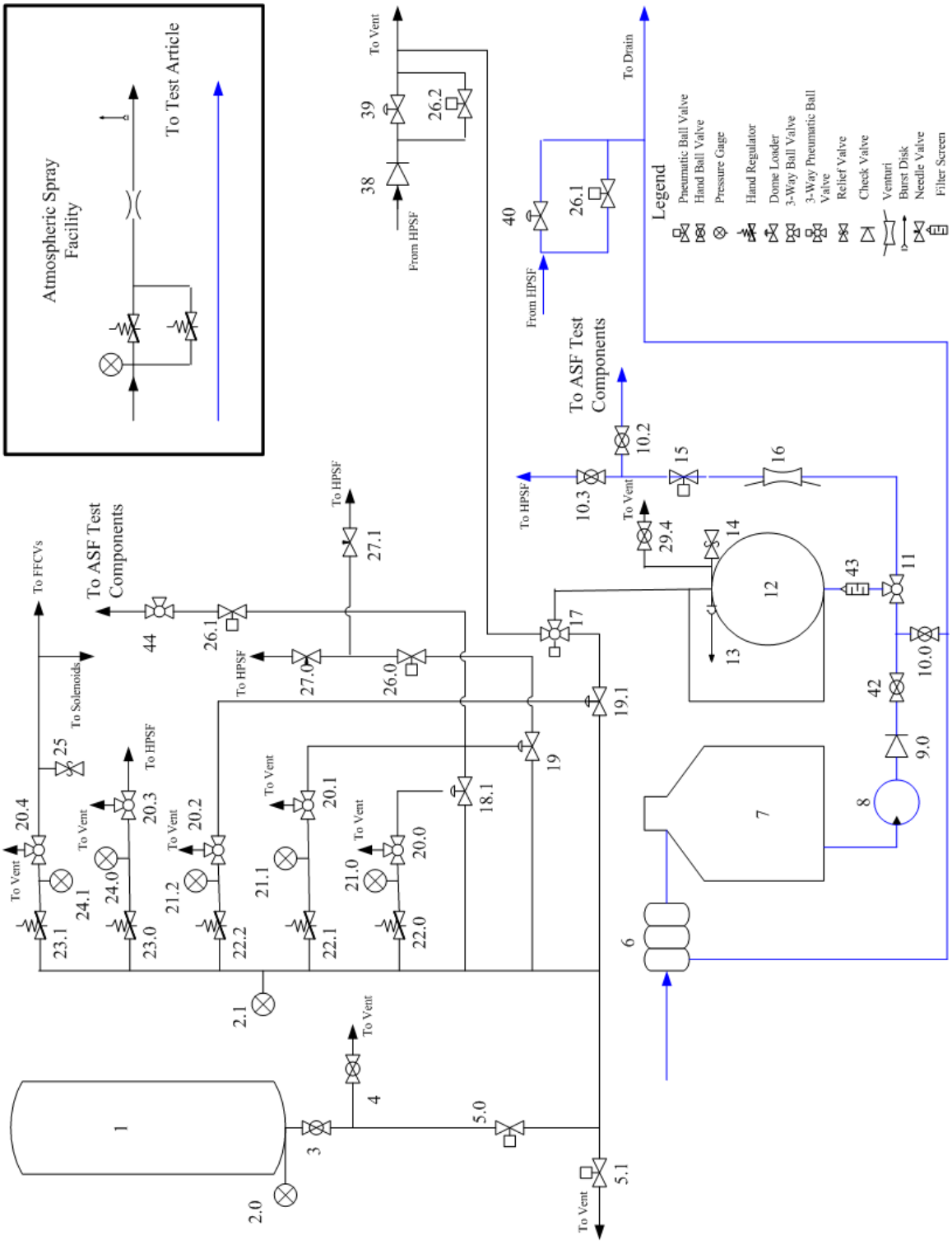

Figure B.1: Spray Facility Piping Diagram

APPENDIX C

ESTIMATIONS OF SWIRL INJECTOR HYDRAULICS

Ideal swirl injector hydraulic characteristics are predicated on the Principle of Maximum Flow [10]. Outside of Russia, this phenomenon was commonly assumed by researchers/practitioners without an explicit proof until the late-1990's when Chinn [11] put the notion as pertaining to the pressure-swirl injector in context with wier flow.

Ideal, inviscid injector hydraulics are governed by conservations of mass, angular momentum, and energy. However, there exists a so-called 'critical' velocity at which gravity waves on the film cannot exceed as flow exits the injector. Since by continuity volumetric flow rate is constant at any point in the liquid film, if the velocity at the injector exit is to be equal to this critical velocity, then the air core and the axial velocity have to adjust to accommodate this condition of maximum flow. This is the Principle of Maximum Flow as understood for the swirl injector.

In Bazarov's [12] ideal calculations, this effect is carried out through the implicit relationship described between film thickness and spray cone angle. However, these ideal calculations do not capture well the dissipative effects that can arise when mass flow is made to deviate for the design point or when an alternative fluid to that

for which the element was designed is introduced. As such, it is common practice to estimate swirl injector hydraulic characteristics by semi-empirical correlation that accounts for such lossy hydraulics and the flow/spray features which are affected. In this study, an expression provided by Suyari and Lefebvre [74] is found to work well in estimating the dissipative hydraulics of the study swirl injector.

$$h_0 = 3.66\{\frac{d_l \dot{m}_l \mu_l}{\rho_l \Delta p_l}\}^{0.25} \tag{C.1}$$

For example, evaluation of the Suyari and Lebebvre correlation for water flow at $\bar{\dot{m}} = 52\ g/s$, $\bar{\Delta p} = 0.27\ MPa$ results in a film thickness estimated at ≈ 636 micrometers. Consider if Bazarov's standard hydraulic parameters are defined by this empirical estimation. First the film thickness term is substituted into the expression of the nozzle fullness ratio, where $\psi = 1 - r_n^2/R_n^2 = 1 - (1 - h_0/R_n)^2$. Next, the injector discharge coefficient, μ, is solved for through the expression $\mu = \psi\sqrt{\psi}/\sqrt{2-\psi}$. The discharge coefficient leads to calculation of the ratio of head end-to-nozzle liquid radii by $\mathfrak{a} = 2(1-\psi)^2/(2-\psi)$. This semi-empirical procedure generally implies that the discharge coefficient must relax from its ideal design point in order to account for dissipative hydraulic characteristics. This notion is consistent with findings from and methods advocated by Khavkin [13], Kenny [71], and Bazarov himself [12].

Consider now the following exercise, wherein a time-averaged image of the spray generated at the stated flow condition is shown in Figure C.1. This image comes from the set of pressure-swirl test cases where the swirl post was recessed by 1 mm, chosen because the set has better image contrast than pressure-swirl images from

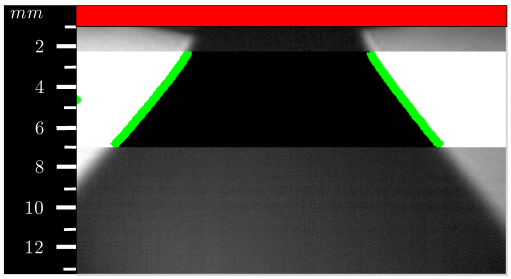

Figure C.1: Time-averaged image of the pressure-swirl spray cone overlaid with binary image and detected boundaries from which spray cone angle is measured.

other tests. The averaged total spray cone angle is measured by objective boundary detection methods applied to the binary region overlaid on Figure C.1, where $\theta = 75.7^o \pm 1.1^o$ on a 95% confidence interval.

Following the above procedure, an estimate of total spray angle can be retrieved by the expression $\theta = 2tan^{-1}(\sqrt{\mathfrak{a}/(1-\mathfrak{a})})$. Recall that at the example flow condition, $h_0 \approx 636$ micrometers; following the above outlined expressions, the spray cone angle is calculated as $\approx 75.5^o$. This value is consistent with measurement and suggests that in this case, dissipative injector hydraulic parameters are well-estimated by semi-empirical calculations based on Suyari and Lefebvre's film thickness correlation.

To extend these calculations to other flow conditions, consider Figure C.3 which plots free cone spray angle computed by the semi-empirical hydraulic calculation procedure along with measurements gathered over a range of test water flow conditions below the design point of the injector. The spray cone generated at these conditions is depicted by imagery in Figure C.2.

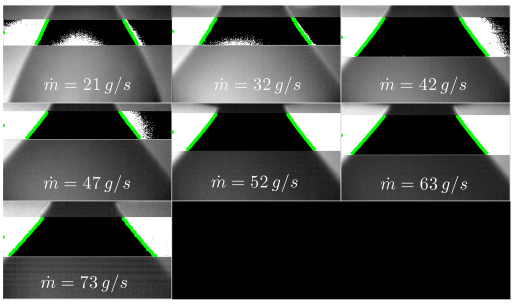

Figure C.2: Time-averaged imagery of pressure-swirl spray cone at different liquid flow conditions with superimposed binary regions where spray cone angle is measured.

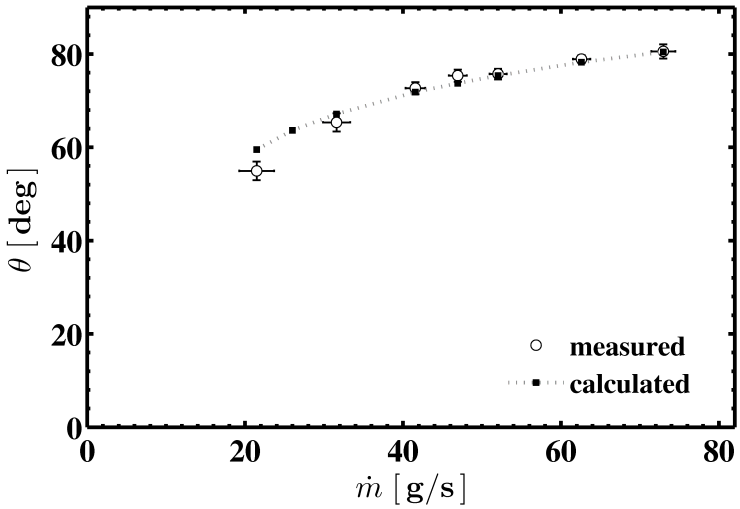

Figure C.3: Measured spray cone angles compared with values by semi-empirical calculations evaluated over the range of liquid mass flow conditions tested in this study.

The angle of the under-developed, 'onion-type' [9] spray cone at 21 g/s is not well captured by semi-empirical estimation. This is likely due to gas core collapse within the injector. However results indicate favorable agreement above 32 g/s suggesting that evaluation of swirl injector features (namely film thickness) based on the semi-empirical hydraulic calculations is sound at all of the flow conditions tested

in this study. These results qualify the basis on which the swirl injector hydraulics are estimated both in how test flow conditions are described and in how they are modelled in this dissertation.

APPENDIX D

ACHIEVED TEST FLOW CONDITIONS

Table D.1: Steady Flow/State Conditions for Parametric Testing at $\Re\Re = 0.30$ (No Recess)

$\bar{\dot{m}}_l$ (g/s)	$\bar{p}_{l,abs}$ (kPa)	$\bar{T}_{l,abs}$ (K)	$\bar{\dot{m}}_g$ (g/s)	$\bar{p}_{g,abs}$ (kPa)	$\bar{T}_{g,abs}$ (K)
20.9	135.8	295	1.5	111.1	292
20.4	133.8	294	1.8	115.1	290
20.5	134.0	295	2.1	122.6	289
20.5	134.2	294	2.5	131.3	288
20.8	135.4	295	2.9	140.9	287
26.5	161.4	294	2.0	118.9	289
26.6	161.7	295	2.4	128.7	289
26.5	161.4	294	2.9	141.1	288
26.6	161.9	294	3.4	155.7	285
26.6	161.7	294	3.8	170.0	285
31.7	191.9	295	2.5	131.1	289
31.2	188.4	295	3.0	144.7	287
31.2	188.1	295	3.6	165.3	287
31.7	191.7	295	4.2	183.6	286
31.6	191.0	294	4.8	207.3	284
42.0	269.4	295	3.5	162.8	286
41.9	268.3	295	4.4	189.6	284
41.6	266.0	295	5.2	222.7	284
41.9	268.6	295	6.1	256.4	282
41.9	268.7	295	7.0	292.2	282
47.0	316.3	295	4.1	179.0	286
47.5	320.9	294	5.1	218.4	283
47.1	317.3	295	6.1	256.6	284
47.0	316.4	294	7.1	296.2	281
47.0	316.6	294	8.2	339.7	281
52.3	371.8	295	4.6	201.4	285
52.0	368.4	294	5.8	245.4	284
52.2	370.5	295	7.0	292.2	284
52.5	374.5	295	8.1	337.2	283
52.2	370.5	294	9.3	384.9	282
62.6	498.7	294	5.8	247.4	284
62.9	502.4	294	7.4	308.0	283
62.9	502.7	294	8.8	365.0	282
62.8	500.7	295	10.3	424.2	282
62.7	499.4	294	11.7	481.8	283
73.1	651.5	294	7.1	296.7	284
73.2	653.7	294	8.9	367.8	282
73.0	649.5	295	10.7	439.5	282

Table D.2: Steady Flow/State Conditions for Parametric Testing at $\Re\Re = 0.42$

$\bar{\dot{m}}_l$ (g/s)	$\bar{p}_{l,abs}$ (kPa)	$\bar{T}_{l,abs}$ (K)	$\bar{\dot{m}}_g$ (g/s)	$\bar{p}_{g,abs}$ (kPa)	$\bar{T}_{g,abs}$ (K)
20.7	134.9	294	1.5	110.0	289
20.4	133.7	294	1.8	115.0	291
20.5	134.0	293	2.2	122.7	288
20.2	133.1	293	2.5	129.9	287
20.4	133.6	293	2.9	139.4	286
26.5	161.3	294	1.9	119.0	290
26.3	160.4	294	2.4	128.8	287
25.8	157.9	293	2.9	141.1	287
26.3	160.1	293	3.4	155.7	285
26.1	159.2	293	3.8	170.9	286
31.2	188.3	294	2.4	130.4	289
31.1	187.6	293	3.0	145.7	286
30.9	186.3	293	3.7	165.1	286
31.6	190.7	293	4.2	184.1	284
31.0	187.2	293	4.8	206.5	284
41.6	266.4	294	3.5	165.3	287
41.5	265.4	294	4.4	192.1	285
41.7	266.7	294	5.2	223.0	284
41.8	267.7	293	6.1	256.1	283
41.8	267.9	294	7.0	291.6	283
47.1	317.0	294	4.0	184.4	287
46.9	315.5	294	5.1	220.0	284
47.1	317.5	294	6.1	259.5	284
47.1	316.7	293	7.2	301.4	290
46.8	314.2	294	8.1	339.4	282
52.0	368.4	294	4.6	209.3	285
53.0	379.2	293	5.8	251.6	284
52.3	371.8	294	7.0	295.7	284
52.1	369.6	294	8.1	338.6	283
52.2	370.3	293	9.3	386.2	284
62.0	490.5	293	5.8	255.8	284
62.3	494.2	293	7.4	312.1	284
62.5	497.4	294	8.8	368.0	284
62.7	499.5	294	10.2	423.5	283
62.8	501.4	294	11.7	480.5	285
73.6	658.9	294	7.0	307.1	285
73.4	655.7	294	8.9	375.4	284
73.4	656.0	294	10.8	447.1	284
73.0	649.5	294	12.5	494.9	284

Table D.3: Steady Flow/State Conditions for Parametric Testing at $\Re\Re = 0.66$

$\bar{\dot{m}}_l$ (g/s)	$\bar{p}_{l,abs}$ (kPa)	$\bar{T}_{l,abs}$ (K)	$\bar{\dot{m}}_g$ (g/s)	$\bar{p}_{g,abs}$ (kPa)	$\bar{T}_{g,abs}$ (K)
21.3	137.3	295	1.4	110.3	294
21.4	137.7	294	1.8	116.2	290
20.6	134.4	294	2.2	127.1	290
20.8	135.2	294	2.5	136.8	289
20.7	134.8	294	2.9	141.6	287
26.3	160.4	294	1.9	(119.4)	293
26.3	160.4	294	2.4	(130.6)	289
26.1	159.3	294	2.9	(142.1)	289
26.3	160.6	294	3.3	(154.6)	287
25.8	158.0	294	3.8	(170.5)	287
31.3	189.3	294	2.4	(131.3)	290
31.2	188.6	293	3.0	(146.6)	289
30.9	186.6	295	3.6	(164.4)	288
31.9	192.6	294	4.2	(183.4)	285
31.5	190.5	294	4.8	(206.2)	285
41.9	268.5	294	3.5	176.0	287
41.7	266.9	294	4.4	206.0	287
41.7	267.0	295	5.3	239.7	286
41.7	267.0	295	6.1	272.3	286
41.7	267.4	295	7.0	308.1	285
47.1	317.2	294	4.1	198.5	286
46.9	315.3	294	5.1	235.0	285
47.2	318.4	294	6.1	274.4	285
47.0	315.9	295	7.1	314.8	285
47.1	317.2	296	8.1	354.3	286
52.1	369.5	295	4.6	219.6	286
52.4	373.5	294	5.8	264.3	284
51.9	367.9	295	7.0	308.5	283
52.5	373.6	295	8.1	352.9	284
52.1	369.1	294	9.3	395.7	284
62.8	500.8	294	5.8	272.0	284
62.9	501.7	294	7.4	327.9	282
62.8	500.7	294	8.8	380.7	282
62.7	499.7	294	10.3	438.6	282
62.7	499.2	294	11.7	486.7	281
73.1	651.5	294	7.0	325.8	283
73.4	656.4	294	8.9	393.9	281
73.0	650.8	294	10.6	457.6	282

Table D.4: Steady Flow/State Conditions for Boundary Testing at $\Re\Re = 0.30$

$\bar{\dot{m}}_l$ (g/s)	$\bar{p}_{l,abs}$ (kPa)	$\bar{T}_{l,abs}$ (K)	$\bar{\dot{m}}_g$ (g/s)	$\bar{p}_{g,abs}$ (kPa)	$\bar{T}_{g,abs}$ (K)
20.3	133.4	295	1.7	113.4	295
26.5	161.2	294	2.4	129.4	289
31.4	189.8	295	3.4	158.3	290
41.3	263.8	295	4.1	180.2	292
47.2	317.9	294	4.7	203.7	292
52.3	371.8	295	5.3	227.0	287
62.6	497.5	294	6.4	271.9	286

Table D.5: Steady Flow/State Conditions for Boundary Testing at $\Re\Re = 0.42$

$\bar{\dot{m}}_l$ (g/s)	$\bar{p}_{l,abs}$ (kPa)	$\bar{T}_{l,abs}$ (K)	$\bar{\dot{m}}_g$ (g/s)	$\bar{p}_{g,abs}$ (kPa)	$\bar{T}_{g,abs}$ (K)
20.8	135.3	294	1.1	103.8	296
26.2	159.9	294	1.4	109.2	292
31.4	189.5	294	1.6	112.6	296
41.8	268.1	294	2.1	123.2	290
47.1	317.0	294	2.2	125.7	292
52.0	368.6	293	2.3	130.6	290
62.6	498.1	294	2.8	143.8	289
73.0	649.9	294	3.3	160.8	290

Table D.6: Steady Flow/State Conditions for Boundary Testing at $\Re\Re = 0.66$

$\bar{\dot{m}}_l$ (g/s)	$\bar{p}_{l,abs}$ (kPa)	$\bar{T}_{l,abs}$ (K)	$\bar{\dot{m}}_g$ (g/s)	$\bar{p}_{g,abs}$ (kPa)	$\bar{T}_{g,abs}$ (K)
20.9	135.5	295	0.8	102.4	297
26.4	161.0	295	0.9	(97.6)	297
31.5	190.3	294	0.9	(98.9)	292
41.8	268.0	295	1.1	107.6	295
46.9	315.3	295	1.2	109.8	295
52.3	372.2	294	1.2	111.7	293
62.8	500.5	295	1.1	112.8	293
73.0	650.1	294	1.3	117.5	292

Table D.7: Steady Flow/State Conditions for Sub-boundary Testing at $\Re\Re = 0.30$

$\bar{\dot{m}}_l$ (g/s)	$\bar{p}_{l,abs}$ (kPa)	$\bar{T}_{l,abs}$ (K)	$\bar{\dot{m}}_g$ (g/s)	$\bar{p}_{g,abs}$ (kPa)	$\bar{T}_{g,abs}$ (K)
20.8	135.3	295	1.6	112.1	293
25.7	157.5	295	2.1	122.4	289
31.1	187.8	295	3.0	145.7	287
41.9	269.2	295	4.0	179.3	286
47.3	319.6	294	4.5	195.4	285
52.0	368.0	294	5.2	222.4	285
62.7	498.8	295	6.0	253.6	284

Table D.8: Steady Flow/State Conditions for Sub-boundary Testing at $\Re\Re = 0.42$

$\bar{\dot{m}}_l$ (g/s)	$\bar{p}_{l,abs}$ (kPa)	$\bar{T}_{l,abs}$ (K)	$\bar{\dot{m}}_g$ (g/s)	$\bar{p}_{g,abs}$ (kPa)	$\bar{T}_{g,abs}$ (K)
20.8	135.3	294	1.1	103.6	295
25.7	157.1	293	1.3	107.3	291
31.4	189.4	294	1.6	111.9	292
41.8	267.5	294	1.9	119.5	289
47.2	317.8	294	2.1	123.2	289
51.9	367.6	294	2.3	128.1	289
62.8	500.6	294	2.7	141.0	289
72.9	648.0	294	3.2	155.6	289

Table D.9: Steady Flow/State Conditions for Sub-boundary Testing at $\Re\Re = 0.66$

$\bar{\dot{m}}_l$ (g/s)	$\bar{p}_{l,abs}$ (kPa)	$\bar{T}_{l,abs}$ (K)	$\bar{\dot{m}}_g$ (g/s)	$\bar{p}_{g,abs}$ (kPa)	$\bar{T}_{g,abs}$ (K)
21.3	137.4	295	0.7	101.0	297
26.4	160.7	295	0.8	(96.6)	296
31.3	189.0	294	0.9	(97.8)	292
41.7	266.9	296	1.0	106.9	295
47.0	316.4	296	1.0	107.7	294
51.9	367.1	294	1.1	109.0	293
52.1	369.2	295	0.8	106.0	292
62.7	499.5	295	1.0	113.7	292

APPENDIX E

PRINCIPAL MODES OF SPRAY OSCILLATION

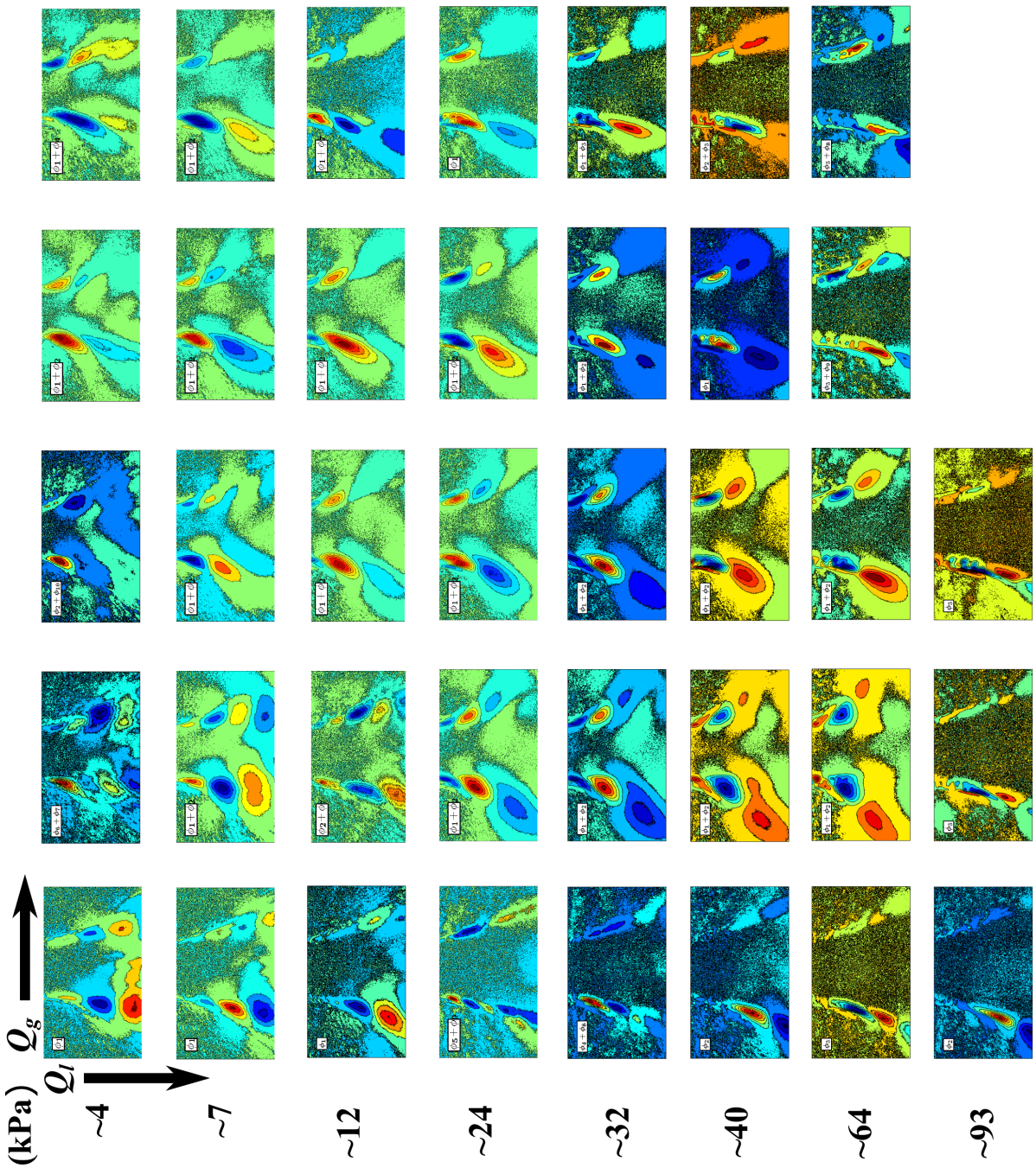

Figure E.1: Spray oscillation modes shapes by POD for all parametric flow conditions at $\Re\Re = 0.30$ (non-recessed).

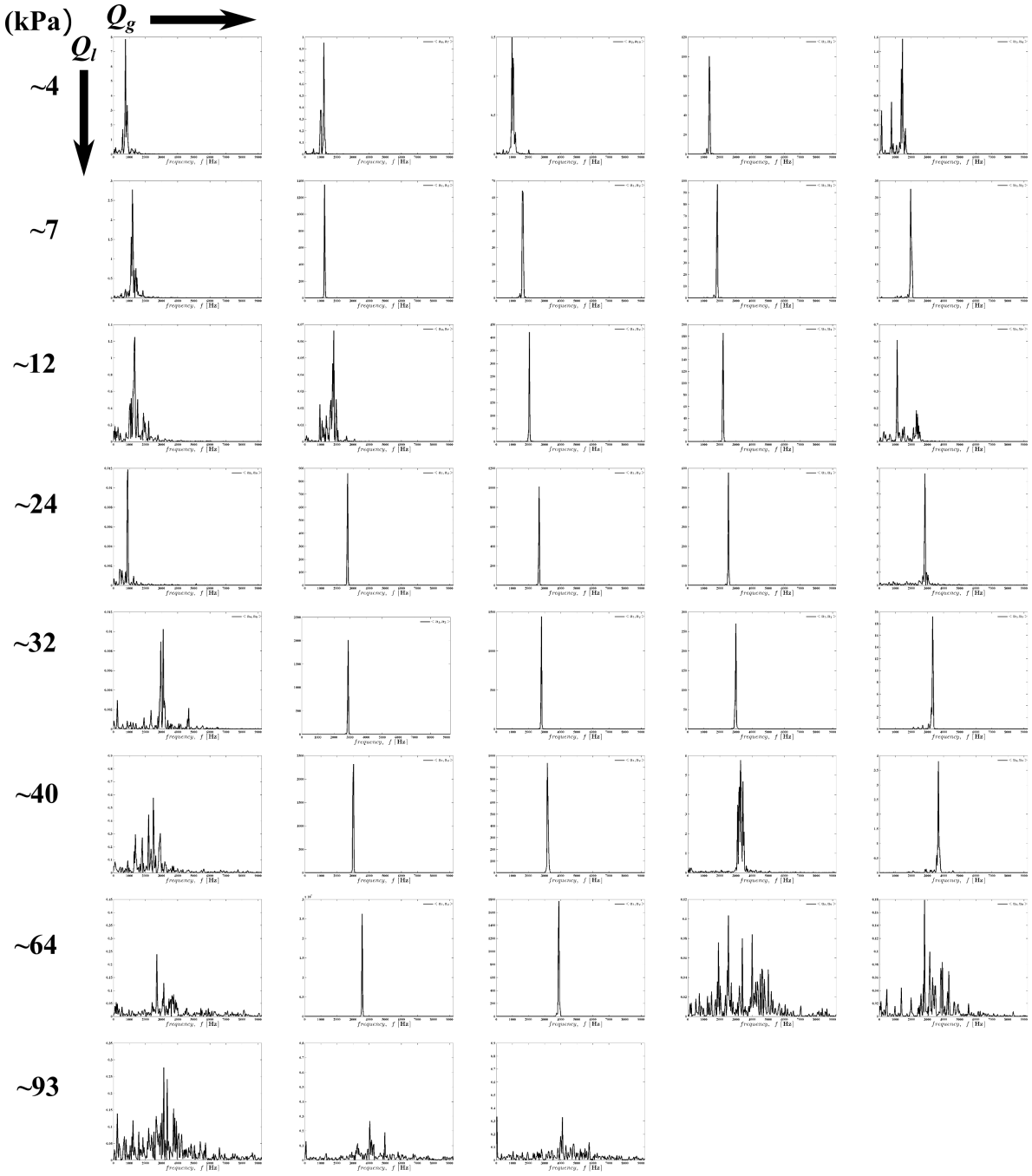

Figure E.2: Spray oscillation spectra belonging to principal POD modes for all parametric flow conditions at $\Re\Re = 0.30$ (non-recessed).

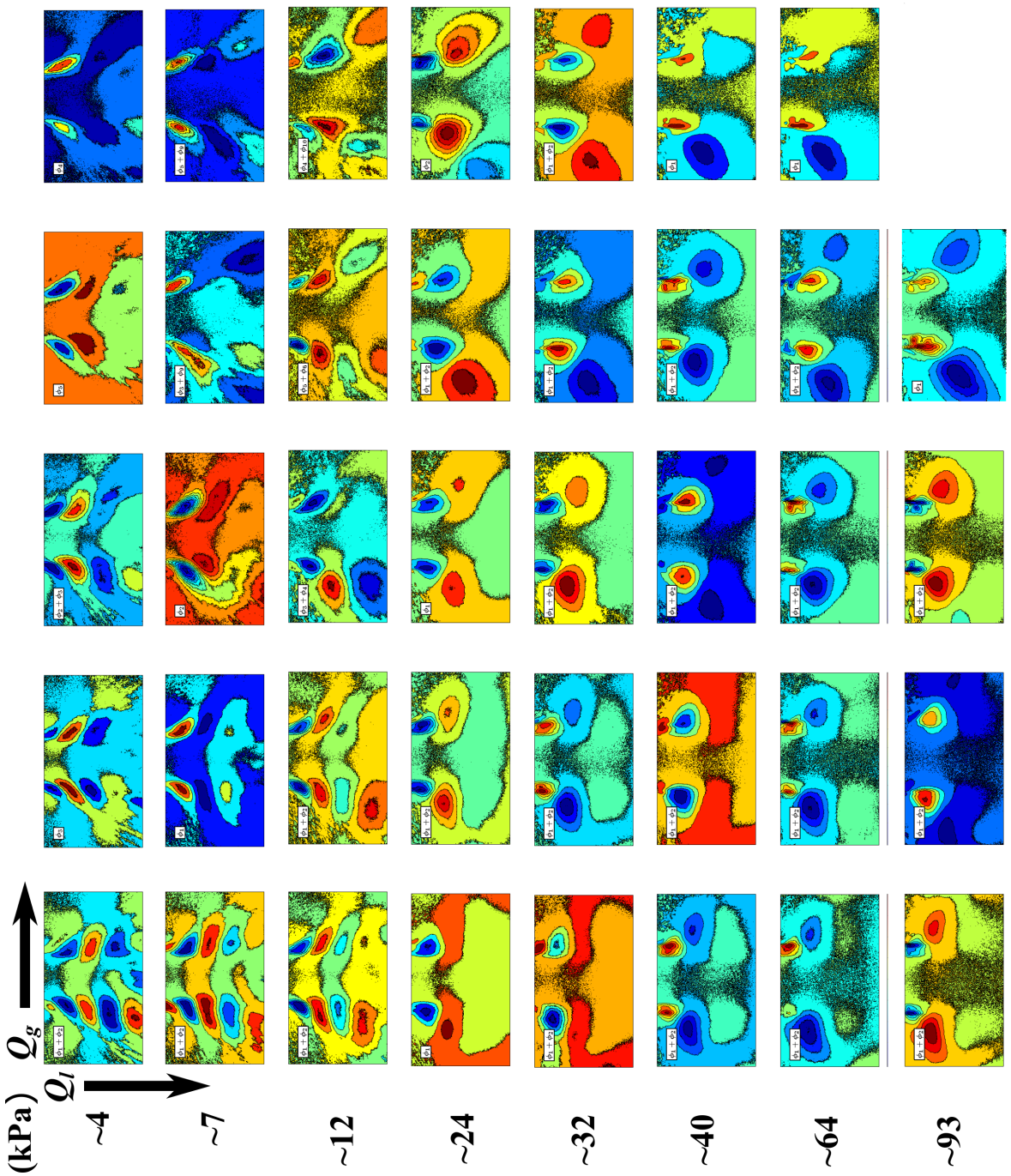

Figure E.3: Spray oscillation modes shapes by POD for all parametric flow conditions at $\Re\Re = 0.42$.

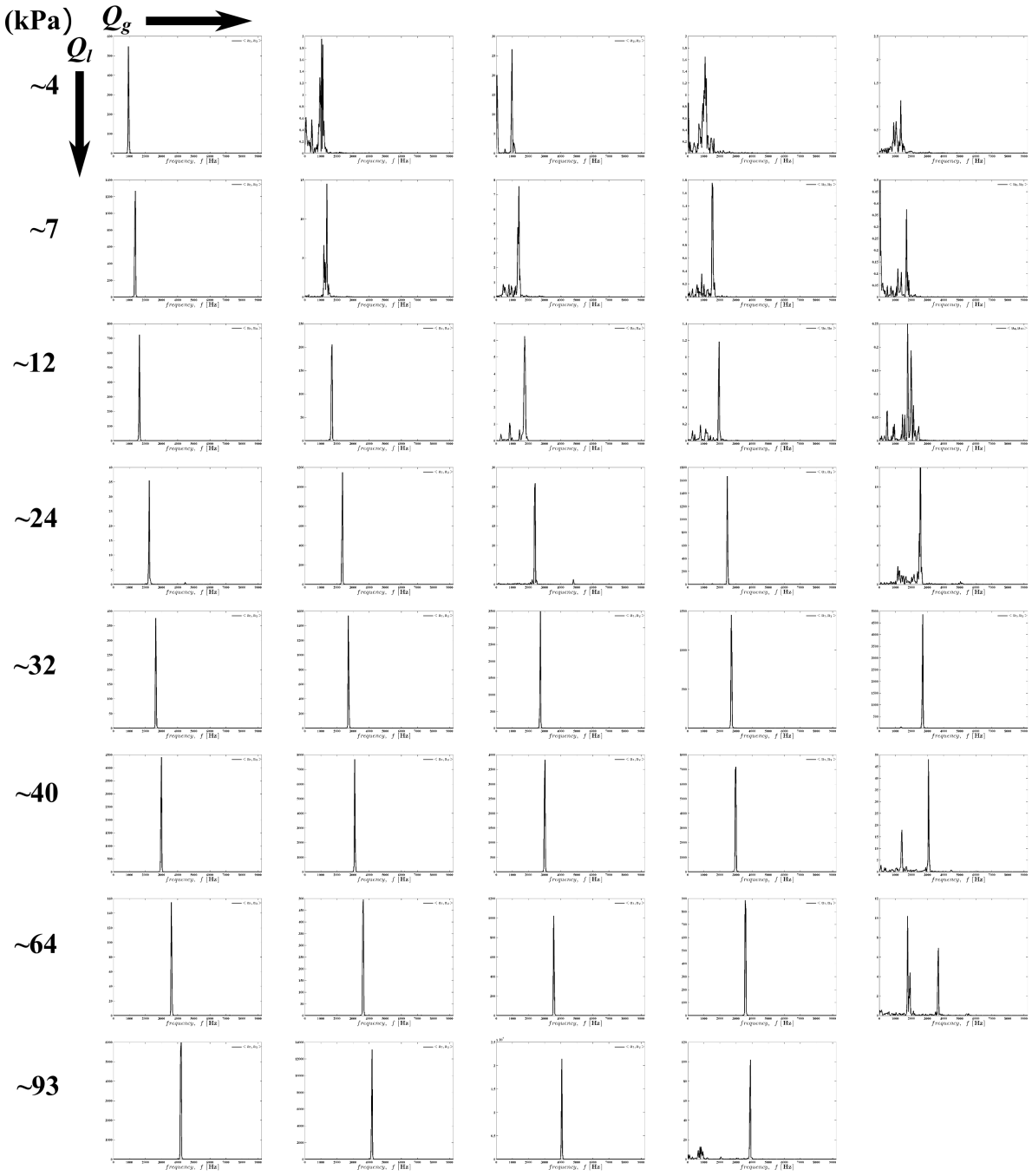

Figure E.4: Spray oscillation spectra belonging to principal POD modes for all parametric flow conditions at $\Re\Re = 0.42$.

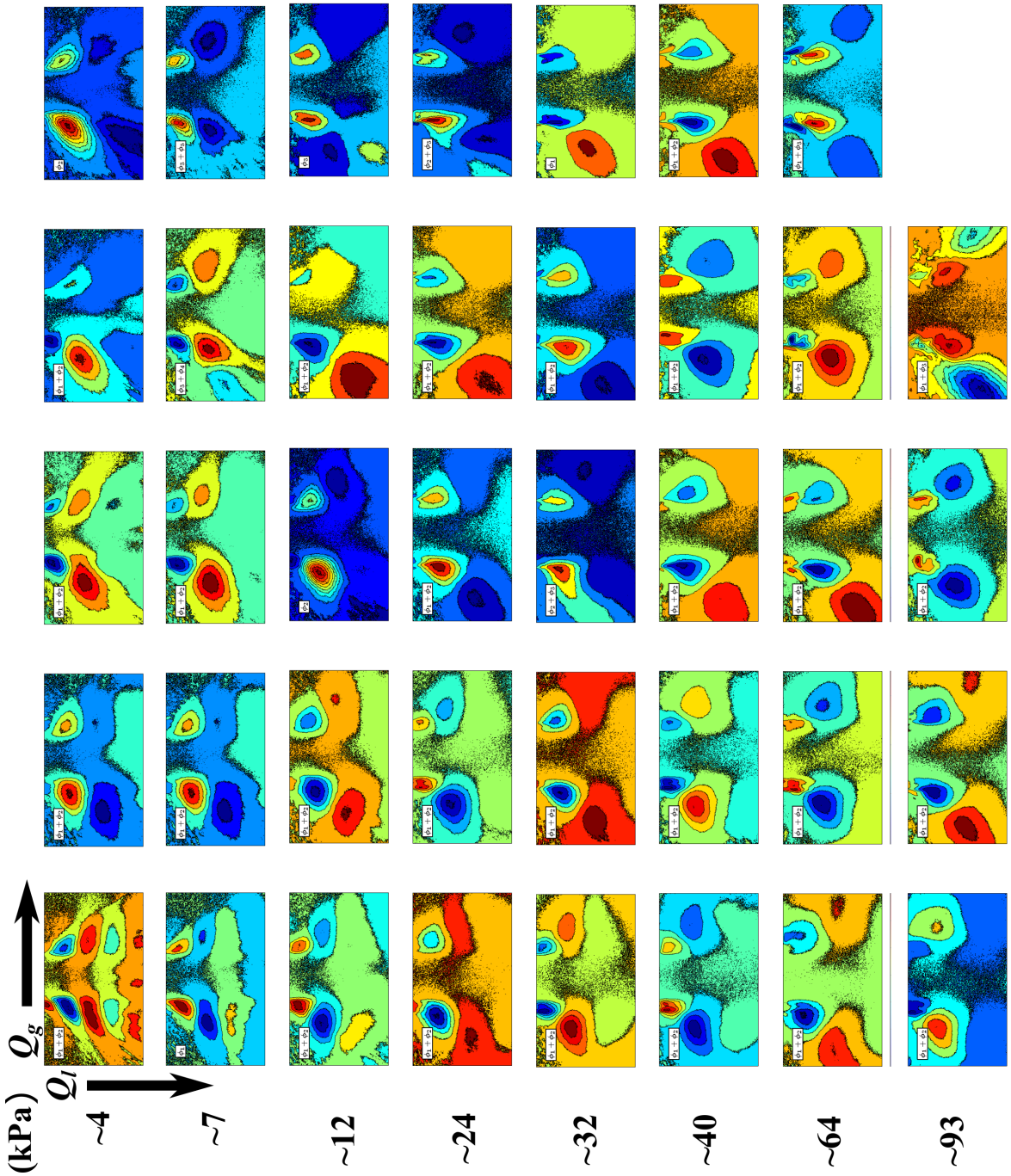

Figure E.5: Spray oscillation modes shapes by POD for all parametric flow conditions at $\Re\Re = 0.66$.

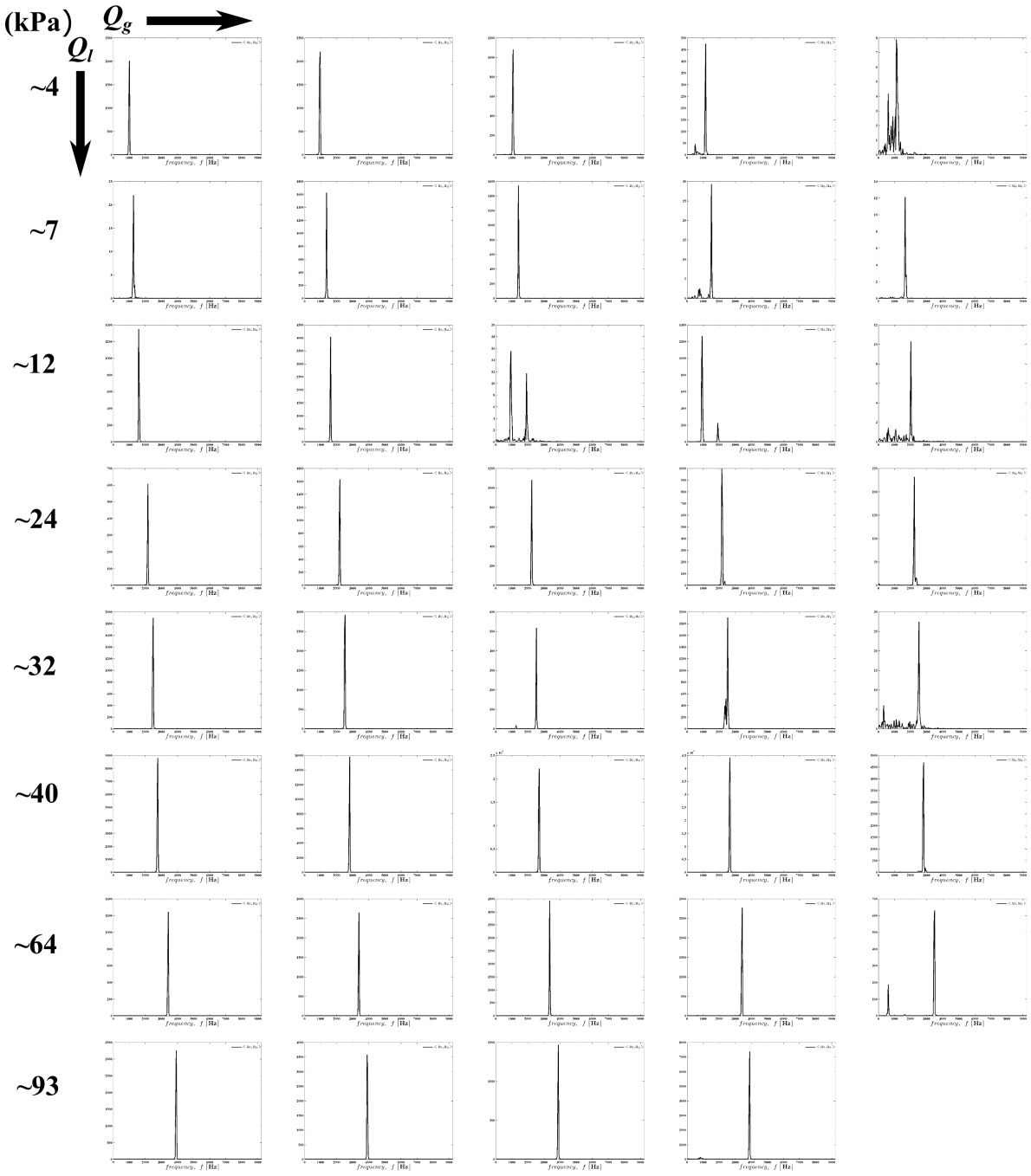

Figure E.6: Spray oscillation spectra belonging to principal POD modes for all parametric flow conditions at $\Re\Re = 0.66$.

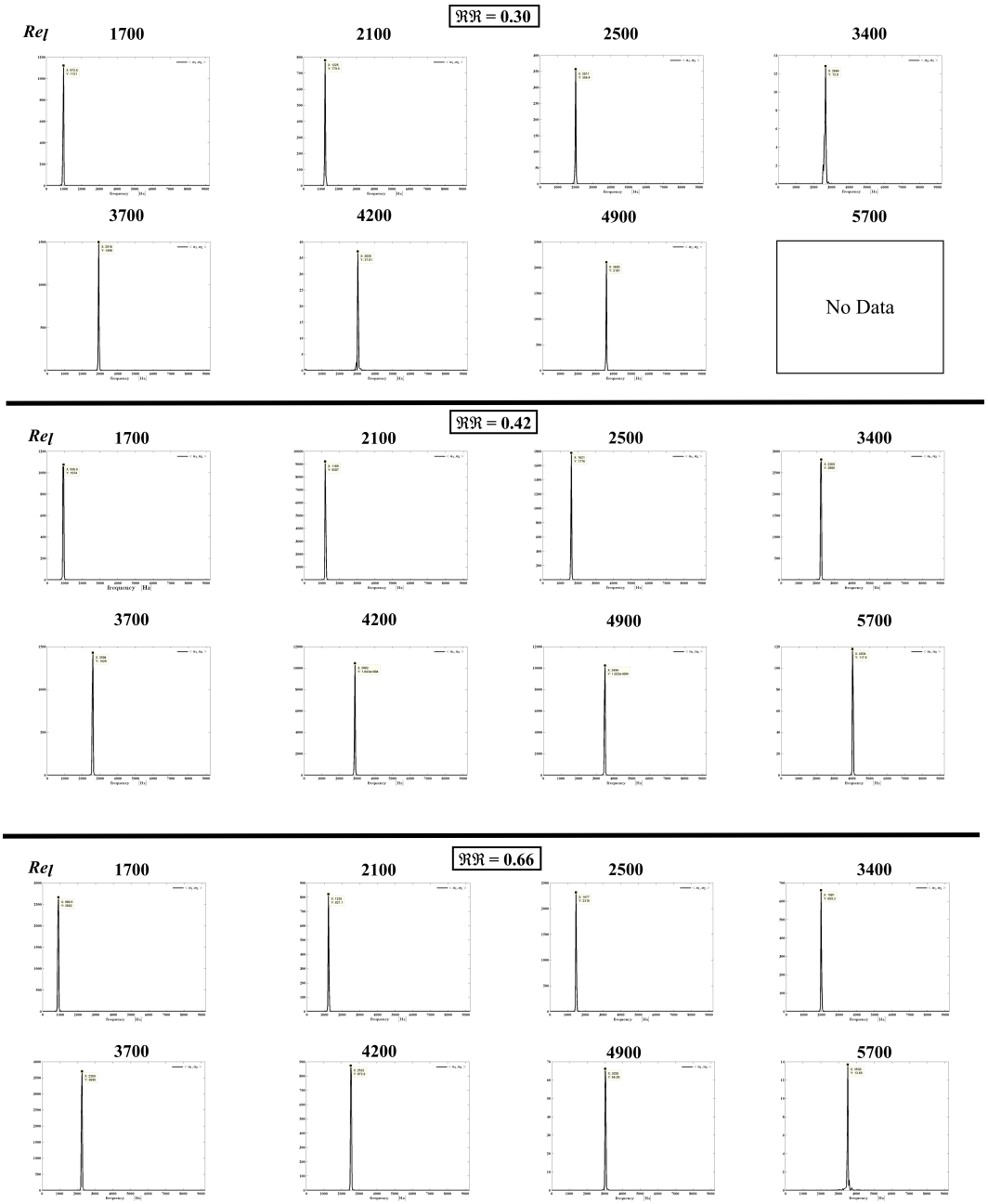

Figure E.7: Spray oscillation spectra belonging to the principal modes of spray oscillation generated during self-pulsations encountered at the lower boundaries for all test recess configurations.

APPENDIX F

SPRAY OSCILLATION STROUHAL NUMBER COMPARISONS

The precursor patterns to self-pulsation that are presented in Chapter 5 are visually consistent with patterns of K-H-type wave growth and also occur within the fiber type breakup regimes where these types of oscillations are known to occur. However, the more nuanced question of whether these patterns are strictly representative of oscillations generated by K-H-type instability or whether they reflect some other type of oscillation(s) cannot be answered for certain in Chapter 5 results.

F.1 Strouhal Number at Excitation

To investigate this aspect of the precursor spray behaviors more closely, the oscillation frequencies identified for the swirl coaxial spray are compared to similar observations with other flows found in the literature. Duke et al. [107] have recently studied various types of oscillation for an annular liquid sheet exposed to air co-flow. The Strouhal number for these oscillations — $St = fh_0/\bar{u}_l$ — was found to correlate well to the Total Momentum Ratio parameter, TMR. This parameter describes the composite shear experienced by the liquid, and is formulated as a simple summation of momentum flux ratio on both the inner and outer surface of the sheet.

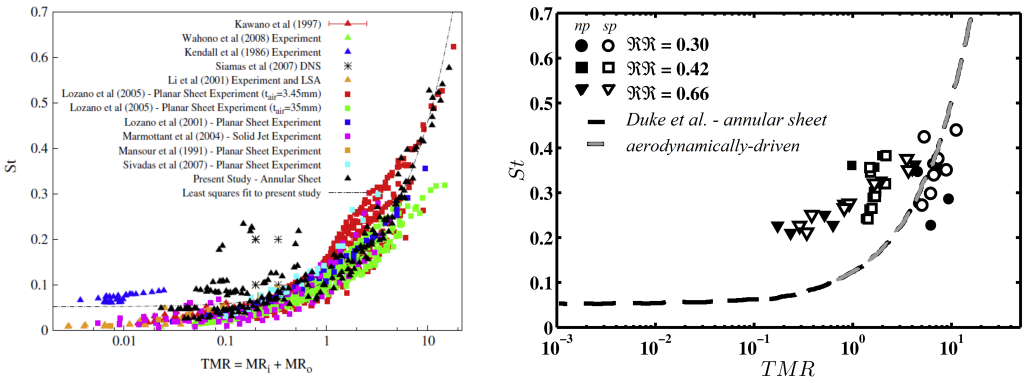

Figure F.1: Spray oscillation Strouhal numbers compiled for a variety of liquid/gas flows [108–117] from Duke et al. [107] (left) alongside liquid-centered swirl coaxial spray oscillation St for the conical liquid sheet near and at the lower boundaries of self-pulsation (right).

Duke et al. [107] also compiled both numerical and experimental data [108–117] that were found to collapse to a similar representative trend. This compilation included different types of sprays, including both planar sheets and round jets exposed to gas co-flow. Based on this result, near-field oscillations measured on the conical sheet in this current study are compared in a similar manner.

A compilation [107] of Strouhal numbers belonging to oscillations for different liquid/gas co-flows [108–117] is depicted in Figure F.1 alongside the swirl-coaxial St calculated for oscillations near and at the lower boundaries of self-pulsation. For liquid-centered swirl coaxial spray oscillations, St is defined in the same way as given in Duke et al. [107]. Here, contributions of shear on the inner surface of the liquid sheet are assumed negligible such that the total momentum ratio is equivalent to the momentum flux ratio defined by Equation 2.2, where $TMR \approx \Phi$.

Figure F.1 establishes that oscillations of the non-recessed liquid-centered swirl coaxial spray measured at conditions near the onset of self-pulsations are related to Kelvin-Helmholtz-type instability. Both non-pulsatile and pulsatile spray oscillations for the non-recessed injector range from $St \approx 0.25$-0.45, and compare favorably with those in the same range presented for the compiled oscillation data. The monotonic trend of St with TMR is also consistent. In this range, the annular sheet oscillations observed by Duke et al. [107] are described to be aerodynamically-driven by shear layer instability, with a wavelength larger than that of the liquid sheet. This type of behavior is also consistent with oscillations that occur during self-pulsation.

F.2 Frequency 'Lock-in' Behavior

For the recessed injector near and at the lower boundaries of self-pulsation in Figure F.1, the overall range of measured St values is consistent ($St \approx 0.25$-0.45) with the range at which oscillations occur for the recessed injector, however an effective bias in momentum flux ratio can be seen. The St-TMR trend for the recessed injector at $\Re\Re = 0.42$ remains generally similar both to that of the non-recessed injector and to that of annular sheet instability shown by Duke et al. [107]. This raises an interesting question about the effect of inner post recess and how similar types of oscillations appear to be sensitive across almost two orders of magnitude in momentum flux ratio. Are these observations a reflection of only natural modes of liquid sheet oscillation, or do they also reflect other underlying oscillations that occur in a similar range of frequencies as the natural modes?

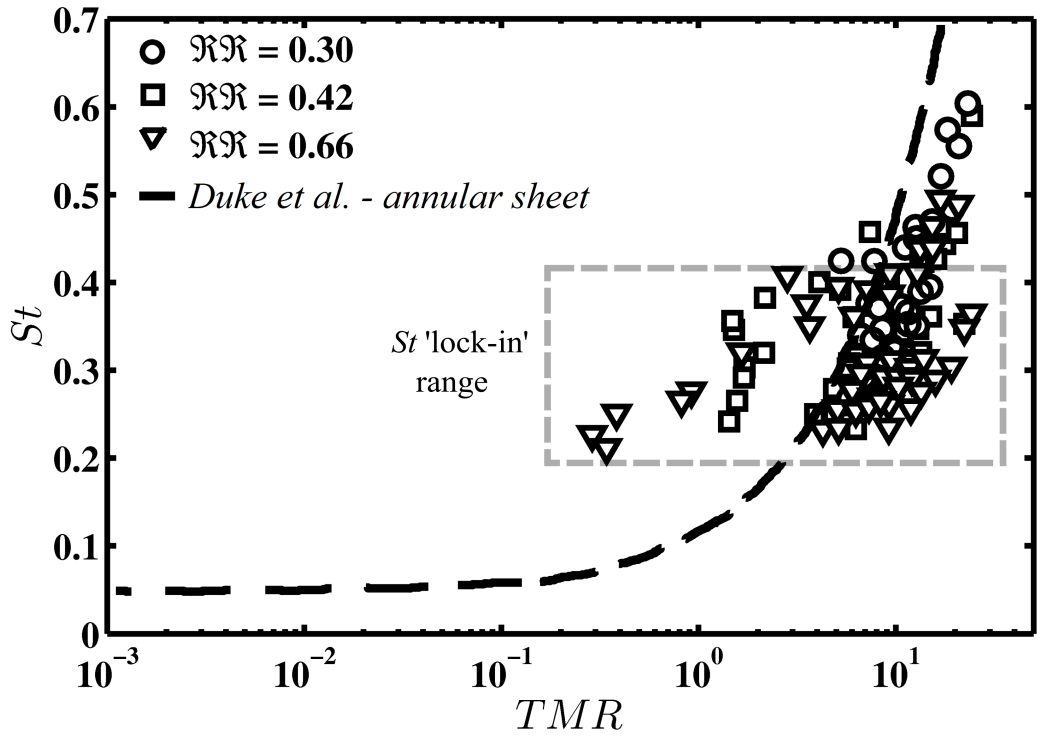

Figure F.2: Strouhal number of liquid-centered swirl coaxial self-pulsation plotted as a function of total momentum ratio.

If the frequency behavior of all self-pulsations is interpreted through its relationship between TMR and St, clues can be seen which further suggest the possibility of other fluid oscillators that participate during self-pulsation response measured here.

Figure F.2 plots the Strouhal number of self-pulsations measured for each configuration of the injector element. When compared with the trend [107] for annular sheet oscillation, it can be clearly seen that self-pulsation St does not fully collapse with higher TMR as it ought to if only the natural modes of the liquid sheet driven by shear instability were to define the frequency of spray oscillation in the pulsatile state. Generally though, the overall St-TMR trend of these data is similar to that shown by Duke et al [107]. However, rather than continue to increase monotonically

to values exceeding $St > 0.7$, the behavior of self-pulsation St is significantly less proportional to TMR.

At $St < 0.4$ in Figure F.2, self-pulsation frequencies seem to remain generally constant with high TMR to indicate a type of frequency 'lock-in' that occurs for most of the inner post recess test cases. Furthermore, there appears no significant shift in the St range for the recessed injector even over almost two orders of magnitude in TMR. This further indicates a self-pulsation St 'lock-in' behavior occurs for many test conditions here. From these results, it seems that in the cases where the injector has inner post recess, underlying oscillations are excited and persist at the same frequency regardless of TMR. 'Lock-in' behavior is a common characteristic of instability-induced fluid resonant oscillations as detailed by Naudascher and Rockwell [53]. These results suggest that resonant self-pulsations may be influenced not only by liquid sheet oscillation by K-H-type instability, but that these oscillations may also couple to other underlying fluid oscillator(s) of the injector to sustain similar frequencies regardless of whether the gas flow conditions change or not.

APPENDIX G

ANALYSIS OF PRESSURE-SWIRL SPRAY DYNAMICS

The spray generated by the pressure-swirl injector is a fundamental aspect of the overall swirl coaxial injector dynamics. Here, modal decomposition analysis is demonstrated on these data, highlighting potential challenges. A brief study is then carried out which aims to resolve similar results described by Im et al. [39]. Due to uncertainties that occur in the interpretation of these data, results from this short study serve to support evidence of K-H-type wave growth activity only in what amounts to a qualitative degree, but support it nonetheless.

G.1 Example Case

The following section will detail the analysis of pressure-swirl injection data. While the POD technique is powerful in extracting spatially-coherent patterns of fluid behaviors and their temporal signatures, it falls short in providing dynamical information pertaining to the stability of the flow field. However, in sacrificing spatially-orthogonal solutions for temporally-orthogonal ones, the DMD technique can be utilized to compliment POD results in such a way that the most dynamically significant (in a temporal sense) fluid modes in a flow field might be identified by

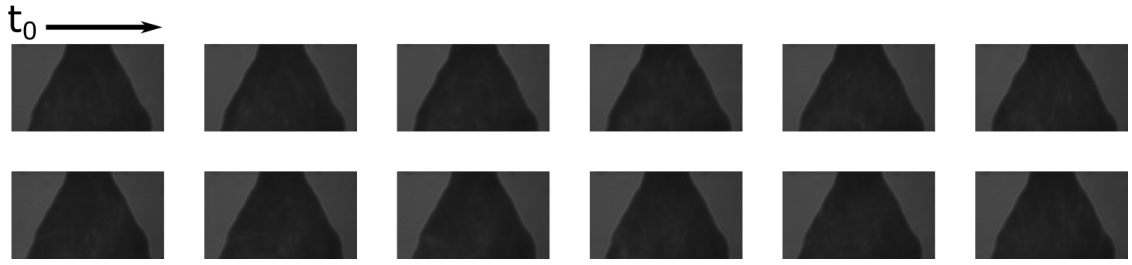

Figure G.1: Moving left-to-right, top-to-bottom; sequence of instantaneous images depicting the propagation of surface waves along the hollow spray cone at $Re_l \approx 1700$. The inter-frame time step is approximately 54.24 μs.

assessing temporal growth rate. Thus, the DMD was implemented as the primary tool in analyzing the high speed imagery of the unsteady liquid spray cone issued during pressure-swirl injection and identifying significant modes of wave motion on the surface of the conical liquid film.

Consider instantaneous images of the hollow spray cone featured in Figure G.1 where liquid is flowing at $Re_l \approx 1700$. Surface waves are manifested as ripples visualized on the edges of the liquid sheet. Note the varying length scales associated with the surface waves, which are a result of amplitude and/or wavelength growth as perturbations propagate from the injection plane. The DMD is applied to an image sequence of identical temporal and spatial parameters as applied to the swirl-coaxial image analyses (369 images over 0.02 seconds with frames cropped at 432x248 pixels) described elsewhere in this dissertation. Figure G.2 plots the DMD spectrum of the data.

Consider contour plots of both the equilibrium mode and the most temporally unstable mode of the spray at $\approx 547\ Hz$ seen in Figure G.3. The equilibrium mode

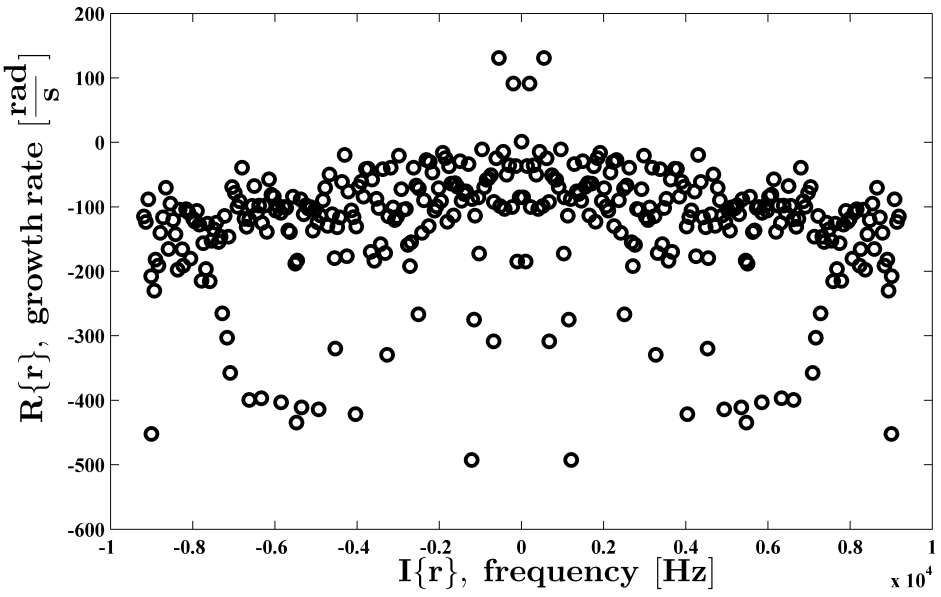

Figure G.2: DMD spectrum of the pressure-swirl injection data.

captures well the mean flow characteristics of the spray—that is a well defined conical liquid sheet that is axisymmetric. Here, hydraulic characteristics such as mean spray cone angle can be readily assessed from this time-averaged component of the flow field.

The lobe pattern of the 547 Hz mode in Figure G.3 captures the streamwise propagation of large amplitude/wavelength surface waves witnessed in the raw imagery; note the axial location of the first lobe along the left hand edge of the spray cone. The is the most temporally unstable mode of spray behavior, and is inferred as the natural mode of sheet oscillation generated by Kelvin-Helmholtz wave growth. Whether this is the varicous or sinuous mode is difficult to comment on for certain since the inner surface of the liquid sheet is not visible; however, the sinuous mode is known to dominant because of higher growth rate.

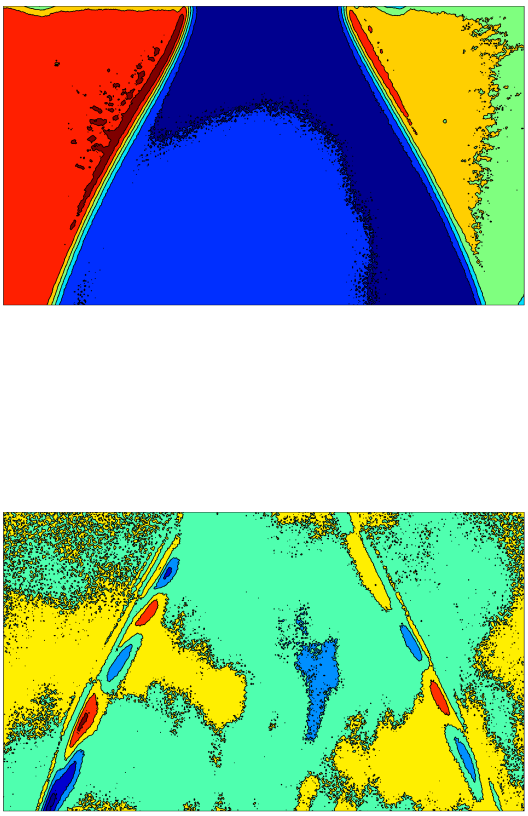

Figure G.3: Contours of the neutrally-stable mode (top) at $\mathbb{I}\{\mathfrak{r}\} = \xi \approx 0$ (color scaling is arbitrary) and the most unstable mode of surface wave propagation (bottom) at 547 Hz.

Further consider contour plots of the lightly damped mode shapes grouped around $\approx$ 1900 Hz that are featured in Figure G.4. These mode shapes describe the propagation of smaller amplitude/wavelength surface waves which originate near the injection plane and propagate the entire streamwise span of the spray cone.

Analysis of the spray imagery by DMD extracts distinct wave patterns that exist on the exterior surface of the liquid spray cone. The equilibrium mode of the

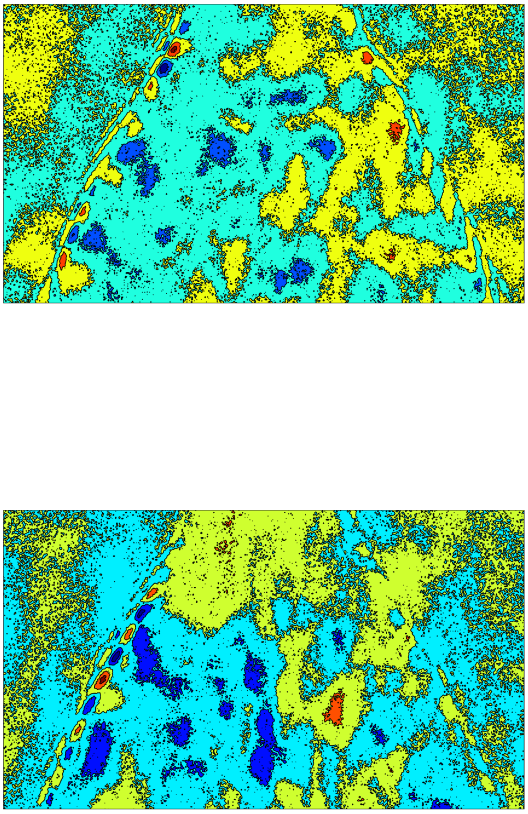

Figure G.4: Contour plots of lightly damped modes of small scale surface wave propagations at 1850 (top) and 1913 (bottom) Hz, respectively.

spray shows axisymmetric qualitities which are consistent with classic time-averaged hydraulic behavior of the liquid spray cone generated by pressure-swirl injectors. Furthermore, the most temporally unstable mode of spray oscillation exhibits a waveform pattern that is consistent with classic descriptions of Kelvin-Helmholtz wave growth on the liquid sheet. These types of waves characterize natural modes of sheet oscillation that lead to liquid breakup at some critical amplitude downstream and that are

known to dominant the primary atomization dynamics of the contiguous liquid sheet. Other higher frequency, smaller scale waveform patterns are also identified that are more temporally damped, but only lightly.

G.2 K-H-type Instability Findings Through Indirect Methods

Im [39] et al. suppose that the dominant waves on the conical liquid sheet are responsible for the onset of self-excited flow oscillation on the spray cone—serving as a fundamental mechanism of excitation to the self-pulsating fluid oscillator system. In their work, Kelvin-Helmholtz-type wave growth is implied responsible for controlling self-pulsation oscillations through analysis of spray frequency as a function of gas Reynolds number. The authors provide indirect evidence of this behavior, wherein the dominant frequency of wave motion on the liquid sheet at $u_g = 0$ was found similar to extrapolation of self-pulsation frequency at $Re_g = 0$. For the sake of comparison, similar analysis exercise is explored here through use of modal decomposition analysis results.

Figure G.5 plots families of self-pulsation frequencies as a function of gas Reynolds number for each $\Re\Re$ configuration. Here, linear trends are plotted and subsequent extrapolations to $Re_g = 0$ are implied similar to that shown by Im et al citeImEtAl.

Consider just a single trend taken from the $\Re\Re = 0.30$ data, wherein the extrapolated value $f_{sp}|_{Re_g=0}$ is approximated near 1370 Hz. Following the analysis by Im et al. [39], this extrapolated value should correspond to the dominant frequency of spray oscillation measured in the downstream spray field of pressure-swirl injection

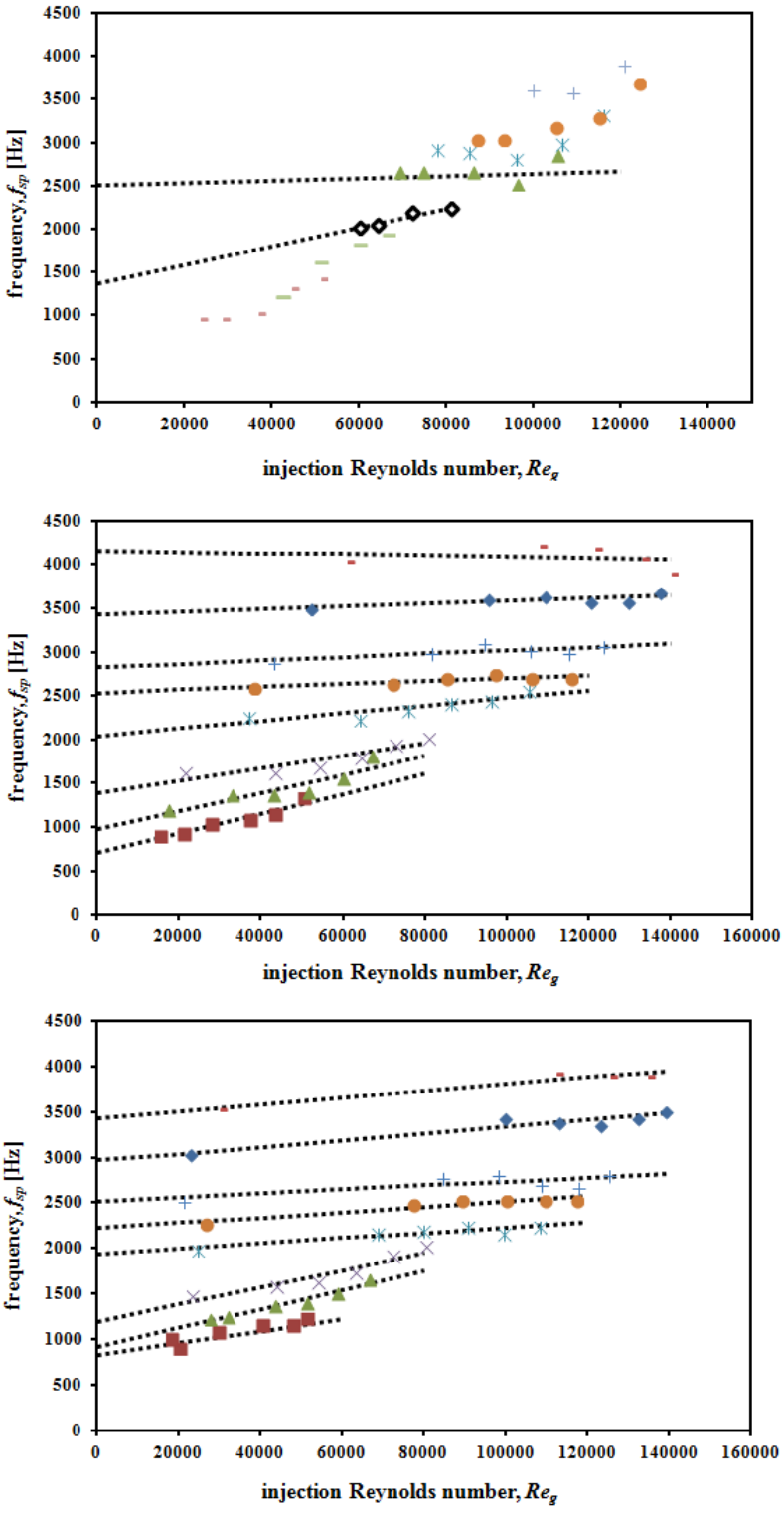

Figure G.5: Self-pulsation frequencies as a function of gas injection Reynolds number for (top-to-bottom) each recess configuration $\Re\Re$ = 0.30, 0.42, 0.66 showing linear extrapolations to $f_{sp}|_{Re_g=0}$ following Im et al. [39] via Lee and Chen [38].

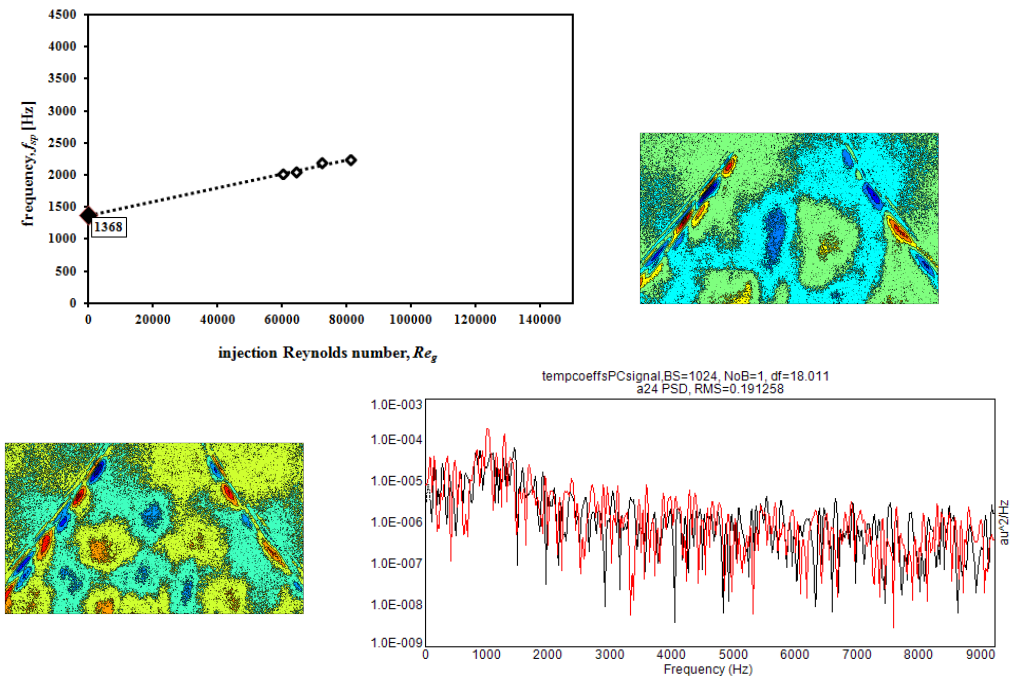

Figure G.6: Extrapolation exercise estimating the frequency of self-pulsation at $Re_g = 0$ (top left); similar small scale surface wave patterns and associated temporal/spectral characteristics extracted by POD provide subjective evidence that organized wave motions on the sheet occur at $\approx$ 1200 (top right) and 1400 (bottom left) Hz near the extrapolated $f_{sp}|_{Re_g=0}$ at 1370 Hz.

where there is no co-annular gas flow present.Figure G.6 plots two spray patterns extracted by POD and their corresponding spectra. Here, each mode is characterized at $\approx$ 1200 and 1400 Hz, respectively. Similarly,Figure G.7 plots DMD spray patterns thought to correspond to the POD mode shapes, wherein each are resolved at 1277 and 1401 Hz and appear lightly damped in nature.

While this particular example successfully yields plausible results, the selection of mode shapes that contain small scale wave patterns is highly subjective for these data. Furthermore, following of this exercise for other test cases yields results that are not as easily interpreted as this example case or the results presented by

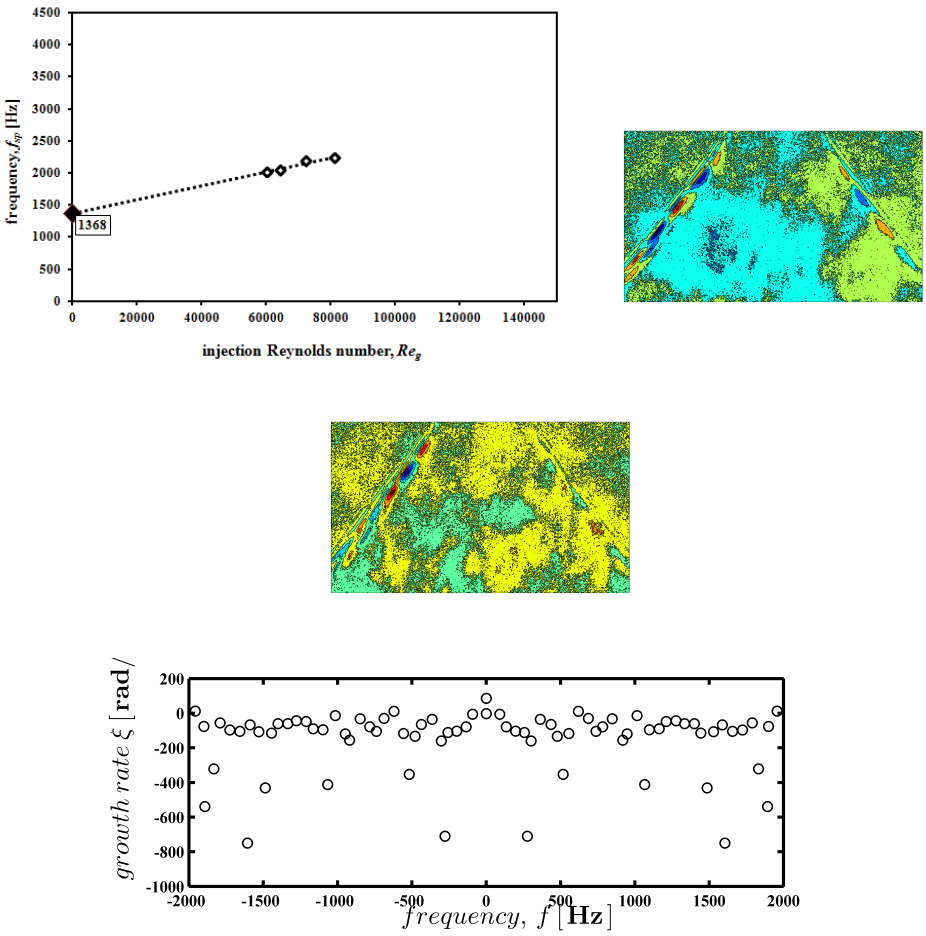

Figure G.7: Extrapolation exercise estimating the frequency of self-pulsation at $Re_g = 0$ (top left); similar small scale surface wave patterns and associated temporal/spectral characteristics extracted by DMD provide subjective evidence that organized wave motions on the sheet occur at ≈ 1277 (top right) and 1401 (mid) Hz near the extrapolated $f_{sp}|_{Re_g=0}$ at 1370 Hz.

Im et al. In some instances such as the one shown in this section, the normalized frequencies $f_{KH}/f_{sp}|_{Re_g=0}$ collapse quite convincingly to suggest self-pulsation frequencies and K-H-type wave growth frequencies are one-in-the-same. However, when considering $\Re\Re = 0.30$ particularly, there exists only sparse agreement. In fact, only two liquid flow conditions at this recess case exhibit a frequency trend confidently approximated as linear with gas injection Reynolds number. Furthermore, the un-

derlying assumption that f_{KH} scales linearly with Re_g at very low values is difficult to follow. For these reasons, a comprehensive analysis of the test data following this 'frequency extrapolation' approach was not carried out.

REFERENCES

[1] G.P. Sutton and O. Biblarz. *Rocket Propulsion Elements*. John Wiley & Sons, Inc., New York, NY, 7^{th} edition, 2001.

[2] R. Atherton. Air Force Reusable Rocket Engine Program XRL129-P-1, Vol. 1., AFRPL-TR-71-1, 1970.

[3] S.K. Elam. Subscale LOX/Hydrogen Testing with a Modular Chamber and a Swirl Coaxial Injector. In 27^{th} *AIAA/SAE/ASME Joint Propulsion Conference*, number AIAA-91-1874, Sacramento, CA, 1991. American Institute of Aeronautics and Astronautics.

[4] J. Hulka, J.A. Schnieder, and C.E. Dexter. Performance and Stability of a Booster Class LOX/H_2 Swirl Coaxial Element Injector. In 27^{th} *AIAA/ASME/SAE/ASEE Joint Propulsion Conference*, number AIAA-1991-1877, Sacramento, CA, 1991. American Institute of Aeronautics and Astronautics.

[5] S.A. Rahman, S. Pal, and R.J. Santoro. Swirl Coaxial Atomization: Cold-flow and Hot-fire Experiments. In 33^{rd} *Aerospace Sciences Meeting*, number AIAA-95-0381, Reno, NV, 1995. American Institute of Aeronautics and Astronautics.

[6] R.K. Cohn, P.A. Strakey, R.W. Bates, and D.G. Talley. Swirl Coaxial Injector Development. In 41^{st} *Aerospace Sciences Meeting*, number AIAA-2003-125, Reno, NV, 2003. American Institute of Aeronautics and Astronautics.

[7] J.R. Hulka and G.W. Jones. Performance and Stability Analyses of Rocket Thrust Chambers with Oxygen/Methane Propellant. In 46^{th} *AIAA/ASME/SAE/ASEE Joint Propulsion Conference*, number AIAA-2010-6799, Nashville, TN, 2010. American Institute of Aeronautics and Astronautics.

[8] P.A. Strakey, D.G. Talley, and J.J. Hutt. Mixing Characteristics of Coaxial Injectors at High Gas/liquid Momentum Ratios. *Journal of Propulsion and Power*, 17(2):402–410, April 2001.

[9] A. H. Lefebvre. *Atomization and Sprays*. Taylor & Francis, New York, NY, 1^{st} edition, 1989.

[10] Y.F. Dityakin, L.A. Klyachko, and V.I. Yagodkin. *Liquid Atomization*. Mashinostroenie, Moscow, Russia, 3^{rd}, in russian edition, 1987.

[11] J.J. Chinn. An Apraisal of Swirl Atomizer Inviscid Flow Analysis, Part 1: The Principle of Maximum Flow for a Swirl Atomizer and its Use in the Exposition and Comparison of Early Flow Analyses. *Atomization and Sprays*, 19(3):263–282, Mar 2009.

[12] V. Bazarov, V. Yang, and P. Puri. Design and Dynamics of Jet and Swirl Injectors. In V. Yang, M. Habiballah, J. Hulka, and M. Poppe, editors, *Liquid Rocket Thrust Chambers: Aspects of Modeling, Analysis, and Design, Progress in Astronautics and Aeronautics, Vol. 200*, pages pp. 19–103. American Institute of Aeronautics and Astronautics, Washington, DC, 2004.

[13] Y.I. Khavkin. *Theory and Practice of Swirl Atomizers*. Taylor & Francis, New York, NY, 1^{st} edition, 2003.

[14] L.P. Bayvel and Z. Orzechowski. *Liquid Atomization*. Taylor & Francis, New York, NY, 1^{st} edition, 1993.

[15] J.J. Chinn. An Apraisal of Swirl Atomizer Inviscid Flow Analysis, Part 1: Inviscid Spray Cone Angle Analysis and Comparison of Invisicid Methods with Experimental Results for Discharge Coefficient, Air Core Radius, and Spray Cone Angle. *Atomization and Sprays*, 19(3):283–308, Mar 2009.

[16] R.D. Ingebo. Atomization of Liquid Sheets in High Pressure Air Flows, NASA-TM-83731, 1984.

[17] D.T. Harje and F.A. Reardon. Liquid Propellant Rocket Combustion Instability, NASA-SP-194, 1972.

[18] J.W. Strutt, Baron Rayleigh. The Explanation of Certain Acoustic Phenomena. *Journal of the Royal Institution of Great Britain*, 8(3):536–542, Mar 1878, Reprinted in The Theory of Sound, 1945.

[19] W.E. Anderson, H.M. Ryan, R.J. Santoro, and R.A. Hewitt. Combustion Instability Mechanisms in Liquid Rocket Engines Using Impinging Jet Injectors. In 31^{st} *AIAA/ASME/SAE/ASEE Joint Propulsion Conference*, number AIAA-95-2357, San Diego, CA, 1995. American Institute of Aeronautics and Astronautics.

[20] W.E. Anderson, K.L. Miller, H.M. Ryan, S. Pal, and and Dressler J.L. Santoro, R.J. Effect of Periodic Atomization on Combustion Instability in Liquid-Fueled Propulsion Systems. *Journal of Propulsion and Power*, 14(5):818–825, Sept 1998.

[21] W.A. Sirignano, J.-P. Delplanque, C.H. Chiang, and R. Bhatia. Liquid-Propellant Droplet Vaporization: A Rate-Controlling Process for Combustion Instability. In V. Yang and W. Anderson, editors, *Liquid Rocket Engine Combustion Instability, Progress in Astronautics and Aeronautics, Vol. 169*, pages pp. 307–343. American Institute of Aeronautics and Astronautics, Washington, DC, 1995.

[22] B. Chehroudi. Physical Hypothesis for the Combustion Instability in Cryogenic Liquid Rocket Engines. *Journal of Propulsion and Power*, 26(6):1153–1160, Nov 2010.

[23] J.J. Hutt and M. Rocker. High-Frequency Injection-Coupled Combustion Instability. In V. Yang and W. Anderson, editors, *Liquid Rocket Engine Combustion Instability, Progress in Astronautics and Aeronautics, Vol. 169*, pages pp. 345–355. American Institute of Aeronautics and Astronautics, Washington, DC, 1995.

[24] J. Hulka and J.J. Hutt. Liquid Oxygen/Hydrogen Instability Phenomena. In V. Yang and W. Anderson, editors, *Liquid Rocket Engine Combustion Instability, Progress in Astronautics and Aeronautics, Vol. 169*, pages pp. 39–71. American Institute of Aeronautics and Astronautics, Washington, DC, 1995.

[25] Anonymous. Summary Report on an Investigation of Combustion Instability for Liquid and Cold Gaseous Hydrogen Propellants, PWA FR-1005, 1964.

[26] N.P. Hannum and E.W. Conrad. Summary Report on an Investigation of Combustion Instability for Liquid and Cold Gaseous Hydrogen Propellants, NASA-TM-X1253, 1966.

[27] V.G. Bazarov. *Liquid Injector Dynamics*. Mashinostroenie, Moscow, Russia, in russian edition, 1979.

[28] M. Wilson. *Evaluation of a Hydro-mechanical Pulsator for Rocket Injector Research*. M.S. Thesis, The University of Alabama in Huntsville, 2010.

[29] W. Thompson, Baron Kelvin. Hydrokinetic Solutions and Observations. *Philosophical Magazine*, 42(281):362–367, 1871.

[30] H. von Helmholtz. *Über* Discontinuierliche Flüssigkeits-Bewegungen (On Discontinuous Movements of Fluids). *Monthly Reports of the Royal Prussian Academy of Philosophy in Berlin*, 23:215–228, 1868, Reprinted in Philosophical Magazine, Vol. 36, No. 244, pp. 337-346, 1868.

[31] W.W. Hagerty and J.F. Shea. A Study of the Stability of Plane Fluid Sheets. *Journal of Applied Mechanics*, 22(4):509–514, 1955.

[32] G.D. Crapper, N. Dombrowski, and G.A.D. Pyott. Kelvin-Helmholtz Wave Growth on Cylindrical Sheets. *Journal of Fluid Mechanics*, 68(3):497–502, March 1975.

[33] Q.-f. Fu, L.-j. Yang, Y.-y. Qu, and B. Gu. Linear Stability Analysis of a Conical Liquid Sheet. *Journal of Propulsion and Power*, 26(5):955–968, Sept 2010.

[34] N. Dombrowski and P.C. Hooper. The Effect of Ambient Air Density on Drop Formation in Sprays. *Chemical Engineering Science*, 4(6):291–305, June 1962.

[35] N. Dombrowski and D.L. Wolfsohn. Some Aspects of Spray Formation from Swirl Spray Pressure Nozzles. *Journal of The Institute of Fuel*, pages 327–331, 1972.

[36] Z. Han, S. Parish, P.V. Farell, and R.D. Reitz. Modeling Atomization Processes of Pressure-swirl Hollow-cone Fuel Sprays. *Atomization and Sprays*, 7(6):663–684, June 1997.

[37] C. Mehring and W.A. Sirignano. Nonlinear Capillary Waves on Swirling, Axisymmetric Free Liquid Films. *International Journal of Multiphase Flow*, 27(10):1707–1734, October 2001.

[38] J.G. Lee and L.D. Chen. Linear Stability Analysis of Gas-liquid Interface. *AIAA Journal*, 29(10):1589–1595, Oct 1991.

[39] J.-H. Im, D. Kim, P. Han, Y. Yoon, and V. Bazarov. Self-pulsation Characteristics of a Gas-liquid Swirl Coaxial Injector. *Atomization and Sprays*, 10(1):57–74, Jan 2008.

[40] J.L. Dressler. Atomization of Liquid Cylinders, Cones, and Sheets by Acoustically-driven, Amplitude-dependent Instabilities. In 5^{th} *International Conference on Liquid Atomization and Spray Systems*, number 41, Gaithersburg, MD, 1991. Institute for Liquid Atomization and Spray Systems.

[41] M. Ismailov and S.D. Heister. Dynamic Response of Rocket Swirl Injectors, Part I: Wave Reflection and Resonance. *Journal of Propulsion and Power*, 27(2):402–411, March 2011.

[42] S. Teshome, I.A. Leyva, D. Talley, and A.R. Karagozian. Cryogenic High-pressure Shear-coaxial Jets Exposed to Transverse Acoustic Forcing. In 50^{th} *AIAA Aerospace Sciences Meeting*, number AIAA-2012-1265, Nashville, TN, 2012. American Institute of Aeronautics and Astronautics.

[43] N.O. Rhys. *Acoustic Excitation and Destruction of Liquid Sheets*. Ph.D. Dissertation, The University of Alabama in Huntsville, 1999.

[44] V.G. Bazarov and L.A. Lul'ka. Self-pulsation of Liquid Flow in Coaxial Air Stream. *Soviet Aeronautics*, 3(1):14–18, 1978.

[45] B.F. Glickman. *Dynamics of Pneumohydraulic Liquid Rocket Engine Systems*. Mashinostroenie, Moscow, Russia, in russian edition, 1983.

[46] A.V. Andreyev, V.G. Bazarov, S.S. Grigoriew, A.L. Dushkin, and L.A. Lul'ka. *Gas-Liquid Injectors Dynamics*. Mashinostroenie, Moscow, Russia, in russian edition, 1991.

[47] V.G. Bazarov and V. Yang. Liquid-propellant Rocket Engine Injector Dynamics. *Journal of Propulsion and Power*, 14(5):798–806, July 1998.

[48] A.L. Andreyev, V. Chepkin, and T.J. Fanciullo. Autovibration of Coax Injector Elements of O_2/H_2 Staged Combustion Liquid Rocket Engines. In 31^{st} *AIAA/ASME/SAE/ASEE Joint Propulsion Conference*, number AIAA-1995-2837, San Diego, CA, 1995. American Institute of Aeronautics and Astronautics.

[49] V.G. Bazarov. Non-linear Interaction in Liquid-propellant Rocket Engine Injectors. In 34^{th} *AIAA/ASME/SAE/ASEE Joint Propulsion Conference*, number AIAA-1998-4039, San Diego, CA, 1998. American Institute of Aeronautics and Astronautics.

[50] J. Zhou, X. Hu, Y. Huang, and Z. Wang. Flowrate and Acoustics Characteristics of Coaxial Swirling Injector of Hydrogen/Oxygen Rocket Engine. In 32^{nd} *AIAA/ASME/SAE/ASEE Joint Propulsion Conference*, number AIAA-1996-3135, Lake Buena Vista, FL, 1996. American Institute of Aeronautics and Astronautics.

[51] M Sasaki, H. Sakamoto, M. Takahashi, T Tomita, and T. Tamura. Comparative Study of Recessed and Non-recessed Swirl Coaxial Injectors. In 33^{rd} *AIAA/ASME/SAE/ASEE Joint Propulsion Conference*, number AIAA-1997-2907, Seattle, WA, 1997. American Institute of Aeronautics and Astronautics.

[52] H. Huang, J. Zhou, X. Hu, and Z. Wang. Acoustic Model for the Self-oscillation of Coaxial Swirl Injector. In 33^{rd} *AIAA/ASME/SAE/ASEE Joint Propulsion Conference*, number AIAA-1997-36468, Seattle, WA, 1997. American Institute of Aeronautics and Astronautics.

[53] E. Naudascher and D. Rockwell. *Flow-induced Vibrations: An Engineering Guide*. Dover Publications, Mineola, NY, 1^{st} edition, 2005.

[54] C.J. Eberhart, D.M. Lineberry, R.A. Frederick, and A.L. Kastengren. A Mechanistic Assessment of Swirl-coaxial Injection by Quantitative X-ray Radiography. *Journal of Propulsion and Power*, 30(4):1070–1079, July 2014.

[55] G.S. Gill and W.H. Nurick. Liquid Propellant Rocket Injector Design, NASA-SP-8089, 1976.

[56] L. Vingert, P. Gicquel, and D. Lourme. Coaxial Injector Atomization. In V. Yang and W. Anderson, editors, *Liquid Rocket Engine Combustion Instability, Progress in Astronautics and Aeronautics, Vol. 169*, pages pp. 145–71. American Institute of Aeronautics and Astronautics, Washington, DC, 1995.

[57] G.B. Cox. Rocket Engine Injection Element Characterization. In 24^{th} *AIAA/ASME/SAE Joint Propulsion Conference*, number AIAA-1988-3135, Boston, MA, 1988. American Institute of Aeronautics and Astronautics.

[58] R.J. Burick. Atomization and Mixing Characteristics of Gas/Liquid Coaxial Injector Elements. *Journal of Spacecraft and Rockets*, 9(5):326–331, May 1972.

[59] R.J. Kenny, J.R. Hulka, M.D. Moser, and N.O. Rhys. Effect of Chamber Backpressure on Swirl Injector Fluid Mechanics. *Journal of Propulsion and Power*, 25(4):902–913, July 2009.

[60] D. Kim, J.-H. Im, H. Koh, and Y Yoon. Effect of Ambient Gas Density on Spray Characteristics of Swirling Liquid Sheets. *Journal of Propulsion and Power*, 23(3):603–611, May 2007.

[61] C.E Dexter, M.F. Fisher, J.R. Hulka, K.P. Denisov, A.A. Shibanov, and A.F. Agarkov. Scaling Technologies for Design, Developement and Test. In V. Yang, M. Habiballah, J. Hulka, and M. Poppe, editors, *Liquid Rocket Thrust Chambers: Aspects of Modeling, Analysis, and Design, Progress in Astronautics and Aeronautics, Vol. 200*, pages pp. 553–600. American Institute of Aeronautics and Astronautics, Washington, DC, 2004.

[62] J.R. Hulka. Scaling of Performance in Liquid Propellant Rocket Engine Combustion Devices. In 44^{th} *AIAA/ASME/SAE/ASEE Joint Propulsion Conference*, number AIAA 2008-5113, Hartford, CT, 2008. American Institute of Aeronautics and Astronautics.

[63] C.J. Eberhart. *Effects of Variable Chamber Pressure on Swirl Injector Atomization.* M.S. Thesis, The University of Alabama in Huntsville, 2010.

[64] H.W. Mulkey. *Development of a Liquid Oxygen Facility for Rocket Engine Injector Performance Testing.* M.S. Thesis, The University of Alabama in Huntsville, 2010.

[65] R.L. Ikard. *Experimental Injector Element Stability Characterization and Combustion Imaging.* M.S. Thesis, The University of Alabama in Huntsville, 2010.

[66] V.G. Bazarov. Lecture Notes. *Advanced Propellant Injectors at The University of Alabama in Huntsville*, 6(3), July 2008.

[67] M. Doumas and R. Laster. Liquid Film Properties for Centrifugal Spray Nozzles. *Chemical Engineering Progress*, 49(10):518–526, Oct 1953.

[68] P.A. Strakey, R.K. Cohn, and D.G. Talley. The Development of a Methodology to Scale Between Cold-flow and Hot-fire Evaluations of Gas-centered Swirl Coaxial Injectors. In 52^{nd} *JANNAF Propulsion Meeting*, number AIAA-2006-4705, Reno, NV, 2004. Joint Army Navy NASA Air Force Inter Agency Propulsion Committee.

[69] H.W. Coleman and G.W. Steele. *Experimentation, Validation & Uncertainty Analysis for Engineers.* Wiley-Interscience Publications, New York, NY, 3^{rd} edition, 2009.

[70] G.S. Settles. *Schlieren and Shadowgraph Techniques.* Springer-Verlag, Berlin, Germany, 1^{st} edition, 2001.

[71] R.J. Kenny. *Influence of Variable Thrust Parameters on Swirl Injector Fluid Mechanics*. Ph.D. Dissertation, The University of Alabama in Hunstville, 2008.

[72] S. Kim, T. Khil, D. Kim, and Y. Yoon. Effect of Geometric Parameters on the Liquid Film Thickness and Air Core Formation in a Swirl Injector. *Measurement Science and Technology*, 20(1):1–11, Jan 2009.

[73] S. Moon, E. Abo-Serie, and C. Baie. Liquid Film Thickness Inside the High Pressure Swirl Injectors: Real Scale Measurement and Evaluation of Analytical Equations. *Experimental Thermal and Fluid Science*, 34(2):113–131, Feb 2010.

[74] M. Suyari and A.H. Lefebvre. Film Thickness Measurements in a Simplex Swirl Atomizer. *Journal of Propulsion and Power*, 2(6):528–533, Nov 1986.

[75] H.B. Bradley. *Petroleum Engineering Handbook*. Society of Petroleum Engineers, Richardson, TX, 2^{nd} edition, 1987.

[76] R.C. Gonzalez and R.E. Woods. *Digital Image Processing*. Pearson Prentice Hall, Upper Saddle River, NJ, 3^{rd} edition, 2008.

[77] G Berkooz, P. Holmes, and J.L. Lumley. The Proper Orthogonal Decomposition in the Analysis of Turbulent Flows. *Annual Review of Fluid Mechanics*, 25:539–575, 1993.

[78] S.B. Pope. *Turbulent Flows*. Cambridge University Press, New York, NY, 1^{st} edition, 2000.

[79] M. Stohr, R. Sadanandan, and W. Meier. Phase-resolved Characterization of Vortex-flame Interaction in a Turbulent Swirl Flame. *Experiments in Fluids*, 51(4):1153–1167, Oct 2011.

[80] M. Wierman, B. Pomeroy, N. Fugger, and W. Anderson. Application of Proper Orthogonal Decomposition to Light Intensity Measurements of Combustion Instability. In 48^{th} *AIAA/ASME/SAE/ASEE Joint Propulsion Conference and Exhibit*, number AIAA-2012-4203, Atlanta, GA, 2012. American Institute of Aeronautics and Astronautics.

[81] M. Arienti and M.C. Soteriou. Time-resolved Proper Orthogonal Decomposition of Liquid Jet Dynamics. *Physics of Fluids*, 21(11):1–15, Nov 2009.

[82] V. Narayanan, M.D.A Lightfoot, S.A. Schumaker, S.A. Danczyk, and B. Eilers. Use of Proper Orthogonal Decomposition Towards Time-resolved Image Analysis of Sprays. In *ILASS Americas* 23^{rd} *Annual Conference on Liquid Atomization and Spray Systems*, Ventura, CA, 2011. Institute for Liquid Atomization and Spray Systems Americas.

[83] J.L. Lumley. The Structure of Inhomogeneous Turbulence. In A.M. Yaglom and V.I. Tatarski, editors, *Atmospheric Turbulence and Wave Propagation*, pages pp. 168–178. Nauka Press, Moscow, Russia, 1967.

[84] K. Pearson. On Lines and Planes of Closest Fit to Systems of Points in Space. *Philosophical Magazine*, 2(11):559–572, Nov 1901.

[85] K. Karhunen. Zur Spektraltheorie Stochastischer Prozesse. *Annales Academiae Scientiarum Fennicae*, A1(34):1–7, 1946.

[86] M. Loève. Fonctions Aléatoires de Second Ordre. *La Revue Scientifique*, 84(9):195–206, Sept 1946.

[87] P. Holmes, J.L. Lumley, G. Berkooz, and C.W. Rowley. *Turbulence, Coherent Structures, Dynamical Systems and Symmetry*. Cambridge University Press, Cambridge, UK, 2^{nd} edition, 2012.

[88] L. Sirovich. Turbulence and the Dynamics of Coherent Structures, Part I: Coherent Structures*. *Quarterly of Applied Mathematics*, 45(3):561–571, July 1987.

[89] P.J. Schmid. Dynamic Mode Decomposition of Numerical and Experimental Data. *Journal of Fluid Mechanics*, 656:5–28, Aug 2010.

[90] P.J. Schmid. Application of Dynamic Mode Decomposition to Experimental Data. *Experiments in Fluids*, 50(4):1123–1130, April 2011.

[91] K.K. Chen, Tu. J.H., and C.W. Rowley. Variants of Dynamic Mode Decomposition: Boundary Condition, Koopman, and Fourier Analysis. *Journal of Nonlinear Science*, 22(6):887–915, Dec 2012.

[92] J.W. Cooley and J.W. Tukey. An Algorithm for the Machine Calculation of Complex Fourier Series. *Mathematics of Computation*, 19(90):297–301, April 1965.

[93] N. Chigier and R.D. Reitz. Regimes of Jet Breakup and Breakup Mechanisms (Physical Aspects). In K.K. Kuo, editor, *Recent Advances in Spray Combustion: Spray Atomization and Drop Burning Phenomena Volume 1, Progress in Astronautics and Aeronautics, Vol. 166*, pages pp. 109–136. American Institute of Aeronautics and Astronautics, Washington, DC, 1996.

[94] M. Barrere, A. Jaumotte, B. Fraeijs de Veubeke, and J. Vanderkerckhove. *Rocket Propulsion*. Elsevier Publishing, Amsterdam, NL, 1^{st} edition, 1960.

[95] L.E. Kinsler, A.R. Frey, A.B. Coopens, and J.V. Sanders. *Fundamentals of Acoustics*. John Wiley and Sons, Inc., Hoboken, NJ, 4^{th} edition, 1999.

[96] R.G. Evans. *Pressure Wave Propagation in Adiabatic Two Phase Flow*. Ph.D. Dissertation, Massachusetts Institute of Technology, 1966.

[97] P.J. van Dijk. *Acoustics of Two-phase Pipe Flows*. Ph.D. Dissertation, Universitiet Twente, 1974.

[98] R.D. Belvins. *Formulas for Natural Frequency and Mode Shape*. Krieger Publishing Company, Malabar, FL, 2^{nd} edition, 2003.

[99] H. Park. *Flow Characteristics of Viscous High-speed Jets in Axial/Swirl Injectors*. Ph.D. Dissertation, Purdue University, 2005.

[100] R. Richardson. *Linear and Nonlinear Dynamics of Swirl Injectors*. Ph.D. Dissertation, Purdue University, 2007.

[101] M. Ismailov. *Modelling of Classical Swirl Injector Dynamics*. Ph.D. Dissertation, Purdue University, 2010.

[102] Q.-f. Fu, L.-j. Yang, and X.-d. Wang. Theoretical and Experimental Study of the Dynamics of a Liquid Swirl Injector. *Journal of Propulsion and Power*, 26(1):94–101, Jan 2010.

[103] T. Khil, Y. Chung, V.G. Bazarov, and Y. Yoon. Dynamic Characteristics of Simplex Swirl Injector in Low Frequency Range. *Journal of Propulsion and Power*, 28(2):323–333, Mar 2012.

[104] B. Ahn, M. Ismailov, and S.D. Heister. Experimental Study of Swirl Injector Dynamic Response Using a Hydromechanical Pulsator. *Journal of Propulsion and Power*, 28(3):585–595, May 2012.

[105] W. Thompson, Baron Kelvin. Vibrations of a Columnar Vortex. *Proceedings of the Royal Society of Edinburgh*, II:155–168, March 1880.

[106] R.M. Sorensen. *Basic Coastal Engineering*. John Wiley and Sons, Inc., New York, NY, 1^{st} edition, 1978.

[107] D.J. Duke, D. Honnery, and J. Soria. The Growth of Instabilities in Annular Liquid Sheets. *Experimental Thermal and Fluid Science*, 68:89–99, November 2015.

[108] S. Kawano, H. Hashimoto, H. Togari, and A. Ihara. Deformation and Breakup of an Annular Liquid Sheet in a Gas Stream. *Atomization and Sprays*, 7(4):359–374, July 1997.

[109] G.A. Siamas and X. Jiang. Direct Numerical Simulation of a Liquid Sheet in a Compressible Gas Stream in Axisymmetric and Planar Configurations. *Theoretical Computational Fluid Dynamics*, 6(21):447–471, November 2007.

[110] A. Lozano, F. Barreras, G. Hauke, and C. Dopazo. Longitudinal Instabilities in an Air-blasted Liquid Sheet. *Journal of Fluid Mechanics*, (437):143–173, June 2001.

[111] A. Lozano, F. Barreras, C. Siegler, and D. Löw. The Effects of Sheet Thickness on the Oscillation of an Air-blasted Liquid Sheet. *Experiments in Fluids*, 39(1):127–139, January 2005.

[112] J. Kendall. Experiments on Annular Liquid Jet Instability and on the Formation of Liquid Shells. *Physics of Fluids*, 29(7):2086–2094, July 1986.

[113] A. Mansour and N. Chigier. Dynamic Behavior of Liquid Sheets. *Physics of Fluids A: Fluid Dynamics*, 3(12):2971–2980, December 1993.

[114] X. Li and J. Shen. Experiments on Annular Liquid Jet Breakup. *Atomization and Sprays*, 11(5):557–573, September 2001.

[115] P. Marmottant and E. Villermaux. On Spray Formation. *Journal of Fluid Mechanics*, (498):73–111, 2004.

[116] V. Sivadas, M.V. Heitoyr, and R. Fernandez. A Functional Correlation for the Primary Breakup Processes of Liquid Sheets Emerging from Air-assist Atomizers. *Journal of Fluids Engineering*, 129(2):188–193, February 2007.

[117] S. Wahono, D. Honnery, J. Soria, and J. Ghojel. High-speed Visualization of Primary Break-up of an Annular Liquid Sheet. *Experiments in Fluids*, 3(44):451–459, March 2008.